# THE EFFECT OF MICROSTRUCTURAL VARIATION ON THE MECHANICAL AND ACOUSTIC PROPERTIES OF SILICON CARBIDE

by

DOUGLAS MICHAEL SLUSARK

A Dissertation submitted to the

Graduate School-New Brunswick

Rutgers, The State University of New Jersey

in partial fulfillment of the requirements

for the degree of

Doctor of Philosophy

Graduate Program in Materials Science and Engineering

written under the direction of

Professor Richard A. Haber

and approved by

_____

_____

_____

_____

New Brunswick, New Jersey

October, 2012

## ABSTRACT OF THE DISSERTATION

The Effect of Microstructural Variation on the Mechanical and Acoustic Properties of Silicon Carbide

By DOUGLAS M. SLUSARK

Dissertation Advisor: Prof. Richard A. Haber

Silicon carbide ceramic materials have many beneficial properties which have led to their adoption in various industrial uses, including its application as an armor material. This is due to the high hardness and stiffness of these materials, as well as a low relative density. The homogeneity of the final properties depends upon the processing history of the material. Factors which affect this include the need for high temperatures and sintering additives to achieve densification, as well as the presence of additive agglomerates and pressing artifacts within the green compact.

This dissertation seeks to determine the effect which microstructural variability has on the acoustic and mechanical properties of sintered silicon carbide materials. Sample sets examined included commercially produced, pressurelessly sintered tiles, as well as additional, targeted tiles which were specifically produced for evaluation in this study. Production of these targeted samples was carried out such that particular aspects of the microstructure were emphasized. These included tiles which were fired with an excess of boron sintering aid as well as tiles which had been pressed to a reduced green body density and then fired.

The sample evaluation procedure which was developed incorporated non destructive evaluation methods, mechanical testing, and both fractographic and image analysis of fractured and polished sections. Non destructive evaluation of the tiles was carried out by Archimedes density and ultrasound scanning at 20 MHz to determine the acoustic attenuation coefficient. Selected samples were chosen for machining into ASTM B-type bend bars on which 4-pt flexure testing was performed. Strength limiting features were designated for each sample set. The correlation between acoustic attenuation coefficient and quasi-static strength was examined both qualitatively and quantitatively. This was done by comparing the primary fracture location of flexure bars to features within the ultrasound maps along with linear regressions of scatter plots of attenuation coefficient and fracture strength.

The analysis showed that while significant variability existed within the strength results from the three sets of flexure bars, the presence of individual strength limiting features were not resolved in the ultrasound scans. However, variations in bulk microstructure corresponding to the three sample sets were represented in the attenuation coefficient values.

**Acknowledgments**

A very wise man once told me that an education is something to be treasured, as it can never be taken away from you. Another wise man has said that graduate school is a marathon, not a sprint, and that you'll never get to the end alone. For me, these statements accurately described the motivation to return to and the process by which I finished graduate school.

First of all, I would like to recognize my dissertation advisor, Prof. Rich Haber. Thank you for your guidance and help during this process, and for helping to direct the research. I would also like to extend my thanks to my dissertation committee: Prof. Dale Niesz, Dr. Steve Miller, and Dr. Vimal Pujari. Thank you to all four of you for your input during the dissertation writing process, and for your suggestions in making this document the best it could be.

We have many fine faculty members in Rutgers Materials Science. Special thanks to Prof. George Sigel for the welcome back, Prof. Roger Cannon for the timely job opportunity, Prof. Lisa Klein for taking a chance, Prof. Victor Greenhut for SEM advice, and Prof. Dunbar Birnie and Prof. Jim Harrington for the year of support. I would also like to thank Dr. Nikolas Ninos of Saint-Gobain Corporation and Dr. Dan Ashkin of BAE Systems, Inc., for preparation of sample sets.

There are some people without which our department would not function. I would like to acknowledge John Yaniero, Phyllis Cassell, and Claudia Kuchinow for their hard work in keeping things together.

For me, one of the best parts of graduate school has been the opportunity to work with a very good group of undergrad students. To Victoria Bartley, Christine Ho, Charlie

McLaren, Sean Quinn, Josh Soltesz, Matt Sulik, and Josh Tan, thank you for helping me get through all of the lab work which formed the basis of this dissertation. Special thanks and gratitude to my right-hand man, Logan Murray. His assistance, especially in these last few months, was a great help in getting this document completed.

The Haber group is one of the largest research groups within Rutgers Materials Science. It would not operate like the well-oiled machine it is without Michelle Sole and Laura Chirichillo to keep things flowing smoothly.

One of the best parts of graduate school for me was the opportunity to work with the great people within this group. Thank you to Steve Mercurio, Dan Maiorano, Rob Wadams, Fatih Toksoy, Steve Bottiglieri, Cari Gulyas, Mihaela Jitianu, Vlad Domnich, Sara Reynaud, Minh Vu, Nick Ku, Vince DeLucca, Bob Bianchini, Steve Bagienski, and Andrew Portune.

I have now spent portions of three decades at Rutgers and have met many fine people who I call friends. To Cari and Chuck Gulyas, Jen Czerepinski, JD Majewski, Ray Brennan and Asha Hall, Will Yourey, Joe Pantina, Sean Quinn, Josh Tan, Jesse Kohl, Ben Groth, and Brian and Meg Viezbicke, I would like to say thank you for being there.

To my buddies Rob, Dan, Fatih, Miller, Stevie B, Steve Merc, Minh, Nick, and Vince, thank you for answering all of my questions and listening to all of my complaints.

To my lifelong friends, I hope that you all know what you mean to me. To Matt and Mike D, Nick, K.E. Lane, Motch and Jen, Guzman and Laina, and Matt Heimann, thank you for keeping me sane and for putting up with the amount of time it took for me to write this document.

Most of all, my greatest thanks goes to my family, for you are my true support system. To my favorite sisters Amy, Em, and Beth, you are the best brothers that a guy could have, and I love you all. Big thanks to Jay, Drew, and Mike for keeping you all so happy, as this definitely increases my quality of life.

To Julie, Helen, Ted, and Walt, thank you for showing me four examples of what hard work and perseverance can lead to, and for setting the example for how I try to live my life.

To my mother and father, Dianne and Walt - How do you thank your parents enough for a lifetime of guidance, support, and most of all, love? Thank you for the gentle encouragement to let me know that I could do this, even when I wasn't always sure.

It's not often that you meet someone in life who just seems to fill all the holes that you didn't even know where there. I found that person in my wonderful and amazing wife Greer. This is an achievement for both of us hun! I would never have gotten through this without your love and support, and I can't wait to see what the future holds for us.

To the staff and faculty of Rutgers Materials Science, and to all of my colleagues, friends, and family, this document is dedicated to you in thanks for all of your support. Well done.

## Table of Contents

## List of Tables

## List of Figures

## 1. Introduction

There is inherent variability in sintered silicon carbide ceramic materials. This is attributed to the methods which are required to form and consolidate dense ceramic bodies. This is referred to as the processing history of a material. This encompasses the pressing or compaction process as well as the firing or sintering process.

The attributes which affect the sinterability of silicon carbide also impart a number of beneficial qualities which lead to widespread industrial use of this material. These properties are the direct result of the strong, covalent bonding between silicon and carbon, which lead to SiC being a hard, stiff material with a relatively low density.[1] Silicon carbide is widely utilized in the abrasives industry, as well as in applications which require good wear resistance. Among those applications which require a material with relatively low weight and high hardness and stiffness, along with good microstructural uniformity, is the use of SiC as an armor material.

Sintering refers to the process where a compact of loosely bound particles is consolidated into a dense, rigid body. The sintering of silicon carbide requires the use of high temperatures and sintering activators to maximize the density of the resultant body. These are required to overcome the low self-diffusion coefficients of Si and C.[2, 3]

One of the challenges facing silicon carbide producers is to maintain homogeneity within the microstructure of the material. Sufficient amounts of sintering aid must be present to enable densification to occur. The presence of a localized excess can lead to the formation of inclusions, or dissimilar materials, which exist in the microstructure. If a difference in mechanical properties exists between these second phases and the host microstructure, they may become sources of stress concentration under loading.

The forming of silicon carbide bodies involves the compaction of loose powder into a semi-rigid form called a green body. One of the most common compaction methods is the process of dry pressing. Agglomerates, or loosely bound masses of particles, may be present within the powder mix. Agglomerates which are not broken up during mixing are then pressed into the green body, which can lead to the formation of inclusions within the sintered part.

Sufficient pressure must be applied during dry pressing to compact and deform individual powder granules to bring them close enough together to eliminate interparticle voids. Voids between particles which have been only been partially compacted, along with agglomerates, may remain after the body has been fired, or sintered, into a rigid mass.

This dissertation seeks to examine the variability in sintered SiC materials, and to determine the effect of this variability on the mechanical and acoustic properties. A number of evaluation techniques will be employed to determine the degree of variability at different scales within the test samples. These will include non destructive techniques such as Archimedes density and ultrasound testing, along with destructive techniques such as four-point flexure testing. Additionally, microstructural observations will be made of features of interest and fracture behavior. These techniques will be applied to a number of sample sets, including commercially available sintered silicon carbide plates, as well as specially produced samples which will emphasize particular aspects of the microstructure. It will be shown that the processing history of these materials has a great effect on the final properties of the sintered body.

## 2. Background

This section will present background information on the structure and forming of silicon carbide, as well as different evaluation techniques. In an effort to present the motivations and methods for forming a research approach in this area of study, previous work on this topic will be examined.

### 2.1. Silicon Carbide

As previously stated, silicon carbide has many beneficial properties that make it suitable for numerous industrial applications. These include high compressive strength and hardness, as well as a high elastic modulus.[1] These properties can be directly attributed to the crystal structure of silicon carbide, and to the strong covalent bonding between atoms.[4]

#### 2.1.1 Crystal Structure

While the long-range structure of silicon carbide is complex, the short-range order may be thought of as a four-coordinate, diamond-like arrangement of alternate silicon and carbide atoms.[4] The long-range order becomes increasingly complicated due to the number of polytypes present in silicon carbide, which can be considered to be closely related crystal structures that exhibit similar lattice energies.[5] All silicon carbide structures are comprised of planes of tetrahedra with the arrangement $AB_4$, either as $SiC_4$ or $CSi_4$.[5] The tetrahedra are ordered such that the three-dimensional lattice is composed of hexagonally patterned bilayers of carbon and silicon.[6] Four-fold coordination is satisfied at each point within the structure through the linking of the corners of

tetrahedral.[6] In reference to the directionality of the tetrahedra, stacking may occur either parallel or anti-parallel to the layer below, as shown in Figure 2.1.[4] Successive parallel/anti-parallel stacking of layers within the structure can lead to an almost infinite number of stacking permutations while preserving the stoichiometry of the system.[6]

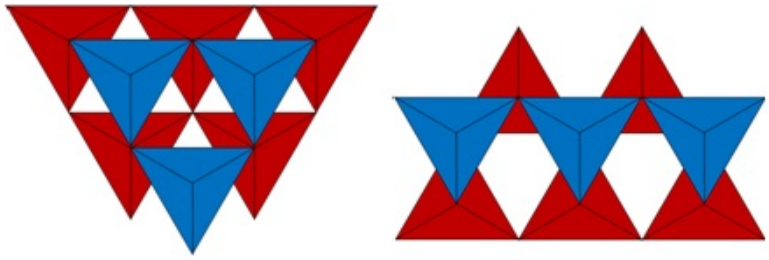

**Figure 2.1** Parallel and anti-parallel stacking of alternating layers in silicon carbide materials, leading to formation of multiple polytypes[4]

As of 2006, more than two-hundred fifty polytypes have been identified in silicon carbide.[7] The atomic arrangement within the polytype SiC-4H is shown in Figure 2.2. In this illustration, carbon atoms are denoted in black, while silicon atoms are denoted in white. Multiple notations have been developed to describe the distribution of silicon and carbon atoms in each polytype. The most common notation currently employed, as developed by Ramsdell, uses the form *nL*, where *n* refers to the periodicity of the stacking and *L* refers to the general crystallographic symmetry of the lattice.[8] Polytypes considered as having important industrial uses include SiC-3C (also known as β-SiC), SiC-4H, and SiC-6H (also known as α-SiC).[9] β-Sic is a metastable form that is the most commonly produced polytype at lower temperatures, while α-SiC is the most stable polytype above 2000°C.[10, 11]

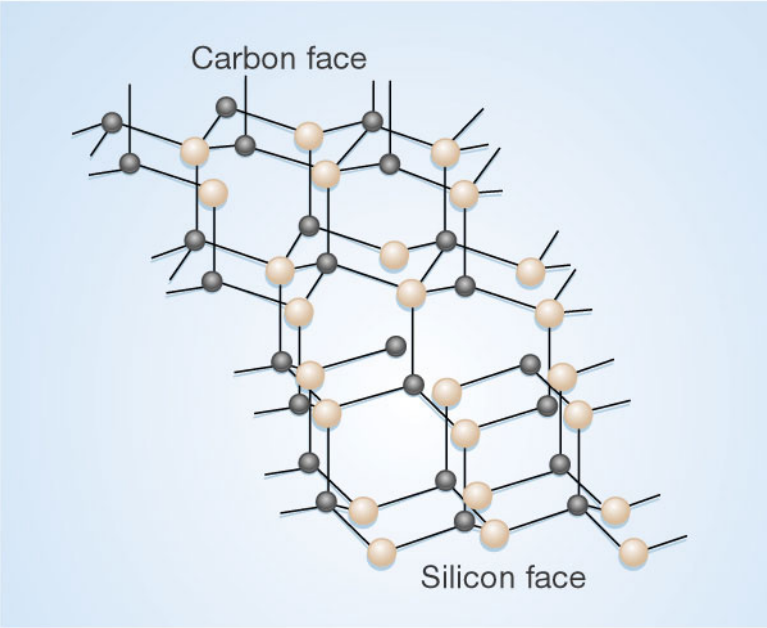


**Figure 2.2** Illustration of crystallographic orientation of $SiC_4$ and $CS_4$ tetrahedra within silicon carbide 4H polytype. Black–carbon atoms. White–silicon atoms[12]

### 2.1.2 Mechanical Properties

SiC has a theoretical density of 3.21 g/cm$^3$, and by weight is comprised of 70.05% Si, and 29.95% C.[13] Silicon carbide materials are characterized by high hardness, high compressive strength, and high elastic moduli. Silicon carbide is considered to be the fourth hardest material available. Only diamond, boron carbide, and cubic boron nitride have higher hardness values.[10, 13] These properties are due to the strong covalent bonding between silicon and carbon.[14] The degree of covalency has been measured at close to 87%, which also contributes to the high melting point and minimal high-temperature induced creep attributed to this material.[14]

As is shown in Table 2.1, the mechanical properties of silicon carbide vary according to the sintering method and form of silicon carbide. Hot-pressed silicon carbide materials tend to have increased quasi-static strength, hardness, and elastic

moduli when compared to the sintered form. This can be attributed to the differences in the concentration and type of activators necessary to achieve pressureless and pressure-assisted sintering, as well as to reduced levels of residual porosity. Flexure strength and microhardness tend to be very sensitive to local changes in the modulus in the interaction area of the test method. What is important to note is that the resultant properties of a piece depend not only on the inherent structure of the material but also on the processing history.

**Table 2.1** Mechanical properties comparison of different forms of silicon carbide[15-18]

| Type of SiC | Young's modulus (GPa) | Shear modulus (GPa) | Flexural strength (MPa) | Knoop hardness ($HK_{0.1}$) |
|---|---|---|---|---|
| | | | | |
| α-SiC, hot-pressed | 440 | 177 | 530 | 3100 |
| α-SiC, sintered | 410 | | 460 | 2800 |
| β-SiC, sintered | 410 | 140-190 | 650 | |

Flexural strength values of 600 MPa, compressive strength values of 2.48 GPa, fracture toughness of 5.2 $MPa \cdot m^{1/2}$, and Knoop hardness of 31 GPa have been reported for silicon carbide materials.[19] In contrast to most materials possessing this combination of high strength and hardness, SiC has a low density value of ~ 3.16-3.20 $g/cm^3$.[20] These properties form the basis of the use of silicon carbide as an armor material.

### 2.1.3 Thermal and Electrical Properties

The structure of silicon carbide also has an effect on thermal and electrical properties. The thermal conductivity of silicon carbide is high when compared to other ceramic materials. This value has been measured at 150 W/m·K at 20°C and 54 W/m·K at 1400°C.[10] Silicon carbide has a low coefficient of thermal expansion (CTE) of 4.7 x $10^{-6}$ between 20 and 1400°C.[10] These two properties lead to silicon carbide having a high thermal shock resistance.

Silicon carbide is also a semiconductor. The band gap for various polytypes ranges from 2.4 to 3.3eV.[16] The band gaps for the 4H and 6H polytypes are 3.26 and 3.03eV, respectively.[10] For this reason silicon carbide is considered to be a wide band gap material. The electronic structure is stable at temperatures of over 550 °C.[16] The conductivity of SiC-based materials may be increased by doping with and nitrogen (N), phosphorous (P), aluminum (Al) and boron (B), which substitute for carbon and silicon in the lattice.[16] The addition of Al and B lead to p-type character, while the addition of N leads to n-type character.[10] The resistivity of silicon carbide may be varied between 0.1 and $10^{12}$ Ohm-cm's through the addition of dopants.[10]

### 2.1.4 Industrial Uses

As stated previously, the many beneficial properties of silicon carbide make it suitable for a number of industrial uses. Of the over 700,000 tons of silicon carbide produced every year, the largest single use is in the abrasives industry, accounting for 50% of total production.[10] The extreme high hardness of silicon carbide makes it useful for grinding and polishing of a wide range of materials. Silicon carbide is used in a loose

form as a lapping material, or may be mixed with a binder to form abrasive sticks and cutoff wheels.[16] It may also be formed into grinding wheels and whetstones, or bonded to cloth and sheets for use as abrasive papers and belts.[10, 16] Carbide grits are also used to increase the wear resistance of concrete.[21]

A further 33% of annual SiC production is used in the metallurgy industry.[10] SiC produces an exothermic reaction upon being dissolved in a molten iron melt. This increases the temperature, which acts to deoxidize the metal and improve homogeneity within the melt, increasing the quality of the final product.[10, 16]

The balance of production is spread amongst different uses. The high thermal shock resistance and low coefficient of thermal expansion of SiC leads to many high temperature uses up to 1600°C. This includes use as furnace heating elements, crucibles, kiln furniture, igniter devices, and furnace walls.[15, 16] Silicon carbide is also used in the production of industrial wear parts such as sand blast nozzles, pump seals, artificial rollers and ball bearings, rocket nozzles, brake discs, and furnace rollers.[15, 16] As a semiconductor, SiC has been used in the development of high voltage/current electronic devices.[21] A lot of research has gone into the use of silicon carbide in the design of turbine, diesel, and gasoline engine blocks. By operating at higher temps, these engines offer the promise of increased efficiency.[15]

### 2.1.5 Armor Ceramics

Armor has been employed by soldiers for thousands of years and has progressed from the use of leather and bone to worked metal and finally to the incorporation of ceramics within an armor system. Some of the earliest uses of ceramics as armor took

place during the Vietnam War where they were utilized for personal body armor and as armor plating for seats in helicopter gunships.[22] One of the motivations for the transition to the use of ceramics was a reduction in the weight of the armor while maintaining adequate protection against ballistic threats.[22] The density of ceramics used as armor materials (2.5-4.0 g/cm$^3$) was found to be half that of traditional steel armors (7.8 g/cm$^3$).[1] Ceramics also possess other advantageous properties that make them suitable for armor applications. These include high compressive strength, high hardness, and high Young's modulus.[9, 23, 24] Table 2.2 shows a summary of the mechanical properties of various ceramics used for armor applications. While armor performance has yet to be linked to a single material characteristic, a number of criteria have been used to determine the feasibility of a material for this application.[25] They include microstructural uniformity, density, hardness, elastic modulus, strength, fracture toughness, and fracture mode.[25]

Evaluation of armor ceramics found that they were unable to function alone in defeating a threat. It was determined that the brittleness and low tensile strength common to almost all ceramics limited their performance as armor materials when compared to tradition steel armors.[26] By incorporating these materials into a multi-layer armor system their performance was drastically improved by highlighting the beneficial properties of ceramics and mitigating the effect of those characteristics that are detrimental to ballistic performance.[27] The utilization of silicon carbide as an armor material is based primarily on the high compressive strength, hardness, elastic modulus, and fracture toughness of these materials.[28]

**Table 2.2** Mechanical properties of ceramic armor materials[22]

| Ceramic Material | Density ($g/cm^3$) | Vickers Hardness (GPa) | Fracture Toughness ($MPa*m^{1/2}$) | Young's Modulus (GPa) | Sonic Velocity (km/s) | Flexural Strength (MPa) |
|---|---|---|---|---|---|---|
| | | | | | | |
| $Al_2O_3$, sintered | 3.60-3.95 | 12-18 | 3.0-4.5 | 300-450 | 9.5-11.6 | 200-400 |
| $Al_2O_3$-$ZrO_2$, sintered | 4.05-4.40 | 15-20 | 3.8-4.5 | 300-340 | 9.8-10.2 | 350-550 |
| SiC, sintered | 3.10-3.20 | 22-23 | 3.0-4.0 | 400-420 | 11.0-11.4 | 300-340 |
| SiC, hot pressed | 3.25-3.28 | | 5.0-5.5 | 440-450 | 11.2-12.0 | 600-730 |
| $Si_3N_4$, hot pressed | 3.20-3.45 | 16-19 | 6.3-9.0 | | | 690-830 |
| $B_4C$, hot pressed | 2.45-2.52 | 29-35 | 2.0-4.7 | 440-460 | 13.0-13.7 | 200-350 |
| $TiB_2$, sintered | 4.55 | 21-23 | 8.0 | 550 | | 350 |
| $TiB_2$, hot pressed | 4.48-4.51 | 22-25 | 6.7-6.95 | 550 | 11.0-11.3 | 270-400 |
| AlN, hot pressed | 3.26 | | 2.5 | 550 | | 350 |

## 2.2 Processing of Ceramics

The production of fully-dense, advanced silicon carbide ceramic products involves many steps. The raw materials are typically mined, beneficiated, milled, and then sieved. The cleaned and sized raw materials are then heated in a large batch furnace to induce a chemical reaction, forming silicon carbide crystals. These crystals are manually selected from the furnace batch, which are then broken down and undergo further milling and sizing. The sintering of silicon carbide powders to full density may

be done with or without pressure assistance, but it does require extremely high temperatures and the use of additive sintering aids. In addition to the previous operations, the manner in which additives are introduced into the batch and the mixing efficacy affect the uniformity of the microstructure of the final part.

### 2.2.1 Production of Silicon Carbide Powders

With the exception of the extremely rare mineral moissanite, silicon carbide is not readily found in nature.[29] Production of silicon carbide therefore relies on the synthesis of high-quality powders.[30] The majority of the silicon carbide generated for all industrial uses is produced by the Acheson process. Patented by Acheson in 1893, this process relies upon the carbothermal reduction of raw materials in a resistance furnace.[31]

A massive graphite rod is surrounded by a finely ground mixture of silica ($SiO_2$) and coke (C) in the center of a cylindrical furnace. The graphite rod and powder core are surrounded by a refractory lining within a steel shell. Current is passed through the rod to generate heat, generating temperatures as high as 2000-2500°C. Heat is transferred from the core throughout the rest of the charge. Once temperatures reach approximately 1500°C, the following reaction begins to occur:[32]

$$SiO_2 + 3C = SiC + 2CO \qquad \text{Eq. 1}$$

The reaction is typically allowed to continue for 40 hours or more. Upon cooling, the sides of the furnace are broken away, exposing a layer of unreacted material surrounding a crystalline cylindrical mass of silicon carbide.[32] The resultant crystals produced by the reaction must be crushed, milled, and sieved before further use.[19] The purity of the material, and its intended application, is a function of the distance from the electrode.

The powder which is harvested closest to the electrode is of the highest purity, and is used in the manufacture of advanced ceramics. Lesser quality materials located away from the core of the furnace are used in the abrasives industry.

Additional methods have been employed to produce silicon carbide powders. These include sol-gel processing and chemical vapor deposition (CVD).[33, 34] Drawbacks such as smaller batch size and higher cost has limited the production output of these methods. By weight, close to 95% of silicon carbide production is carried out by the Acheson process.[32]

### 2.2.2 Sintering of Ceramics

Sintering is a thermally driven process by which a loose powder compact is transformed into a solid body. The intended result is generally an increase in density of the initial compact through a reduction in porosity.[35] This is accomplished by mass transport within a material, and is driven by atomic diffusion that leads to a reduction in the surface energy of individual powder particles.[36] Matter is conveyed from a starting position, or "source," within a powder particle to a "sink," which is often a neck that is formed between adjacent particles. Although the temperatures at which this is carried out are very high (T>1500°C), they are usually well below the melting temperature of the constituent materials.

The sintering process can be divided into multiple stages. These are the initial, intermediate, and final stages. The initial stage is characterized by the movement of material to the neck area, as well as the formation of grain boundaries and a smoothing of the surface of particles.[37, 38] The greatest increase in density occurs during the

intermediate stage, where an increase from 60 to 90% theoretical density is possible.[37] This is characterized by a decrease in overall porosity, along with the initiation of grain growth, with the majority of the porosity being located in channels between grains.[38] The increase in density is less dramatic during the final stage of sintering, but the change in microstructure of the sintered piece is vitally important to the resultant mechanical properties. This stage of the process sees the formation of enclosed porosity, located commonly at the intersection of grain boundaries, but also possible within grains.[37] This is a manifestation of the elimination of open pore channels within the piece. This stage is also characterized by high mobility of grain and pore boundaries, leading to increased rates of diffusion.[37]

#### 2.2.2.1 Driving Force and Mass Transport Mechanisms

Sintering results from an overall reduction of surface energy associated with surfaces.[37] This occurs by the elimination of solid/vapor interfaces between particles in favor of solid/solid interfaces, which have a lower surface energy.[39] The localized driving force for sintering results from a difference in energy between surfaces with different radii of curvature. This can be explained by examining the concentration of vacancies and vapor pressure that exist around concave, convex, and flat surfaces.[37-39] The concentration of vacancies beneath a concave surface is greater than that beneath a flat surface, which is greater than that beneath a convex surface.[37, 39] This results in a difference in chemical potential, and a counter-directional transport of vacancies and material at these locations.[37] There is also a difference in vapor pressure above these three types of surfaces. The vapor pressure is greater above a convex surface, followed

by a flat surface, followed by a concave surface. The difference in pressure encourages material flow during sintering. The driving force for sintering is also dependent on the radius of curvature of a spherical object. The sintering rate can be thought to be inversely proportional to the size of a particle.[39] This is shown by the increased driving force associated with smaller particles due to a lower radius of curvature.

Taking this into account, as shown in Figure 2.3, the driving force for material transport during the initial stage of sintering can be explained by the difference in curvature that exists at the point of contact between two spherical particles. In contrast to the convex shape of the particle, a slightly negative radius of curvature (concave shape) exists at the point of contact, resulting in reduced vapor pressure.[39] This leads to material transport from the surface of the particle to the point of contact, beginning formation of the particle neck.

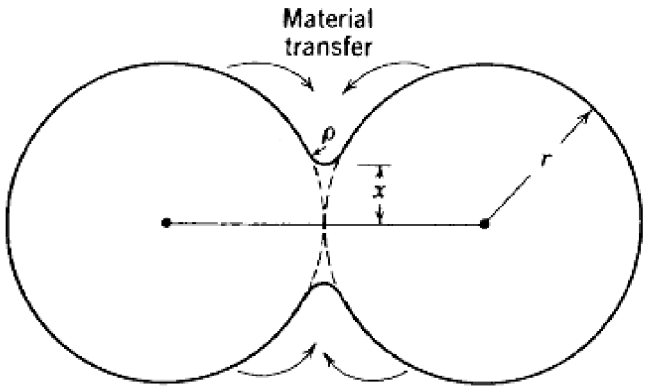


**Figure 2.3** Material transport to interparticle necks during initial stages of sintering[39]

During sintering, the transport of material from the source to the sink may occur by a number of diffusion paths. A list of these is shown in Table 2.3. Matter may be transported from the surface of a particle, from the grain boundary between two particles,

or from the volume of a dislocation. In all cases, the target of diffusion is the neck between two particles to enhance the cohesiveness. At any point in time, the diffusion mechanism which is active will be the one which is the most energetically favorable at that moment.[39]

**Table 2.3** Paths of material transport during the sintering process[39]

| Mechanism Number | Transport Path | Source of Matter | Material Sink |
|---|---|---|---|
| | | | |
| 1 | Surface diffusion | Surface | Neck |
| 2 | Lattice diffusion | Surface | Neck |
| 3 | Vapor transport | Surface | Neck |
| 4 | Boundary diffusion | Grain boundary | Neck |
| 5 | Lattice diffusion | Grain boundary | Neck |
| 6 | Lattice diffusion | Dislocations | Neck |

A visual representation of the various transport mechanisms active during the initial stages of sintering is shown in Figure 2.4. Arrows in the figure indicate the location of the source and sink and the directionality of the diffusion. The mechanisms are labeled to correspond with the description in Table 2.3. While all of these mechanisms contribute to a reduction of the free energy of a system, densification occurs due to those mechanisms which lead to a reduction of the distance between the centers of two particles.[38, 39] These include boundary and lattice diffusion from the grain boundary to the neck, and the transport of material from a dislocation to the neck by lattice diffusion. As is shown in Figure 2.4, the movement of material from the surfaces of the particles to the neck by surface, lattice, and vapor transport do not promote diffusion as these mechanisms do not lead to a reduction in mean particle centroid separation

distance.[38] Volume and grain boundary diffusion play an important role in the later stages of sintering in the reduction of pore volume.[39]

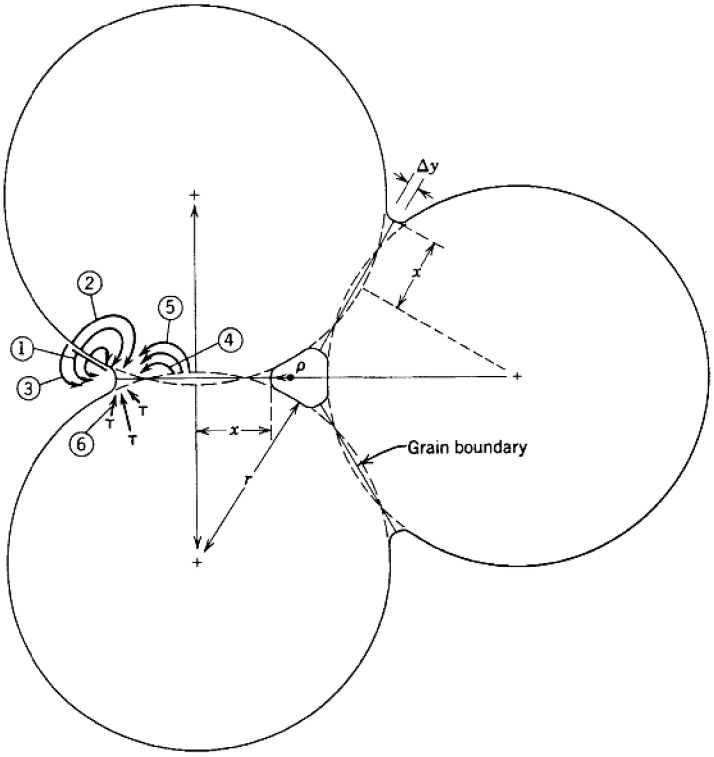


**Figure 2.4** Mass transport mechanisms during the sintering process[39]

### 2.2.2.2 Coarsening and Densification

Sintering may proceed on more than one path. A visual depiction of these competing processes is shown in Figure 2.5. Coarsening is driven by a reduction in the total surface area of the powder compact, leading to an increase in the average size of particles.[37] For advanced ceramic materials, the more beneficial result is often densification, as an increase in the mean size of particles is also accompanied by an increase in the average pore size, leading to a reduction in density. A carefully sintered

material will result in densification through the elimination of open porosity and the creation of grain boundary area, followed by controlled grain growth.

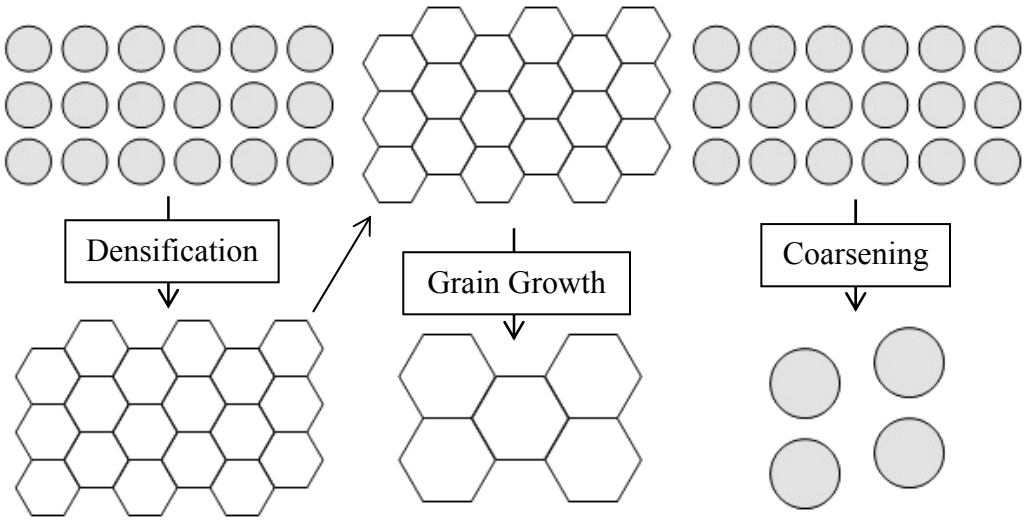


**Figure 2.5** Illustration of densification/grain growth and coarsening in a porous powder compact under heating[37]

While a number of factors play a role in determining which sintering path is undertaken, there is a strong dependency on the energy associated with the interfaces between grains and pore volumes, and the angle between these microstructural phases. The reduction of surface energy associated with these interfaces is the driving force of the process. As shown in Figure 2.6, $\gamma_{gb}$ is the surface energy associated with a grain boundary, while $\gamma_{sv}$is the surface energy of the interface between a grain boundary and a vapor phase, or pore. The angle between these phases, or the dihedral angle, is represented as $\phi$. In order for sintering to occur, $\gamma_{gb}$should be less than twice $\gamma_{sv}$.[37]

The parameters for fulfilling these conditions may be calculated through the use of the following equation:[38]

$$\cos\frac{\phi}{2} = \frac{\gamma_{gb}}{2\gamma_{sv}} \qquad \text{Eq. 2}$$

Where $\gamma_{gb}$ is the grain boundary surface energy, $\gamma_{sv}$ is the solid/vapor interface surface energy, and $\phi$ equilibrium dihedral angle. According to this equation, for densification to occur, $\phi$ must be less than 180°.[37]

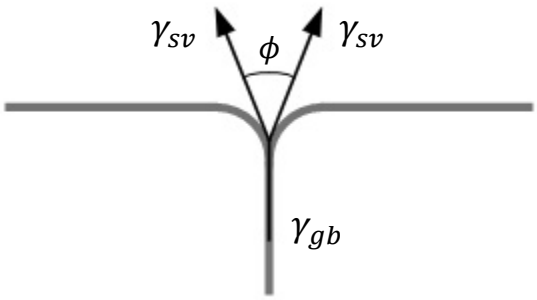


**Figure 2.6** Surface energy considerations of solid-state sintering at interparticle boundaries[37]

The mechanisms described above are all applicable to solid-state sintering. This is sintering which is carried out in the absence of an appreciable liquid phase. This often occurs at very high temperatures, and with relatively high additive content.[40, 41] Another route to achieve densification of a powder compact is through liquid-phase sintering, or sintering carried out with the aid of a liquid phase. A liquid phase may be present in small amounts within materials which had traditionally thought to have been completely solid-state sintered.[42]

Two advantages to liquid-phase sintering are the speed and homogeneity of the densification.[37] To achieve this, the liquid phase infiltrates open porosity channels between adjacent grains. Surface tension acts to pull grains towards each other. For this to occur, the liquid must be capable of wetting the surrounding solid material.[37] The

conditions for this to occur are dependent on the relationship between the surface energy of the liquid/solid phase, the liquid/vapor phase, and the solid/vapor phase, according to the equation:[37]

$$\gamma_{sv} = \gamma_{sl} + \gamma_{lv}\cos\Theta \quad \text{Eq. 3}$$

Where $\gamma_{sv}$ is the free energy associated with the solid/vapor interface, $\gamma_{sl}$ is the surface energy of the interface between the liquid and the solid, and $\gamma_{lv}$ is the energy of the liquid/vapor interface, and $\Theta$ is the contact angle between them. To provide a driving force for sintering, it can be seen that a high solid/vapor surface energy, and low solid/liquid and liquid/vapor surface energies are required.

### 2.2.3 Forming Methods

Many forming methods exist to accomplish sintering of silicon carbide ceramics. A brief overview of two of these methods, pressure-assisted sintering and pressureless sintering, will be given in the following sections. As the samples examined in this dissertation were produced by pressureless sintering, the discussion will include the advantages of this forming method, along with the sintering additives commonly employed to achieve densification.

#### 2.2.3.1 Pressure-Assisted Sintering

Sintering via pressure-assisted sintering methods involves the application of both heat and pressure to densify a material. As demonstrated by Alliegro in 1956, a widely used method to densify covalently bonded ceramic materials such as silicon carbide is hot-pressing. The basic components of a hot-press are a hydraulic ram, which applies

uniaxial pressure, an induction furnace, and a graphite die into which a powder compact is placed.[43] The uniaxially applied pressure, which applies additional stress to boundaries between particles, acts with the reduction of surface energy as the driving force of sintering.[37, 39, 43]

While the degree of grain growth that occurs is dependent on the maximum temperature, it is insensitive to the applied pressure.[39] Applied pressure acts against pore pressure and causes transport of vacancies from the neck to the space between particles, which acts to remove large pores and promote densification.[37, 38] The applied pressure allows densification to occur at a lower temperature. The result is a material which has been sintered to a high density at a low enough temperature and a short enough time as to not induce significant grain growth.[39] Negative aspects of this sintering method generally deal with the expense and low production rate. This is not a continuous process, and is one that needs to be done in vacuum or a controlled atmosphere.[37, 43] Adding to the expense is the short lifetime of the dies, as they undergo the same heating and thermal stresses as the powder compact sample.[39]

Spark plasma sintering is a modern, high-speed densification method that may be applied to both conductive and non-conductive materials.[44] As with the hot-press method, densification occurs through the application of high temperatures and uniaxial pressure. Heating is thought to be achieved by the generation of spark plasma at the contact points between particles through the "on/off" pulsing of a low-voltage, high-amperage DC current source.[44] Temperatures greater than 10,000°C are generated at the location of the spark.[44] Heating is concentrated on the surface of particles, resulting in vaporization of surface layers. This leads to material transport from the surface to

interparticle necks. The resultant density of the piece is dependent on both the heating time and the maximum cycle temperature.[45]

In addition to a uniaxial pressure mechanism and DC pulse power generator, a spark plasma sintering unit includes a vacuum chamber, punch electrodes with water cooler, atmosphere control mechanism, and units to measure both the position of the ram and the temperature.[46]

Sintering and densification occurs through a number of mechanisms. Plastic deformation on the surface of particles occurs at the spark generation point due to the extreme temperatures produced at these locations.[44, 46] The applied electric field causes high speed transfer of heat and diffusion throughout the entire powder compact.[44, 46] Rate of diffusion is enhanced by the intensity of the pulse current.[45] Joule heating, or heating due to resistance to current, occurs in dies and punches, resulting in their acting as heating elements, further heating the powder compact.[45]

One of the major advantages of spark plasma sintering is the ability to densify materials in shorter times when compared to other densification methods. This acts to control grain growth during the process. Of great importance to materials research is the ability to spark plasma sinter nanocrystalline materials, and to sinter without the use of binders.[44] Spark plasma sintering has similar disadvantages to other pressure-assisted methods that prevent it from being utilized in low-cost, mass production of sintered materials. While the sintering cycle occurs in a comparatively short period of time, this is still a batch process. Replacement of graphite punches and dies add to the cost per part.

#### 2.2.3.2 Pressureless Sintering

Sintering and densification may also occur without the application of external pressure. As first demonstrated by Prochazka in 1975, pressureless sintering provides the capability to sinter sub-micron powder compacts of SiC to greater than 95% density.[47] Sintering occurs though both solid-state and liquid-state mass transport mechanisms. Typical sintering additives for this forming method include boron and carbon.[48] Sintering can occur with minimal amounts of additives, typically in the range of 0.5 wt% boron and 1-3 wt% carbon.[49] Sintering temperatures may vary between 1900 and 2100°C.[49] Sintering of pieces should be carried-out in an inert atmosphere to avoid creation of surface deficiencies in the final part.[48]

Equiaxed, fine-grained microstructures may be realized through careful control of sintering conditions and additive mixing.[49] Pressureless sintering has been found to be very applicable to industrial production as it allows densification of parts with complex shapes. Any machining operations are typically carried out on the undensified soft green body. This reduces the total cost of each unit, and also prevents introduction of machining damage into the final part. The part throughput is greatly increased over pressure-assisted methods, which tend to be batch processes.

Pressure-assisted sintering does have its advantages. Hot-pressed SiC materials typically have higher densities, hardness, and flexure strength in comparison to pressureless sintered materials. Densification may also be achieved with pressure-assisted methods with a reduced additive content. This is important as additives may agglomerate and form stress concentrators in the resultant part. Furthermore, the high

temperatures and long soak times associated with pressureless sintering may lead to anisotropic grain growth, which is less of an issue in pressure-assisted sintering.[49]

### 2.2.4 Sintering Additives

#### 2.2.4.1 Carbon Sintering Additives

The manufacture of dense, pressureless sintered bodies of silicon carbide requires the presence of carbon to achieve sintering of porous green compacts.[2, 50] This is due to the strong covalent bonds that exist within the silicon carbide structure, leading to the low self-diffusion coefficient of SiC.[2, 3, 51] It has been shown that the optimum concentration to achieve sintering and densification of SiC is approximately 3 wt%.[52] Numerous theories exist as to the role that carbon plays during this process.

Early work focused on the theory that carbon acted to reduce the grain-boundary/surface energy ratio, thus inducing the driving force for mass transport to occur.[2] It was believed that it was impossible for sintering to occur when this ratio was too high.

Work has also focused on the reaction of carbon with species within the compact, including $SiO_2$, SiC, and elemental silicon, and its effect on the diffusion rates of these species.

It is believed that carbon reacts with the silica passivation layer which coats SiC particulates within the compact.[3, 53] At T > 1520°C, the reaction between excess carbon and the $SiO_2$ passivation layer occurs according to the equation:[54]

$$SiO_2 + 3C \rightarrow SiC + 2CO \qquad \text{Eq. 4}$$

This leads to the reduction of $SiO_2$, and the removal of gaseous CO through open porosity.

The effect of carbon on the diffusion of species within the SiC green bodies has also been the subject of theorization. It is believed that the presence of carbon inhibits mass transport mechanisms which are detrimental to the sintering process.[50] At increased temperatures, T > 1870°C, the following reaction between silica and silicon carbide directly becomes energetically favorable:[55]

$$2SiO_2 + SiC \rightarrow 3SiO + CO \quad \text{Eq. 5}$$

This reaction is considered to be detrimental, as the volatility of SiO can lead to vapor transport of species, inhibiting densification and leading to coarsening.[56] The presence of carbon tends to reduce the vapor pressure of SiO through reduction, by reaction of carbon and SiO directly, resulting in the production of SiC and CO.[3] The role of carbon may also be to react with the silica passivation layer at a temperature which is below the onset temperature of the reaction shown in Equation 3. This has been shown to prevent the formation of a network of large pores that cannot be removed with subsequent heat treatment.[54]

Carbon may also limit the surface diffusion of elemental silicon.[3] At T > 1950°C, the following reaction becomes favorable:[57]

$$SiC + SiO \rightarrow 2Si + CO \quad \text{Eq. 6}$$

It is believed that the presence of well-distributed excess carbon will block the loss silicon through transport along the surface.[3] In both of the two previous cases, the enhancement of bulk diffusion was accomplished through the limitation of surface diffusion and vapor transport. It has also been theorized that the presence of carbon

results in the formation of vacancies within silicon carbide, resulting in an increased rate of diffusion.[54]

#### 2.2.4.2 Boron Sintering Additives

Along with carbon, boron is one of the most frequently used and effective sintering additives for the densification of silicon carbide.[51] It was employed with success by Prochazka in his groundbreaking work on the pressureless sintering of SiC.[2] It has been shown that boron induces sintering in fine-grained SiC powders, resulting in near theoretical densities being achieved through the addition of several tenths of a percent of sintering activator.[2]

Complete densification is not possible through the sintering of only SiC powder, and may be as low as 70% theoretical density.[51] The addition of boron shows a marked increase in densification, reaching values of up to 95%.[51] With the addition of carbon and boron, density values of over 99% have been achieved.[51]

The solubility limit of boron in SiC is 0.2 wt %.[2] The optimum concentration of boron that leads to the maximum amount of densification without causing exaggerated grain growth is just over this limit, between 0.2-0.5 wt%.[42, 52] Within this concentration range, SiC grain growth is equiaxed, and shows flat grain boundaries.[52] Beyond this concentration range, rapid, anisotropic grain growth may occur, with a rounding-off of grain boundaries, which lead to the presence of large pores that cannot be removed through subsequent heat treatments.[51, 52]

As with the effect of carbon on the densification of SiC, a number of theories, supported by experimentation, have been postulated to explain the role it plays. It was

originally believed that boron acted with carbon to reduce the grain-boundary/surface energy ratio, enabling diffusion to occur.[2] The presence of boron in grain boundaries of sintered SiC as found by high-resolution electron energy-loss Spectroscopy (EELS) seems to support this hypothesis.[58] Boron is also thought to increase atomic mobility within grain boundaries.[51] Studies of the reduction of surface area of SiC powder compacts during sintering point to the fact that boron reduces transport of matter by surface diffusion.[59] This acts to promote densification at higher temperatures by limiting the process of coarsening at temperatures below 1500°C.[59] Gupta et al. have also suggested that a boron-rich liquid-silicon-carbon phase plays a role in the activation of densification.[42]

#### 2.2.4.3 Heterogeneities in Silicon Carbide

Sintered ceramics are not ideal materials in that they contain heterogeneities such as foreign material inclusions, porosity, discontinuous large grains, and additive agglomerates.[41, 60] The presence, concentration, and spatial distribution of these second phases have a profound effect on the mechanical properties of a material.[61] They may be introduced as contamination during processing, or as artifacts resulting from the sintering process. Identifying and characterizing these second phases through the use of optical and electron microscopy techniques is a necessary exercise in determining their contribution to the performance of a material.[41, 60-63]

One of the challenges facing producers of silicon carbide is the use of sintering additives to overcome the low self-diffusion coefficients of Si and C and the high surface energy of grain boundaries, which are both impediments to densification.[3, 62] These

impediments are overcome through the use of sintering activators. The additive concentration and manner in which it is added have an influence on the final properties of the material. Sufficient quantities or additives must be present to allow for densification to occur.[41] The addition of additives in excess of what is necessary for densification may be as detrimental as having too little. Another important consideration is the mixedness of additives within the initial batch formulation. Improper mixing of additives can lead to localized additive deficient or additive-saturated regions.[60] Additive-deficient regions may not achieve full-density, while a localized excess of sintering aids can become a source of defects in the finished material through the formation of porous agglomerates.[64, 65]

Unreacted carbon additives have been found to form both amorphous carbon and graphitic inclusions.[60, 62, 66] Carbon may be added in the form of graphitic powders, phenolic resins, and surfactant coatings.[3, 50, 54, 67] Carbon may often be added in concentrations that are greater than what is stoichiometrically necessary to ensure the complete removal of the $SiO_2$ passivation layer, leading to the formation of porous inclusions.[62] The presence of these inclusions can have an effect on both the quasi-static and dynamic performance of a material. Bakas et al. in a study of the ballistic rubble of hot-pressed silicon carbide, found the presence of large graphitic inclusions near fracture initiation locations.[66] Conclusions reached by Hamminger et al. through work on the formation of carbonaceous inclusions in sintered silicon carbide indicated the benefits of reducing carbon additive content by increasing the efficiency of these additives through better homogeneity.[62] This is increasingly important as work by Rosa et al. on silicon carbide plates found that fracture was more likely to result from an intrinsic flaw such as

a sintering-aid inclusion or pore than due to an extrinsic feature such as a surface scratch.[68] In the instance of this sample set, the flaw distribution between intrinsic and extrinsic features was near 4:1.[68]

The presence of excess boron may also lead to agglomeration during sintering. Small amounts of boron may be dissolved into the silicon carbide matrix, but the formation of second phases may occur once the solubility limit is reached.[2] This may include the formation of very small precipitates within silicon carbide grains and on the grain boundaries.[58, 69] Exceeding the solubility limit of boron in the presence of excess carbon can result in the formation of porous boron carbide inclusions.[64] These inclusions become stress concentrators during quasi-static loading since due to their porous nature the effective modulus is much lower than either dense silicon carbide or boron carbide.

The processing and sintering efficacy also have an effect on the formation of other second phases within the microstructure. These include isolated pores, clusters of pores, and anomalously large, discontinuous grains.[60] Sintering in a region containing the proper amount of additives results first in the reduction of mean pore size, followed by a closing-off of porous channels, resulting in isolated pores which then decrease in size.[39] Following this stage, the remaining sintering time should be limited as discontinuous grain growth may occur with further heating. A microstructural feature which contributes to a disruption of the overall local modulus can become a stress concentrator, leading to a reduction in local flexure strength.

## 2.3 Fracture Behavior of Ceramic Bodies

### 2.3.1 Brittle Fracture

The application of stress (σ) to a body elicits a response from the material. This takes the form of strain (ε), or a deformation of the crystal structure of the material in the direction of the applied stress. This is measured as the change in length in proportion to the initial, unstressed length ($\delta L/L$). Upon relaxation of the stress, providing that a critical value has not been reached, relaxation of the structure of the material occurs. This is referred to as elastic deformation.

The degree of induced strain is directly proportional to the applied stress, as given by:[39]

$$\sigma = E\varepsilon \qquad \text{Eq. 7}$$

Where $\sigma$ is the stress, $E$ is Young's modulus, both measured in Pascals (Pa), and $\varepsilon$ is the strain. The Young's modulus is a measurement of the stiffness of a material, and is directly related to the strength of inter-atomic forces. While a high modulus material will deform less than a lower modulus material, as will be shown later, the Young's modulus has a direct effect on the amount of strain that a material can tolerate before fracture.

Fracture, or failure of a material, is considered to have occurred when two sections of an object have been totally separated from one another by the application of stress. The fracture behavior of two different classes of materials is shown in Figure 2.7. The example on the right experiences significant amounts of plastic deformation, or necking, before the onset of failure. The cracks caused by the formation and connection of voids within the material are stable in that they will not grow without the application

of additional stress. Failure of the material tends to be gradual. This is typical of ductile materials such as metals.

In contrast, brittle fracture, shown in the example on the left occurs over a much shorter period of time and without warning.[70] A linear relationship between stress and strain exists until the point of fracture, with a minimal amount of plastic deformation occurring.[37] This behavior, typical of the hard ceramic materials examined in this dissertation, is typified by the build-up of elastic strain energy within the structure of the material with increasing stress. Fracture occurs at the point where the amount of elastic strain energy exceeds the limits of the material.

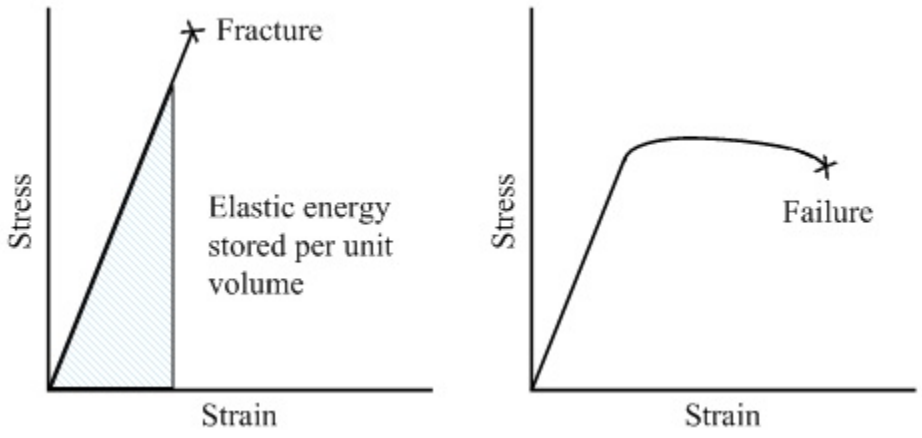


**Figure 2.7** Fracture behaviors. Example on left is of brittle fracture, while material on right undergoes significant plastic deformation before gradual failure[37]

### 2.3.2 Strength of a Material

The theoretical strength of a material is dependent upon the inter-atomic bonding force between planes of atoms.[39] As defined above, fracture is the separation of a body into two parts. Consider two planes of atoms on either side of the break. In an unstressed

material, neighboring atoms within these two planes occupy equilibrium spacing positions based upon energy considerations. A decrease in this separation distance results in the development of a strong repulsive force between the planes of atoms. As a tensile stress is applied to the material and the separation distance begins to increase, a strong attractive force develops between the two planes. This force reaches a maximum, considered to be the theoretical strength, before diminishing with increasing separation distance. Based upon this example, the Orawan estimate of the theoretical fracture strength of a material is:[39]

$$\sigma_{th} = \left(\frac{E\gamma}{a_o}\right)^{1/2} \quad \text{Eq. 8}$$

Where $\sigma_{th}$ is the theoretical fracture stress, $E$ is the Young's modulus, $\gamma$ is the energy per unit length required to create two new surfaces, and $a_o$ is the equilibrium atomic spacing. The surface energy $\gamma$ is considered to be the energy per broken bond times the number of bonds.[37]

It should be noted that fracture strengths as calculated using Equation 8 represent the strength of an "ideal," defect-free material. "Real" materials are much more complex. While theoretical strengths for dense ceramic materials are within the range of 10's of GPa, subsequent experimental work has shown that the true fracture strengths are more on the order of 100's of MPa.[39, 71] The disparity between the theoretical and actual strength values can be attributed to features within the microstructure which interrupt the ordered lattice of atoms. These include, but are not limited to, dislocations, inclusions, pores, and microcracks.[70]

### 2.3.3 Mechanics of Crack Growth

Differences in mechanical properties between these "second phases" and the host matrix provide the basis for crack extension under stress that leads to mechanical failure. While it has been agreed upon that ceramics under tensile stress fail in brittle fashion due to the presence of pre-existing cracks, multiple explanations have been put forth to describe the crack growth mechanism.[37, 39, 70-72]

Griffith proposed that a pre-existing crack propagates when stored elastic strain energy exceeds the energy required to introduce two new surfaces into a material.[73] This treatment, as follows, is based upon the conservation of energy within a material.[71]

As stated by The First Law of Thermodynamics:[74]

$$dU = dQ - dW \qquad \text{Eq. 9}$$

Where $U$ is the internal energy of the system, $dU$ is positive for an increase in internal energy, $dQ$ is the flow of heat into the specimen, and $dW$ is the work done by the system on its surroundings.

It was proposed by Griffith that the internal energy of the system $U$ is comprised of the sum of the elastically stored energy $U_e$ and the surface energy of a crack, $U_s$, of length $c$.[73] There is sufficient energy to grow a crack from length c to c + dc when:[71]

$$\frac{dU_e + dU_s + dW}{dc} \geq 0 \qquad \text{Eq. 10}$$

Where $dU_e$ and $dW$ supply the necessary energy to account for the additional energy associated with the new crack surface, $dU_s$. The necessary amount of energy for the crack to just begin to grow is considered to be when the above equation is equal to zero.[73]

Taking the work done by the system on its surroundings to grow a new crack surface to be:[71]

$$dW = -2dU_e \quad \text{Eq. 11}$$

the Griffith energy balance equation to achieve crack growth becomes:[71]

$$\frac{dU_e}{dc} = \frac{dU_s}{dc} \quad \text{Eq. 12}$$

When examined under the consideration of plane stress as is encountered under the tensile loading of a thin plate, the energy required associated with a surface is:[71]

$$U_s = 4\gamma c \quad \text{Eq. 13}$$

Where $\gamma$ is the surface energy per unit area, and $c$ is the crack length. Plane stress is considered to occur when one of the dimensions of a body is small compared to the other two, resulting in the principal stress associated with that dimension being zero.

Based upon the work of Inglis in 1913, Griffith deduced that the value of the stored elastic energy at the tip of a sharp elliptical crack to be:[71, 75]

$$U_e = \frac{\pi c^2 \sigma^2}{E} \quad \text{Eq. 14}$$

Where $c$ is the crack length, $\sigma$ is the applied tensile stress, and $E$ is the Young's modulus.

By a combination of Equations 12, 13, and 14, the Griffith equation for fracture stress of a thin plate under plane stress conditions containing a sharp elliptical crack is given as:[73]

$$\sigma_f = \left(\frac{2E\gamma}{\pi c}\right)^{1/2} \quad \text{Eq. 15}$$

Where $c$ is the crack length, $\sigma_f$ is the fracture stress, $E$ is the Young's modulus, and $\gamma$ is the surface energy per unit area.

For conditions of plane strain, in which one of the dimensions of a body is much larger than the other two such that strain in the largest dimension is considered to be zero, the necessary fracture stress is calculated as:[71]

$$\sigma_f = \left(\frac{2E\gamma}{\pi(1-\nu^2)c}\right)^{1/2} \quad \text{Eq. 16}$$

Where $c$ is the crack length, $\sigma_f$ is the fracture stress, $E$ is the Young's modulus, $\gamma$ is the surface energy per unit area, and $\nu$ is the Poisson's ratio of the material

A related explanation of the crack growth mechanism in a sample loaded under tensile stress is the idea of the strain energy release rate. Following the work of Griffith, Irwin put forth the notion of the "crack-extension force," denoted as *G*.[76] As stated previously, the application of tensile stress to a dense ceramic body induces the buildup of potential energy in the form of strain. Crack growth occurs when the energy available to grow a crack, the strain energy, is greater than the energy associated with mechanisms which act to dissipate the crack-extension force, which in brittle materials includes the energy attributed to creating new surfaces.

The energy release rate *(G)* is defined as such:[76]

$$G = -\left(\frac{dW}{dA} + \frac{dU_e}{dA}\right) \quad \text{Eq. 17}$$

Where, as in the Griffith approximation, $dW$ is representative of the work done on the system by its surroundings and $dU_e$ is a measure of the elastically stored energy. Once again taking into account Equation 11, the strain energy release rate becomes:[71]

$$G = \frac{dU_e}{dA} \quad \text{Eq. 18}$$

One difference between this and the Griffith consideration is that here the differentiation is done with respect to $A$, which is taken to be the fracture area (change in crack length times the thickness).[76] Crack growth occurs when $G \geq G_c$, the critical energy release rate, below which there is insufficient strain energy to overcome the dissipation mechanisms.

One of the differences between this and the Griffith approximation is that here the differentiation is performed with respect to $A$, which is taken to be the fracture area (change in crack length times the thickness).[76] Crack growth occurs when $G \geq G_c$, the critical energy release rate, below which there is insufficient strain energy to overcome the dissipation mechanisms.

One of the most important aspects of this approximation is the concentration of stress at the crack tip. Calculated stresses indicate the stress applied to the area around the crack ($\sigma_{yy}$), but not necessarily the stress at the crack tip ($\sigma_{tip}$). The delivery of stress is important as it supplies the necessary driving force to break bonds directly in front of the crack tip, leading to crack propagation. Various factors can lead to an apparent multiplication of the stress applied at the crack tip. These factors are called stress concentrators, which include aspects of the crack geometry and shape, as well as the crack location.[75] For example, the concentration of stress at the tip of an elliptical shaped internal crack increases as the radius of curvature decreases. A longer initial crack length also increases the area over which the applied stress can act. Therefore, the stress concentration for a long and thin crack is much greater than for a short, circular shaped crack.[71]

These considerations resulted in the development of the concept of the stress intensity factor, or *K*. With units MPa · $m^{1/2}$, the stress intensity factor is calculated as:[39]

$$K = Y\sigma\sqrt{c} \qquad \text{Eq. 19}$$

Where Y is a unit-less dimensionality constant based upon the crack shape which relates the applied stress $\sigma$ to the stress at the crack tip, and $c$ is the crack length. As can be seen, the stress intensity factor is dependent upon the relationship between the normal applied stress, the geometry and location of the crack, and the initial length of the crack.

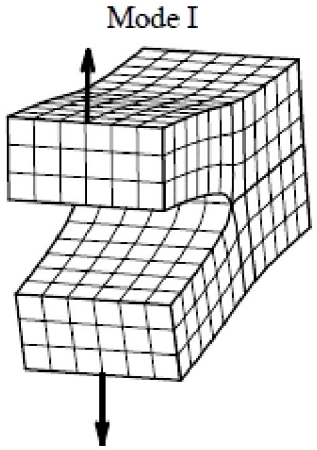


**Figure 2.8** Representation of Mode I crack opening. Crack growth occurs perpendicularly to the tensile applied stress[71]

The stress intensity factor is also dependent upon the directionality of the applied stress in relation to the crack length, as this determines the crack opening behavior mode. Application of tensile, uniaxial stress which is normal to the crack length results in Type I opening, where the crack opens in the direction of the applied stress. A schematic representation of Mode I opening is shown in Figure 2.8. The stress intensity factor for this type of loading is termed $K_I$.

The previous energy-based crack growth treatments can also be considered in terms of applied stress. There exists a critical stress intensity factor, $K_C$, below which crack propagation will not occur. For an elliptical, embedded crack within a body, stress applied perpendicularly to the crack length ($\sigma_{yy}$), supplies stored elastic strain energy, causing the crack to grow. Growth of the crack causes stress at the crack tip to drop to zero. In other words, the crack will proceed to grow until the driving force, the elastic strain energy, is depleted. Equations relating the strain energy release to the critical stress intensity factor are defined as:[71]

$$G = \frac{{K_{IC}}^2}{E} \qquad \text{Eq. 20}$$

For plane stress conditions, and:[71]

$$G = \frac{{K_{IC}}^2}{E}(1 - \nu^2) \qquad \text{Eq. 21}$$

Under plane strain conditions. In both conditions, $K_{IC}$ is the critical stress intensity factor for a perpendicular applied stress, $E$ is the Young's modulus, and $\nu$ is Poisson's ratio.

Related to both of these is the concept of a material's fracture toughness, or resistance to crack growth, also denoted as $K_{IC}$ for Type I opening. The fracture toughness is attributed to a particular crack geometry within a specific material. The equation used to calculate fracture toughness takes on the same form as Equation 19, the equation used to calculate the stress intensity factor. The only exception is that $\sigma$ is now $\sigma_f$, the fracture stress. While the shape parameters *(Y)* have already been defined, the other factors can be experimentally determined to find which combinations of stress, and crack size and shape will cause fracture in a material.

### 2.3.4 Strength Testing of Ceramics

#### 2.3.4.1 Tensile Testing

The application of tensile stresses to ceramic bodies causes the propagation of cracks that exist due to the presence of pre-existing flaws.[72] Continued application of stress can result in cracks that grow so large that failure of the piece occurs. Tensile strength testing involves the uniform distribution of stress across the ends of circular or rectangular sample. The sample is gripped on both ends by an apparatus such that the displacement between the grips is increased at a constant rate. The tensile strength as measured at the instant of fracture is:[71]

$$\sigma_T = \frac{P}{A} \qquad \text{Eq. 22}$$

Where $P$ is the applied force, in N, and A is the cross-sectional area, in square meters ($m^2$). As the test specimen is subject to a rapid increase in strain rate, this is considered to be the instantaneous strength.[71] The cross section of the test specimen is subject to a uniform stress distribution that is not dependent on the elastic properties of the material.[77]

In addition to measuring the instantaneous strength of a test piece, other modes of failure can be addressed by altering the applied load or strain rate. When conducting a stress rupture test, the applied load is held at a constant rate below the instantaneous stress load, and the time to failure is measured.[78] This is dependent on the magnitude of the applied stress. The cyclic fatigue resistance of a material can also be measured by cycling the load between a maximum value which is again below the instantaneous stress value and a minimum. Finally, the fracture toughness of a specimen can be determined by introducing a crack of known length and depth into the edge of a sample. As

explained previously, fracture toughness describes the resistance of a material to crack growth.[73]

### 2.3.4.2 Flexure Testing

An alternative to tensile testing is flexure testing, which is a much more widely employed method.[72] Difficulties in the precise gripping of the test component during tensile testing can introduce additional forces and stress concentrations into the test process. The machining involved to produce a tensile test specimen is more complex and expensive.[71] In contrast, flexure testing requires the machining of much simpler, and less expensive, rectangular or circular samples.[71, 72] Flexure testing involves the application of stress to a sample through contact points, often steel bearings, which extend across the width of a sample.[71] A full description of a flexure sample test fixture will be discussed in Section 4.4. In practice, the sample is placed upon two support bearings. The load is transferred to the sample through one or two upper loading bearings, depending upon the test method. The platform upon which the test fixture is placed is raised at a constant rate such that the top of the test fixture is put in contact with a load measuring device, or load cell, which converts force into an electrical signal. The contact of the upward travelling test fixture with the load cell causes compression of the sample between the upper and lower contact points. This induces a bending moment within the test specimen.

The stress state of a flexure bar under 3-pt loading, one of several such loading configurations commonly used, is shown in Figure 2.9. This test configuration utilizes two lower support pins and one upper loading pin. When a load is applied to the bar at the location of the three contact pins, the top surface of the bar is put into compression,

while the bottom surface is placed into tension. The applied bending moment causes deflection of the center of the bar such that the upper and lower surfaces of the bar are bent into an arc.[71] Within the sample there exists a plane that does not change in length as deflection of the sample occurs. This is considered to be the neutral plane or axis, as indicated in Figure 2.9. The strain induced in each element of the sample is proportional to the distance from the neutral axis.[71] For a symmetrical sample such as an ASTM standard rectangular cross-section flexure bar, the neutral axis is located halfway between the top and bottom surfaces of the bar.

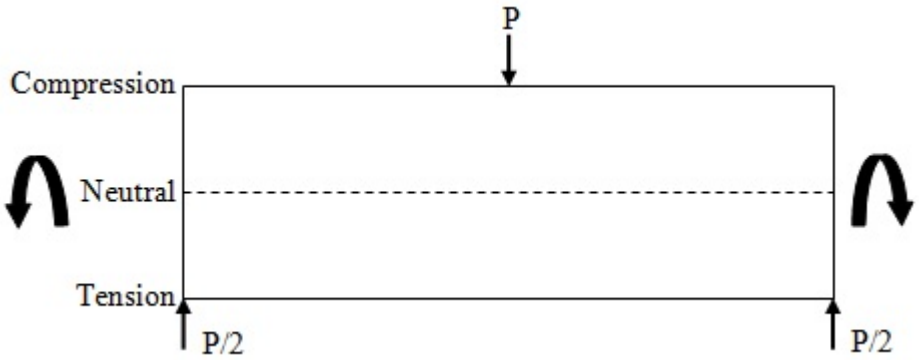


**Figure 2.9** Distribution of stress within a rectangular flexure sample under 3-pt loading. Stress state drops to zero at the plane of the neutral axis. Top of sample is put into compression, bottom of sample is put into tension

As is shown in Figure 2.10, the bending moment is at a maximum only at the center of the bar. The moment decreases to zero at the position of the bottom support pins. No bending moment exists outside of either support pin.[71] Likewise, stress is at a maximum at the position of the upper loading pin and at the top and bottom surfaces of the bar. The distribution of stress throughout the bar can be found according to:[71]

$$\sigma = \frac{P}{2I} xy \qquad \text{Eq. 23}$$

For $0 \leq x \leq L/2$, where $P$ is the applied load, in newtons (N), $y$ is the distance in m from the neutral axis, and $x$ is the distance in meters (m) from the lower support pin. According to this, stress is also at a maximum only at the center of the bar. This highlights one of the major differences between a flexure test and a tensile test. Within a tensile test specimen, the tensile stress is evenly distributed across the cross section of the sample. A flexure test sample experiences maximum tensile stress within a much smaller region that is located on the surface of the specimen that corresponds to the lower support pins.

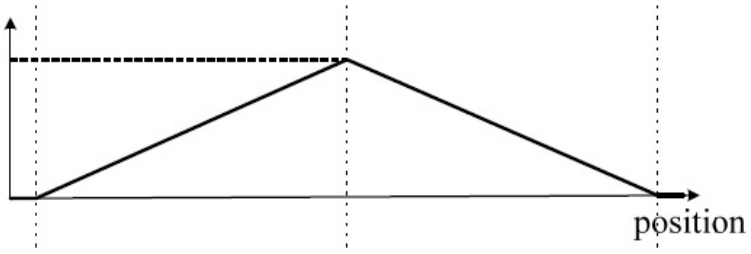


**Figure 2.10** Bending moment diagram of a 3-pt flexure specimen[71]

The maximum deflection at the center of the bar is:[79]

$$\delta = \frac{PL^3}{48EI} = \frac{PL^3}{4Eh^3d} \qquad \text{Eq. 24}$$

Where $P$ is the applied load, in N, $L$ is the distance, in m, between the lower loading pins, while $h$ and $d$ are the height and cross-sectional width of the bar, in m, and $E$ is the Young's modulus, in units of Pa. The maximum stress for a 3pt loaded flexure bar is given as:[71]

$$\sigma_{max} = \frac{PLh}{8I} = \frac{3PL}{2h^2d} \qquad \text{Eq. 25}$$

Where *P* is the applied load, in N, *L* is the distance, in m, between the lower support pins, while *h* and *d* are the height and cross-sectional width of the bar, in m. This highlights one of the other differences between a tensile and flexure test. Unlike a tensile test, the degree of the bar deflection and amount of tensile stress are dependent on the Young's modulus of the material of which the sample is composed.

A related loading configuration of flexure bars is the 4-pt bend test. In this method, there are two lower support contact points and two upper loading points. The 4-pt bend test is the preferred method as a greater volume of the test bar is under maximum stress.[72] This increases the likelihood of activating pre-existing flaws within the sample. Variations include either $^1/_4$ pt or $^1/_3$ pt loading, which describe the spacing of the upper loading pins in relation to the locations of the lower support pins. The loading configuration and bending moment of a 4-pt, ¼ pt specimen is shown in Figure 2.11. When measured from the left support pin, the locations of the two upper pins are at $^1/_4$ and $^3/_4$ of the distance, with a distance of $^L/_2$ between the upper loading pins.

As with the 3-pt bend test, maximum tensile stress occurs along the bottom surface of the bar. As can be seen, the entire area of the bar between the upper loading pins is under the maximum, uniform stress. In relation to $^1/_3$-pt loading, a greater proportion of the test bar under $^1/_4$-pt loading experiences the maximum bending moment. The bending moment for both configurations decreases to zero at the location of the bottom support bearings. Similarly, the bending moment and applied stress drop to zero at the location of the neutral axis.

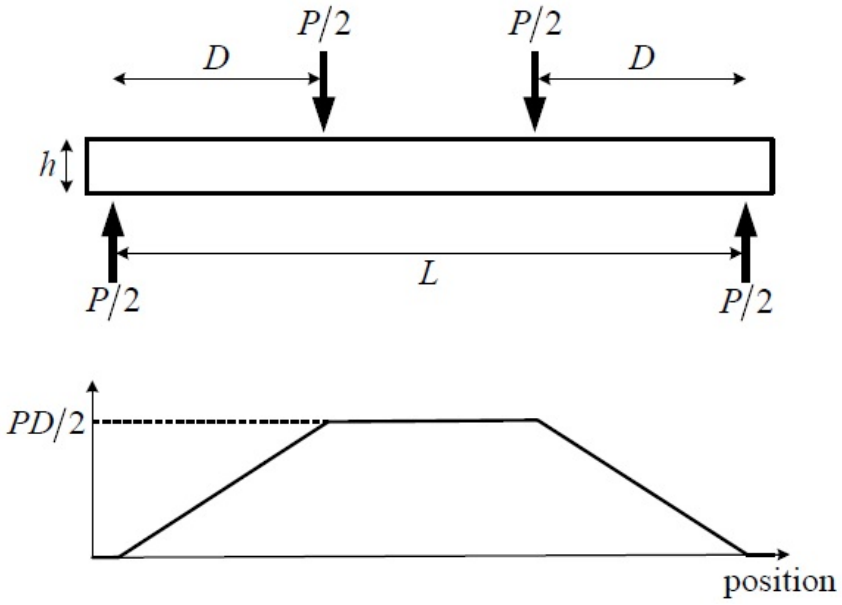


**Figure 2.11** Loading configuration and bending moment diagram of a 4-pt rectangular flexure specimen[71]

The deflection of the center of the bar in relation to the location of the outer loading pins is given as:[71]

$$\delta = \frac{PD}{48EI}(3L^2 - 4D^2) = \frac{PD}{4Eh^3d}(3L^2 - 4D^2) \qquad \text{Eq. 26}$$

Where $P$ is the applied load, in N, $D$ is the distance, in m, between the upper and lower loading pins on either side of the bar, $L$ is the distance, in m, between the lower support pins, $h$ and $d$ are the height and cross-sectional width of the bar, in m, and $E$ is the Young's modulus of the material, in Pa. This method solves for the maximum deflection in three segments: between the left support and loading pins, between the upper loading pins, and between the right loading and support pins.

The maximum stress may be calculated according to the equation:[71]

$$\sigma_{max} = \frac{PDh}{4I} = \frac{3PD}{h^2d} \qquad \text{Eq. 27}$$

Where $P$ is the applied load, in N, $D$ is the distance, in m, between the upper and lower loading pins on either side of the bar, while $h$ and $d$ are the height and cross-sectional width of the bar, in m.

In addition to fracture strength measurements, the 4-pt bend test can be used to measure the fracture toughness of a material. Two common test specimens include the edge-cracked and chevron-notched bars.[71] In either case, a "flaw" of known size is introduced into the bar. By measuring the load at which slow crack growth initiates, the fracture toughness of the material may be determined.[80]

### 2.3.5 Statistical Distributions

As was explained in the previous section, the size of a flaw within an element of a ceramic body has a profound effect on the strength of the body. The number and range of flaw sizes may be represented by a number of statistical distributions.

#### 2.3.5.1 Normal Distribution

One of the most widely employed distributions is the Gaussian or normal distribution. As shown in Figure 2.12, the data within a normal distribution are represented by a peak with the familiar bell shape. The normal distribution is defined by the mean and the standard deviation. Where the mean, $x_m$, is the average of all values within the distribution, the standard deviation describes the spread within the data. The variance $s$ is the square of the standard deviation.

The distribution function of a normal distribution which applies to flaw sizes within a ceramic body is defined as:[71]

$$F(x) = \frac{1}{s(2\pi)^{\frac{1}{2}}} e^{-\frac{(x-x_m)^2}{2s^2}} \qquad \text{Eq. 28}$$

Where $s$ is the variance in the flaw size data and $x_m$ is the mean flaw size. As can be seen in the above figure, one of the defining aspects of the normal distribution is that it is symmetrical around the mean value.

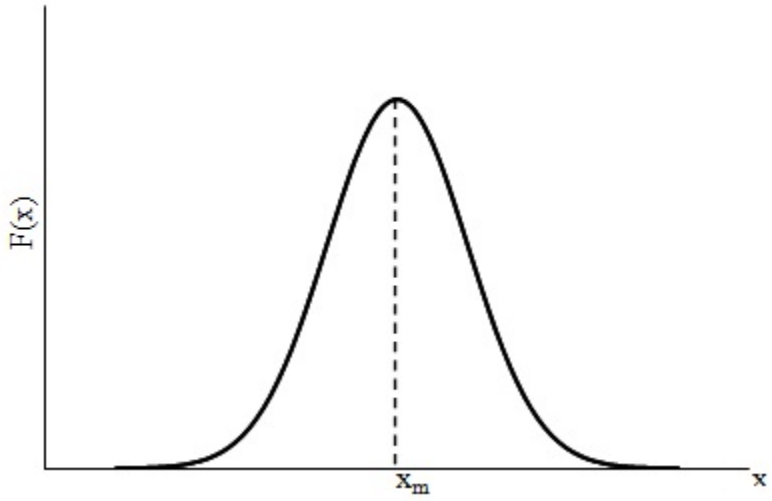


**Figure 2.12** Gaussian distribution curve, or "bell" curve

The applicability of the normal distribution in describing flaw sizes within a ceramic body has been subject to experimental verification. It has been shown that the normal distribution is most applicable when values under consideration are located near the mean value.[70] It is for this reason that flaw sizes which approach the tails are better described by utilizing an extreme value distribution. Extreme value distributions deal with the examination of regions of a probability function which are far from the mean value. This takes on special significance in relation to the fracture strength of ceramic bodies.

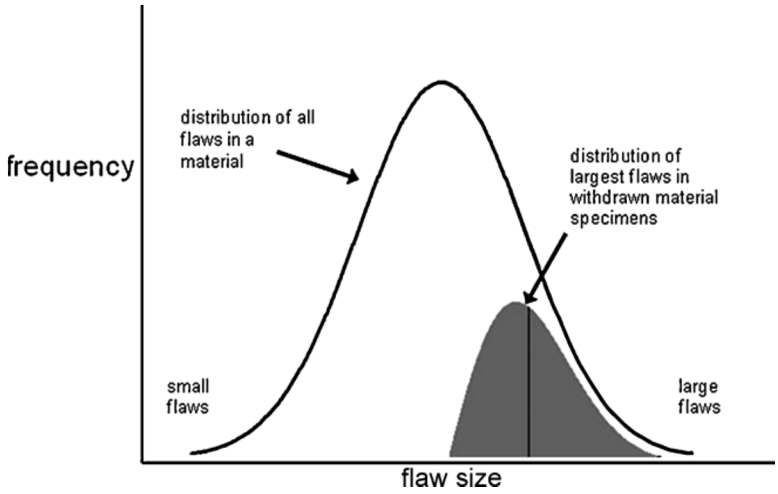


**Figure 2.13** Region of "largest flaws" sub-distribution from within a normal distribution of flaw sizes[70]

If elements are removed from a ceramic body, the flaw size distribution of each element should match that of the original piece. Each of these elements will contain a largest flaw, that when subjected to tensile stress will most likely become the source of fracture for that element. As the size of each element being removed increases, the likelihood of encountering a very large flaw within that element also increases. This has the effect of moving the "largest flaw" sub-distribution towards the right tail of the original normal flaw size distribution. This is shown in Figure 2.13. Extreme value theory holds that a data set which has been generated from the maximum values contained in a parent data set may only be described by one of the three extreme value distributions.[81]

### 2.3.5.2 Weibull Distribution

Along with the Gumbel and Frechet distributions, the Weibull distribution is an example of an extreme value distribution.[70] The application of Weibull statistics to describe the distribution of strength values within a ceramic body relies upon two

assumptions. One is the idea of the weakest link theory, in which failure of one element of a body causes failure of the entire body. The other assumption is that there are strength values associated with each element within a body that can be described by a distribution function.[72]

As put forth by Weibull in his 1951 treatise, the variable $X$ is assigned to an attribute of an element within a given population. The distribution function of $X$ is denoted as $F(x)$.[82] The probability of selecting at random an individual from this population with a value of $X$ less than or equal to $x$ is:[82]

$$P(X \leq x) = F(x) \qquad \text{Eq. 29}$$

A general form of any distribution function may be written as:[82]

$$F(x) = 1 - e^{-\varphi(x)} \qquad \text{Eq. 30}$$

Where $\varphi(x)$ is an as yet undefined function.

As stated previously, the weakest link theory applies to the failure of ceramic bodies. Failure of any chain in the link, or element within the body, results in the failure of the entire chain or piece. The generalized form of Equation 8 may be applied to determine the probability of failure, $P_f$, within a population of previously measured strength results. What is important to realize is that the probability of non-failure of all the body (1- $P_f$) is equal to the simultaneous non-failure of all elements within the body. Stated another way, $\left(1 - P_f\right) = (1 - P)^f$. Therefore, the probability of failure of an element within a body becomes:[82]

$$P_f = 1 - e^{-\varphi(x)} \qquad \text{Eq. 31}$$

There are a number of necessary conditions that the function $\varphi(x)$ must satisfy. It must be a positive, nondecreasing function which vanishes at $x_u$. The simplest form of the function which satisfies these conditions is given as:[82]

$$\varphi(x) = \left[\frac{x - x_u}{x_o}\right]^m \quad \text{Eq. 32}$$

Where $x_o$ is a scale parameter and $m$ is a shape parameter. A combination of Equations 15 and 16 leads to the general form of the Weibull distribution:[70]

$$F(x) = 1 - e^{-\left[\frac{x-x_u}{x_o}\right]^m} \quad \text{Eq. 33}$$

A re-assignment of the variables to the context of the distribution of strength values within a tested ceramic body, Equation 17 becomes:[71]

$$P_f = 1 - e^{-\left[\frac{\sigma-\sigma_u}{\sigma_o}\right]^m} \quad \text{Eq. 34}$$

Where $P_f$ is the probability of failure of the piece, $\sigma$ is the applied stress, $\sigma_u$ is the stress level below which there is zero probability of failure, $\sigma_o$ is the characteristic strength of the piece, or the strength at which the probability of failure is 63.2%, and $m$ is the distribution shape parameter or Weibull modulus, which describes the degree of variance within the strength data.[72] The parameters $m$, $\sigma_u$, and $\sigma_o$ are all generated from experimentally obtained data.

This is considered to be the three parameter form of the Weibull distribution. Additionally, the two parameter form of the Weibull distribution also exists, which has found common use in describing the strength distribution of elements within a ceramic body. When dealing with ceramic bodies, the possibility always exists that there will be

a large, strength-limiting flaw present within the piece such that $\sigma_u$ is taken to be zero.[70] This leads to the simplified, two parameter form of the Weibull distribution:[79]

$$P_f = 1 - e^{-\left[\frac{\sigma}{\sigma_o}\right]^m} \quad \text{Eq. 35}$$

Where the convention of assigning variables is the same as for the three parameter form. Through the use of both the two and three parameter Weibull distributions, the probability of failure of an entire ceramic body may be determined through the integration of the probability of failure for each individual element.[72]

Both the size of the test specimens and the number of samples tested has an effect on the validity of the survival estimates as generated from Weibull statistics. A minimum of ten samples should be tested to calculate the mean strength, while at least thirty strength values are necessary to have confidence in the generated Weibull parameters.[72] Mechanical testing of two different sized samples will result in different mean strengths. This is due to the different effective volumes of the two sample sizes, and the likelihood of encountering a strength-limiting flaw in the effective volume. The effective volume is considered to be the volume of the sample that is subjected to the maximum applied stress during the test. A larger sample with a corresponding larger effective volume will tend to have a lower average strength due to the increased likelihood of encountering a larger flaw in a greater volume. Average strength values as measured in different sized samples of the same material can be compared by:[72]

$$\left(\frac{\sigma_{m1}}{\sigma_{m2}}\right) = \left(\frac{V_{E2}}{V_{E1}}\right)^{\frac{1}{m}} \quad \text{Eq. 36}$$

Where $V_{E1}$ and $V_{E2}$ are the effective volumes of the two different size samples, $\sigma_{m1}$ and $\sigma_{m2}$ are the mean strengths associated with those strength values, and $m$ is the Weibull modulus associated with the material.

## 2.4 Analysis Techniques

### 2.4.1 Linear Regression

Scatter plots are used to graphically examine the association between two groups of data.[83] The numerical association between two data sets, or correlation, may be determined through the use of regression analysis.

For two data sets designated as $x$ and $y$, the variability within each data set is given as:[83]

$$s^2{}_x = \frac{\sum(x_i - \bar{x})^2}{n-1} \quad \text{Eq. 37}$$

$$s^2{}_y = \frac{\sum(y_i - \bar{y})^2}{n-1} \quad \text{Eq. 38}$$

Where $\bar{x}$ and $\bar{y}$ are the arithmetic means of the two independent data sets, and $n$ is the population of either data set. The covariance of the two data sets, or the degree to which they vary together, is calculated by:[83]

$$s_{xy} = \frac{\sum(x_i - \bar{x})(y_i - \bar{y})}{n-1} \quad \text{Eq. 39}$$

The covariance describes the degree that a linear relationship exists between the two data sets. The covariance may be normalized by dividing it by the standard deviation of each data set. This quotient is the Pearson correlation coefficient, $r$, which is given as:[83]

$$r = \frac{s_{xy}}{s_x s_y} = \frac{\sum(x_i - \bar{x})(y_i - \bar{y})}{\sqrt{\sum(x_i - \bar{x})^2 \sum(y_i - \bar{y})^2}} \quad \text{Eq. 40}$$

The Pearson coefficient can take on values from -1 to 1. A value of one is indicative of an absolute linear relationship between values within the two data sets, while a value of -1 indicates a linear relationship and a negative slope. A Pearson coefficient value of zero is reflective of the two data sets not having a linear relationship.

Another manner to determine the correlation between two data sets is the calculation of a linear least squares fit line. This involved applying a straight line fit to the data, and determining the applicability of that fit.

The standard equation of a line takes the form:[84]

$$y = mx + b \quad \text{Eq. 41}$$

Where $y$ is the dependent variable, $x$ is the independent variable, $m$ is the slope of the line, and $b$ is the y-intercept. The least squares regression line takes the form:[83]

$$\hat{y} = b_1 x + b_0 \quad \text{Eq. 42}$$

Where

$$b_1 = \frac{s_{xy}}{s^2{}_x} = \frac{\sum(x_i - \bar{x})(y_i - \bar{y})}{\sum(x_i - \bar{x})^2} \quad \text{Eq. 43}$$

and

$$b_0 = \bar{y} - b_1 \bar{x} \quad \text{Eq. 44}$$

Where $\bar{x}$ and $\bar{y}$ are the arithmetic means of the two data sets, and $\hat{y}$ is the predicted value of y for a given $x$. The predicted value of y is compared to the actual value at each data point. The error in this prediction is called the residual, which is calculated as:[83]

$$e_i = y_i - \hat{y}_i \quad \text{Eq. 45}$$

The residual is the vertical distance from each data point to the best fit line. The sum of squares due to error (SSE) is given as:[83]

$$SSE = \sum (y_i - \hat{y}_i)^2 \quad \text{Eq. 46}$$

The regression operation is iterated in order to minimize the SSE. The output of the linear regression analysis is $R^2$ the coefficient of determination. $R^2$ can take on the values from 0 to 1. A value close to 0 means that the dependent variable $\hat{y}$ cannot be predicted from the independent variable set. The value $R^2$ can be calculated according to:[85]

$$R^2 = \frac{(\sum(x_i - \bar{x})(y_i - \bar{y}))^2}{\sum(x_i - \bar{x})^2 \sum(y_i - \bar{y})^2} \quad \text{Eq. 47}$$

### 2.4.2 Fractography

Fractography is the study of fracture surfaces and fracture behavior. This includes investigation of the fracture path and microstructural features, and most importantly, the determination of the critical feature. While general fractography techniques may be applied to a multitude of materials, those described in this section where used in the analysis of polycrystalline ceramic materials examined in this dissertation.

Optical and electron microscopy form the basis of fractographic analysis. The reflection of light from the smooth mirror region surrounding the critical feature makes locating the fracture initiation point easier with an optical microscope. Furthermore, for the same reason, machining scratches are much more evident when viewed with a light microscope. The contrast and greatly increased magnification provided by electron microscopy makes it easier to locate and identify the critical feature on a fracture surface.

This is especially true in polycrystalline ceramics as inclusions in the microstructure would be challenging to identify optically as they tend to be the same color as the surrounding matrix material.

The critical feature is considered to be the feature from which fracture is believed to have initiated. Based upon fracture mechanics, this will be the weakest feature, which may be comprised of a dissimilar material than the matrix. Fracture initiates at this point and radiates outward.

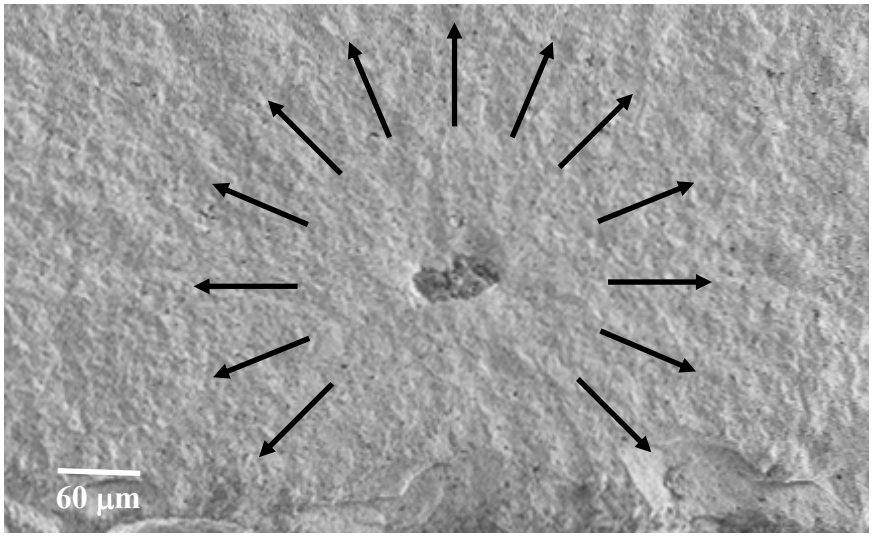


**Figure 2.14** Mirror plane in polycrystalline ceramic material

The critical feature is surrounded by a smooth region called the mirror. The size of the mirror region is dependent on the fracture strength. High energy, high strength fractures result in a short mirror length. As the fracture strength decreases, the size of the mirror region increases.[71] Mist and hackle regions are located at the edge of the mirror plane and result from a change in velocity during crack propagation. These features are very noticeable in glass, but with the exception of the mirror place, are extremely difficult

to discern in polycrystalline ceramics. A SEM image of a mirror plane surrounding a critical feature on the fracture surface of a ceramic material is shown in Figure 2.14.

The determination of fracture behavior is also one of the primary goals of fractography. In polycrystalline ceramics, fracture may occur transgranularly or intergranularly. In the case of transgranular fracture, the fracture path predominantly cuts through the grains, resulting in a somewhat smooth surface. In the occurrence of intergranular fracture, the fracture path tends to travel around the grains, through the grain boundaries, resulting in a fracture surface which is more faceted. Examples of both types of fracture behavior in ceramic materials are shown in Figure 2.15.

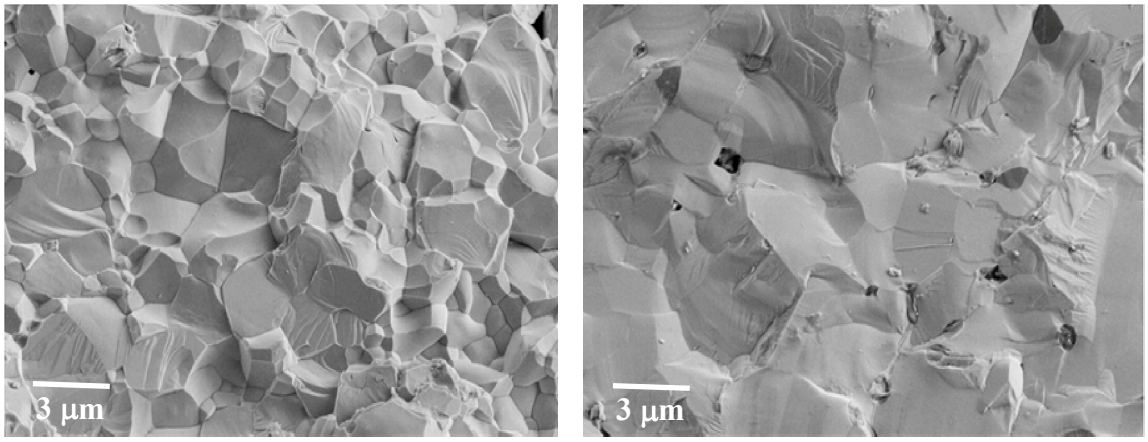


**Figure 2.15** SEM images of fracture surfaces of polycrystalline ceramic material. The material in the image on the left experienced predominantly intergranular fracture, while transgranular fracture dominated in the material in the right image

Analysis of the topography or texture in an image of a fracture surface will lead to a determination of the fracture path, which will tend to point back to the critical feature. The fracture front travels as a wave through the material that interacts with microstructural features, including pores and inclusions.[86] During uniaxial loading of a flexure sample, the stress is applied to the bar in only one direction. The localized stress

field at any point within the sample is much more complex due to the random orientation of grains and the addition of second phases.

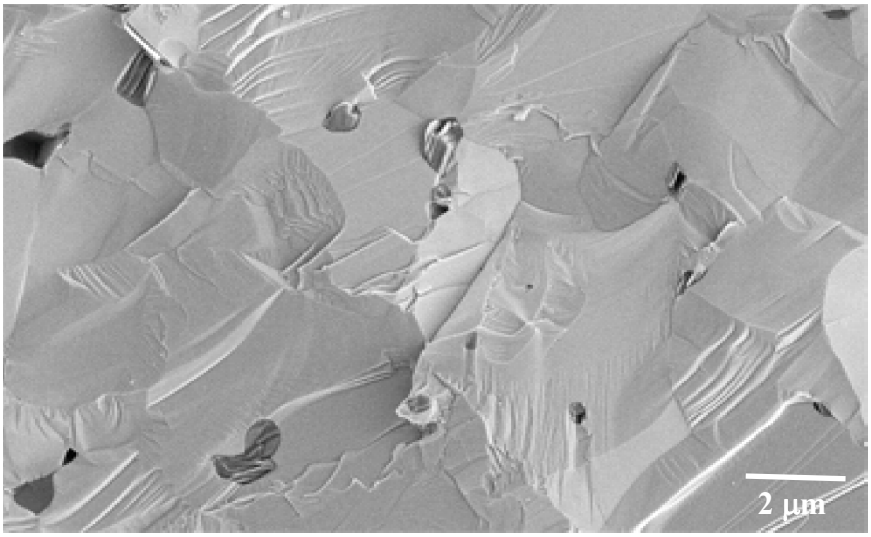


**Figure 2.16** Hackle lines on a polycrystalline ceramic material fracture surface

The presence of hackle lines can indicate the direction of stress. These post testing microstructural features occur parallel to the direction of cracking.[86] A type of hackle line, called wake hackle, occurs on the end of a microstructural feature opposite to the direction of propagation. Hackle lines in a polycrystalline ceramic microstructure are shown in Figure 2.16.

## 2.5. Ultrasound

The term ultrasound refers to sound energy that lies beyond the range of human hearing. Human beings have the ability to hear sounds with a frequency of approximately 20 Hz to 20 kHz.[87] Ultrasound energy is comprised of sound waves of frequencies greater than 20 kHz.

This dissertation relies upon the use of ultrasound energy as an evaluation tool of the microstructural variation present within silicon carbide materials. In this section, the

fundamentals of sound will be discussed. This includes sound production and propagation modes, interfacial sound wave behavior, as well as loss mechanisms such as absorption and scattering. The differences between sound and electromagnetic (EM) wave physics will be detailed, along with the influence of structure on the acoustic properties of a material. The components and function of an ultrasound test set will also be detailed.

### 2.5.1 Sound Production and Propagation

Sound waves are produced as a result of a change in pressure directly in front of a vibrating body, which causes particles to compress and then expand, called rarefaction. Sound travels as acoustic pressure waves that require an elastic medium to propagate. Propagation of sound waves through a medium occurs due to vibrations of atoms within the material.[88] The movement of the wave causes particles to oscillate back and forth from their equilibrium positions. Restorative forces within the material are generated due to the displacement of the particle, and through the coupling with inertial forces, oscillations are produced.[88] An oscillatory motion of one atom causes adjacent atoms to oscillate within the tightly bound matrix.[89] Elastic forces enable the oscillations to pass from one plane of particles to another, allowing them to move in unison, resulting in the propagation of the wave energy.[88] The amount of time that it takes the wave to transmit from plane to plane results in a lag within the material, and regions of compression and rarefaction. These zones travel at a constant velocity and with a uniform interval throughout the material.

In air, compression and rarefaction of particles occurs only in the direction of propagation. In non-gaseous materials, the number of vibrations, and therefore the types of sound waves propagated in the material are dictated by the structure. In solid materials, sound may propagate as longitudinal waves, shear waves, surface waves, and plate waves.[88]

Surface waves travel along the surface of thick materials at a depth of only one wavelength, and combine both a longitudinal and transverse motion to create on elliptic orbit motion.[90] These waves show enhanced sensitivity to surface defects as they follow the surface around curves. Plate waves exhibit similar behavior to surface waves but with the stipulation that they may only be generated in materials that are a few wavelengths thick.[90]

The two most useful types of waves utilized in ultrasonic testing are longitudinal and shear waves. For longitudinal waves, the compression and rarefaction moments occur in the direction of wave propagation. Particle oscillation occurs perpendicularly to the direction of travel during propagation of shear waves.[88] Shear waves are not effectively propagated in materials such as liquid or gasses as an acoustically solid material is required for propagation.[88] A graphical representation of the direction of amplitude displacement verses the direction of propagation for longitudinal and shear waves is shown in Figure 2.17.

The equation which governs the propagation of sound waves through an elastic medium is given as:[91]

$$y(x,t) = y_o \sin\left(\frac{2\pi x}{\lambda} - \omega t\right) \qquad \text{Eq. 48}$$

Where $y$ is the displacement of the propagating wave with respect to the distance, $x$, and time, $t$, $y_o$ is the amplitude of the wave, $\lambda$ is the wavelength, and $\omega$ is the angular wave frequency. It should be noted that this equation describes the behavior of longitudinal waves only.

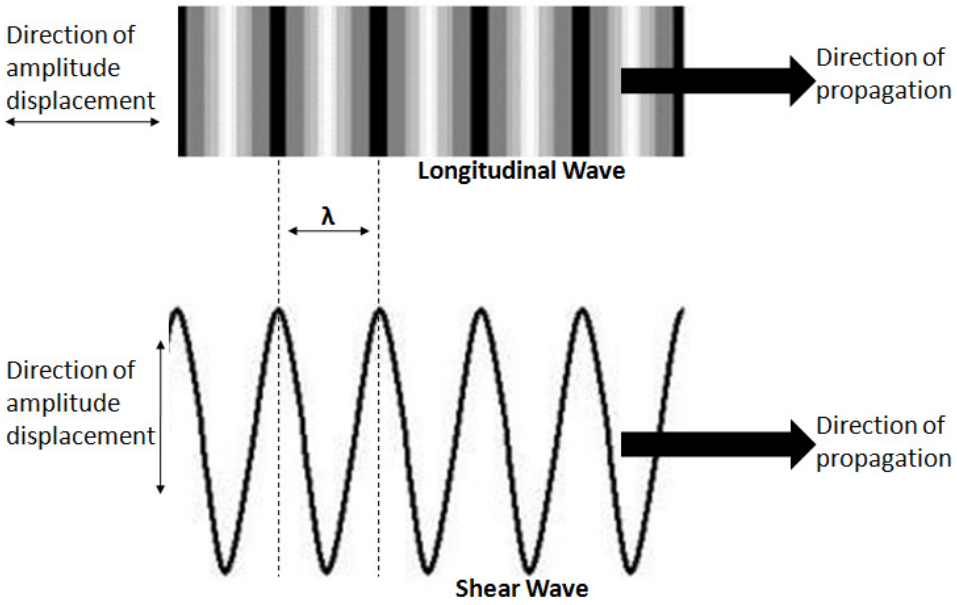


**Figure 2.17** Graphical description of longitudinal and shear wave propagation. Waves travel by compression and rarefaction of particles either perpendicularly or parallel to the direction of propagation[92]

### 2.5.2 Comparison to Electromagnetic Waves

Sound waves and electromagnetic waves have many analogous characteristics and phenomena. These include reflection, transmission, and refraction at an interface, as well as other wave properties. Common to all wave motion is a travelling disturbance. The disturbance is manifested by a change in electrical and magnetic fields for electromagnetic waves, while in reference to acoustic waves it takes the form of changes in pressure and density.[93] It is for this reason that while EM waves may travel through a vacuum, acoustic waves require a medium to propagate.[94]

For all waves, the amplitude of a wave is the maximum deflection from the equilibrium condition. The time to complete one wave cycle is called the period, or T, which is measured in seconds.[92] The wavelength, or λ, is the distance that the wave travels in one cycle, as measured in m. The number of oscillations per second is known as the frequency ($v$), measured in Hertz (Hz), with units of $sec^{-1}$. The frequency and the period are inversely proportional to one another, as given by the equation:[91]

$$v = \frac{1}{T} \qquad \text{Eq. 49}$$

In electromagnetism, the wavelength and frequency of a wave are related by the speed of light in a vacuum, $c$, according to the equation:[95]

$$c = \lambda\nu \qquad \text{Eq. 50}$$

In acoustic mediums, the relationship between frequency, wavelength, and the speed of sound also behaves according to the above equation where $c$ is the speed of sound in a medium. While the speed of light in a vacuum is constant, it varies based upon the index of refraction of different mediums. Likewise, the speed of sound also varies based upon the medium of propagation.

A prevalent difficulty when performing optical measurements is the phenomenon of dispersion, or frequency dependence of the speed of light in a medium.[96] For many dense materials, the speed of sound may be considered to be a constant.[97] This has beneficial consequences for ultrasound scanning of samples. The frequency of acoustic energy used in an evaluation can be chosen such that the wavelength of the waves in the sample will be of sufficient size to interact with microstructural features. Based upon

past work of ultrasound scanning in high density, high hardness ceramics, this was shown to be in the frequency range of megahertz (MHz).[98, 99]

### 2.5.3 Relationship between Density and the Speed of Sound

The speed of sound $c$ in a medium is directly dependent on the structure of the medium through which it is propagating. The speed of sound is dependent on both the elastic modulus ($M$) and density $\rho$ of the medium as given by the equation:[93]

$$c = \sqrt{\frac{M}{\rho}} \qquad \text{Eq. 51}$$

Where $M$ may either be the Young's or shear modulus, dependent upon whether the longitudinal or shear wave velocity is being considered. The above equation is applicable for isotropic materials. When determining the speed of sound in an anisotropic material, the above equation may be modified by considering Poisson's ratio, $\nu$, as shown in the equation below:[100]

$$c = \sqrt{\frac{M}{\rho}\,\frac{(1-\nu)}{(1+\nu)(1-2\nu)}} \qquad \text{Eq. 52}$$

Materials with a higher elastic modulus tend to exhibit higher sonic velocities. Stronger bonds within the material allow for faster elastic oscillations, and a higher velocity.[101] Gases tend to exhibit low sonic velocities, followed by liquids. Materials with ionic or covalent bonding such as ceramics typically have higher acoustic velocities when compared to metals, which exhibit metallic bonding.[93]

**Table 2.4** Acoustic properties of common materials. Fields include density, longitudinal velocity, and acoustic impedance[19, 22, 102-105]

| Material | Density ($g/cm^3$) | Longitudinal Velocity ($C_L$) (m/s) | Acoustic Impedance (Z) ($10^5$ $g/cm^2.s$) |
|---|---|---|---|
| Air | - | 330 | 0.0004 |
| Water | 1.00 | 1,480 | 1.5 |
| Oil | 0.88 | 1,700 | 1.5 |
| Glycerin | 1.26 | 1,900 | 2.4 |
| Carbon | 1.47 | 2,250 | 6.3 |
| Iron | 7.69 | 5,900 | 45.4 |
| Steel | 7.80 | 5,850 | 45.6 |
| SiC (sintered) | 3.16 | 11,820 | 37.5 |
| SiC (hot pressed) | 3.21 | 12,100 | 39.0 |
| $Al_2O3$ (sintered) | 3.98 | 10,600 | 43.0 |
| AlN (hot pressed) | 3.26 | 10,700 | 35.0 |
| $B_4C$ (sintered) | 2.51 | 14,090 | 35.4 |
| $Si_3N_4$ (sintered) | 3.05 | 11,000 | 33.5 |
| $TiB_2$ (sintered) | 4.50 | 11,400 | 51.3 |
| WC (sintered) | 15.80 | 9,500 | 114.0 |
| $Al_2O3$ (green) | - | 1,600 | 2.4 |
| WC (green) | - | 1,400 | 2.8 |

### 2.5.4 Wave Phenomena

#### 2.5.4.1 Acoustic Impedance, Reflection, and Transmission

The acoustic impedance ($Z$) of a material is a measure of the resistance to sound propagation in a medium. It is dependent on the structure, as denoted by the equation:[97]

$$Z = c_L \rho \qquad \text{Eq. 53}$$

Where $C_L$ is the longitudinal velocity and ρ is the density. Acoustic impedance is analogous to the index of refraction ($n$) in electromagnetic wave propagation.[91] When an acoustic wave encounters an interface between materials with different acoustic impedance, a percentage of the wave energy with be either reflected or transmitted at that boundary.[97] This difference in $Z$, known as the acoustic impedance mismatch, dictates that amount of energy reflected at that interface.[106] The higher the acoustic impedance mismatch, the greater the amount of energy that will be reflected.[106] The proportion of energy that is reflected or transmitted at an interface may be quantified according to:[107]

$$R = \frac{(Z_2 - Z_1)^2}{(Z_2 + Z_1)^2} \qquad \text{Eq. 54}$$

$$T = \frac{4Z_1Z_2}{(Z_2 + Z_1)^2} \qquad \text{Eq. 55}$$

Where $Z_1$ and $Z_2$ are the acoustic impedance values of the original and secondary mediums. It should be noted that the calculated values are applicable to a wave which is normal to the interfacial boundary. The proportion of the wave energy that is reflected or transmitted is the same whether the wave propagates from a low to high impedance material, or in the reverse direction. When the intention is to couple the maximum amount of energy from one material into another, it is preferable to keep the acoustic impedance mismatch as low as possible. However, when trying to detect a flaw or defect, a high impedance mismatch is beneficial. A compilation of the density, longitudinal velocity, and acoustic impendence of a number of materials is shown in Table 2.4.

### 2.5.4.2 Refraction and Mode Conversion

When a wave encounters the interface between two materials at an oblique angle, both reflected and refracted waves will be produced.[108] As an acoustic wave encounters a medium of different density or elastic modulus, the change in velocity of the wave will cause it to bend.[109] This is the process of refraction. The behavior of waves at an interface are described by Snell's Law:[96]

$$\frac{\sin(\theta_1)}{C_1} = \frac{\sin(\theta_2)}{C_2} \qquad \text{Eq. 56}$$

Where $\theta_1$ and $\theta_2$ are the angles of incidence and refraction, and $C_1$ and $C_2$ are the speeds of sound in mediums 1 and 2, respectively. Waves entering a medium with a reduced speed of sound slow down and bend towards the interface.

Refraction of a wave at a solid interface is the cause of mode conversion. This is the transformation of wave energy from one type of wave to another.[110] This phenomenon has important implications to ultrasound testing. Water and other low viscosity fluids do not support the propagation of shear waves.[111] Mode conversion makes it possible to probe both the longitudinal and shear moduli through the use of a longitudinal wave transducer during immersion based measurements.[97] The transfer of wave energy between propagation modes is reversible. Shear waves produced by mode conversion are converted back to longitudinal waves at the interface of the top surface of the sample and the immersion fluid.[97, 112, 113] This allows the measurement of the shear moduli using an immersion based longitudinal wave transducer. Another approach to measuring the elastic properties of a sample involves using both shear wave and longitudinal wave transducers in contact with the sample.[111]

### 2.5.4.3 Superposition

The principle of linear superposition describes the property which allows two waves travelling through a medium in opposing directions to interact with each other while retaining the original information of each individual wave.[91, 92] This permits waves of different velocities, phases, or frequencies to travel simultaneously through the same propagation medium, such as the acoustic pulses produced by a broadband ultrasound transducer. The waves may interact and undergo either constructive or destructive interference. Constructive interference involves an addition of the information contained within the wave, such as amplitude. A subtraction of wave information is destructive interference. When taking a time-based snapshot of the wave form, constructive and destructive interference produces well defined peak shapes.

### 2.5.4.4 Resonance

Resonance is the harmonic coupling of oscillations in the presence of a driving force. As shown in the work of Uberall et al., features within a dense microstructure may resonate when driven by periodic pulses of acoustic energy.[114, 115] If the features are of a correct size and sonic velocity, they will begin to oscillate with increasing amplitude when driven by the emitted acoustic energy of the transducer. Oscillating features will emit low amplitude acoustic waves. Resonance may show up in an ultrasound C-Scan if the waves generated by the oscillating feature fall within the acceptance range of the ultrasound transducer.[116]

### 2.5.5 Sources of Loss

Propagation of acoustic energy through materials that contain grain boundaries, inclusions, and pores results in attenuation of the signal.[117] Factors which contribute to the reduction of intensity of the ultrasound signal due to loss may be separated as shown by:[118]

$$\alpha_{Total} = \alpha_{GS} + \alpha_{GA} + \alpha_{HS} + \alpha_{HA} + \alpha_{Reflection} + \alpha_{Diffraction} \quad \text{Eq. 57}$$

Where $\alpha_{Total}$ is the overall loss, $\alpha_{GS}$, $\alpha_{GA}$, and $\alpha_{HS}$ are the loss factors due to grains, heterogeneities, scattering, and absorption, and $\alpha_{Reflection}$ and $\alpha_{Diffraction}$ denote attenuation by reflection and diffraction of the beam, respectively. Attenuation due to the first four factors depends not only on the size and type of features within the microstructure but also on the frequency of the ultrasound beam.[118] The degree of loss due to reflection and diffraction do not depend on the size of microstructural features, and will be discussed in the following sections.[113] An illustration of the interactions of the ultrasound beam with microstructural features is shown in Figure 2.18. Beam path A is indicative of acoustic propagation with minimal interaction with the microstructure, as peak reflections are only seen at the position of the top and bottom surfaces of the sample. Paths B and C contain reflections from within the bulk of the material, indicating loss due to interaction with the microstructure.

Two mechanisms which affect the ability of acoustic energy to propagate through a material, in particular sintered silicon carbide, are absorption and scattering.[118] Absorption is the conversion of energy within the ultrasound beam to heat.[119] Loss due to absorption tends to dominate at low frequencies.[120] Loss in this frequency regime is dependent upon the thermal and elastic properties of the propagation medium in addition

to the beam conditions stated above.[121] Absorptive losses may be divided into many sub-groups. The applicable mechanisms that cause loss in sintered silicon carbide will be discussed in the following sections. It was found in the work of Portune et al. in sintered silicon carbide that attenuation in second phases such as pores and inclusions differed from that of the matrix material.[122]

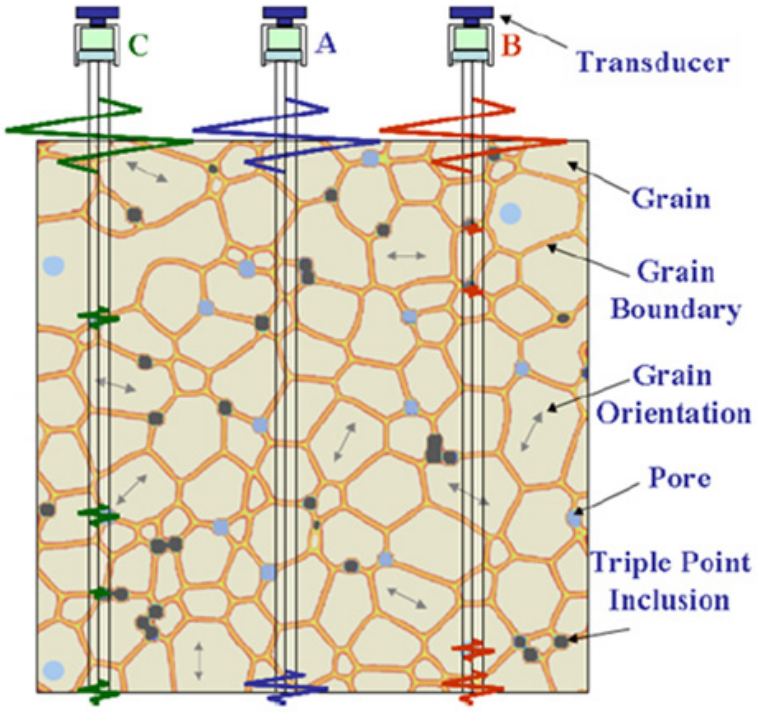


**Figure 2.18** Examples of signal attenuation due to interaction with microstructural features in dense, polycrystalline ceramics[98]

Scattering is the redirection of the acoustic wave to any orientation which causes it to go unmeasured.[123] Scattering occurs when acoustic energy encounters an interface between materials where a difference in acoustic impedance occurs.[93] The degree of loss increases when the features are randomly orientated such that the acoustic energy is redirected from the normal path. Scattering loss mechanisms tend to dominate at higher frequencies when the wavelength of the acoustic energy begins to approximate the size of

the features within the microstructure.[124] As in the case with absorptive losses, the scattering regime may be broken down further into sub-regions. These are based upon the relationship between the wavelength of the ultrasound energy and the size of the scattering feature.

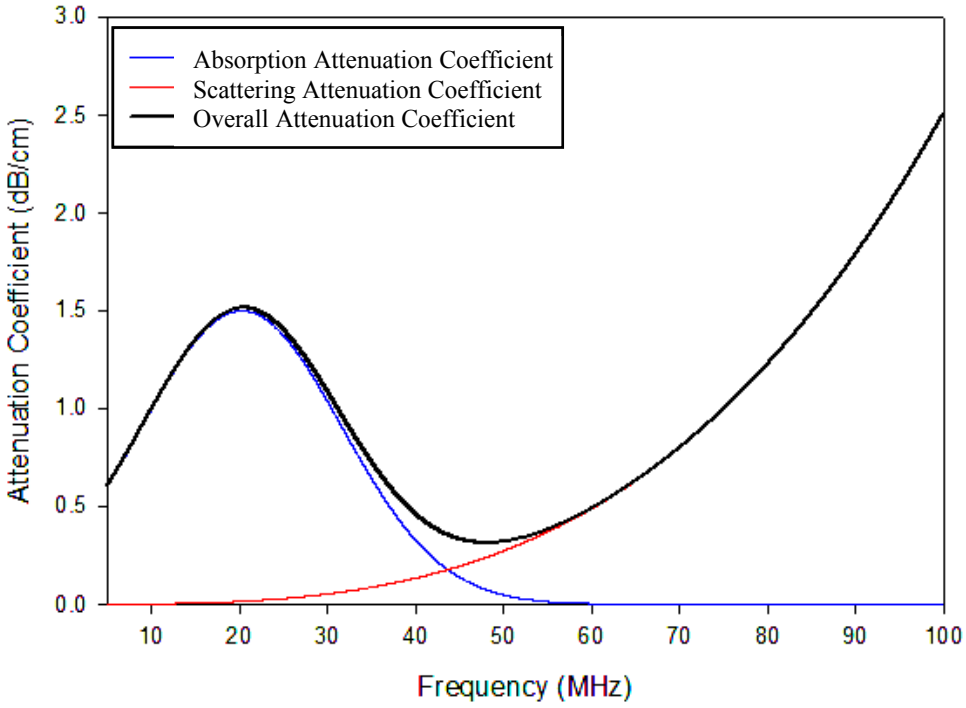


**Figure 2.19** Acoustic attenuation as a function of frequency in an ideal material[125]

The attenuation spectrum of a material which shows "ideal" attenuation behavior is shown in Figure 2.19. While loss at any frequency is due to a combination of factors, it can be seen that absorptive losses tend to dominate at low frequencies, while loss due to scattering is the dominant loss mechanism at higher frequencies. The separation in frequencies of the dominant mechanisms makes it possible to study their contribution to loss separately. While the ultrasound testing in this dissertation was for the most part performed in the "low" frequency range, it is important to consider all contributions to

loss in understanding the relationship between microstructure, mechanical properties, and acoustic loss.

### 2.5.6 Absorption

Absorption is a conversion of ordered particle motion into heat. The driving force for this loss mechanism comes from the pressure of a propagating acoustic wave. Acoustic absorption may be broken down into further subsets. These include: thermal conduction absorption, viscous absorption, chemical relaxation absorption, dislocation damping absorption, hysteresis absorption, and thermoelastic absorption. Thermoelastic absorption is the most prevalent absorption mechanism in dense, polycrystalline ceramics and will be the primary focus of the following discussion.[122]

#### 2.5.6.1 Thermal Conduction, Viscous, Chemical Relaxation, Dislocation Damping, and Hysteresis Absorption

Propagation of acoustic waves causes heating of a material by the conversion of ordered particle motion into disordered motion.[121] The degree of thermal conduction absorption is controlled by the thermal conductivity of a medium. It was also found that the slight differences in the elastic modulus of a material when changing from adiabatic to isothermal thermodynamic conditions also contributed to acoustic loss.[121] Under adiabatic conditions, there is no net heat flow into or out of a system, while an isothermal process occurs without a change in the net temperature of a system.[74]

The equation which governs attenuation by thermal conduction absorption is given as:[121]

$$\alpha = \pi\left(\frac{V}{V_o}\right)^2 \left(\frac{E_A - E_I}{E_I}\right)\left(\frac{f f_o}{f^2 + f_o^2}\right) \quad \text{Eq. 58}$$

Where $\alpha$ is the attenuation, $V$ is the longitudinail velocity of the material, $V_o$ is a theoretical frequency that is defined by the density and stiffness of the material, $E_A$ and $E_I$ are the elastic moduli under adiabatic and isothermal conditions, respectively, $f$ is the frequency of the acoustic wave, and $f_o$ is the frequency of maximum attenuation. Increased attenuation results in materials with increased thermal conductivity and smaller differences in elastic moduli between adiabatic and isothermal conditions. It has been shown that thermal conduction absorption is prevalent in materials which exhibit acoustic wave dispersion[121]. For this reason, this mechanism will not be a significant contributor to overall attenuation in dense, polycrystalline ceramics.

Viscous drag absorption results from the heating which occurs due to friction from the slight movement of a higher density particle within a lower density fluid medium under the influence of pressure from the propagation of an acoustic wave.[126] The movement of the particles and the resulting heating and attenuation occur from a sonic velocity mismatch between the suspended particles and the fluid medium. Acoustic loss resulting from viscous absorption was predicted to follow the following behavior:[127]

$$\alpha_\eta = 4\pi n k R^2 (1 - \delta) R e^{\left(i\frac{\lambda}{D}\right)} \quad \text{Eq. 59}$$

Where $\alpha_\eta$ is the attenuation caused by viscous drag absorption, $n$ is the concentration of second phase particles within the suspension, $k$ is the wavenumber of the acoustic waves, $R$ is the radius of the suspended particles, $\delta$ is the ratio of densities between the suspended particles and the fluid medium, $\lambda$ is the wavelength of the acoustic wave, and $D$ is a term that is used to maintain continuity between the suspended particles and fluid

medium. Viscous drag absorption was shown to most prevalent in fluid suspensions, and should not be an active loss mechanism in ceramic materials.[128]

Chemical relaxation absorption occurs from pressure-induced increases in temperature that results in a loss of equilibrium of a chemical state.[129] While this mechanism is most clearly associated with gasses and viscous liquids, it occurs in solids when the wavelength is very large when compared to the mean free path of thermal phonons, or heat induced vibration of the crystal lattice of the material.[119] Acoustic absorption by chemical relaxation may be described according to:[130]

$$\alpha = \frac{2\omega}{c} \sin\left(\frac{\omega \Gamma \ln(\gamma)}{2\sqrt{1 + \omega^2 \Gamma^2}}\right) \quad \text{Eq. 60}$$

Where $\alpha$ is the chemical relaxation attenuation, $\Gamma$ is the relaxation time, $c$ is the speed of sound, and $\omega$ is the wavenumber. This loss mechanism is not expected to be prevalent in dense ceramics due to the high chemical stability of this class of materials.

Loss due to dislocation damping absorption involves dislocation glide within the microstructure of a material due to pressure from the propagation of an acoustic wave. Factors which affect the degree of attenuation include the orientation of the dislocations to the acoustic wave direction, the stiffness of the matrix, and the amplitude of the wave energy.[131] An initial condition for a material to be susceptible to this type of loss is the presence of dislocation with sufficient mobility and damping ability, which is contingent on internal friction.[132] As dislocations are sufficiently pinned within the microstructure in silicon carbide materials, this mechanism should not have an effect on acoustic attenuation measurements performed in this dissertation.

Hysteresis absorption is the result of a physical relaxation of bonds within the material due to propagation of an acoustic wave.[133] It is most prevalent in materials

where there exists a metastable state which is susceptible to minute changes in pressure. This is considered to be an irreversible process which results in an overall increase in entropy of the system.[133] The degree of attenuation is dependent upon the wavelength of the acoustic energy and the temperature of the medium. As with previous absorption mechanisms, it is not expected to be a significant contributor to loss within dense ceramic materials.

#### 2.5.6.2 Thermoelastic Absorption

Propagation of an acoustic wave within a polycrystalline material leads to a distribution of stresses within the propagation zone. Through a coupling of the elastic and thermal fields within the medium, pressure-induced stress fluctuations will lead to temperature inhomogeneities, and ultimately to regions of localized heat flow.[134] Heat flow between regions of compression and rarefaction is irreversible, resulting in measurable acoustic loss.[121] The degree of loss is dependent upon the thermal conductivity of the material, the orientation of grains to the ultrasound beam, and pressure changes induced by the acoustic energy.

Of the absorptive loss mechanisms which have been discussed, thermoelastic absorption is the primary source of absorptive acoustic attenuation in dense, polycrystalline silicon carbide ceramic materials, as was shown by the work by Portune, et al.[122] In this type of materials, equalization of both the thermal and elastic fields occurs within features, and also across boundaries between neighboring features, which may include pores, inclusions, and the matrix material. This leads to absorption which may by designated as occurring either intraparticle or interparticle.

### 2.5.6.3 Intraparticle Thermoelastic Absorption

Development of an understanding of thermoelastic absorption of single crystals was first undertaken by Zener.[135] The feature in question was considered to be a one-dimensional reed bound at both ends such that only the center of the feature is free to respond to applied stress. The stress conditions and the response of the material at three different times during one wave cycle are shown in Figure 2.20.

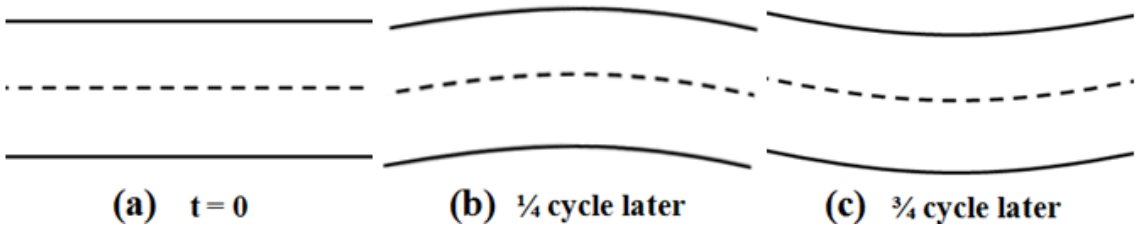


**Figure 2.20** Stress state of a one-dimensional feature subject to acoustic wave pressure. (a) At t=0, no stress, (b) ¼ λ, top surface in tension, bottom in compression, (c) ¾ λ, top surface in compression, bottom surface in tension[121]

At t=0, there is no stress on the feature. After a quarter of a cycle, a portion of the feature has been put into compression, while the opposite portion is in tension. A half cycle later, the stress state has been reversed. Differential heating occurs within the portion of the feature which has been put into compression. Heat flow occurs from the compressed side to the dilated side to enable the feature to reach thermal equilibrium.[121]

Attenuation of a single particle due to intraparticle thermoelastic absorption is described by:[136]

$$\alpha = 2\pi\left(\frac{E_S - E_T}{E_S}\right)\left(\frac{f f_o}{f^2 + f_o^2}\right) \qquad \text{Eq. 61}$$

Where $\alpha$ is the absorption, $E_S$ and $E_T$ are the elastic moduli under adiabatic and isothermal conditions, $f$ is the frequency of the acoustic wave, and $f_o$ is the frequency of maximum attenuation. The parameter $f_o$ may be calculated according to the following equation:[136]

$$f_o = \frac{2\chi}{C_V d^2} \qquad \text{Eq. 62}$$

Where $\chi$ is the thermal conductivity, of units W/mK, and $d$ is the diameter of the attenuating feature, and $C_V$ is the specific heat at constant volume.

The thermodynamic conditions and the resultant degree of heating associated with intraparticle thermoelastic absorption exhibit strong frequency dependence. At short wavelengths, the attenuating features vibrate very quickly. Thermal equilibrium is then reached under adiabatic conditions without heat flow. Acoustic energy of sufficiently large wavelengths induces an even stress distribution between surrounding particles. As the heat distribution is therefore homogeneous, thermal equilibrium is reached under isothermal conditions.[135] The degree of acoustic absorption is minimal under both of these thermodynamic conditions.[121] As irreversible heat flow determines the degree of attenuation, it was shown that peak absorption occurs in between these maximum conditions.[135]

Studies of intraparticle thermoelastic loss measurements in glass and polycrystalline metals detailed the loss dependence on elastic properties and the size of features.[134] Peak absorption occurs in lower frequencies in metals than in ceramics due to larger grains in metals.[132] The work of Portune on dense ceramics in the MHz range showed that this is the dominant absorption mechanism in this type of material.[122]

### 2.5.6.4 Interparticle Thermoelastic Absorption

Loss due to thermal elastic absorption at boundaries between features is dependent upon a difference in thermal and elastic properties, as well as the orientation of the features, at these boundaries. These include interfaces between inclusions and grains, inclusions and inclusions, and between adjacent grains. Differences in these properties lead to temperature gradients which results in heat flow and mechanical energy absorption.[137]

The temperature gradient is also due to the different orientation of grains in respect to the propagating acoustic waves. As the wave propagates in only one direction, differential heating of surrounding grains occurs due to the varied orientations.[121] Irreversible heat flow from hotter to cooler grains leads to ultrasonic absorption.[137] Larger temperature gradients require more energy absorption to reach thermal equilibrium. Increased interparticle absorption is also caused by an increase in the elastic anisotropy between adjacent features.

Interparticle thermoelastic attenuation is described by:[121]

$$\alpha = \kappa_a \left(\frac{C_P - C_V}{C_V}\right)\left(\frac{f f_o}{f^2 + f_o^2}\right) \qquad \text{Eq. 63}$$

Where $\alpha$ is absorption, $\kappa_a$ is an anisotropy factor, $C_P$ and $C_V$ are the specific heats at constant pressure and volume, $f$ is the frequency of the acoustic wave, and $f_o$ is the frequency of maximum attenuation. The maximum attenuation frequency, which is dependent upon the thermal properties and size of the attenuating features, may be calculated according to:[121]

$$f_o = \frac{3\pi}{2}\frac{\chi}{C_V a^2} \quad \text{Eq. 64}$$

Where $\chi$ is the thermal conductivity, of units W/mK, $C_V$ is the specific heat at constant volume, and $a$ is the diameter of the attenuating feature. The frequency of maximum attenuation for interparticle absorption is approximately three times that for intraparticle absorption.[122]

Interparticle thermoelastic absorption also shows a strong dependence on frequency. At short wavelengths, thermal equilibrium is, therefore, reached under adiabatic conditions. At large wavelengths, thermal equilibrium is reached under isothermal conditions. As with the case of intraparticle absorption, the degree of acoustic absorption is minimal under both of these conditions.[121] It has been shown that the time scale for thermal transfer between grains is too long in comparison to the period of MHz acoustic waves for interparticle absorption to occur substantially in polycrystalline ceramics.[138]

### 2.5.7 Scattering

As scattering is the redirection of a wave to any orientation which causes it to go unmeasured, it is a contributor to acoustic loss.[123] Scattering of energy occurs at interfaces between mediums at which there exists a difference of acoustic impedance.[118] These may include the boundary between the matrix material and pores and porous inclusions, as well as grain boundaries. Three wave interactions may occur at each interface. These are the incident wave, the scattered wave, and the wave emitted by the scatterer.[139] The degree of scattering is dependent upon the wavelength of acoustic energy, the acoustic impedance mismatch, and the size of the scatterer.[140]

Three scattering regions have been defined based upon the relationship between the wavelength of the acoustic wave and the size of the scattering feature. These are the Rayleigh, stochastic, and diffuse scattering regimes. The Rayleigh regime refers to the scattering behavior when the wavelength of the acoustic energy is much larger than the scattering feature. Within the stochastic regime, the wavelength of the acoustic wave is on the order of the size of the scattering feature. Finally, diffuse regime describes the scattering behavior when the size of the scatterer is much larger than the wavelength of the acoustic energy. While distinct boundaries between the regimes have not been defined, an overlap of the Rayleigh and stochastic regime occurs as the wavelength and size of the scattering feature begin to approximate one another.[118]

Two relationships have been set forth for defining the three scattering regimes, as shown in Table 2.4.2. The first of these is found by multiplying the wavenumber, $k$, by the size of the scatterer, $a$, which relates the frequency and the wavelength of the acoustic energy to the scattering feature size:[141]

$$ka = \frac{2\pi}{\lambda}a = \frac{2\pi f}{c}a \qquad \text{Eq. 65}$$

The relationship between attenuation and frequency has also been defined, where $\alpha$ is the attenuation, $a$ refers to the average diameter of all scattering features, and $f$ is the frequency of the acoustic wave.[140] The terms $C_R$, $C_S$, and $C_D$ are material-dependent prefactors.

**Table 2.5** Scattering regimes detailing the relationship between the size of the scatterer and the wavelength of the acoustic energy, as well as expressions relating the acoustic attenuation coefficient to frequency[140]

| Scattering Regime | ka Relationship | $\alpha$ to Frequency Relationship |
|---|---|---|
| Rayleigh | $ka << 1$ | $\alpha_R = C_R a^3 f^4$ |
| Stochastic | $ka \approx 1$ | $\alpha_S = C_S a f^2$ |
| Diffuse | $ka >> 1$ | $\alpha_D = \frac{C_D f^0}{A}$ |

Initial work by Rayleigh on the interaction of acoustic waves and elastic mediums focused on the examination of the scattering cross section of a material as a means of determining attenuation due to scattering.[93, 142] Two methods were developed to calculate the scattering cross section based upon the elastic properties of the host medium and the scattering feature.[143] The first method could be applied irrespective of the morphology of the scattering feature, but was only applicable when a slight elastic mismatch existed between the host medium and the scattering feature. The second method could be applied, no matter, what the elastic property mismatch, but assumed that the scattering features were spherical. The second method would be more closely associated with dense, polycrystalline ceramics due to the elastic property mismatch between the host matrix and porosity or porous inclusions. Using this method, the scattering cross section may be calculated according to:[142]

$$\sigma_d(\gamma) = \frac{V_C \pi^2}{\lambda^4}\left[\frac{\kappa_S - \kappa_O}{\kappa_O} + \frac{3\,(\rho_S - \rho_O)}{2\rho_O}\cos\gamma\right]^2 \qquad \text{Eq. 66}$$

Where $\sigma_d$is the scattering cross section, $\gamma$ is the angle of incidence between the acoustic wave and the scattering feature, $V_C$ is the volume of the spherical scattering feature, $\lambda$ is

the wavelength of the acoustic wave, $\kappa$ is a factor which describes the compressibility, $\rho$ is the density of the medium, and $s$ and $o$ refer to the properties of the scattering feature and the medium.

Further work on understanding of the scattering of waves within materials focused on developing a generalized solution that was not bound by the many constraints associated with the methods of Rayleigh.[144] The method set forth by Mie was developed as a solution to Maxwell's wave equations, which were found to be applicable to acoustic waves by developing a term to account for the acoustic impedance mismatch between the scattering feature and the host medium, and by assuming once again that the scattering features were spherical. Using this method, the scattering cross section may be calculated as:[145]

$$\alpha_M = \frac{2\pi}{k^2}\sum_{n=1}^{\infty}\{(2n+1)(|a_n|^2 + |b_n|^2)\} \quad \text{Eq. 67}$$

Where $\alpha_M$ is the Mie scattering cross section, k is the wavenumber, and $a_n$ and $b_n$ are the Mie coefficients.

### 2.5.8 Loss Mechanisms in Silicon Carbide

Loss in dense, pressureless sintered silicon carbide is dependent on the interaction of the acoustic beam with features within the microstructure of the material. These include grains of the silicon carbide matrix material, porosity, grain boundaries, and porous agglomerates of sintering additives. Scattering will occur at all wavelengths of energy within the ultrasound beam, particularly within the Rayleigh regime. Scattering loss from porous agglomerates will be greater than that from silicon carbide grains due to

the acoustic impedance mismatch between SiC and $B_4C$ and C. Scattering may enter the stochastic region for larger sintering aid agglomerates on the order of tens of microns (μm) in size. The dominant contributor to loss in the range of wavelengths where measurements were performed should be thermoelastic intraparticle absorption.[122]

### 2.5.9 Ultrasound Test Set Components

An ultrasound test set contains the necessary components to carry out the non destructive evaluation of samples. Two options for accomplishing this include purchasing a pre-built, off the shelf system, or constructing a test set of individual components. Advantages of purchasing an off the shelf system are ease of use and installation and technical support from the manufacturer. However, these systems tend to be more expensive, and may be more difficult to upgrade. Furthermore, the user may have less of an understanding of the interaction between components within the system. The ultrasound evaluation that took place for this dissertation was carried out on a purpose-built system that was assembled from separately integrated components. Assembly and integration of the test set components and authoring of the control and data acquisition software was performed at Rutgers by Brennan et al. and Portune et al.[98, 122]

Off the shelf or custom-built test sets share similar types of components. Required equipment would include a system to translate the transducer, a system to collect the ultrasound signal, and a system to input the test parameters, display the oscilloscope trace, and store the data from the test. The components of a generalized ultrasound set are shown in Figure 2.21. These include: a pulser-receiver, remote pulser, ultrasound transducer, motion controller, motor drivers, scanning gantry, analog-to-

digital converter card, a timer-counter card, and a personal computer. The function of each component will be discussed in the following section.

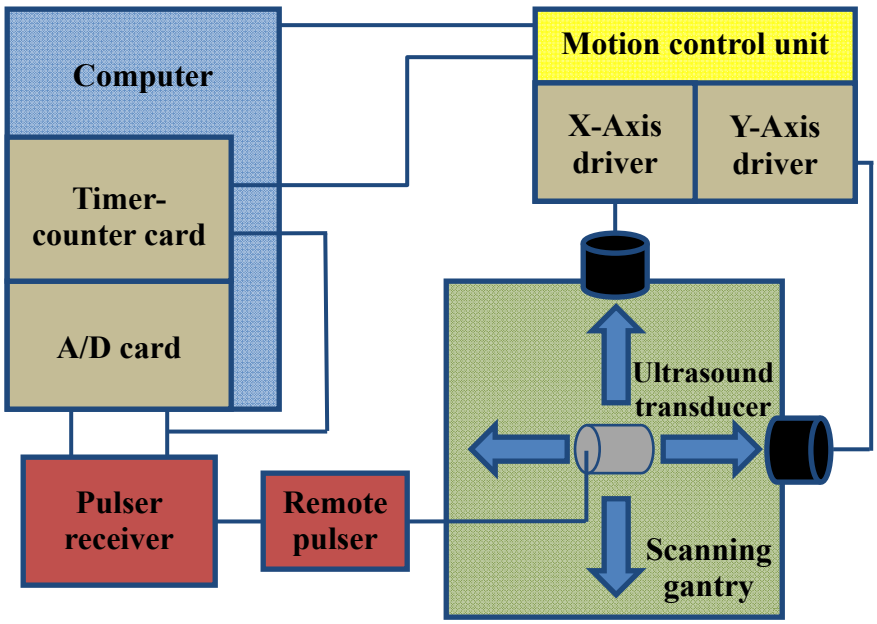


**Figure 2.21** Schematic of generalized ultrasound test set. Components include: the personal computer, timer-counter card, A/D card, pulser receiver, remote pulser, motion control unit, X and Y-axis drivers, scanning gantry, and ultrasound transducer

The ultrasound transducer is the heart of the ultrasound evaluation system. The function of the transducer is to emit and receive acoustic energy, allowing for the interaction with the microstructure of the sample. The frequency response of a transducer is a factor of the geometry of the active elements within the transducer module.[146] In this section, the basic principles of the ultrasound transducer, including the physical structure, acoustic wave components, and transducer classes will be discussed.

Operation of ultrasound transducers relies upon the principle of piezoelectricity. A piezoelectric is that class of material which experiences mechanical strain in the presence of an electric voltage.[37] The effect is reversible in that the application of an

external stress to these materials results in the production of an electric voltage.[37] A piezoelectric crystal comprises the active element in a transducer module. In this application, the crystals have poles assigned such that constriction of the material occurs in the same direction. An illustration of this phenomenon is shown in Figure 2.22.

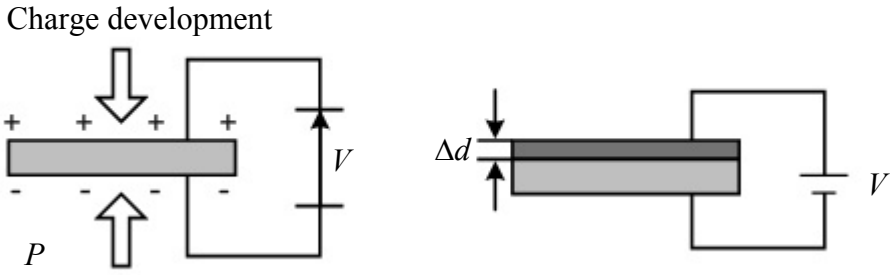


**Figure 2.22** Illustration of piezoelectric effect[37]

The active element of commercially available ultrasound transducers are comprised of quartz, barium titanate, and ceramic composites such as PMNT (lead magnesium niobate titanate) and PZT (lead zirconate titanate).[147, 148] The vibrational frequency of the active element is dependent upon the thickness of the piezoelectric crystal. The wavelength of the vibration is twice the thickness for a thin element.[149]

Two metrics used to characterize the performance of a transducer are the specification for axial and lateral resolution. The term resolution refers to the ability to discern the separation distance between two closely spaced features. Two factors which affect the resolution of an ultrasound transducer are the wavelengths present within the beam and the beam diameter.

Axial resolution denotes the ability of the ultrasound beam to discern features which are located at different depths in the sample, located along the direction of the

beam.[146] The acoustic impedance mismatch between the feature and surrounding material must be large enough to produce a strong enough reflection of the ultrasound beam.[97] The axial resolution of the transducer is dependent on the wavelengths of energy that comprise the ultrasound beam. Since the frequency and wavelength of a wave have an inverse relationship, as the frequency of the beam increases, the wavelength decreases, resulting in an increase in resolution. The minimum detectable separation distance between two features is three times the maximum wavelength of the beam ($3\lambda$).[89]

The main factor which affects the lateral resolution of a transducer is the beam diameter. Lateral resolution refers to the ability of the beam to acoustically separate two features which are located close together on a plane which is orthogonal to the propagation direction of the beam. The shape of the ultrasound beam within a material can be approximated as a cylinder.[122] A decrease in the diameter of the beam results in increased intensity, which causes more intense reflections from within the microstructure.[150] A reduction in the beam diameter may be accomplished by decreasing the size of the aperture in the transducer faceplate.

While various types of ultrasound transducer designs are in use, the main variants may be broken down into three classes. These are planar, focused, and array transducers. The two former types each contain one active element, while the latter type is comprised of a series of elements which may be activated in a controlled manner in order to shape the resultant wavefront.[151]

Planar transducers, the type used for evaluation within this dissertation, do not contain focusing elements, thereby achieving focusing only through refraction and diffraction of the beam.[150] The long focal length and resultant intense reflections

associated with this type of transducer make it suitable for use with thick samples.[150] While planar transducers have reduced axial resolution in comparison to focused transducers, the lower cost and increased obtainability of this type of transducer make it a well-accepted choice for ultrasound evaluation.

Focusing of the acoustic beam is achieved in the second type of ultrasound transducer through the use of focusing lens, or by machining of the active element.[150] The resultant focal length is a function of the radius of curvature of the machined element or lens. Focused transducers can be manufactured to have a very short focal length, leading to increased axial resolution in comparison to unfocused transducers.[151]

One aspect which has precluded the use of focused transducers in this dissertation is the effect of focusing gain.[150] This is manifested by an increase in the signal amplitude within the focal zone, leading to an increase in amplitude of subsequent surface reflections within the oscilloscope A-Scan. Accounting for the contribution of focusing gain on peak amplitude within an A-Scan is not easily accomplished.

Phased array transducers contain multiple active elements.[150] The simplest type contains a lateral array of elements, while other geometries are also utilized.[152] The additional elements allow a wide area of coverage and greatly decreased scanning times. Uses of this type of transducer include inspection of welds, tubes, and bridge structures.[150] Phased array transducers are comprised of thins rods of piezoelectric material embedded in a polymer matrix, divided by metal plating.[152] The elements may be fired all at once to maximize the signal intensity, or fired sequentially to shape the acoustic beam. Use of a phased array transducer requires large amounts of processing

power to interpret the signal received from all of the elements. This has limited the manufacture of phased array transducers above 40MHz.[152]

The pulser-receiver performs two functions within the ultrasound test set. One is to provide the pulse to activate the transducer, while the other is to receive and process the return signal from the transducer. Firing, or activation of the transducer is generally performed by a remote pulser module, which is located in-line between the remote-pulser and the transducer. This configuration helps to keep the length of the cables short in order to reduce the generation of noise within the signal.[153] Adjustable parameters include the duration and amplitude of the initial electric pulse. While the pulser-receiver covers a wide range of frequencies, the remote pulser should be frequency-matched to work with a specific transducer. A short duration, high amplitude electric pulse is emitted by the pulser-receiver, which is then amplified by the remote pulser.[154] This amplified pulse is applied to the transducer, which results in an emission of acoustic energy.

Following propagation through the sample, the acoustic beam interacts with the transducer and is converted back into an electrical signal, which is then processed and amplified by the pulser-receiver.[155] Selectable high and low-pass filers can be used to alter the signal. The intent of the filters is to block induced noise without eliminating the portions of the signal that correspond to surface peak reflections.

The transducer firing pulse may be activated by either external or internal triggering. Internal triggering refers to the transducer being fired based upon a set value, such as a designated interval of time. When operating in external trigger mode, the

pulser-receiver is prompted to fire the transducer by a signal received from an external component.[98]

The analog-to-digital converter (A/D) card converts the analog pulse signal received from the pulser-receiver into a digital signal for interpretation by an oscilloscope or software with an oscilloscope emulator function.[156] The hardware specifications and performance of the A/D card dictates the time resolution, time range, and amplitude resolution of the resultant oscilloscope trace.

The amplitude resolution of an analog-to-digital converter card is a function of the voltage range and the amount of bit registers of the device. The amplitude resolution refers to the minimum detectable separation, in volts, between two amplitude measurements.[122] The resolution limit can be calculated by dividing the voltage range by two raised to the power of the number of bit registers.

The extent of the time range, or abscissa, in each scan is dependent on the amount of on-board memory. Having an extended time range within the scan becomes important for testing low sonic velocity or deep samples due to the greater amount of time for acoustic energy to propagate through the sample and for surface reflections to appear in the oscilloscope trace.

One of the most important specifications of an A/D card as pertains to ultrasound evaluation is the sampling rate. The sampling rate, measured in Hertz (Hz), refers to how many times per second the analog waveform is digitized. This forms the basis for the time resolution of the oscilloscope trace. In order to discern between two different waveforms within the signal, a wave within the oscilloscope trace must be comprised of

at least five data points.[122] In order for this to occur consistently, the sampling rate should be at least five times greater than the maximum frequency of the transducer.

Carrying out ultrasound B- and C-Scans requires a system to allow the translation of the transducer to specific scanning positions across the area of the sample. This is accomplished through the use of the motion controller, motor system, and scanning gantry. The scanning gantry acts as the attachment point for the ultrasound transducer. Movement of the transducer assembly is achieved through the use of the motor system. This may include the use of either stepper or servo motors which are connected to the scanning gantry by a gearing or belt system, or a combination of both. The range of motion of the transducer assembly is a function of the motor drivers. The motion controller is the frame that contains the motor drivers. Typically, each motor driver controls a motor that corresponds to one axis of motion. The motor driver provides the signal to the motor that determine the length of time and the direction that the motor operates.

The motion controller also has additional functions. One of these is to append positional tags within the ultrasound data. This is to provide the location as to where the ultrasound signal was collected. The physical connections within the test system differ as to what type of motor system is utilized. Servo motor systems are designed such that positional data are supplied and encoded through the driver system.[157] A detector is included within the motor module which provides feedback through the motor driver within the motion controller. The use of microstepper motors requires that a physical connection is made between the motor driver and the timer-counter card within the computer.

The timer-counter card provides an electronic link between the pulser-receiver and the motor drive control modules. Usually located as an expansion card within a personal computer, the timer-counter card monitors the number of motion steps of the microstepper motors. After the number of steps that correspond to the lateral scanning position step size, a high voltage pulse is sent to the motion controller in order to fire the transducer.[158] This also provides a positional tag as to where each ultrasound data point was located in reference to the sample.[98] The timer-counter card is only required by test sets that utilize microstepper drivers, as stated previously, newer systems that contain servo motors do not require the additional hardware.

As stated previously, reflections within the components of a test set, including cables, introduce noise within the signal, at all frequencies. The length of the cables used can have an effect on the measurement of the ultrasound signal. Due to loss within the cables, signal strength decreases with increasing cable length. Work performed by Portune et al. on the effect of cable length on ultrasound methods showed that shorter cables were shown to have increased attenuation at lower frequencies, while longer cable were found to have increased attenuation at higher frequencies.[122] Therefore, cable length should be optimized for the frequency range that matches the transducer.[122]

The personal computer acts as the control and communications hub within the ultrasound test set. The computer should fulfill the hardware requirements for the collection of ultrasound C-Scan data. This includes having a sufficiently powerful processor and memory capacity to allow for acquisition, processing, and storage of the vast amount of data contained in the ultrasound scans. The computer also provides the

mounting location for any expansion cards which are part of the test set. These cards allow for communication between components of the test set, and provide the link for the data stream between the test set components and the computer.

### 2.5.10 Ultrasound Scanning Practices

#### 2.5.10.1 Transducer Configurations

Ultrasound scanning relies upon the introduction of acoustic energy into a medium, and then processing the received signal following propagation through the medium.[111] Three primary scanning configurations are utilized. These are: through-transmission, pulse-catch, and pulse-echo. While all three methods make use of ultrasound transducers for the introduction and detection of the ultrasound signal, there are differences that exist in the geometric orientation and the number of transducers that are required. Each of the three methods is applicable to samples of different geometry, and for detecting different types of features. Pulse-echo is the most widely used method, and the one employed for use in this dissertation.[93]

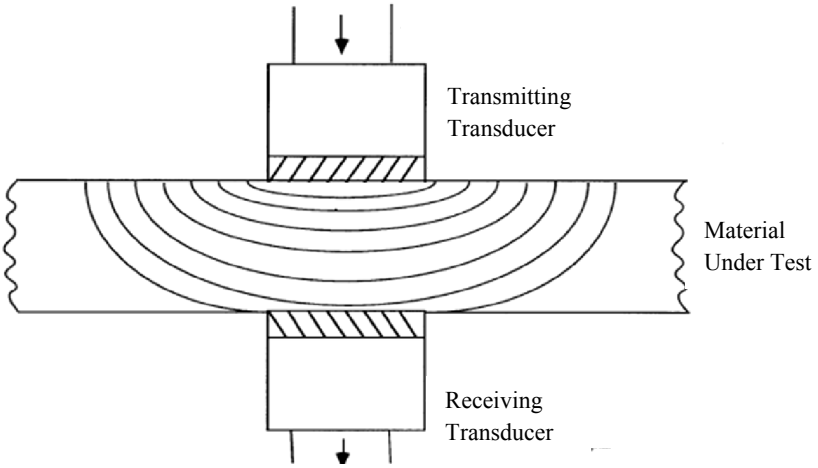


**Figure 2.23** Diagram of through-transmission ultrasound scanning configuration utilizing two ultrasound transducers[159]

In the through-transmission method, two ultrasound transducers are mounted on opposite sides of the sample. One transducer acts as a pulser, or the source of the ultrasound energy, while the other acts as a receiver. A schematic of this arrangement is shown in Figure 2.23. As the ultrasound energy makes only one pass through the sample, the received signal is stronger when compared to the other two methods.[159] This method is highly applicable for the evaluation of multi-layered or multi-component samples that are highly attenuating.[159] It may be employed with the transducer in contact with the sample, or in non-contact mode with air or water as the propagation medium.

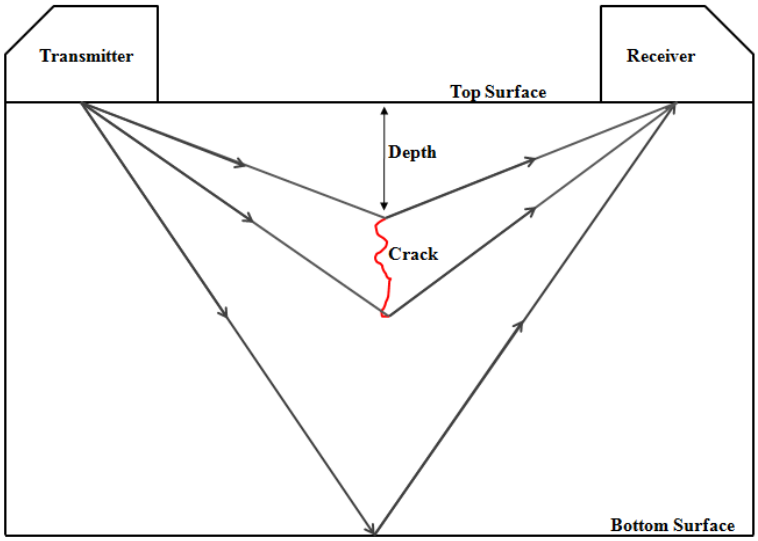


**Figure 2.24** Diagram of pitch-catch ultrasound scanning configuration utilizing two ultrasound transducers[160]

The pitch-catch method of ultrasound scanning arrangement also requires the use of two transducers, which are mounted on the same side of the sample. A schematic of this configuration is shown in Figure 2.24. Acoustic energy is introduced into the sample and is reflected off of any defects, and the opposite surface of the sample, before being received by the 2nd transducer. This method is most useful for examining cylindrical

tubes and objects with nonlinear parallel sided surfaces.[159] It has also been employed where only one side of the sample is accessible, such as for inspecting welds on an aircraft.[111] As the acoustic energy that is detected at the receiving transducer has taken an angled trajectory through the medium, the path length of the beam is longer when compared to the other two methods. Therefore, this scanning method is not applicable for highly attenuating samples.

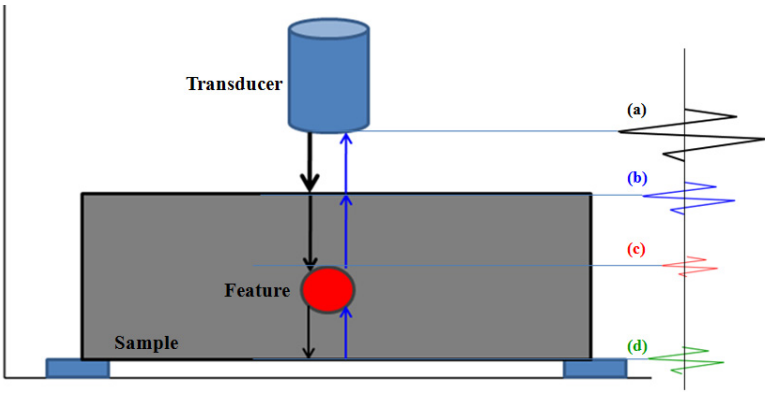


**Figure 2.25** Diagram of pulse-echo ultrasound scanning configuration where a) is the initial ultrasound pulse, b) is the top surface reflection, c) is a reflection from the imbedded feature, and d) is the reflection from the bottom surface/water interface[98]

One of the main advantages of the pulse-echo configuration is that it employs only one transducer which acts as both the source and the receiver of acoustic energy.[111] A representation of this type of system is shown in Figure 2.25. This results in a simpler and less expensive system as only one transducer needs to be purchased. In addition to cost, another advantage to employing only one transducer is the simplification of the test analysis in that the frequency response of the individual transducers does not need to be taken into account.[97] For this reason, this is the preferable method for frequency based measurements.[97] As the ultrasound energy must make two passes through the sample,

this method has limited usefulness for evaluation of highly attenuating materials.[112] Pulse-echo testing may be employed with a high viscosity medium, water, or air as the propagation medium, in either contact or non-contact mode.[93, 159, 161]

**2.5.10.2 Ultrasound Scanning Modes**

There are a number of scanning modes that are employed for ultrasonic evaluation of samples. They differ in the amount of area scanned and in the displayed output. A diagram of three of the scanning modes is shown in Figure 2.26. They are: the A-Scan, B-Scan, and the C-Scan.[162] An A-Scan is a point measurement, B-Scans are a linear compilation of A-Scans, while a C-Scan is an X,Y array of A-Scans.[146]

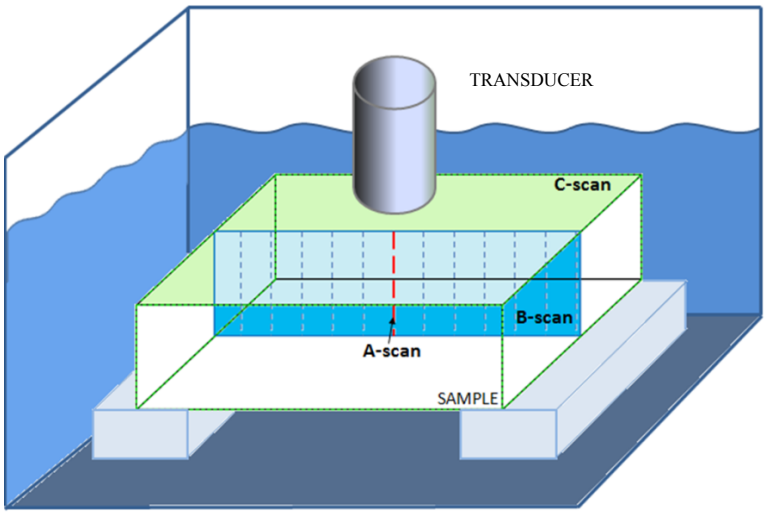


**Figure 2.26** Ultrasound scanning modes. A-Scan (point scan), B-Scan (linear compilation of point scans), C-Scan (X,Y raster of point scans)[122]

A-scans, the most commonly used ultrasound scanning mode, involve the production and reception of one pulse of acoustic energy, or point scan. The received signal is processed and displayed on an oscilloscope. An example of an A-Scan of a sintered silicon carbide sample is shown in Figure 2.27. In the displayed oscilloscope

trace, the ordinate is the signal amplitude, in units in mV, while the abscissa is the scan time, in units of μs. While this is the scanning mode that requires the shortest amount of time and least amount of material investment to perform, information about the sample is only provided on the volume that is interacted with by the ultrasound beam at that position.[163]

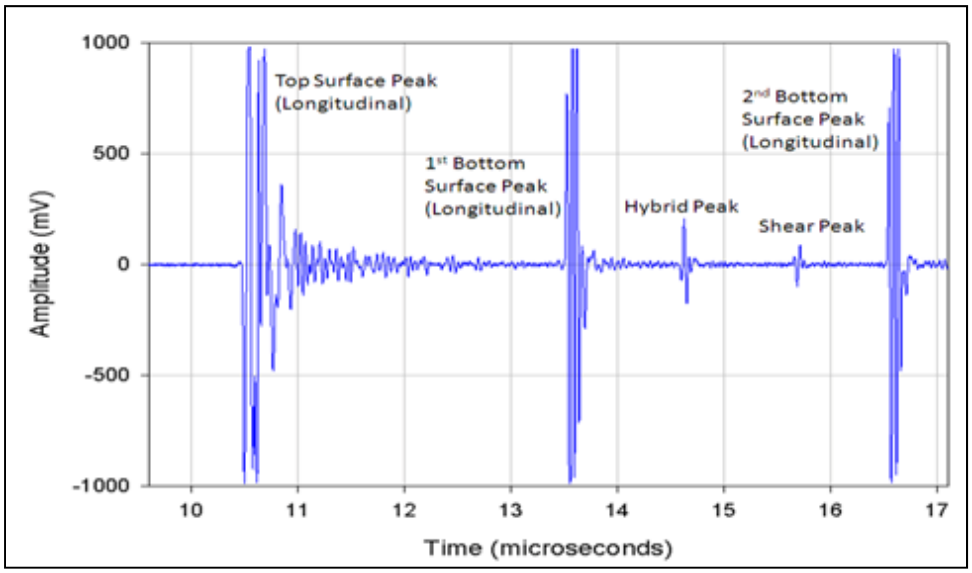


**Figure 2.27** A-Scan of sintered silicon carbide sample showing surface reflection peaks. Ordinate – signal amplitude (mV). Abscissa – scan time (μs)[122]

The A-Scan contains a number of distinct peaks that are characteristic of reflections of acoustic energy from multiple surfaces of the sample. These include the top surface peak, 1st bottom surface peak, the hybrid and shear peaks, and the 2nd bottom surface peak.[122] Determination of the temporal position and amplitude of these peaks forms the basis of ultrasound evaluation.

As stated previously, ultrasound B-Scans are a linear compilation of A-Scans that are generally performed in the X or Y direction in relation to the sample geometry. An example of a B-Scan of a pressure tube is shown in Figure 2.28. In this figure, reflections

from the top and bottom surface of the tube are noted, as well as the reflections from a defect within the wall of the tube. The X-axis indicates the transducer travel direction, the Y-axis is the scan time, while the Z-axis is the signal amplitude.[162] B-Scans necessitate additional investment in equipment as a motion apparatus is required to traverse the transducer over the sample.

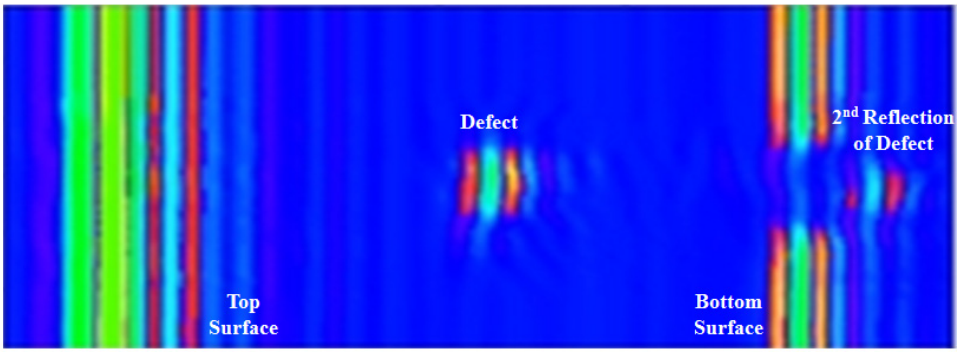


**Figure 2.28** B-Scan of a laminar flaw between top and bottom surface of a pressure tube. X-axis – transducer travel direction. Y-axis – scan time. Z-axis – signal amplitude[164]

Finally, an ultrasound C-Scan is considered to be an X,Y array of point measurements across a large sample area. Multiple A-Scans are performed in a pre-defined raster array of scanning points. This is typically an automated measurement as it requires the synchronization of the motion apparatus and the scanning equipment. Of the three methods discussed, this test mode requires the greatest amount of time and most equipment to complete, but does cover the greatest sample area.[111]

C-Scan testing results can be used to compile graphical maps of materials properties over a large area. An example of this type of map is shown in Figure 2.29. This is a property map of the measured longitudinal speed of sound ($C_L$) of a sintered Hexoloy® silicon carbide tile. The X and Y-axes represent the transducer scanning

directions, while the Z-axis represents the signal amplitude. An important aspect to consider is that these are two-dimensional maps that are depicting a system that exists in three dimensions. These maps can provide information on the location of a feature in the X,Y plane, but they are unable to determine where in the depth this feature may be located.[163] C-Scan property measurements were the primary scanning mode employed during this dissertation.

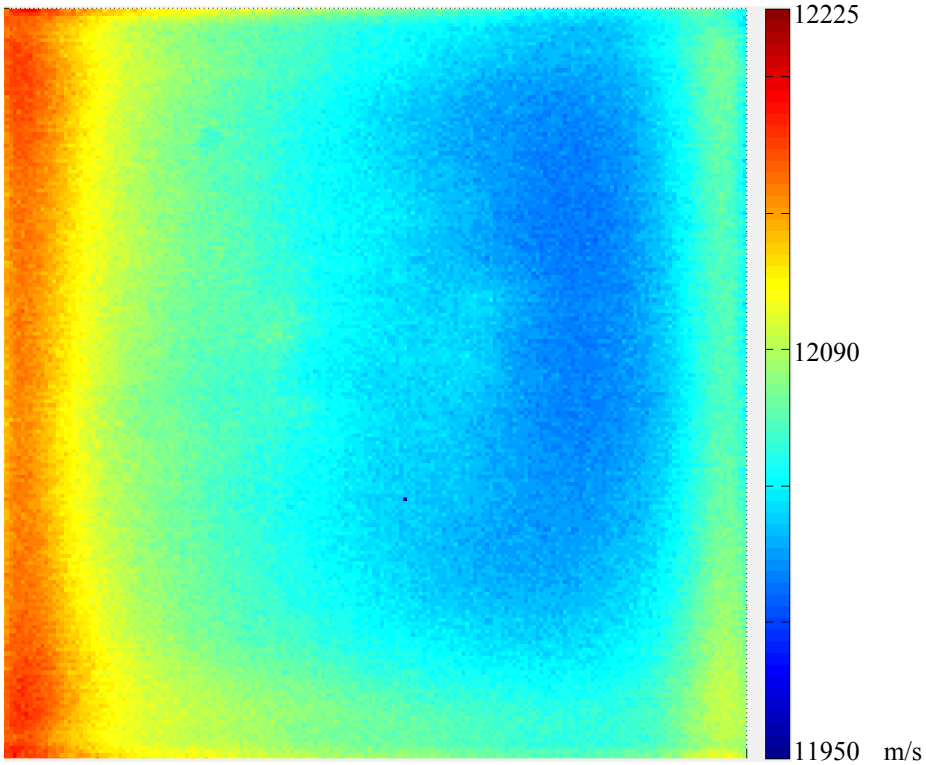


**Figure 2.29** Assembled ultrasound C-Scan map of Hexoloy® silicon carbide tile. Map of longitudinal speed of sound ($C_L$). Scale – 12,225 m/s (maximum), 11,950 m/s (minimum). X and Y-axes – Transducer scanning directions. Z-axis – signal amplitude[165]

#### 2.5.10.3 Peak Measurement

As was shown in Figure 2.27, the oscilloscope output of an A-Scan contains characteristic peaks that are the result of reflection of the ultrasound energy from the top

and bottom surfaces of the sample. By measuring the temporal position and amplitude of these peaks it is possible to determine the longitudinal and shear velocities of the propagation medium, as well as the degree of acoustic attenuation at the frequency range of the ultrasound energy within the material.

**2.5.10.4 Time of Flight Measurements**

One of the measurement modes when conducting ultrasound scanning is the determination of the time of flight (TOF) of the acoustic wave within the material. This is done by measuring the temporal position of peaks within the oscilloscope trace that correspond to reflections from the top and bottom surfaces of the sample.[166] By utilizing the knowledge of the location of these peaks, it is possible to calculate the sonic velocities, elastic properties, and thickness of the sample being evaluated.[167]

TOF is the amount of time between waves of a particular type within the oscilloscope trace. Several methods exist for determining the type of flight of an acoustic wave within a material, all of which depend on defining an electronic gate for measuring the temporal position of the peak. These methods include determining the temporal position of the first peak inflection, the temporal position where the peak enters the gate (threshold method), and the temporal position of the maximum amplitude of the peak. A graphical representation of each measurement method is shown in Figure 2.30. Different values for the temporal position of a peak may be recorded depending on which of the three methods is employed. This is due to differences in the way that the peak position is measured for each method, as well as inherent errors associated with each method. Sources of error include signal noise, amplitude reduction, and peak broadening.[160]

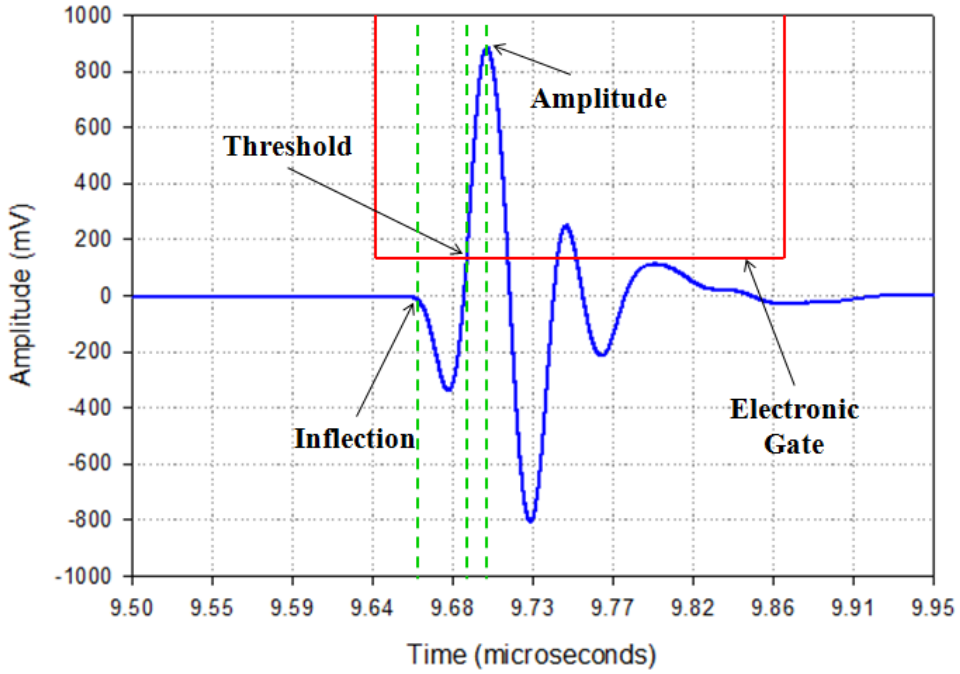


**Figure 2.30** Representative oscilloscope trace detailing three methods for determining the temporal position of a surface reflection peak. These are: the position of the first inflection, the position where the peak crosses the gate, and the position of the maximum peak amplitude[168]

Signal noise due to electronic reflections within the hardware is present as high frequency static within each point of the oscilloscope trace, and is a source of error that affects all three measurement methods. Signal noise is caused by reflections within interconnect cables, which can be exacerbated by the use of longer cables.[168] This type of error is manifested by superposition of the noise with the signal by constructive and destructive interference. This can have the effect of changing the shape or amplitude of the measured peak, altering the measured position of the peak. The effect of this source of error can be mitigated by the use of high and low pass filters within an ultrasound test set.

The determination of the temporal position of a peak by the threshold and amplitude methods can be affected by reduction of the measured amplitude of the peak. This can occur at the location of a large inclusion or reduction in density encountered in the sample. As these scanning positions, a reduction in the amplitude of the peak can occur, altering the position that the peak encounters the electronic gate and resulting in a different time of flight being recorded.

A third source of error in the measurement of the temporal location of a peak is due to peak broadening. This occurs due to the differential attenuation of acoustic waves of different frequencies within the material.[146] Higher frequencies are more greatly attenuated, and as the measured width of the peak is determined by the least attenuating frequency, broadening of the peak occurs with subsequent surface peak reflections.[111]

**2.5.10.5 Calculation of Sonic Velocity**

The amount of time it takes sound to travel a certain distance is dependent on the speed of sound in that medium, as shown in the familiar equation:[91]

$$velocity = \frac{distance}{time} \qquad \text{Eq. 68}$$

The speed of sound in a medium can be calculated by measuring the time of flight of the acoustic wave between two of the characteristic reflection peaks, along with the thickness of the sample.[109] The longitudinal time of flight ($TOF_{LONGITUDINAL}$) may be determined by measuring the time in microseconds (μs) between the temporal location of the top surface reflection and the 1st bottom surface reflection peaks. The longitudinal wave sonic velocity can be calculated according to the following equation:[92]

$$C_L = \frac{2x}{TOF_{LONGITUDINAL}} \quad \text{Eq. 69}$$

Where $x$ is the thickness of the samples. A factor of 2x is applied as the ultrasound energy makes two passes through the sample.[112] Rather than using the top surface reflection peak as a reference, the temporal locations of the 1st and 2nd bottom surface reflection peaks are utilized as they have similar amplitudes, which leads to reduced error in the measurement.[169]

The shear wave time of flight may be determined by measuring the propagation time between the top surface and shear peaks.[170] The shear wave sonic velocity is then calculated using the thickness of the sample and shear wave time of flight according to the equation:[92]

$$C_S = \frac{2x}{TOF_{SHEAR}} \quad \text{Eq. 70}$$

The process of determining the temporal position or amplitude of the shear wave is beset by a number of difficulties when performing ultrasound evaluation by non-contact, immersion-based methods. The first is that the transducers used for evaluation of samples in this dissertation are designed to only emit longitudinal waves. The second is that shear waves are not conducted through low viscosity fluids such as water.[88]

In the ultrasound evaluation performed for this dissertation, shear waves are generated by the process of mode conversion at the interface of the sample surface and the water bath. Mode conversion is the exchange of a portion of the acoustic energy from one type of wave to another. At these interfaces a portion of the acoustic energy within the ultrasound beam will be converted from longitudinal to shear waves. This process may also be reversed with the conversion of shear waves to longitudinal waves. The

proportion of the acoustic wave that is converted is subject to frequency dependent diffraction and refraction that occurs at the boundary, and upon the angle that the incident energy makes with the boundary.

At the introduction of acoustic energy into the sample, a proportion of the longitudinal wave energy is converted to shear waves. Additional mode conversion occurs with the interaction of the propagating acoustic waves with the interface of the bottom surface of the material. The speeds with which the various types of waves travel through the material are shown by the temporal positions of the reflection peaks within the representative A-scan in Figure 2.4.12. The faster longitudinal waves arrive at the upper surface of the sample first, followed by the slower shear waves. That wave energy that is comprised of either longitudinal-shear or shear-longitudinal converted waves arrives at a point in time exactly between the longitudinal and shear wave components. This peak is known as the hybrid peak, as it contains both the longitudinal and shear wave components. As is shown in Figure 2.4.12, the hybrid peak is more intense than the shear peak, and is therefore preferentially used for the calculation of the shear wave sonic velocity. This can be done according to the following equation:

$$C_S = \frac{2x}{2TOF_{HYBRID} - TOF_{LONGITUDINAL}} \qquad \text{Eq. 71}$$

Where $TOF_{HYBRID}$ is the time, in μs, between the positions of 1st bottom surface reflection peak and the hybrid peak.

**2.5.10.6 Determining Elastic Properties**

The calculation of the elastic properties of a material is based upon the relationship between sonic velocity and Poisson's ratio (ν).[100] Poisson's ratio is a

unitless parameter that relates the degree of strain induced in perpendicular planes to an applied axial stress. Poisson's ratio is used in the calculations to account for any anisotropy present in the material.[171] The Poisson's ratio of a material is calculated according to:[100]

$$\nu = \frac{1 - 2(\frac{C_S}{C_L})^2}{2 - 2(\frac{C_S}{C_L})^2} \quad \text{Eq. 72}$$

Following the calculation of Poisson's ratio, the elastic moduli of the material may be determined.[100] The Young's modulus (E) is, and calculated according to the equation:[79, 100]

$$E = \frac{C_L^2 \cdot \rho \cdot (1 - 2\nu) \cdot (1 + \nu)}{(1 - \nu)} \quad \text{Eq. 73}$$

Where ρ is the density of the material. The shear modulus (G) is the ratio of applied shear stress to the induced shear strain, and may be calculated using the following equation:[79, 100]

$$G = \frac{E}{2 \cdot (1 + \nu)} \quad \text{Eq. 74}$$

The bulk modulus (K) is the measurement of a material's resistance to compression, and is calculated according to the equation:[79, 100]

$$K = \frac{E}{3 \cdot (1 - 2\nu)} \quad \text{Eq. 75}$$

The Young's, shear, and bulk moduli are measured in units of Pascals (Pa).

### 2.5.10.7 Thickness Measurements

Calculations for the longitudinal and shear wave velocities require the thickness of the sample to be measured. One method for measuring the thickness of the sample is to take an average of manual measurements made with a caliper or micrometer. This method assumes that the thickness across the surface of the sample does not vary a great deal from the average. A second method uses a time of flight C-Scan measurement to back calculate the thickness of the sample. This method makes an assumption that the sonic velocity of the sample is constant. The assumptions involved in both of these methods can lead to error within the measurements of the elastic properties of the sample. For the measurements made in this dissertation, a method developed by Bottiglieri et al. was utilized to measure the thickness of the samples. This method measures the thickness at each scanning position, and is believed to introduce less error into the measurement.

This method uses differences in the time of flights between the face of the ultrasound transducer and sample surface reflections to calculate the thickness of the sample. A schematic of the time of flights used to calculate the thickness is shown in Figure 2.31. These include: the time of flight between the face of the ultrasound transducer and the top surface of the sample ($t_2$), between the face of the transducer and bottom surface of the water bath ($t_1$), and between the bottom surfaces of the sample and the water bath ($t_3$). The sum of the times of flight between the transducer and the top surface of the sample and the bottom surface of the sample and the bottom of tank are subtracted from the time of flight between the transducer and the bottom of the tank,

based upon the temporal position of each in the oscilloscope A-Scan.[113] The difference in these values is the time of flight through the sample ($t_4$). It should be noted that this would be the time of flight if the sample where made of water. By assuming that the speed of sound in water is constant at room temperature, and that pure water is used as the propagation medium, the thickness of the sample can be calculated by multiplying the time of flight by the sonic velocity of water at room temperature.[113] A factor of two should be applied to the product of time and velocity as the ultrasound energy makes two passes through the material when using the pulse-echo method.

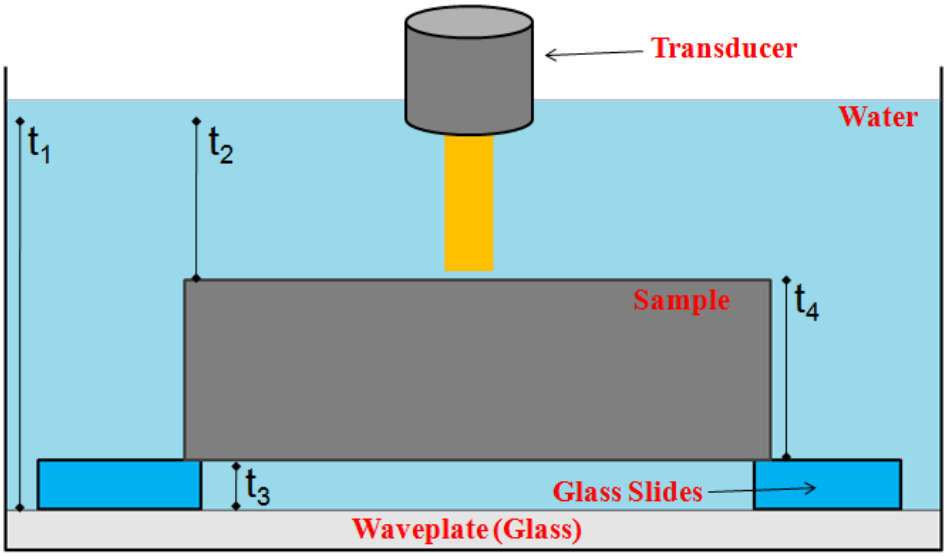


**Figure 2.31** Graphical representation of time of flight thickness map measurement. Time of flights: $t_1$ – transducer and bottom surface of tank; $t_2$ – transducer and top surface of sample; $t_3$ – bottom surface of sample and bottom surface of tank; $t_4$ – through sample[113]

### 2.5.10.8 Amplitude Measurements

Amplitude based measurements represent a second type of ultrasound testing methods. Where time of flight measurements make use of the temporal position of a

surface reflection peaks, amplitude measurements take into account the maximum amplitude of these peaks. As longitudinal wave peaks tend to be more intense than peaks corresponding to shear waves within the oscilloscope trace, this type of waves form the basis for amplitude based measurements. Amplitude C-Scan maps of bottom surface reflection are used to examine the spatial homogeneity of a sample. Regions of reduced amplitude in the map may correspond to the presence of a large pore, inclusion, or a large grain within the microstructure.[98]

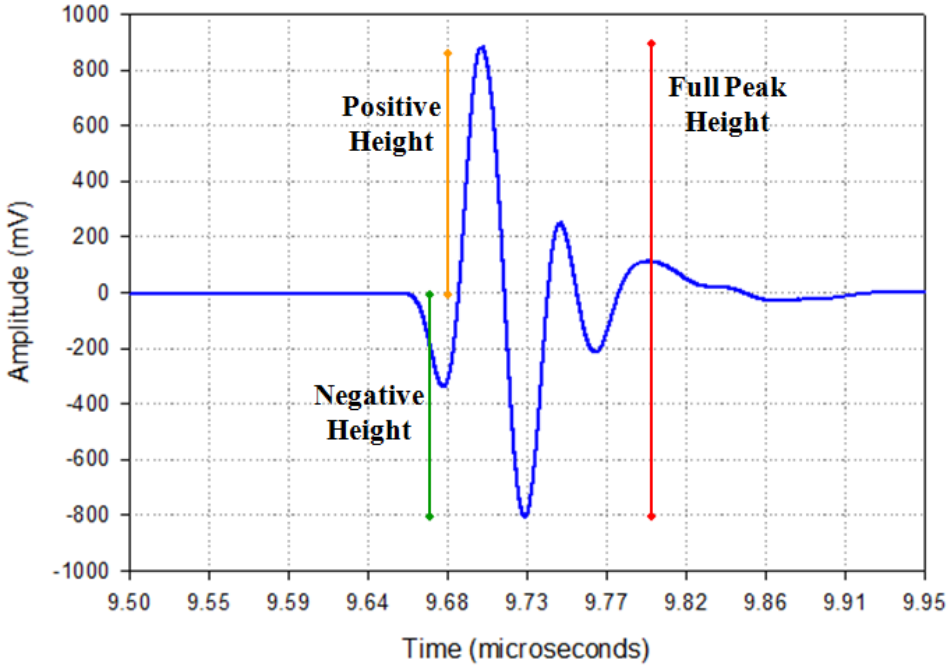


**Figure 2.32** Representation of an oscilloscope trace showing sample peak. Indicated in the graph are the three different portions of a surface reflection peak that may be utilized for peak amplitude measurements. These are: full peak height, positive height, and negative height[168]

Four modes exist for the measurement of peak amplitude, or height. As with times of flight measurements, each measurement method may return a slightly different value for the peak amplitude. The determination of peak amplitude relies upon the

process of rectification, where a portion of the wave form is selected for measurement. The four measurement modes are shown in Figure 2.32. They include: selection of the full peak height, using the absolute value of the full peak height, and using only either the positive or negative heights.[172] While the latter three methods have been used to identify the presence of large defects within a sample, through a large change in peak intensity, measurement of the full height of the peak used utilized in this dissertation as it was believed that the additional information contained in the full peak was more indicative of inhomogeneities contained within the microstructure.

**2.5.10.9 Amplitude Coefficient Measurements**

Absolute measurement of the energy associated with each peak is not possible as signal amplification and gain correction are present within many of the components within the ultrasound test set. Measurements of loss are more accurately taken by measuring the amplitude of successive surface reflection peaks as these factors affect the shape of both peaks.[118] The measurement of acoustic attenuation coefficient encompasses the contribution of individual loss mechanisms by determining the loss due to all sources within the material.

Acoustic attenuation may be determined by using a rearrangement of the familiar Beer-Lambert Law, and taking into account the relationship between the amplitude and intensity of an acoustic wave. The Beer-Lambert Law is given as follows:[91]

$$I = I_o e^{-\alpha x} \qquad \text{Eq. 76}$$

Where $I_0$ is the initial intensity, I is the intensity after propagating through a medium, $\alpha$ is the attenuation coefficient, and $x$ is the thickness of the medium. In this form, the

attenuation coefficient has units of Nepers per meter (Np/m).[173] The intensity of an acoustic wave is proportional to the amplitude of the wave, as shown by the equation:[91]

$$I = \frac{1}{2}\rho c(\omega y_o)^2 \qquad \text{Eq. 77}$$

Where I, the intensity, is measured in $W/m^2$, ρ is the density, ω is the angular frequency, and c is the speed of sound. As the amplitude of the wave decreases, the energy contained within the wave also decreases.

Taking this into account, and using the conversion factor that 1dB = 0.115Np, a more familiar unit, the decibel (dB), may be used to describe the attenuation coefficient. The rearranged equation has the form:[97]

$$\alpha = -\frac{8.686}{2x} ln(\frac{A^2}{A_o^2}) \qquad \text{Eq. 78}$$

Where $A_0$ is the initial amplitude of the acoustic wave, A is the amplitude after propagating through the sample, *x* is the sample thickness, and the factor 8.686 is used to convert from Nepers to decibels.[122] It should be noted that this is considered to be the overall signal attenuation coefficient that is not specific to any one frequency of the energy within the ultrasound beam.[174]

## 3. Method of Attack

The densification of silicon carbide is reliant upon the use of high temperatures and sintering-activators due to the strong bonding between silicon and carbon and the low self-diffusion coefficients of these elements. These factors contribute to the inherent microstructural variability within these materials. The fundamental goal of this dissertation was to examine the variability present in silicon carbide ceramic samples and to characterize its effect on the mechanical and acoustic properties of these materials. This occurred through a combination of non destructive evaluation and stratification, mechanical testing, and microstructural analysis.

### 3.1 Objective 1: Establish Parameters for Comparison

As a means of comparing the mechanical and acoustic properties of the samples examined in this dissertation, a testing regime was defined to determine the variability within each sample set.

#### 3.1.1 Archimedes Density

Archimedes density by immersion was performed to determine the range of density values in the sample sets. Density is an important figure of merit for silicon carbide producers.[175] A lower than expected density in a sintered piece is a good indicator of the presence of residual porosity, which can affect the performance of the sample.

### 3.1.2 Ultrasound Evaluation

Non destructive evaluation was carried out by ultrasound C-Scan to determine the acoustic properties for each sample and each sample type. An Olympus 20 MHz planar unfocused transducer will be utilized in pulser/receiver configuration. Scanning parameters included a 0.1 mm lateral step size, resulting in NDE maps which contained over 1 million data points. At each scanning position, the values of the longitudinal wave and shear wave times of flight ($TOF_{Longitudinal}$ and $TOF_{Shear}$), and the thickness of the sample ($x$) were calculated. From these parameters, the longitudinal wave ($c_L$) and shear wave ($c_S$) velocities, Poisson's ratio ($\nu$) and the elastic modulus (E) were calculated, along with the acoustic attenuation coefficient ($\alpha$). Following the scanning operation, the raw data were assembled into graphical maps. Ultrasound information was evaluated both quantitatively, by examining statistical information in the raw data, and qualitatively, by looking at trends within the maps.

### 3.1.3 Mechanical Testing of Samples

Mechanical testing consisted of 4-pt flexure testing. Selected samples were machined into ASTM C1161 B-type flexure bars.[176] The machining of flexure bars was conducted offsite by a qualified machinist to limit the effect of improper surface finish on strength test results. One of the key aspects of the machining process was to keep track of the position, identity, and orientation of each bar in relation to the original tile. This was to allow for the correlation of the mechanical properties of the flexure bars to the acoustic properties of the starting tiles.

The quasi-static flexure strength was determined for each bar. Bars were broken in accordance with the specifications set forth in ASTM Standard C1161.[176] Bars were broken using a semi-articulating, four-point testing fixture, and a crosshead speed of 0.5 mm/min. Before testing, the height and width of each bar was measured, and all bars were visually inspected.

The flexure testing of each set of bend bars determined the degree of variability in mechanical properties that existed between each group of samples. As the strength of a properly machined flexure bar will depend on intrinsic factors such as its processing history, the strength testing results gave insight to the degree of microstructural variability that exists amongst the flexure samples from each starting tile.[68]

### 3.1.4 Determination of Critical and Microstructural Features

An important component of the strength testing and Weibull analysis was the use of optical and electron microscopy techniques to examine the fracture surfaces of bars of interest. It was necessary to determine the primary fracture position of each flexure bar sample. This was considered to be the fracture position that contained the fracture initiating, or critical, feature. In this exercise, each piece of a broken bar must be examined. In addition, electron microscopy techniques were employed to examine features of the microstructure, including inclusion sizes and fracture behavior.

## 3.2 Objective 2: Determination of Correlation

Following the strength testing, the distribution of strength values was examined at different scales throughout the sample set. Strength statistics were calculated for each

group of bars. These included minimum, maximum, and average strength, as well as Weibull statistics.

The distribution of strength within the original tiles was related to both the qualitative and quantitative features within the NDE ultrasound C-Scan maps. This included the determination of whether a flexure sample fractured at the location of an anomalous feature in the NDE maps. The fracture strength of each bar was also compared to values within the NDE maps at the fracture location.

### 3.3 Objective 3: Defining Sample Sets for Experimentation

In order to achieve the goals set forth above, a number of sample sets for experimentation were defined. The initial stage of this study focused on commercially available sintered silicon carbide tiles. After analysis of these tiles, additional tiles were produced for evaluation which emphasized a particular aspect of the microstructure.

#### 3.3.1 Commercial Silicon Carbide Samples

Initially, this study focused on commercially available silicon carbide samples. Hexoloy® silicon carbide tiles were obtained from U.S. Army Research Laboratory representatives. Hexoloy® silicon carbide, a pressureless sintered material, is manufactured by Saint-Gobain S.A. Ceramics Division.[17] The tiles used in this study were considered to be armor grade materials. In this exercise, a large group of commercial tiles was stratified based upon non destructive evaluation by ultrasound and Archimedes density. Group breakdowns were chosen such that all the tiles in each group

will have similar acoustic properties. One tile from each group was then selected for analysis.

### 3.1.2. Targeted Silicon Carbide Samples

Following the analysis of the commercial samples, routes of experimentation were identified for producing specialized silicon carbide samples. These samples were designed such that a specific aspect of the microstructure was emphasized for each group. Two approaches were identified for production of these 'targeted samples.'

The first approach involved the manufacturing of silicon carbide tiles with increased levels of residual porosity, and therefore reduced density. These tiles were pressed to a lower green density as compared to the commercial samples, and then pressurelessly sintered. The second approach relied upon manufacturing tiles that contained an excess of boron sintering additives. These tiles were pressed to a routine green density for commercial silicon carbide tiles and then pressurelessly sintered. The intention with this method was to produce tiles with enhanced clustering of porous boron carbide inclusions.

## 4. Experimental Procedures

The goal of this dissertation was to determine the extent of the variability that exists within sintered silicon carbide samples. This was accomplished through a combination of non destructive evaluation, mechanical testing, and an investigation of microstructural features. Sample sets that were examined include commercially available silicon carbide, as well as targeted samples that were prepared to emphasis specific aspects of the microstructure for investigation.

A number of methods were utilized to accomplish this goal. The process for carrying out these methods will be explained in the following section. This includes the evaluation of the sample sets using Archimedes density and ultrasound C-scans. The machining of flexure bars will be examined, as well as the steps involved in 4-pt bend testing. The methods used to examine the distribution of strength within the sample sets will be discussed, as well as the quantitative and qualitative comparison between the strength distribution and the ultrasound testing results. FESEM images of polished sections will also be examined. The procedure for preparing these images using image processing software will be discussed.

In this study, the evaluation process was first carried out on a sampling of commercially available tiles. The tiles were stratified based upon the results of the initial evaluation. Selected tiles were then chosen for mechanical testing and microstructural evaluation. Based upon these results, areas of concentration were selected for producing and evaluating targeted samples. This resulted in a slightly different evaluation process for the various sample sets. What will be presented in this section are the methods that were employed for evaluating the initial group of commercial samples. Differences in

evaluation methods that were employed for the two groups of targeted samples will be noted in the Results and Discussion section.

### 4.1 Archimedes Density

Archimedes density measurements were performed on all tiles used in this dissertation. The tiles were first cleaned with isopropyl alcohol to remove any dirt, oil, or fingerprints, as the presence of any residue on a tile can affect the measured weight. Samples were weighed using an ADAM PGW 753e analytical balance, with a 750g capacity and an accuracy of 0.001g. Five dry weight measurements of each tile were recorded, with the balance being zeroed between each measurement. The tiles were then suspended within a wire cradle from the balance into a water bath, as shown in Figure 4.1. Five weight measurements were recorded with the tile suspended in the water bath. The density was then calculated by the equation:

$$\rho = \frac{dry\ weight}{dry\ weight - suspended\ weight} \qquad \text{Eq. 79}$$

Where ρ was the density, with units of g/cm$^3$, and *dry weight* and *suspended weight* were the averages, in g, of the dry and suspended weight measurements. The difference between the dry weight and the suspended weight was the volume of the test sample, with units cm$^3$. This is what is considered to be the Archimedes principles. The volume of an object is equal to the volume of water that it displaces. The mass of 1 milliliter (mL) of water is approximately equal to 1 gm at room temperature.[177] Therefore, the volume of an object may be determined by the change in weight between it being submerged and not submerged.

When dealing with porous or un-densified samples, it is often necessary to boil the samples in water for at least ½ hour. This allows the water to infiltrate any open porosity within the sample. The samples are then removed from the boiling water and weighed on the balance. When measured in this manner, the density is calculated as

$$\rho = \frac{dry\ weight}{wet\ weight - suspended\ weight} \qquad \text{Eq. 80}$$

Where ρ is the density, with units g/cm$^3$, *dry weight, wet weight,* and *suspended weight* are the averages, in g, of the dry, boiled, and suspended weight measurements. The difference between the wet weight and the suspended weight is the volume of the test sample, with units cm$^3$. Boiling of the test pieces was not necessary for the samples used in this study as they were fully-densified plates.

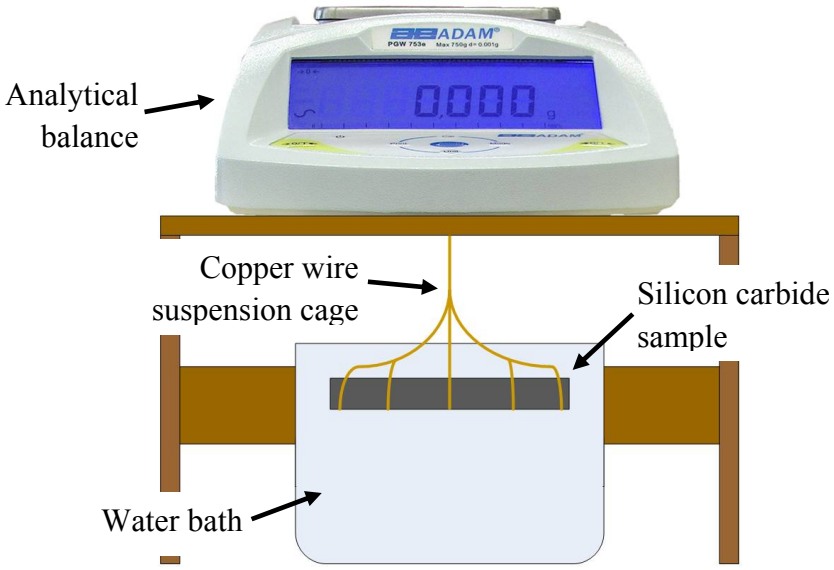


**Figure 4.1** Schematic of Archimedes density setup. ADAM 750g capacity analytical balance with 0.001g accuracy. Samples were suspended in a copper wire cage into the water bath

A number of procedures was used to increase both the accuracy and precision of these measurements. The water used for the suspended measurements had previously been boiled, as it then contained less dissolved gas. A few drops of Kodak Photo-Flo® wetting agent were added to reduce the surface tension of the water, to minimize the likelihood of the adherence of bubbles to the underside of the tile. Bubbles which had adhered to the suspension cage were also wiped away. A thin-gauge copper wire was used to construct the suspension cage to minimize the mass of the cage that was suspended along with the sample in the water.

## 4.2 Ultrasound Evaluation

In this dissertation, ultrasound scanning was utilized as an evaluation technique to determine the acoustic properties of the ceramic tiles that comprised the various sample sets. Ultrasound C-Scans were used to create two-dimensional maps of the acoustic properties of these tiles. This section will include a discussion of the components used in the ultrasound test set, as well as the scanning methods and procedures.

### 4.2.1. Ultrasound Test Set Components

The function of the components of an ultrasound test set was detailed in Section 2.5.6. In this section, the components comprising the ultrasound test set used for the evaluation of samples will be discussed. These components were broken down into three subsystems. These were the signal acquisition system, the transducer translation system, and the control system. The signal acquisition system was comprised of the pulser-receiver, remote pulser, and the ultrasound transducer. The transducer translation

system included the motion control unit, the stepper motors, and the gantry unit. The computer, expansion cards, and the software that was written to perform the testing comprised the control system.

The transducer that was utilized for evaluating samples in this dissertation was a commercially available Olympus transducer. This was a planar wave, immersion type transducer with an aperture of 3.1mm. This transducer had a central emission frequency of 20 MHz. The usable bandwidth of the transducer, which was considered to be the frequency range where the output was one quarter the strength at the central emission frequency, varied depending on the level of acoustic attenuation within the sample. For the materials studied, the bandwidth was approximately 16 to 32 MHz. The power spectral density of this transducer as reflected from the top surface of a highly polished silicon carbide mirror is shown in Figure 4.2.

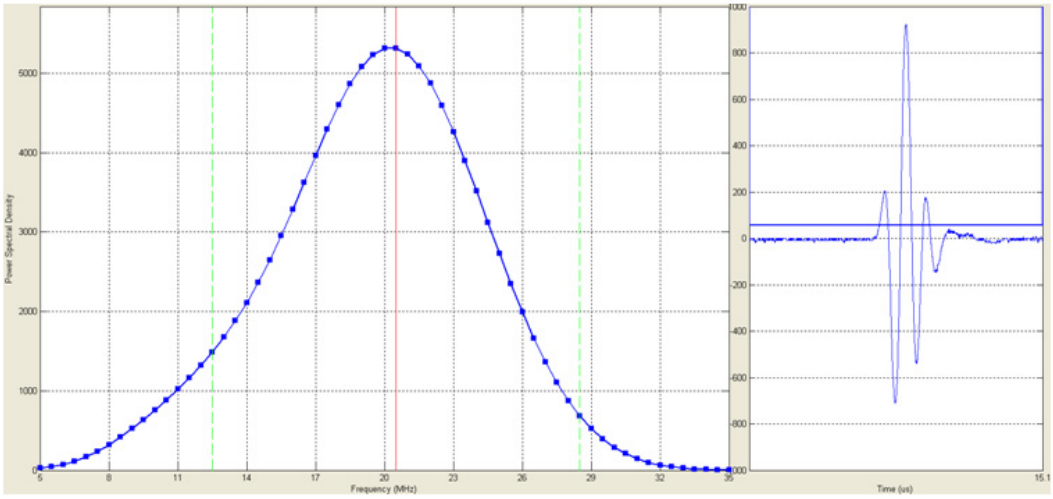


**Figure 4.2** Power spectral density of Olympus 20MHz transducer as measured from top surface of polished silicon carbide mirror[168]

The pulser-receiver was manufactured by JSR, a division of Imaginant, model # DPR500. The bandwidth could be tailored to match the transducer through the choice of

high and low-pass filters. For this application, a bandwidth of 145 MHz was selected through the use of a 5 MHz high-pass and a 150 MHz low-pass filter.

The remote pulser was also manufactured by JSR. Like the selectable filters in the pulser-receiver, this remote pulser was chosen to be used as it had a bandwidth that matched with the transducer. The remote pulser used was designated RP-L2, with a bandwidth of 1 – 65 MHz. In an effort to minimize noise, the damping applied to the signal was kept at a maximum setting of 300Ω, and short cables with noise reflection inhibiting connectors were used to connect the remote pulser to the transducer.

The transducer translation subsystem was comprised of the motion control unit, the stepper motors, and the scan gantry table, all manufactured by Techno-Isel. The stepper motors were controlled by microstepper drivers within the motion controller, a series C-10 model. This combination allowed for discrete lateral step sizes of 0.0125mm. Two stepper motors were mounted to a Gantry II Cartesian Robot X-Y scanning frame. With a table size of 850mm by 750mm, the system provided a usable X-Y scanning area of 500mm x 540mm. The motion control unit/stepper motors provided X and Y axis positioning control of the transducer, while Z-axis, pitch, and yaw control were provided by a manual rotational goniometer. The transducer was attached to this goniometer.

The role of the computer in this system was to handle control of and communications between the components of the test set, and to handle data acquisition, processing, and storage. Components were selected for the custom-built system such that it was capable of the sufficient processing power required to handle the large amounts of data present within each acoustic property map. These included an Intel 2.83 GHz quad

core processor, 8GB PC6400 800 MHz DDR2 RAM, 750GB 7200rpm hard drive, an EVGA GeForce 9400 GT 512MB PCIe graphics card, and a 700W ATX power supply.

Data collection and processing were handled through custom-coded software modules, designated Legacy and Hermes. These modules were built in the MATLAB programming language by students at Rutgers University. Legacy was used for data acquisition, component control, test parameter input, and data formatting. The main function of Hermes was data processing and manipulation. Functions available in Legacy included the viewing of oscilloscope traces and attenuation coefficient spectra, and the ability to define electronic gates for data collection. Hermes had the capability to display A-Scan and C-Scan data from the assembled acoustic property maps, and it allowed for the selection of portions of the available data set for statistical analysis.

A flowchart of the signal interaction between the components of the ultrasound scanning system is shown in Figure 4.3. It diagrams the connection between the different test set subsystems. In order to provide a positional tag to the ultrasound data, a connection was made between the X-axis driver within the motion controller and the timer-counter card, which occupied a PCI slot within the computer. This card was a PCI-CTR05 5-channel board manufactured by Measurement Computing. The timer-counter card received a 5V signal from the motion controller with each step of the stepper motors. After a pre-defined amount of steps, which corresponded to the lateral step size, a signal was sent through the A/D card to the pulser-receiver to fire the transducer.

The A/D card, which handled communication between the computer and the pulser-receiver, was a GaGe Cobramax high-speed digitizer. This card was also mounted to a PCI slot on the motherboard within the computer. It featured dual channels, 384 MB

of on-board memory, a 1.5 GHz bandwidth, 8 bit vertical resolution, and provided for a 3000 Giga-Samples Per Second (GS/s) sampling rate. Measurement capabilities of the card included a 64 μs time range, with a temporal resolution of 0.3ns, and a ±1000mV amplitude range, with an amplitude resolution of 7.1825mV.

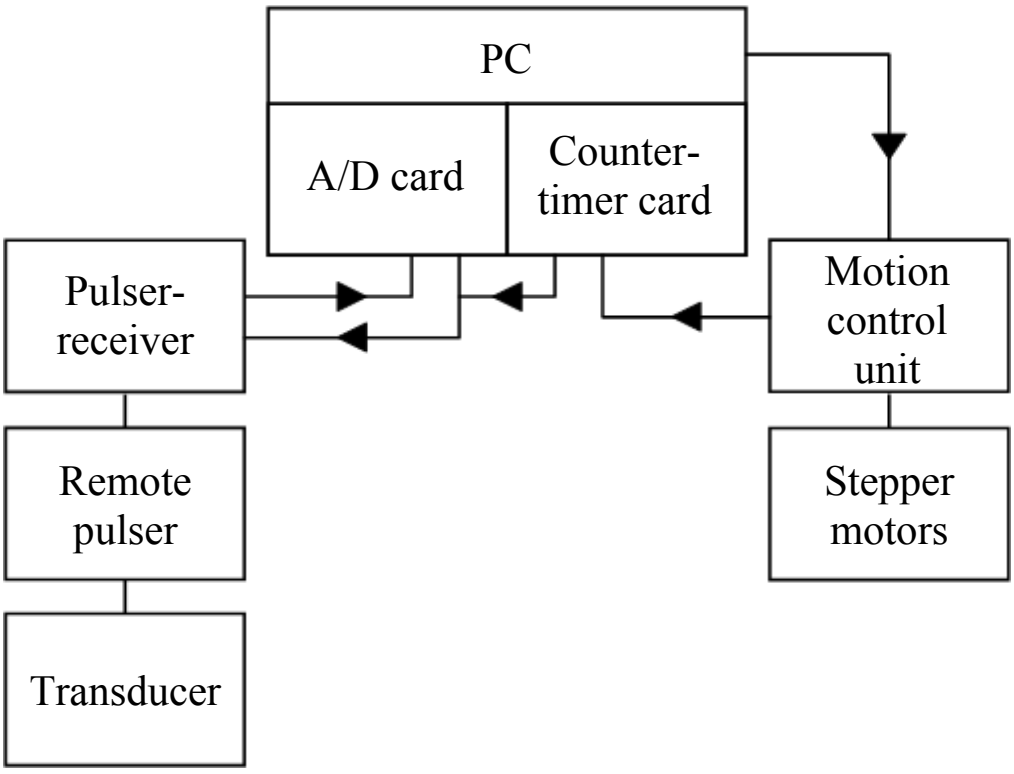


**Figure 4.3** Diagram showing signal interaction within ultrasound test set. Components include custom-built PC, A/D card, counter-timer card, motion control unit, stepper motors, pulser-receiver, remote pulser, and transducer

### 4.2.2 Ultrasound Testing Procedure

The procedure for ultrasonically evaluating ceramic tiles was kept consistent for the different groups within this dissertation. After being cleaned with isopropyl alcohol, samples were placed on top of glass microscope slides within the immersion bath to elevate them from the bottom of the tank. This was to provide the necessary acoustic

impedance mismatch to produce reflection of the ultrasound energy at the sample bottom surface/water interface. The immersion bath was filled with water to a height of at least one inch above the upper surface of the tile to allow for coupling of the ultrasound energy into the sample.

The transducer was then screwed into a connector attached to the rotational goniometer. Using manual control of the translational stage within the Legacy software, the transducer was positioned over the center of the sample. The height of the bottom surface of the transducer above the sample was adjusted such that the temporal position of the top surface reflection peak within the oscilloscope A-Scan was positioned at 10μs.

After installing and vertically positioning the transducer, the X,Y extents for transducer translation were set through the Legacy software. Minimizing the area scanned had the effect of reducing the total scanning time for each, which was important as many samples were evaluated.

Several setup operations were carried out using the oscilloscope A-Scan as a reference. The first, as has been discussed, was to set the height of the transducer from the top of the sample. The second operation was performed to maximize the amplitude of the oscilloscope signal by adjusting the yaw and pitch of the transducer by adjusting the rotational goniometer. This was done so that the aperture of the transducer was parallel to the top surface of the sample.

The third operation was to determine the level of amplifier gain that was applied to the electric signal. The gain setting was adjusted within the software so that the height of the first bottom surface reflection peak was approximately 800 mV in the oscilloscope A-Scan.

Additional parameters included setting the distance in millimeters (mm) between lateral scanning positions. A closer separation distance resulted in increased scanning positions in the ultrasound evaluation, and a longer scanning time.

The final step was to define electronic measurement gates for measurement of peak amplitude or temporal position. The peak chosen for measurement was dependent upon the acoustic property that was being measured. As explained previously, these values were used to calculate the value of the measured acoustic property at each scanning position.

### 4.3 Flexure Bar Machining

Selected tiles from within the sample sets were chosen for machining into flexure bars. The machining was performed offsite by a qualified machinist to limit the effects of improper machining on the strength results. Procedures for machining bend bars were found in ASTM Standard C1161.[80] These procedures included specifications for dimensionality, the grit size of the grinding media, maximum material removal rates, and machining direction.

All grinding was to be done in the presence of adequate lubricant such that removed material was carried away from the grinding wheel to limit contamination and scratching of the sample. Bars were ground longitudinally, parallel to the long axis of the bend bar, such that large scratches were parallel to the axis of the applied stress. Bars were ground in from each edge such that an equal amount of material was removed from the top and bottom and the left and right surfaces of the sample.

The grit size of the grinding wheels was decreased from coarse grit, to intermediate sizes, and down to fine grit sizes. Maximum material removal rates per pass were set for each grit size wheel. The maximum grit size for coarse grinding wheels was 150 grit, followed by 240-320 grit for intermediate wheels, and 400-600 grit for fine grinding wheels.[80] Following the final surface grinding steps, the four edges of each bar were to be chamfered, or beveled, to an angle of 45°. This was done as the 90° edge between two sides of a flexure bar can be a stress concentration point, leading to a reduced measured strength.

While the bar machining process was consistent for all of the samples examined in this study, the regions from within each tile chosen for bend bar machining varied between the different sample sets. Bend bar selection regions for the additional sample sets will be detailed in Sections 5.2.2.4 and 5.2.3.4. The machining regime for the commercial samples will be detailed below, as they represented the initial focus of the study, and the most numerous samples chosen for machining.

As an example, the machining diagram for the commercial silicon carbide tiles is shown in Figure 4.4. The different colored lines in the diagram represent the order of the cuts. The tiles were first cut in half, as indicated by the red line. The horizontal bend bar positions were then cut from the two halves, as shown by the white lines. Each horizontal position section was cut into three, leading to the three layers of bars, as signified by the yellow lines.

One-hundred and two bars were machined from Tile 11, which contained 17 rows of bars, while one-hundred and eight bars were machined from the remaining five tiles, each which contained 18 rows of bars. The identification, position, and orientation of the

bars were maintained throughout the machining process. A black dot was placed on the top left edge of all bars as an indication of direction and orientation. Bars were also labeled with the number of the starting tile and the bar number. B-type bend bars were chosen as the width of the original tiles were just over twice the length of a B-type bar.[80]

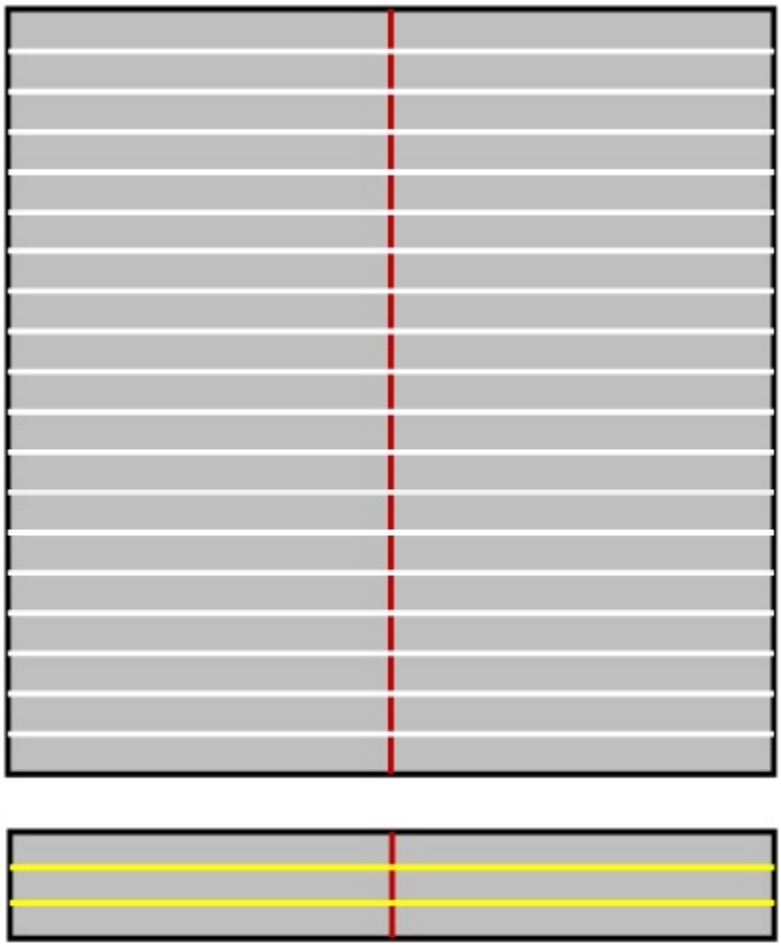

**Figure 4.4** Machining diagram of commercial silicon carbide tiles, showing longitudinal and latitudinal cuts. Order of cuts: red line, white lines, yellow lines, respectively

**4.4 Flexure Testing**

Upon being received from the machinist, all bend bars were visually inspected to locate any detrimental machining artifacts which would extrinsically affect the strength of the bar. The height and width of each bend bar were measured with a micrometer, to the nearest thousandth of a millimeter. This would allow for the calculation of the maximum fracture stress, in megapascals (MPa) from the applied fracture load, in Newtons (N). These measurements were made in the center of the bar, as this was directly in the middle of the region of the bend bar which received the maximum applied load. All bars were labeled with the original tile number and bar number. The positions of the loading pins were also marked on the bars, as shown in Figure 4.5. This aided in the fractographic reconstruction of the bars. Finally, a piece of masking tape was applied to the top surface of the bar to keep the bar intact in the case of multiple fracture locations. As the tape was applied to the compressive surface of the bar, it should not have altered the strength of the bar.


**Figure 4.5** Bend bar labeling diagram. Positions of loading pin contact zones and bar orientation marks where marked on the top and bottom surfaces of each bend bar

The bars were broken in a semi-articulating 4-point test fixture, as shown in Figure 4.6. This was considered to be a semi-articulating fixture in that the upper loading pins are free to pivot and roll inward, and the lower loading pins are free to roll outward. The load was transferred from the test fixture to the sample through the upper and lower

contact bearings. Contact was made between the top of the test fixture and the load cell through the steel ball bearing which was recessed into the top of the fixture. The contact bearings and ball bearing were replaced after every four samples so that any deformation of the bearings did not affect the test results.

Bars were broken in accordance with the procedures set forth in ASTM Standard C1161.[80] The procedures and values set forth in this standard dictated the dimensions of the samples, the diameter of the contact bearings, the loading span, and the traverse speed of the crosshead. Samples were 4mm wide, 3 mm high, and at least 45 mm long. The upper loading span of the test fixture measured 20 mm, while the bottom loading span measured 40mm. The ASTM standard recommended a contact bearing size of 4.5 mm, and calls for a crosshead speed of 0.5 mm/min.[80]

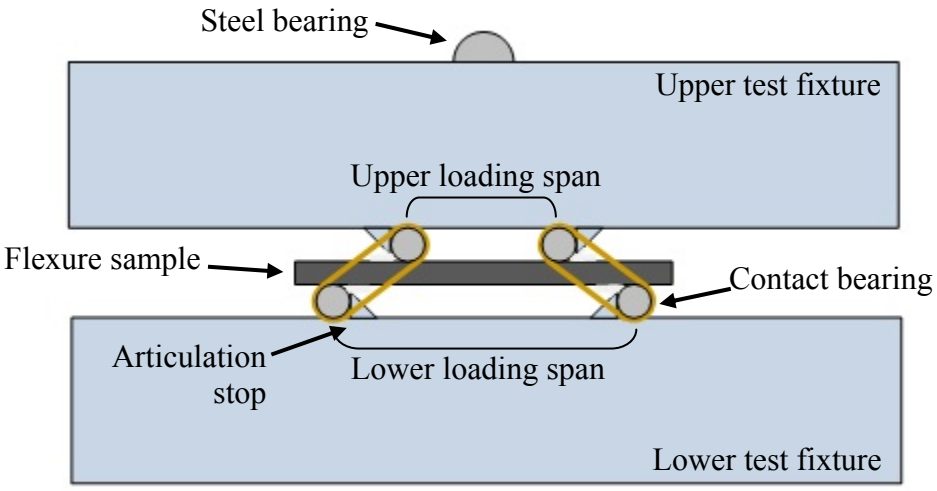


**Figure 4.6** Diagram of assembled, semi-articulating 4-point testing fixture. Hardened tool steel. Dimensions – 110 mm x 25 mm x 25.5 mm (lxwxh). Contains upper and lower halves of the test fixture, upper and lower contact bearings, and steel contact ball bearing

Bars were broken using an Instron 4500/4505 computer controlled test frame. The major components of the testing system are shown in Figures 4.7 and 4.8. These include the control board, crosshead, and load cell. The crosshead was the only moving component during the test. The upwards movement of the crosshead caused the test fixture to come into contact with the load cell, transferring the load to the sample. The load cell contained a pressure sensor that was used to measure the load applied to the test fixture during the test. The control board was used to manually perform a test, and contained readouts for the load cell, and the amount of crosshead traverse. For the testing of these samples, the traverse of the crosshead and the data collection were automatically performed through computer control.


**Figure 4.7** Instron 4500 Test Frame Control Board. Allowed for manual operation of crosshead and measurement of applied load

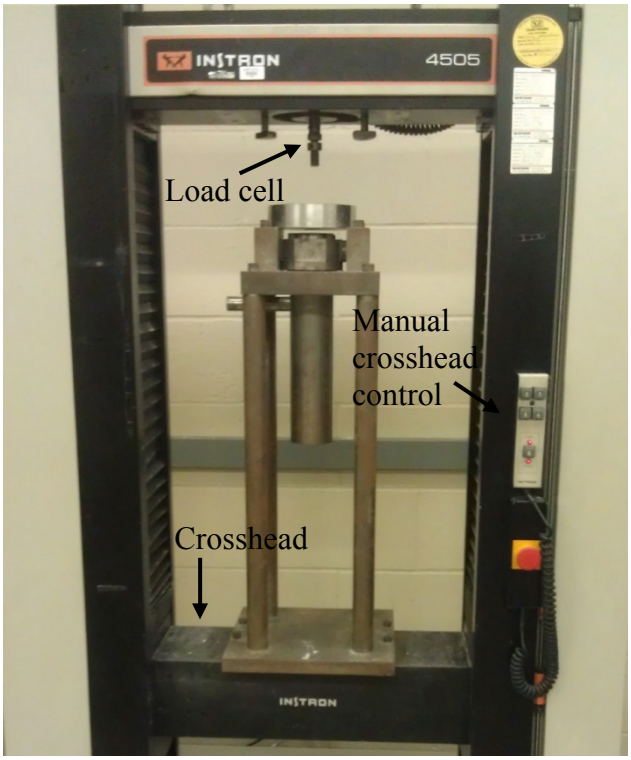


**Figure 4.8** Instron 4505 Test Frame. Contained moving crosshead, mounting point for load cell, and attachment point for the manual crosshead control

The test fixture was first assembled before each test run. Contact bearings were placed up against the stops on the lower portion of the test fixture. The sample was then placed on the bearings within the center of the lower portion of the test fixture, with the 4mm dimension parallel to the upper and lower faces of the test fixture. Two additional contact bearings were then balanced on the top of the sample. Next, the upper portion of the test fixture was placed on top of this assembly. Small rubber bands were placed around the ends of the contact bearings at the four corners of the test fixture. These were used to keep the contact bearings in firm contact with the articulation stops of the test fixture. A Kimwipe® tissue was folded and placed underneath the bend bar to cushion the edges of the broken of the test sample after fracture. After assembly, the position of the bend bar was readjusted to ensure that it was located within the center of the test

fixture. Finally, a steel ball bearing was placed within the recess on top of the test fixture.

After turning on the test setup, the load cell reading was zeroed and computer control was enabled using the test frame control board. The direction of travel of the crosshead, the crosshead speed, and the load sampling rate were controlled through the Instron Series IX software.

Before each test run, the assembled test fixture was placed in the center of the crosshead. The crosshead was raised using the manual crosshead control until the top fixture ball bearing just made contact with the load cell.

Tests were run until fracture of the bar, at which point the test was automatically terminated by the software and the crosshead automatically lowered back to the start position. The software displayed a graph of load verses time, and recorded the maximum load. The fracture load of each bar was recorded on a data sheet, along with the bar designation and dimensions, along with any comments. After testing, the broken bars were placed into individual containers to be kept for further analysis.

**4.5 Weibull Analysis**

Following strength testing, the fracture load and dimensions for each bend bar were entered into a Microsoft Excel worksheet. An excerpt from this worksheet can be seen in Table 4.1. Fields include the bar #, bar width and depth (mm), the width of the outer support span (mm), and the fracture load (N). When using the ASTM recommended 4.5 mm diameter bearing, the width between the outer loading pins is 40 mm. For this exercise, the diameter of the contact bearings used was 4.369 mm. This

increased the overall outer loading span to 40.2625 mm. The stress at fracture was calculated for each bar according to the equation:[176]

$$S = \frac{3PL}{4bd^2} \quad \text{Eq. 81}$$

Where $P$ was the fracture load, in N, $L$ was the length of the outer support span, in m, and $b$ and $d$ were the bar width and depth, respectively, was measured in m.

**Table 4.1** Excerpt from flexure test worksheet, for calculating fracture stress. Fields include bar width, bar depth, outer support span, and fracture load. Values used to calculate fracture strength

| Bar # | Bar width (mm) | Bar depth (mm) | outer support span (mm) | fracture load (N) | $S_{(4,40)}$ (MPa) |
|---|---|---|---|---|---|
| | | | | | |
| **1** | 3.996 | 2.998 | 40.2625 | 515 | 433 |
| **2** | 3.992 | 2.999 | 40.2625 | 526 | 442 |
| **3** | 3.999 | 2.997 | 40.2625 | 588 | 494 |
| **4** | 3.997 | 3.000 | 40.2625 | 692 | 581 |
| **5** | 3.995 | 2.998 | 40.2625 | 602 | 506 |

The next step in the analysis of the flexure strength results was the development of Weibull statistics. Strength values were sorted in order from weakest to strongest, and given a rank ($i$). The natural log of each strength value was taken. The probability of survivability ($P_s$) was calculated for each bar according to the equation:[176]

$$P_s = 1 - \frac{i - 0.5}{N} \quad \text{Eq. 82}$$

Where $i$ was the ranking of each bar, and N was the total number of samples in the analysis.

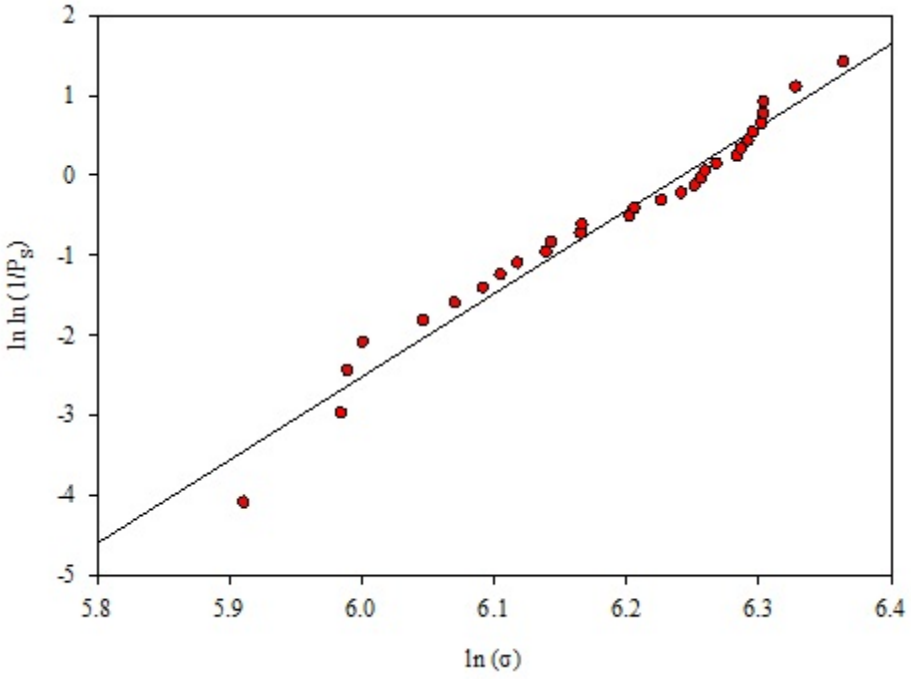


**Figure 4.9** Example of Weibull plot. Linear regression line drawn through data

**Table 4.2** Excerpt from flexure test worksheet, for calculating Weibull statistics. Fields include bar ranking, bar #, fracture strength, and $P_s$

| *i* | Bar # | $S_{(4,40)}$ (MPa) | ln (σ) | $P_s$ | lnln (1/$P_s$) |
|---|---|---|---|---|---|
| | | | | | |
| *1* | 40 | 284 | 5.6481 | 0.9946 | -5.2122 |
| *2* | 97 | 325 | 5.7846 | 0.9837 | -4.1081 |
| *3* | 76 | 365 | 5.9003 | 0.9728 | -3.5918 |
| *4* | 29 | 369 | 5.9115 | 0.9620 | -3.2497 |
| *5* | 72 | 391 | 5.9687 | 0.9511 | -2.9927 |

For each bar, the natural log of the natural log of the probability of survivability was calculated. These calculations are shown in Table 4.2, which shows an additional excerpt from the strength testing worksheet. The data were then graphed using SigmaPlot as an X,Y scatter plot, with from the column ln ln (1/$P_s$) as the ordinate, and ln

($\sigma$) as the abscissa, as shown in Figure 4.9. A linear regression line was added to the diagram, the slope of which is equal to the Weibull modulus. Weibull diagrams were constructed for each group of bars.

### 4.6 Primary Fracture Location

The primary fracture position of all bend bars was determined. This is considered to be the fracture position that contained the likely fracture initiating feature. For low-strength flexure samples, this was often the only fracture position due to the relatively low amount of stress necessary to initiate fracture. For higher fracture strength examples, this became a more challenging exercise. As the stress applied to the flexure sample increased, the amount of energy built-up in the bar also increased. Upon fracture, a shockwave was created which propagated through the sample and reflected at the interfaces between the sample and the surrounding air. This often lead to multiple fracture initiation events.

As a general rule, for a low-strength bar, the primary fracture position was the only fracture position. Low-strength bars that appeared as outliers in the Weibull diagrams had to be examined to determine the cause of fracture. If fracture occurred from an extrinsic cause such as a deep surface flaw, or misalignment of the test fixture, the strength value was removed from the statistics.

ASTM Standard C1161 contains examples of fracture behaviors in a 4-pt bend test that can aid in this determination.[80] A more in-depth discussion of fracture behavior in quasi-statically loaded flexure bars will be found in Section 5.1.3.3.

### 4.7 Scanning Electron Microscopy

Many of the flexure bar samples were chosen for examination in the scanning electron microscope (SEM). The SEM was used for investigation of the fracture surfaces of bend bars and for microstructural evaluation on polished sections.

Polished samples were prepared from sections of flexure bars. Bars were sectioned using a LECO VC-50 low-speed saw and a rotary diamond blade. After sectioning, the cut pieces were washed with water, and then cleaned in an ultrasonicator in a container of acetone, followed by rinsing with isopropyl alcohol. These cut pieces were mounted in rigid epoxy using a Buehler SimpliMet® 1000 automatic thermo-set mounter to prepare them for polishing.

Polishing was carried out using a Buehler AutoMet® 3000 polisher and EcoMet® 2000 power head. Polishing media included a combination of diamond impregnated polishing pads or water-based diamond suspensions applied to nylon cloths. Polishing pads and cloths were applied with adhesive to metal platens, which were magnetically attracted to the rotating platen of the polisher. Mounted samples were secured in a barrel-type specimen holder, capable of holding six samples at once, which was then mounted to the spindle of the power head. During polishing, the specimen holder spun in a clockwise direction at 60 RPM.

The polishing recipe for all samples is shown in Table 4.3. The RPM values listed in the table indicate the rotational speed of the polishing pad or cloth, which spun either in the same direction, or counter to, the polishing specimens. The power head applied pressure to the sample holder, between 4 and 7 lbs per sample. The times listed

were used as guidelines, as the aim of each step of the polishing process was to continue until all induced scratches from the previous step had been removed.

**Table 4.3** Polishing procedure for silicon carbide samples

| Media Size | Diamond Type | Time (minutes) | RPM | Rotation Direction | Pressure (lbs per sample) |
|---|---|---|---|---|---|
| | | | | | |
| 45μm | Pad | 10 | 220 | Contra | 4 |
| 15μm | Pad | 5 | 220 | Contra | 4 |
| 9μm | Suspension | 5 | 160 | Contra | 5 |
| 6μm | Suspension | 5 | 160 | Contra | 5 |
| 1μm | Suspension | 5 | 160 | Complimentary | 6 |
| 0.25μm | Suspension | 10 | 160 | Complimentary | 7 |

Both types of samples required preparation before examination. The surfaces of the fractured bend bars were cleaned with acetone, followed by isopropyl alcohol. Fractured bars were mounted vertically on specialty 90° SEM pin mounts such that the fracture surface was perpendicular to the electron beam. A layer of carbon tape was applied to the mount, to which the bar was adhered. A strip of carbon tape was then wrapped around both the bar and mount.

Both the polished samples and the fracture surface samples were examined using a Zeiss Σigma® field emission SEM, as shown in Figure 4.10. The secondary electron detector was utilized to examine the topography of the fracture and polished surfaces. Operating conditions included an accelerating voltage of between 3.0 and 5.0 kV at a working distance of between 7.0 and 10.0 mm. Images were resolved using Line Integration as a noise cancelling method.


**Figure 4.10** Zeiss Σigma® Field Emission Scanning Electron Microscope (FESEM)[178]

### 4.8 Fracture Position Overlay Maps

While it was necessary to determine the primary fracture position of each bend bar in the process of determining the Weibull statistics of each group of bars, this information was also used to examine the correlation between mechanical and acoustic properties in these materials. The intent was to investigate whether the primary fracture position of the bars corresponded to the location of an acoustic anomaly or variation in acoustic property in the ultrasound maps. The belief was that a feature that was large enough to be a fracture origin may also have produced a noticeable acoustic response in the ultrasound property maps.

In this case, a scale diagram of the bend bar positions within each type of tile was constructed using Microsoft Visio, a component of the Microsoft Office suite. The fracture locations for each layer of bend bars were plotted on the maps, represented by colored tabs. The diagrams, containing the fracture location indicators, were then overlaid on top of the NDE map for the original tile. This was made possible since the identity, position, and orientation of each bar were maintained throughout the machining, testing, and analysis process.

### 4.9 NDE Quantitative Analysis

Additional methods were employed to explore the correlation between the mechanical and acoustic properties of these materials. A comparison was made between the measured strength values and acoustic values from the ultrasound maps within the regions of the bend bars.

This was accomplished through the use of Hermes software that made it possible to graphically manipulate and interpret the raw data from an ultrasound C-scan. A screenshot of this software is shown in Figure 4.11. Raw data were loaded into the program as a .txt file. As long as data were present in the file, the user may select from multiple data sets with which to work. The input boxes on the left were used to define the X,Y space for analysis, as well as to set the scale in the image. By default, the program selects all of the data contained in the file, which, in the case of this study, was the full X and Y extents of a tile. Statistical information such as maximum and minimum value, the range and average value, and the standard deviation were displayed for the selected region. For all bars, a region 1 mm to the left and right of each primary fracture

position was defined, and the average acoustic value within the area was extracted and compared to the strength value of the bar.

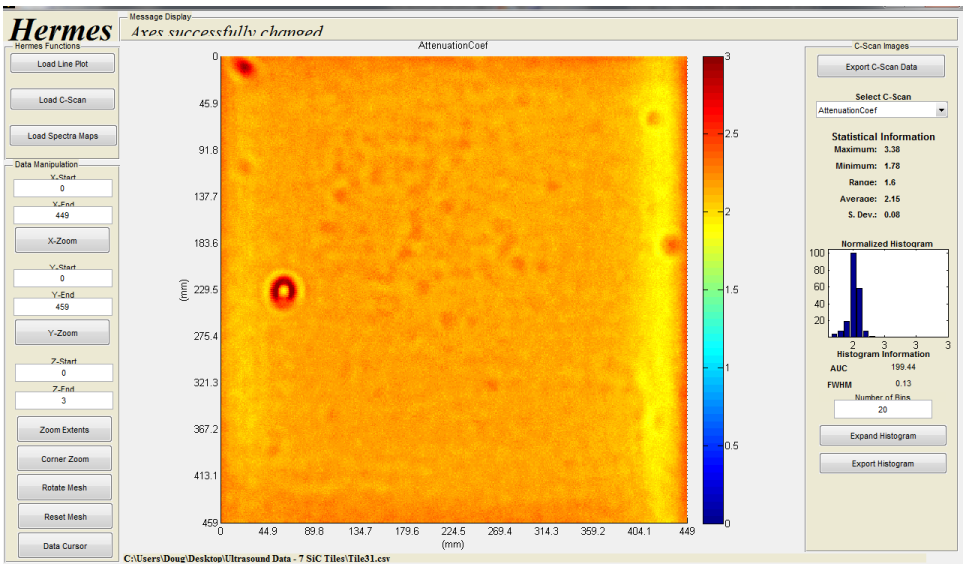


**Figure 4.11** Screenshot of Hermes software, showing acoustic attenuation coefficient data for a Hexoloy commercial silicon carbide tile. A section of acoustic property map may be defined from which to generate statistics

## 4.10 Image Analysis

Images of polished sections were analyzed using free image processing software and included tools with the Microsoft Windows OS. The selected processing package was ImageJ Version 1.45s (created by Wayne Rasband, National Institutes of Health, USA). Microsoft Paint was utilized to remove the hard-coded annotation bar within the Zeiss scanning electron microscopy images.

Images were rendered using a Carl Zeiss Sigma® Field Emission Scanning Electron Microscope (FESEM). Image resolution was set at 2048 pixels by 1536 pixels. Images were recorded using Line Integration scanning mode, speed 6. The resultant size of the .TIFF files was approximately 3 MB.

The process of preparing a file for image analysis, and the motivation for each step, was as follows:

1. Open Microsoft Paint and select the image to be analyzed
2. Using the "Select Rectangular Selection" tool, the area in the image not including the annotation bar was selected
3. Use "Crop" tool to remove the annotation bar. The resultant image resolution was 2048 pixels wide by 1380 pixels high. For a 1000x magnification image, this corresponds to an area of 300 μm wide by 202 μm high.
4. Save the cropped image, and Open ImageJ
5. Open the saved, cropped image
6. Select Analyze -> Set Scale
    a. This was done to apply the scale for the image. Results will then be displayed in units of square microns ($\mu m^2$) and not the number of pixels. The scales for 2048 x 1380 pixels FESEM images were:
        i. 2000x image: 13.653 pixels/micron
        ii. 1000x image: 6.827 pixels/micron
        iii. 500x image: 3.413 pixels/micron
        iv. 200x image: 1.365 pixels/micron
8. Select Process -> Binary -> Make Binary. An automatic thresholding operation which converts a grayscale FESEM image into black and white was performed. This was required to use the following Binary tools. During thresholding, pixels above a set grayscale value were given a value of "1," while those below were

assigned a value of "0." Following the operation, all "1" pixels were colored black while all "0" pixels were colored white.

9. Select Process -> Binary -> Close. This was used to smooth features and remove isolated pixels noise from the noise, and to keep small features in the image.[179]
10. Select Analyze -> Binary -> Fill Holes. A hole was considered to be an isolated white pixel inside of a region of black pixels.
11. Select Analyze -> Analyze Particles. This command was used to count the number of objects within an image. The edge of each object was determined using a wand tool, and the number of pixels contained within the object was measured. This procedure included a number of options:
    a. Size. Objects outside of this size range were excluded from the counting operation.
    b. Circularity. Particles with a shape factor outside of these bound were excluded from the counting. This may was used to differentiate between a pore and an inclusion.[180]
    c. Show Outlines. A secondary figure showing outlines of counted objects was displayed
    d. Display results. This displayed tabulated results of the counting operation. Fields include number and measured area of each object. This tool allowed the user to determine which objects were counted. These results were saved to a tab-delimited text file for processing in Microsoft Excel.
    e. Exclude on edges. This excluded features which interact with the edge of the image from the counting operation.

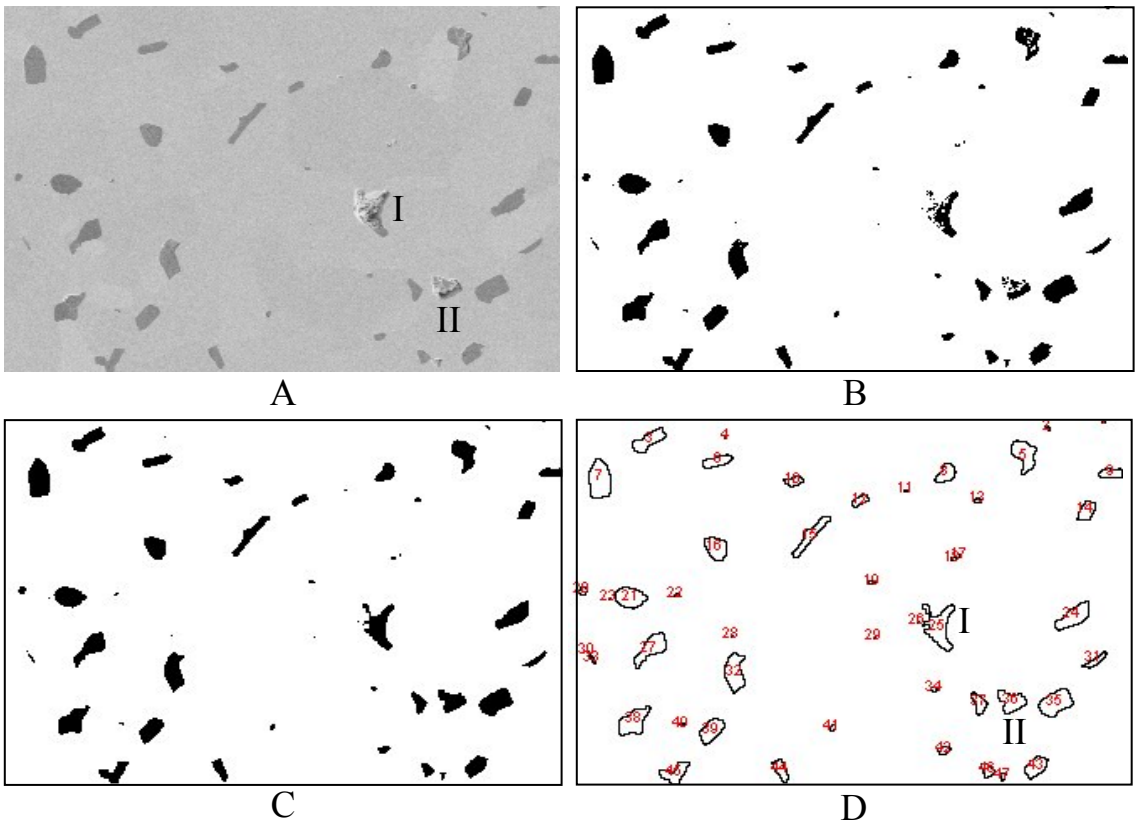


**Figure 4.12** Image analysis process of polished SiC surface. A: cropped image; B: binary image; C: close and fill holes, D: outline of measured features. 1000x magnification

As an example, the image analysis of a polished commercial SiC flexure bar was performed. FESEM images which corresponded to the steps in the process are shown in Figure 4.12. A portion of a 1000x micrograph is shown in Image A. The image contained what are believed to be numerous inclusions and polishing pullouts. The image was then converted to binary, as shown in Image B. The features became more well-defined following the *"close"* and *"fill holes"* operation, as shown in Image C. One of the outputs of the counting operation is an outline of each measured feature, as shown in Image D. By comparing Image D and Image A, it was determined that two of the features (Features I and II) were polishing pullouts. The areas corresponding to these features were removed from the counting statistics.

# 5. Results and Discussions

## 5.1 Characterization of Commercial Samples

### 5.1.1 Archimedes Density

The Archimedes density ($\rho$) was determined for the Hexoloy® 4"x4" tiles contained in the initial group of commercial silicon carbide samples. Before measuring, identification numbers were randomly assigned to all tiles. The measured values are shown below in Table 5.1. Density values ranged from a maximum of 3.17 g/cm$^3$ to a minimum of 3.15 g/cm$^3$. The average value was found to be 3.16 g/cm$^3$. The density of all tiles was greater than the 3.13 g/cm$^3$ specification set forth by the manufacturer.[18]

**Table 5.1** Archimedes density values of original 41 commercial Hexoloy® silicon carbide tiles. Mean value: 3.16 g/cm$^3$

| Tile | $\rho$ (g/cm$^3$) | Tile | $\rho$ (g/cm$^3$) | Tile | $\rho$ (g/cm$^3$) |
|---|---|---|---|---|---|
| | | | | | |
| 1 | 3.17 | 15 | 3.17 | 29 | 3.16 |
| 2 | 3.16 | 16 | 3.17 | 30 | 3.16 |
| 3 | 3.17 | 17 | 3.17 | 31 | 3.15 |
| 4 | 3.17 | 18 | 3.17 | 32 | 3.16 |
| 5 | 3.17 | 19 | 3.16 | 33 | 3.16 |
| 6 | 3.17 | 20 | 3.17 | 34 | 3.16 |
| 7 | 3.17 | 21 | 3.17 | 35 | 3.15 |
| 8 | 3.16 | 22 | 3.17 | 36 | 3.15 |
| 9 | 3.17 | 23 | 3.17 | 37 | 3.16 |
| 10 | 3.17 | 24 | 3.17 | 38 | 3.16 |
| 11 | 3.17 | 25 | 3.16 | 39 | 3.16 |
| 12 | 3.17 | 26 | 3.15 | 40 | 3.16 |
| 13 | 3.17 | 27 | 3.15 | 41 | 3.16 |
| 14 | 3.17 | 28 | 3.17 | | |

### 5.1.2 Ultrasound Evaluation

Non destructive evaluation of the commercial SiC tiles was carried out by immersion-based ultrasound C-Scans utilizing an Olympus planar unfocused transducer in pulser/receiver configuration. The useful output of the transducer was measured at between 16 and 32 MHz, with a central frequency of 20 MHz. Scanning parameters included a 0.1mm lateral step size, resulting in NDE maps containing over one million data points. At each scanning position, the Young's and shear moduli were calculated, along with the acoustic attenuation coefficient. Values were stored in array format for further analysis.

**Table 5.2** Ultrasound C-Scan average values. 20 MHz attenuation coefficient. Hexoloy® commercial SiC tiles. Average: 2.18 dB/cm

| Tile | $\alpha_{(20MHz)}$ (dB/cm) | Tile | $\alpha_{(20MHz)}$ (dB/cm) | Tile | $\alpha_{(20MHz)}$ (dB/cm) | Tile | $\alpha_{(20MHz)}$ (dB/cm) |
|---|---|---|---|---|---|---|---|
| | | | | | | | |
| 1 | 2.16 | 11 | 2.20 | 21 | 2.16 | 31 | 2.15 |
| 2 | 2.21 | 12 | 2.21 | 22 | 2.13 | 32 | 2.19 |
| 3 | 2.17 | 13 | 2.20 | 23 | 2.30 | 33 | 2.19 |
| 4 | 2.18 | 14 | 2.24 | 24 | 2.20 | 34 | 2.21 |
| 5 | 2.24 | 15 | 2.19 | 25 | 2.16 | 35 | 2.16 |
| 6 | 2.23 | 16 | 2.18 | 26 | 2.19 | 36 | 2.18 |
| 7 | 2.17 | 17 | 2.16 | 27 | 2.14 | 37 | 2.17 |
| 8 | 2.30 | 18 | 2.06 | 28 | 2.17 | 38 | 2.17 |
| 9 | 2.18 | 19 | 2.17 | 29 | 2.14 | 39 | 2.18 |
| 10 | 2.15 | 20 | 2.19 | 30 | 2.22 | 40 | 2.16 |
| | | | | | | 41 | 2.10 |

**Table 5.3** Ultrasound C-Scan average values. Young's modulus. Hexoloy® commercial SiC tiles. Average: 424 GPa

| Tile | *E* (GPa) | Tile | *E* (GPa) | Tile | *E* (GPa) | Tile | *E* (GPa) |
|---|---|---|---|---|---|---|---|
| | | | | | | | |
| 1 | 425 | 11 | 428 | 21 | 416 | 31 | 418 |
| 2 | 426 | 12 | 427 | 22 | 424 | 32 | 422 |
| 3 | 427 | 13 | 429 | 23 | 426 | 33 | 430 |
| 4 | 427 | 14 | 425 | 24 | 425 | 34 | 425 |
| 5 | 424 | 15 | 428 | 25 | 422 | 35 | 417 |
| 6 | 426 | 16 | 426 | 26 | 424 | 36 | 423 |
| 7 | 426 | 17 | 426 | 27 | 417 | 37 | 424 |
| 8 | 426 | 18 | 426 | 28 | 424 | 38 | 421 |
| 9 | 426 | 19 | 425 | 29 | 422 | 39 | 417 |
| 10 | 425 | 20 | 418 | 30 | 423 | 40 | 421 |
| | | | | | | 41 | 420 |

**Table 5.4** Ultrasound C-Scan average values. Shear modulus. Hexoloy® commercial SiC tiles. Average: 181 GPa

| Tile | *S* (GPa) | Tile | *S* (GPa) | Tile | *S* (GPa) | Tile | *S* (GPa) |
|---|---|---|---|---|---|---|---|
| | | | | | | | |
| 1 | 181 | 11 | 182 | 21 | 182 | 31 | 178 |
| 2 | 182 | 12 | 182 | 22 | 185 | 32 | 180 |
| 3 | 182 | 13 | 182 | 23 | 182 | 33 | 182 |
| 4 | 183 | 14 | 179 | 24 | 181 | 34 | 180 |
| 5 | 181 | 15 | 183 | 25 | 180 | 35 | 179 |
| 6 | 182 | 16 | 182 | 26 | 182 | 36 | 181 |
| 7 | 182 | 17 | 182 | 27 | 178 | 37 | 182 |
| 8 | 181 | 18 | 182 | 28 | 183 | 38 | 180 |
| 9 | 181 | 19 | 181 | 29 | 180 | 39 | 181 |
| 10 | 181 | 20 | 183 | 30 | 181 | 40 | 180 |
| | | | | | | 41 | 181 |

The collected ultrasound data were evaluated both quantitatively and qualitatively. An average was taken of each property across the surface of the tile. The average value of the 20 MHz attenuation coefficient, Young's modulus, and shear modulus for each tile are shown in Tables 5.2, 5.3, and 5.4, respectively. For the respective properties, the average value was found to be 2.10 dB/cm (attenuation coefficient), 424 GPa (Young's modulus), and 181 GPa (shear modulus).

The ultrasound raw data were also assembled into graphical maps utilizing the Legacy software package developed at Rutgers University. While the original size of the maps was proportionate to the dimensions of the tiles, approximately four inches by four inches, they are presented in this document in a reduced size format. The scale was kept constant within each group of maps to allow for comparisons to be made between the results for each tile. The effect of scaling on the features present within the maps will be discussed later on in this section.

The C-Scan property maps of the 20 MHz attenuation coefficient for the 41 commercial SiC tiles are shown in Figure 5.1 and 5.2. The scaling applied to the images, 1.6 to 2.7 dB/cm, was chosen as it allowed for the variation in average attenuation value between the tiles to be presented, and highlighted some of the important features of interest found within the maps. Among these is the presence of acoustic anomalies, which appear as circular artifacts within the attenuation coefficient maps. Acoustic anomalies appear in at least twenty-six of the maps within this sample set, including maps 3 and 31. With the exception of the presence of acoustic anomalies, many of the maps appear to be homogeneous. However, there are a number which contain regional variations of either increased or reduced attenuation coefficient.

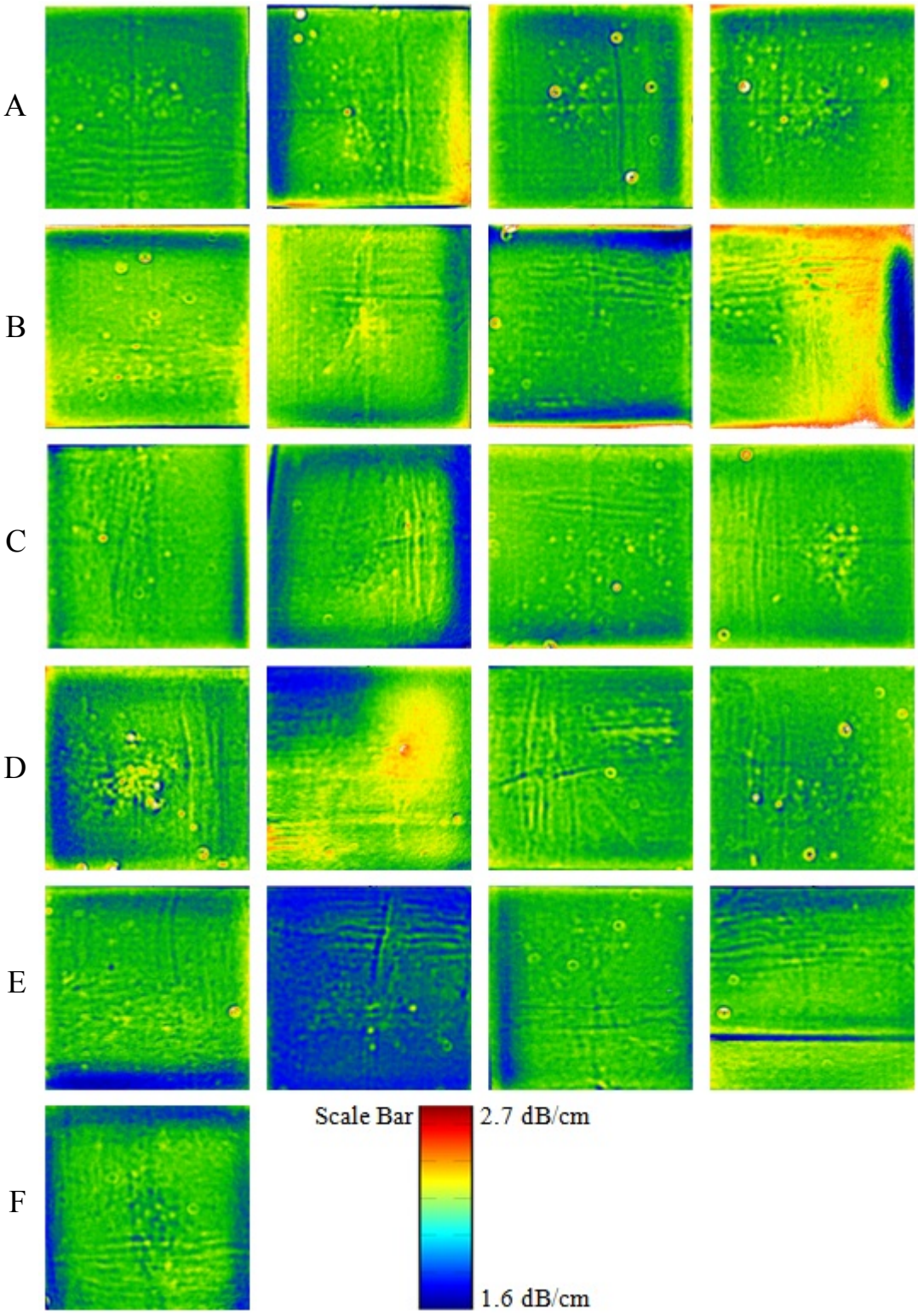


**Figure 5.1** Ultrasound C-Scan maps of Hexoloy® commercial SiC tiles. 20MHz Attenuation Coefficient. Row A: 1–4, Row B: 5-8, Row C: 9-12, Row D: 13-16, Row E: 17-20, Row F: 21. Scale: 1.6 dB/cm – 2.7 dB/cm

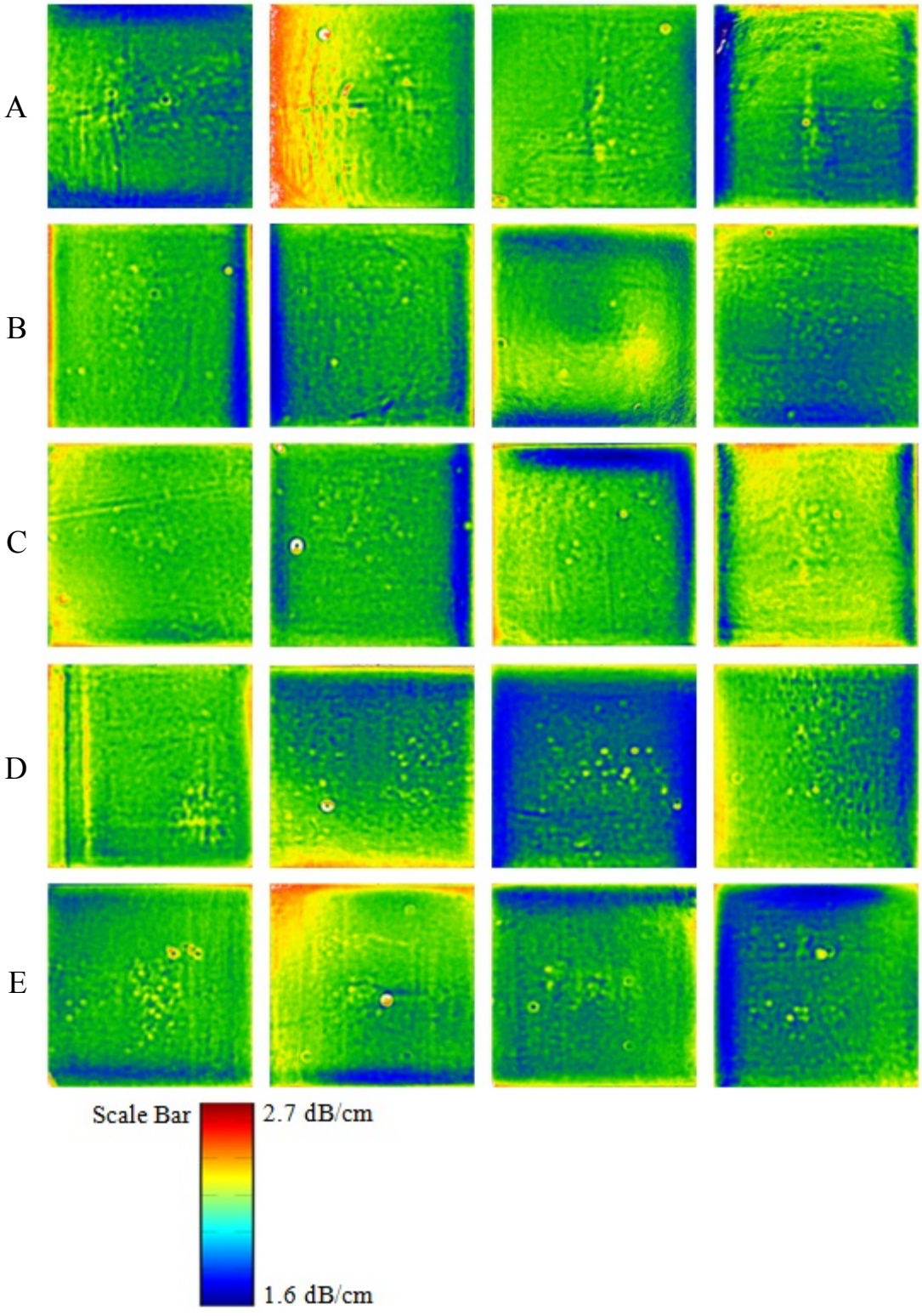


**Figure 5.2** Ultrasound C-Scan maps of Hexoloy® commercial SiC tiles. 20MHz Attenuation Coefficient. Row A: 22–25, Row B: 26-29, Row C: 30-33, Row D: 34-37, Row E: 38-41. Scale: 1.6 dB/cm – 2.7 dB/cm

C-Scan property maps of the Young's modulus are shown in Figures 5.3 and 5.4, scaled between 410 GPa to 440 GPa. In comparison to the attenuation coefficient maps, a much narrower scale was chosen to account for the reduced variability in the maps. Maps of the shear modulus of these tiles are shown in Figures 5.5 and 5.6, with an even tighter scale of 176 to 186 GPa. As with the attenuation coefficient measurement, acoustic anomalies also appear in these maps, typically occurring at the same spatial positions. One of the consistent behaviors that were observed was a gradient in values, where higher values were seen in the top-left corner which decreased in traversing to the bottom-right edge. These gradients were also present in the C-Scan maps of both the shear and longitudinal sonic velocities. It is believed that they could be attributed to slight variations in density within the tiles, possibly from the stacking configuration of the tiles during the firing process. It must be stated that, based upon the very tight scales used when processing the maps, these are slight variations in modulus.

It was observed in a number of maps that corners are missing from the image. Examples of this occurred in the maps for tiles 28 and 33. These correspond to scanning positions where the hybrid peak within the oscilloscope trace moves outside of the defined measurement gate. This causes the measured shear wave time of flight to be a small, negative number, resulting in a very large negative number to be calculated for the shear wave sonic velocity. Erroneous values are then calculated for Poisson's ratio, and the Young's and shear moduli. This effect is thought to result from the top and bottom surfaces of a tile not being closely parallel to each other.

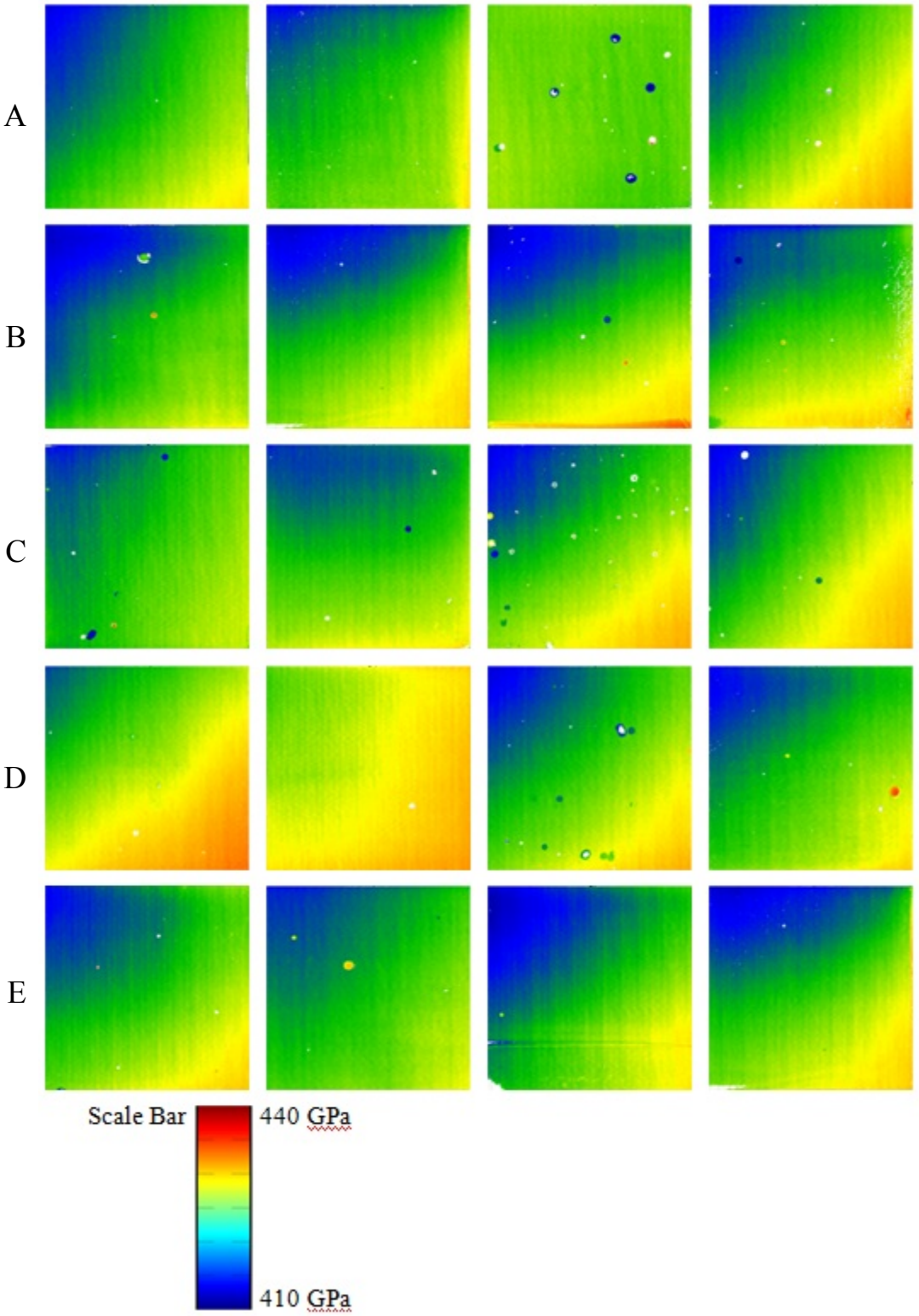


**Figure 5.3** Ultrasound C-Scan maps of Hexoloy® commercial SiC tiles. Young's modulus. Row A: 1–4, Row B: 5-8, Row C: 9-12, Row D: 13-17, Row E: 18-21, Missing: 14. Scale: 410 GPa – 440 GPa

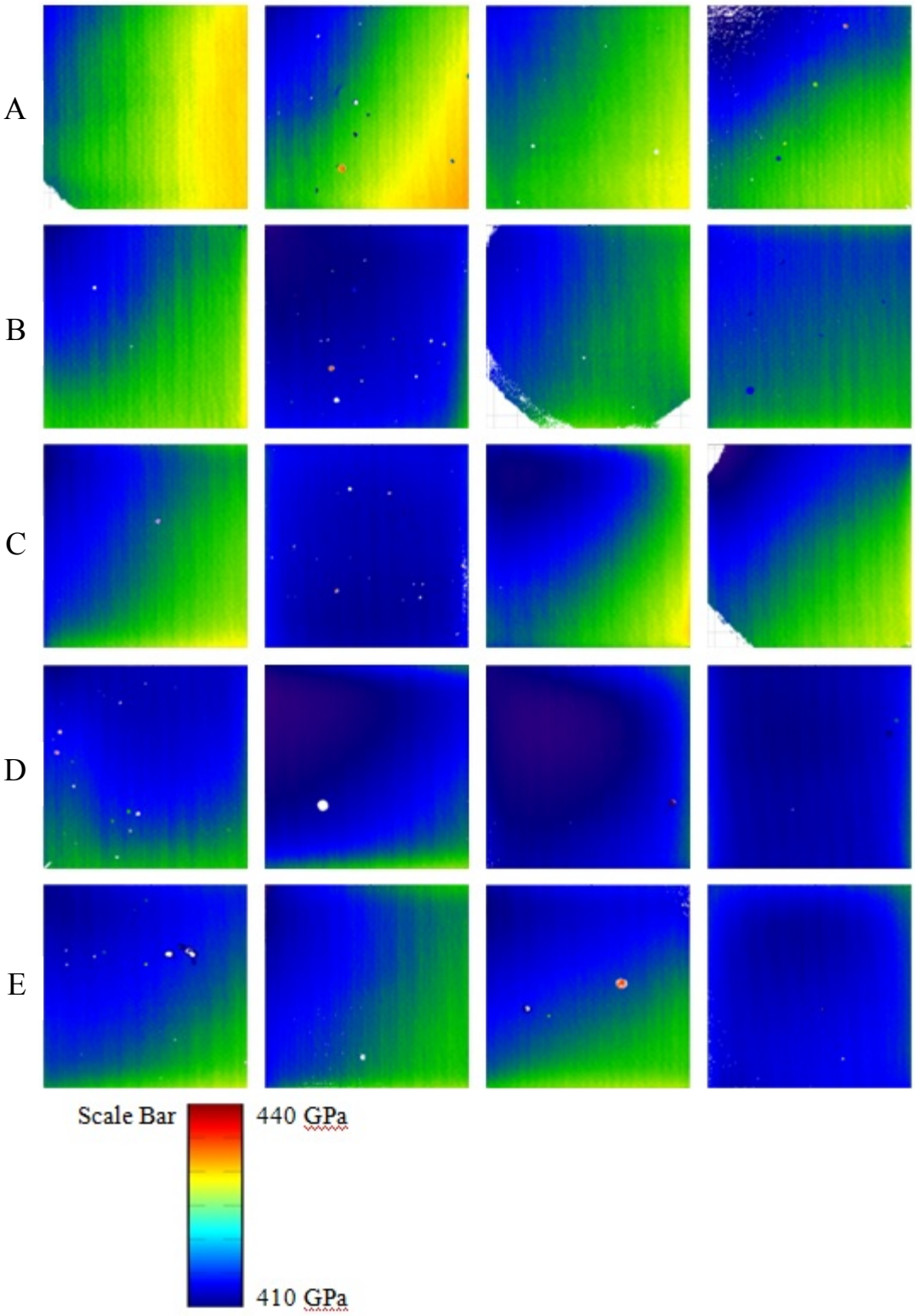


**Figure 5.4** Ultrasound C-Scan maps of Hexoloy® commercial SiC tiles. Young's modulus. Row A: 22–25, Row B: 26-29, Row C: 30-33, Row D: 34-37, Row E: 38-41. Scale: 410 GPa – 440 GPa

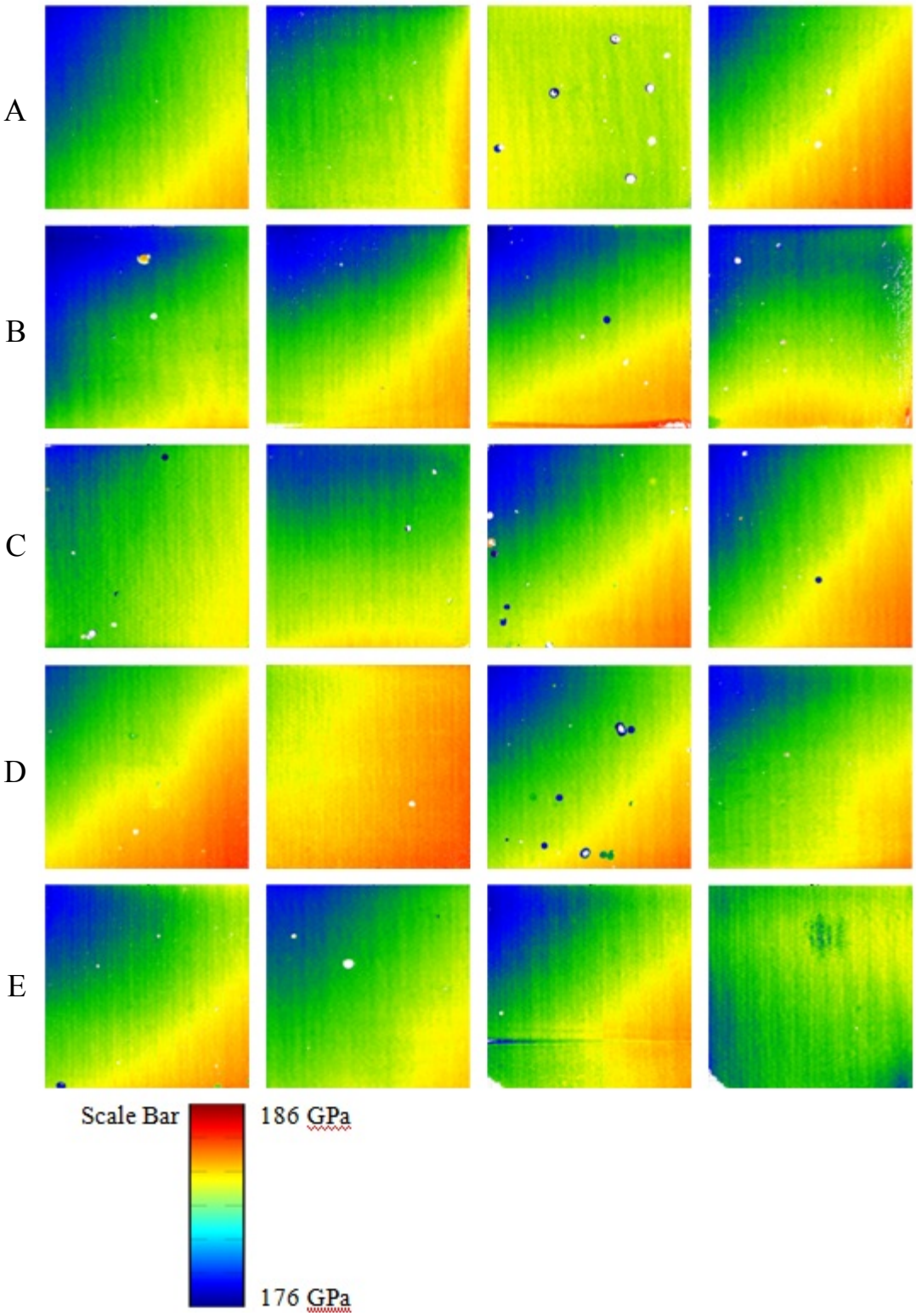


**Figure 5.5** Ultrasound C-Scan maps of Hexoloy® commercial SiC tiles. Shear modulus. Row A: 1–4, Row B: 5-8, Row C: 9-12, Row D: 13-17, Row E: 18-21, Missing: 14. Scale: 176 GPa – 186 GPa

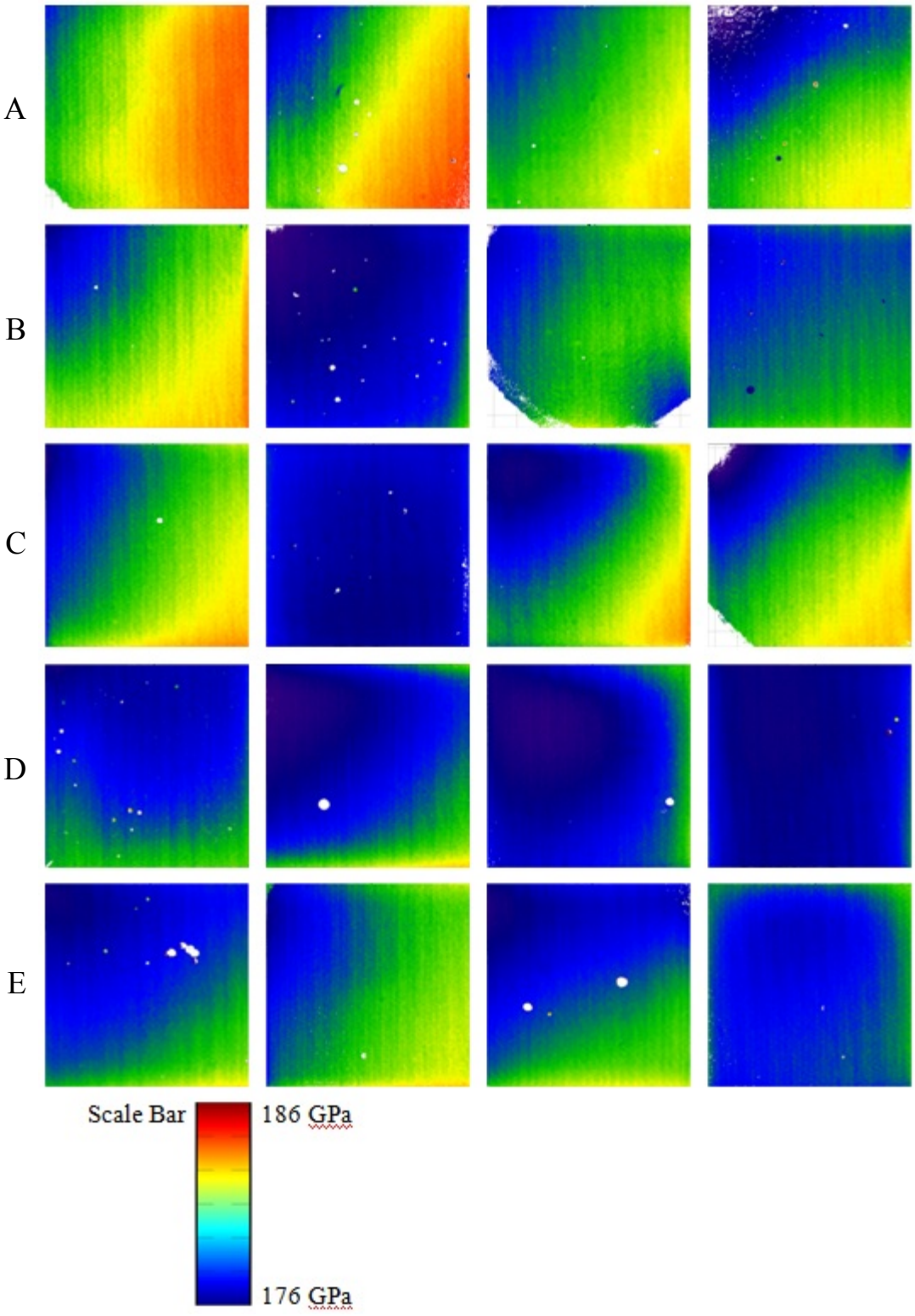


**Figure 5.6** Ultrasound C-Scan maps of Hexoloy® commercial SiC tiles. Shear modulus. Row A: 22–25, Row B: 26-29, Row C: 30-33, Row D: 34-37, Row E: 38-41. Scale: 176 GPa – 186 GPa

#### 5.1.2.1 Separation of Tiles/Group Breakdown

Tile separation groups were designated such that all tiles within each group would have similar acoustic properties. Six group headings were chosen, as shown in Table 5.5. The development of the group headings was based upon an analysis of the numerical ultrasound raw data, as well as an empirical examination of the assembled C-Scan maps.

**Table 5.5** Commercial SiC tiles. Ultrasound group designations

| | |
|---|---|
| Group 1 | High Mean Attenuation Coefficient |
| Group 2 | High Mean Longitudinal Velocity/Young's Modulus |
| Group 3 | High Mean Shear Velocity/Shear Modulus |
| Group 4 | Low Mean Attenuation Coefficient |
| Group 5 | High Zone Variations |
| Group 6 | Low Zone Variations |

Tile headings were chosen such that they reflected the ultrasound energy interaction mechanisms inherent in the C-Scan property measurements. Two of the group headings take into account the measured longitudinal and shear wave sonic velocities, and from these, both the Young's and shear moduli. Two of the other headings take into account the summation of acoustic loss mechanisms represented by the attenuation coefficient. Also reflected in the group breakdown designations where the type of ultrasound measurement, in that both times of flight measurements and peak amplitude measurements were taken into account.

The headings for Groups 5 and 6 were based upon observations of trends or features within the ultrasound maps. At the scales chosen for the attenuation coefficient maps in Figures 5.1 and 5.2, many of the maps appear to be fairly homogeneous. However, there were other maps that contained regional variations or gradients in the

value of attenuation coefficient. There were also numerous maps which contained acoustic anomalies. Tiles which appeared to be homogeneous were placed into Group 6, while those which contained the previously mentioned features where grouped within Group 5.

Overall, tile group designations were selected to support the underlying goals of this study, which was to further the understanding of how microstructural features affect both acoustic properties and strength. These included whether the presence of a circular acoustic anomaly within an attenuation coefficient indicated the presence of a strength limiting feature at the same spatial position or whether microstructural features which contribute to a higher or lower average attenuation have an effect on the strength of a material.

One tile from each group was selected for machining into flexure bars, as shown in Table 5.6. In most cases, the tile with the highest value within a category was chosen for mechanical testing. There were many instances where a tile met the requirements to be placed into more than one group. In the situation where a tile had the highest value in more than one category, the tile with the next highest value was chosen.

**Table 5.6** Commercial SiC tiles selected for bend bar machining/mechanical testing

| Group 1 | Group 2 | Group 3 | Group 4 | Group 5 | Group 6 |
|---|---|---|---|---|---|
| | | | | | |
| Tile 8 | Tile 11 | Tile 4 | Tile 31 | Tile 2 | Tile 19 |

In the initial evaluation of the ultrasound property maps, a consistent scale was applied to allow comparisons to be made within each group of maps. After selection, the property maps attributed to each tile were re-scaled. It was felt that having a specific

scale for each map may better represent the features and data contained within each image. Re-scaled ultrasound C-Scan property maps for the selected tiles are shown in Figures 5.7 through 5.12. Scales were adjusted to fit the dynamic range present in the data within each image. Having a consistent scale for many images can result in compression of the dynamic range where the average value was located either too close to the upper or lower bounds of the scale. It should be noted that in general the scales were adjusted such that the average value was moved towards the upper register of the scale as human eye is more responsive to longer wavelengths of light.

Information about the re-scaled maps of the commercial SiC tiles chosen for mechanical testing is shown in Table 5.7. The information contained in this table includes the tile designation, the type of C-Scan property map, the scaling applied to the image, as well as the average value of the measured property, along with the standard deviation.

**Table 5.7** Commercial SiC tiles selected for machining. NDE map information and statistics

| Tile # | Type of map | unit | Scale (max) | Scale (min) | Average value | Std dev |
|---|---|---|---|---|---|---|
| | | | | | | |
| 8 | att coeff | dB/cm | 3.25 | 0 | 2.31 | 0.09 |
| 11 | Young's modulus | m/s | 440 | 405 | 428 | 4 |
| 4 | shear modulus | GPa | 235 | 165 | 182 | 3 |
| 31 | att coeff | dB/cm | 3.00 | 0 | 2.15 | 0.05 |
| 2 | att coeff | dB/cm | 3.00 | 0 | 2.21 | 0.07 |
| 19 | att coeff | dB/cm | 3.10 | 0 | 2.17 | 0.05 |

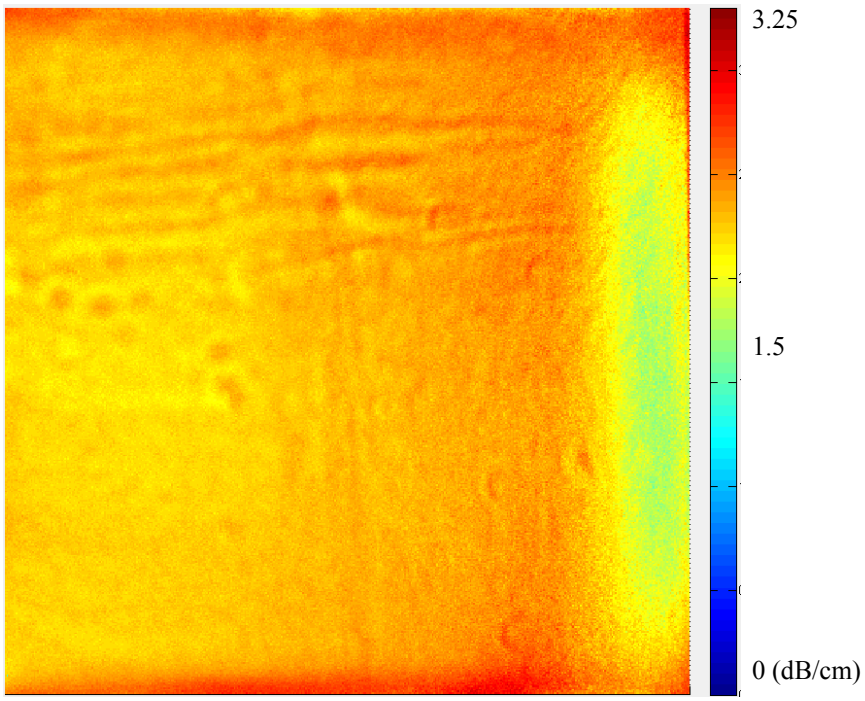


**Figure 5.7** Ultrasound C-Scan map of Hexoloy® commercial SiC tiles. 20MHz Attenuation Coefficient map. Tile 8. Group 1

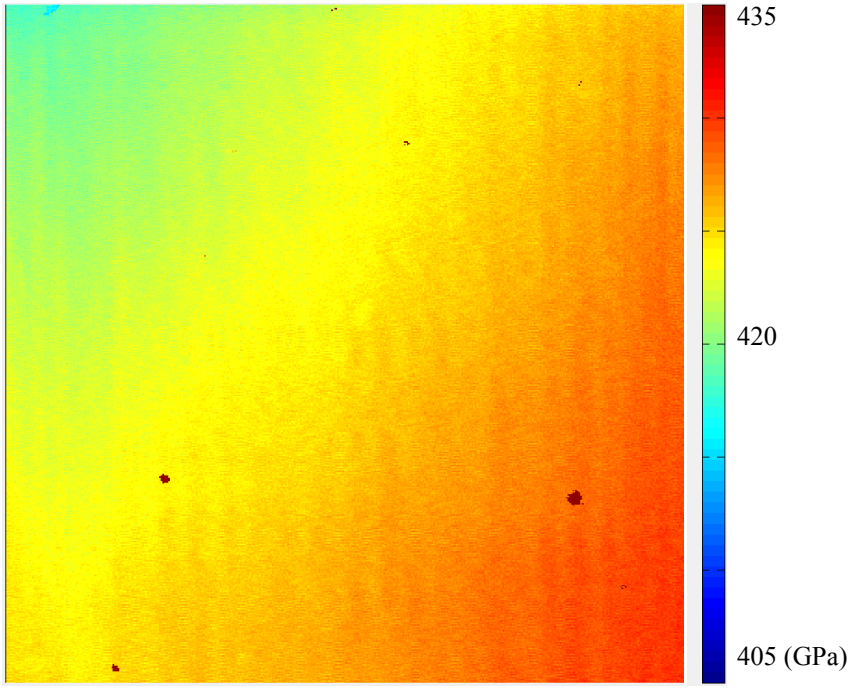


**Figure 5.8** Ultrasound C-Scan map of Hexoloy® commercial SiC tiles. Young's modulus map. Tile 11. Group 2

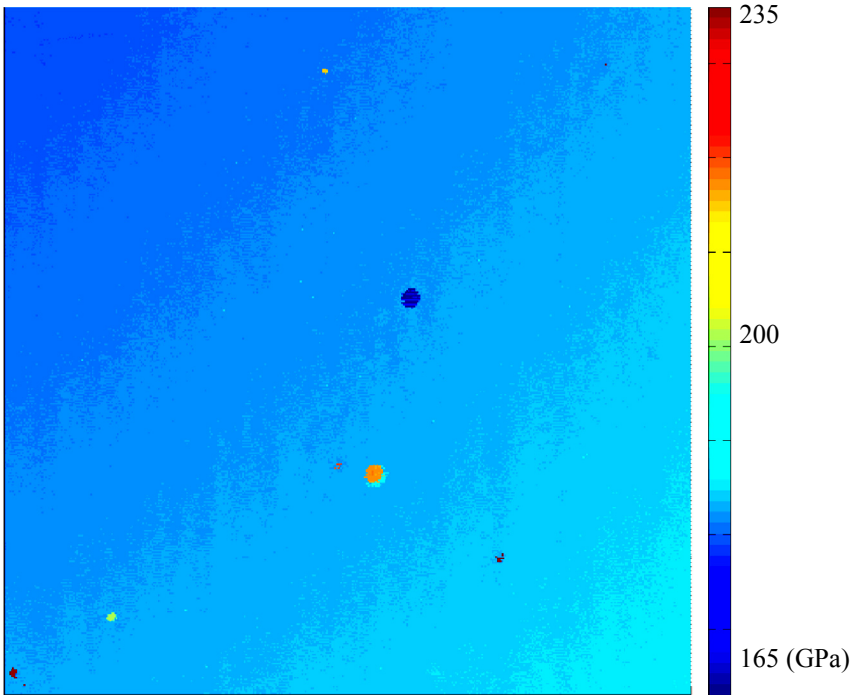


**Figure 5.9** Ultrasound C-Scan map of Hexoloy® commercial SiC tiles. Shear Modulus map. Tile 4. Group 3

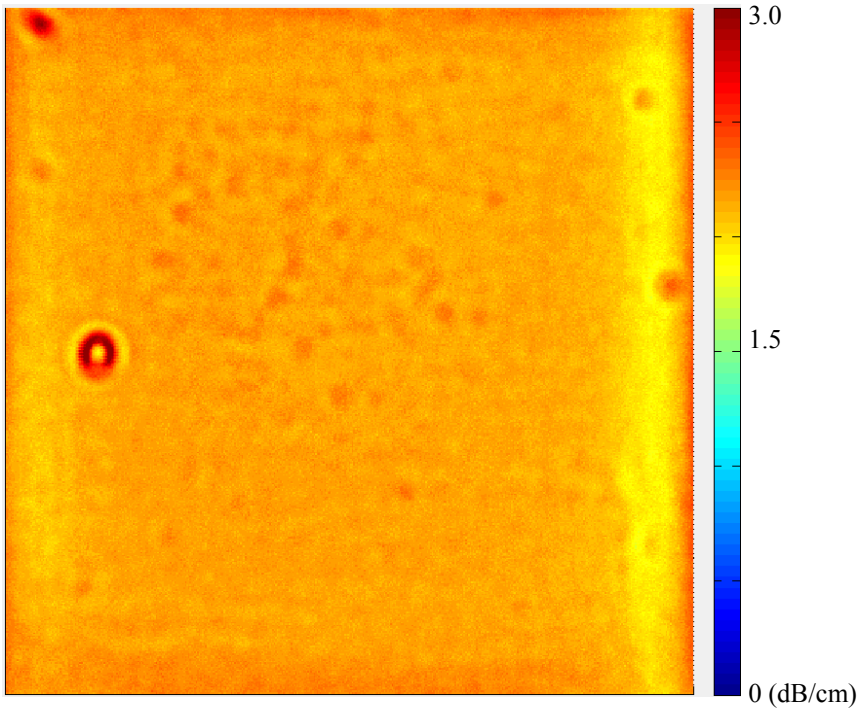


**Figure 5.10** Ultrasound C-Scan map of Hexoloy® commercial SiC tiles. 20MHz Attenuation Coefficient map. Tile 31. Group 4

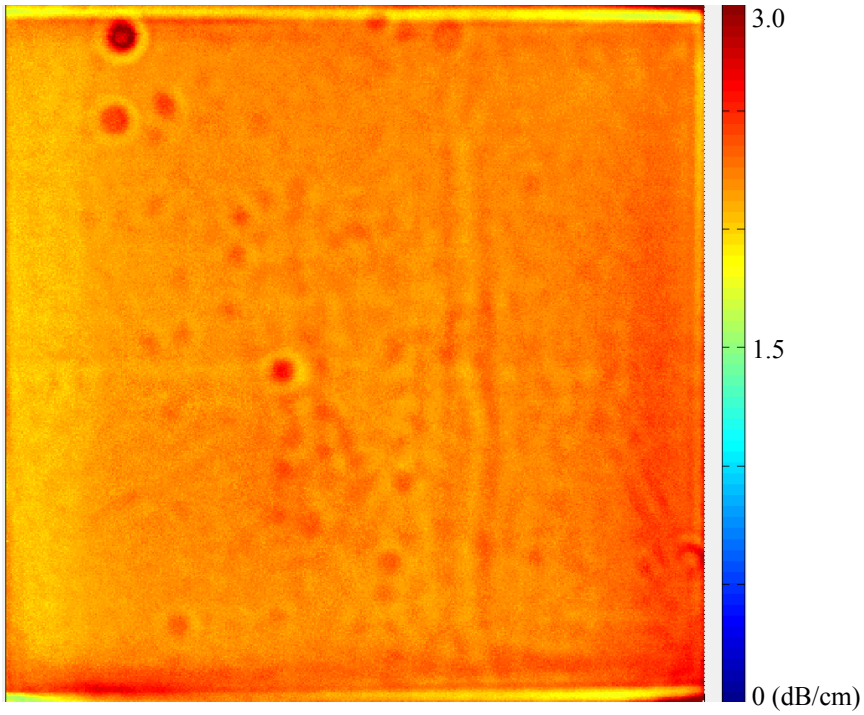


**Figure 5.11** Ultrasound C-Scan map of Hexoloy® commercial SiC tiles. 20MHz Attenuation Coefficient map. Tile 2. Group 5

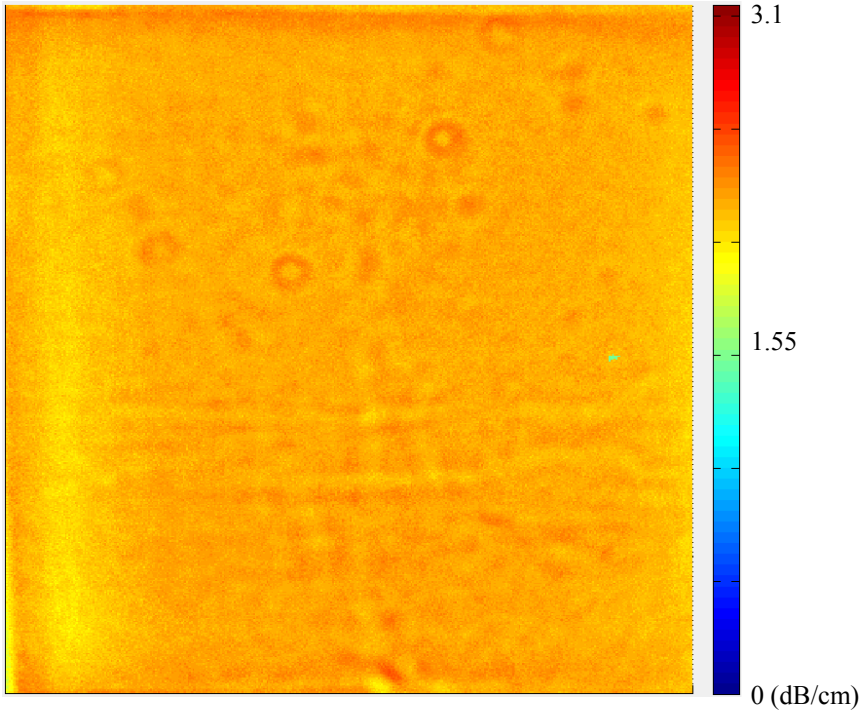


**Figure 5.12** Ultrasound C-Scan map of Hexoloy® commercial SiC tiles. 20MHz Attenuation Coefficient map. Tile 19. Group 6

### 5.1.3 Mechanical Testing

The results of the mechanical testing of the commercial Hexoloy® SiC tiles will be presented in this section. The motivations in selecting the flexure bar size and the machining configuration will be discussed, as well as the methods used to determine the primary fracture position of each strength sample. A discussion of fracture types, strength statistics, and strength limiting features will be followed by analysis of Weibull distribution plots. An analysis of the mechanical testing results of this material plays a role in the goal to determine if a detectable correlation exists between ultrasonically measured acoustic properties and quasi-static strength results.

#### 5.1.3.1 Flexure Bar Machining

One tile from each group was selected for machining into ASTM B-type bend bars, with dimensions of 4mm x 3mm x 50mm (width x height x length). Multiple factors were considered in choosing the B-bar, the most popular bend bar size.[72] The intent of the bend bar size selection, and the machining configuration, was to maximize the tested volume of the tile and the number of samples while keeping testing considerations in mind.

Other ASTM bend bar types are the "A" bar and the "C" bar. Dimensions (width x height x length) of each are 2mm x 1.5mm x 20mm and 8mm x 6mm x 90mm, respectively. Dimensions of the starting tiles were nominally 101.5mm x 101.5mm x 14.5mm. Testing of the ASTM "C" type bar is carried out with a 40mm upper loading span. Of the three available sizes, this is the largest tested volume per bend bar. Machining of flexure bars requires an additional 1mm of material surrounding each

dimension of the bar to allow for final machining to take place.[181] This effectively changes the dimensions of the "C" type bar to 10mm x 8mm x 92mm. This results in the ability to machine only one layer of bars from each starting tile.

Use of the "A" type bar, a much smaller bar, would certainly increase the amount of samples tested. However, the small size of the bars lends itself to other difficulties in the testing process. Machining of the starting tile to maximize the number of samples contained in each tile would result in four hundred samples from each tile. This would result in twenty-four hundred samples from six tiles. Storing and keeping track of this amount of samples would have proven to be difficult and prohibitive. The small size of the bar would increase the difficulties in handling and fixture alignment during the testing process, increasing the degree of error in the measurement. Additionally, the testing frame used to measure the strength of the bars was too robust for this type of bar in that it could not match the slow loading rate required for this bar.

In addition to these considerations, other factors to the decision to decide on the "B" type bend bar. The length of the "B" bar is just under half the width of the starting tile, resulting in the machining of two columns of bars. The height of the bar was also small enough to machine three layers of bars. The size of the "B" bar was considered to be a manageable size for the testing process, and was a match to the size and capabilities of the testing frame.

The chosen bend bar machining configuration for the commercial silicon carbide tiles is shown in Figure 5.13. Each tile was machined with two columns and three layers of bars. The configuration for Tile 11 included seventeen rows or bars, while the remaining five tiles included eighteen rows. The 4mm dimension of the bend bar was

machined such that it was parallel to the 101.5mm by 101.5mm plane of the starting tile. Each tile was intended to be machined into between one-hundred and two to one-hundred and eight "B" type flexure bars. This was considered to be a manageable number of bars to handle, in terms of testing time, identification, storage, and analysis. One of the key aspects of the machining process was to keep track of the position, identity, and orientation of each bend bar in relation to the original tile to allow for the relating the properties of the bend bars to the ultrasound C-Scan maps.

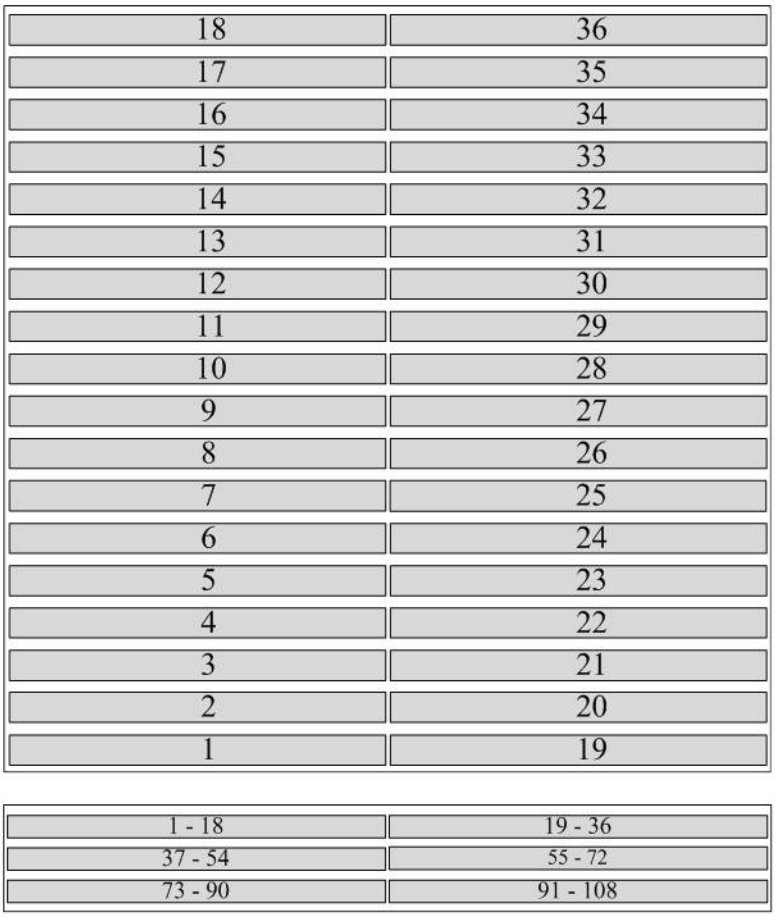


**Figure 5.13** B-type bend bar machining diagram for Hexoloy 4"x4" commercial SiC tile. Each tile contained two columns, seventeen or eighteen rows, and three layers of bars. Shown actual size

### 5.1.3.2 Flexure Testing

In total, six-hundred thirty out of the possible six-hundred forty-two bars survived the machining operation and were returned for evaluation. Four-point flexure testing was carried-out on the surviving six-hundred thirty bend bars. A further six bars were destroyed without result during flexure testing. Testing was performed according to the procedures set forth in ASTM Standard C1161. The included an upwards crosshead speed of 0.5 mm/min. Loading of the samples was carried out until fracture of the test bar occurred.

The results of this testing are shown in Tables 5.8 through 5.14. Each table contains the maximum and minimum values for each layer of bars, as well as the average value and the standard deviation. The average strength value for each tile is shown in Table 5.14, along with the standard deviation. Tiles have been placed in order from strongest to weakest. The average strength value for all of the six-hundred thirty bars was found to be 484 MPa.

**Table 5.8** Flexure testing results for commercial SiC tiles. Tile 8. Group 1. Top, middle, and bottom layers

| Layer | avg (MPa) | max (MPa) | min (MPa) | std dev (MPa) |
|---|---|---|---|---|
| | | | | |
| Top | 485 | 569 | 412 | 45 |
| Middle | 469 | 565 | 404 | 40 |
| Bottom | 481 | 555 | 402 | 40 |

**Table 5.9** Flexure testing results for commercial SiC tiles. Tile 11. Group 2. Top, middle, and bottom layers

| Layer | avg (MPa) | max (MPa) | min (MPa) | std dev (MPa) |
|---|---|---|---|---|
| | | | | |
| Top | 482 | 564 | 369 | 51 |
| Middle | 495 | 600 | 395 | 53 |
| Bottom | 482 | 565 | 385 | 52 |

**Table 5.10** Flexure testing results for commercial SiC tiles. Tile 4. Group 3. Top, middle, and bottom layers

| Layer | avg (MPa) | max (MPa) | min (MPa) | std dev (MPa) |
|---|---|---|---|---|
| | | | | |
| Top | 495 | 595 | 396 | 54 |
| Middle | 494 | 583 | 389 | 49 |
| Bottom | 499 | 592 | 384 | 52 |

**Table 5.11** Flexure testing results for commercial SiC tiles. Tile 31. Group 4. Top, middle, and bottom layers

| Layer | avg (MPa) | max (MPa) | min (MPa) | std dev (MPa) |
|---|---|---|---|---|
| | | | | |
| Top | 452 | 537 | 367 | 47 |
| Middle | 454 | 576 | 370 | 56 |
| Bottom | 450 | 522 | 367 | 49 |

**Table 5.12** Flexure testing results for commercial SiC tiles. Tile 2. Group 5. Top, middle, and bottom layers

| Layer | avg (MPa) | max (MPa) | min (MPa) | std dev (MPa) |
|---|---|---|---|---|
| | | | | |
| Top | 483 | 561 | 389 | 49 |
| Middle | 497 | 561 | 408 | 33 |
| Bottom | 504 | 595 | 431 | 45 |

**Table 5.13** Flexure testing results for commercial SiC tiles. Tile 19. Group 6. Top, middle, and bottom layers

| Layer | avg (MPa) | max (MPa) | min (MPa) | std dev (MPa) |
|---|---|---|---|---|
| | | | | |
| Top | 494 | 581 | 369 | 56 |
| Middle | 476 | 555 | 391 | 43 |
| Bottom | 475 | 537 | 403 | 43 |

**Table 5.14** Flexure testing results for commercial SiC tiles. Average strength values for all bars contained within each tile

| Tile | avg (MPa) | std dev (MPa) |
|---|---|---|
| | | |
| 2 | 494 | 43 |
| 4 | 494 | 53 |
| 11 | 487 | 52 |
| 19 | 480 | 48 |
| 8 | 479 | 42 |
| 31 | 453 | 50 |

#### 5.1.3.3 Determining Primary Fracture Position

As a component of the strength testing analysis, the primary fracture position was determined for each flexure bar sample. This was considered to be the fracture position that contained the fracture initiating feature. In this exercise, each piece of the fractured bar was examined. ASTM Standard C1161 contains examples of fracture behavior encountered in a 4-pt bend test and tips that can aid in this determination.[176] The fracture position analysis was carried out by the guidelines set forth in this standard.

During the quasi-static loading of a sample during a flexure test, an increase in the applied stress results in an increase in the stored elastic energy corresponding to the staining of bonds within the material. Low-strength samples typically contain a large, fracture initiating feature which results in failure of the sample before the build-up of a large amount of energy. Therefore, for a low-strength sample, the primary fracture position is generally the only fracture position. In contrast, the behavior encountered in a medium or high energy fracture can be more complex. Examples of the fracture behavior exhibited by flexure bars in this study are shown in Figure 5.14, as reproduced from ASTM Standard C1161. Examples are listed in order of increasing fracture energy. For each fracture behavior example, the positions of the upper loading pins from the flexure test have been indicated.

The diagram of bar (a) is of a fractured, low-strength bend bar. As is typical of low-strength bars, fracture has initiated at only one location. This fracture location corresponds to the presence of a cantilever or compression curl. This type of feature occurs as a result of the crack encountering the stress state on the compressive stress portion of the bar, which causes it to slow down and curve.[182] Further behavior which is

indicative of a primary fracture position is that the crack front is perpendicular to the long axis of the flexure sample.

While not a typical behavior, fracture may also occur outside of the primary loading zone of the bend test. This is shown by example (b). A sample exhibiting this type of fracture behavior would contain a large, anomalous feature outside of the position of the upper loading pins which has limited strength. The presence of this feature must be verified by microscopy. This fracture type was not encountered during this testing, as all fracture positions occurred within the loading zone of the bend test.

Behaviors attributed to higher energy fractures are detailed in the following examples. The fracture pattern of a low to medium strength bend bar is shown in diagram (c). In this example, the flexure bar has fractured at only one position. Vertical crack branching occurred during fracture, resulting in the formation of a "*double cantilever curl*."[182]

Fracture may also occur at more than one location. A proportionate amount of energy is built-up in the bar as the applied stress increases before the onset of fracture. At this point, a shockwave is generated by the sudden release of energy, which reflects off the interfaces of the flexure bar and can result in secondary fractures. When this occurs, it is necessary to determine at which location fracture likely initiated.

| Fracture energy | Fracture Behavior |
|---|---|
| low | one fracture location compression curl, fracture perpendicular to tensile surface |
| low | one fracture location, fracture occurred outside loading zone of bend test, presence of large flaw |
| low – medium | one fracture location, double crack branch, formation of double cantilever curl |
| medium | two fracture locations, secondary fracture at location of upper pin, primary fracture near opposite loading pin |
| medium – high | multiple fracture locations, secondary fracture at upper loading pins, double crack branch, formation of double cantilever curl |
| medium – high | multiple fracture locations, secondary fracture at upper loading pins, crack branching to tensile surface, one side of primary fracture |
| high | multiple fracture locations, secondary fracture at upper loading pins, crack branching to tensile surface, both sides of primary fracture |

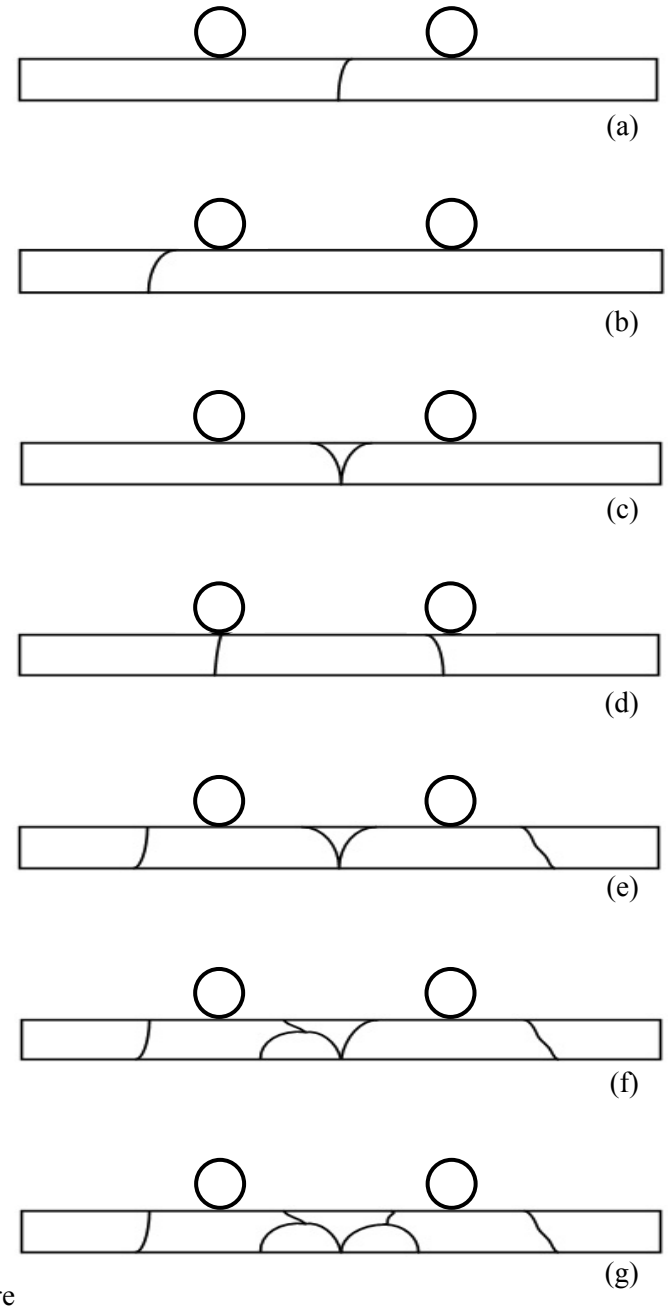


**Figure 5.14** Fracture behavior of low, medium, and high energy bend bar samples. Increased energy results in additional fracture locations[176, 182]

A simple type of secondary fracture behavior is shown in diagram (d). In this case, fracture has occurred at two locations within the bar. The primary fracture position is located near the position of an upper loading pin, while a secondary fracture has

occurred at the location of the opposite pin. At the initiation of the primary fracture, the remainder of the bar is temporarily intact. In other words, the pin opposite to the primary fracture location is still applying stress to the bar. Concentration of the stress at this position results in a second fracture at the location of the second loading pin.

Related examples of a medium/high and high energy fracture are shown by diagrams (d), (e), and (f). In all three cases, secondary fractures have occurred near the locations of both upper loading pins. The secondary fractures on the left side of each bar resemble an upside-down cantilever curl, caused by the reflection of the strain energy release shockwave off of the interfaces of the bend bar. Secondary fracture has also occurred at the location of the opposite loading pin, where the crack grew at an angle to the plane perpendicular to the long axis of the sample. In all cases, a double cantilever curl has occurred at the primary fracture location. In the lowest energy case, example (d), the crack grows all the way to the compressive side of the bar, causing fracture of the bar. In the two highest-energy cases, the crack curves back towards the tensile surface after branching.

#### 5.1.3.4 Relationship of Fracture Energy and Fracture Strength

While the two terms cannot be used interchangeably, a relationship between stored elastic fracture energy and fracture strength was determined from the strength testing data. As has been stated previously, loading of a flexure bar during a strength test results in the build-up of strain energy. The greater the stress before fracture, the greater the amount of energy released. Based upon the strength test results for the commercial SiC flexure bars, the breakdown between fracture type and fracture strength is shown in

Figure 5.15. The correlation between fracture strength and stored fracture energy can clearly be seen. Definitive demarcations between low, medium, and high energy fracture events are not present, as there is an overlap in strength between each fracture type. Low energy fractures correspond to fracture strengths of approximately 150 to 400 MPa. Medium energy fractures occur at strengths between 400 and 500 MPa. Above this, high energy fractures begin to occur.

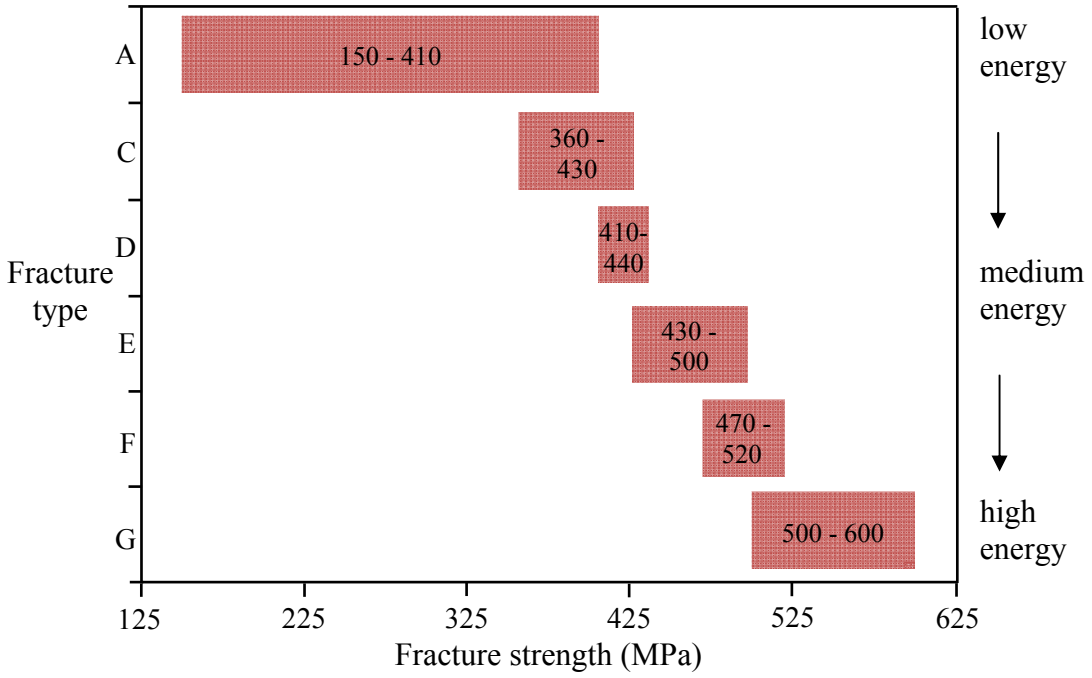


**Figure 5.15** Bend strengths of commercial SiC flexure bars attributed to each type of fracture behavior. Type a: 150-410 MPa, Type c: 360-430, Type d: 410-440 MPa, Type e: 430-500 MPa, Type f: 470-520 MPa, Type g: 500-600 MPa

Type A fractures encompass the greatest range of fracture strengths. As such, variations in fracture behavior in the vertical and horizontal axes exist in this strength region. The degree of cantilever curl that exists in the fracture is dependent upon fracture strength. Very low strength bars, or those that break at a strength below 200 MPa, separate into two pieces with an almost vertical fracture plane. With these types of

fractures only the smallest bit of curl occurs at the top of the bar. The degree of curl becomes more pronounced as the fracture strength increases.

As with the vertical axis, the least complex horizontal axis fracture behavior is a straight line that cuts perpendicularly across the tensile surface of the flexure bar. Fractures such as these tend to occur at strengths of less than 200 MPa. Above 200 MPa, the crack path across the tensile surface becomes more jagged. More complex fracture behaviors are evident in increased strength fractures. The most prevalent of these is crack branching. In this case, the crack branches perpendicularly to the long axis of the flexure bar during fracture. A diagram of this behavior is shown in Figure 5.16. The branching need not be symmetrical on both sides of the initial fracture location. The crack initiating feature will generally be located at the location of the branch.

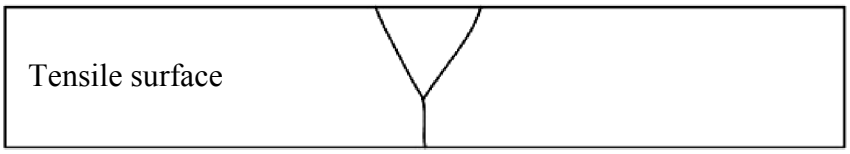


**Figure 5.16** Crack branching across the tensile surface of a low to medium strength flexure bar. Crack initiating feature typically found at location of branch

#### 5.1.3.5 Strength-Limiting Features in Sintered Silicon Carbide

This section seeks to define a number of types of strength-limiting features encountered in the quasi-static testing of Hexoloy® commercial sintered silicon carbide. These will include features which are both intrinsic and extrinsic to the design of the material. This should not be considered to be a catalog of every type of fracture initiating feature as this dissertation seeks to focus on features which result in low strength fractures. Features will be examined in order of increasing fracture strength. Segregated

Weibull distribution data will be presented following an examination of extrinsic and intrinsic strength limiting features in this material. This is an important distinction as fractures which result from microstructural features which are not inherent to the design of the material should be eliminated from strength statistics, or at a minimum denoted.[70]

Examples of each fracture type under consideration will be provided. These will include the fracture type and a range of fracture strengths attributed to each type of feature, as well as scanning electron microscopy (SEM) images of fracture behavior. For each example, the likely fracture path will be indicated, along with the likely fracture initiating feature.

Composite images of primary fracture surfaces will be introduced in this section. These are images which are comprised of a minimum of nine separate SEM micrographs which have been stitched together. Arrows in the image will indicate the region where fracture is thought to have originated. The magnification of all composite fracture surface images is 200x. In the analysis of these images, the top or bottom or left and right side of the bar is in reference to the top image. Images of features of interest may also be composite images, as will be indicated in the write-up.

#### 5.1.3.6 Extrinsic Strength-Limiting Features

The quasi-static strength of ceramic materials is very dependent upon the quality of the surface finish of the material under test.[183] The presence of surface irregularities in the tensile surface of a flexure bar can affect the tested strength of the material. Under tensile loading, the locations of these irregularities can become points of stress concentration which lead to the failure of the bar. It was for this reason that ASTM

Standard C1161 was developed such that the surfaces of ceramic flexure test samples would be prepared in a consistent manner in order to allow strength values of samples prepared by different machining shops to be compared.

#### 5.1.3.7 Side Surface and Transverse Tensile Machining Scratches

Fracture of a number of the low strength flexure bars were found to have initiated at locations which corresponded to the presence of scratches on either the tensile or side surfaces of these bars. Fracture strengths attributed to these types of scratches ranged between approximately 150 to 350 MPa. The fracture type would be considered to be Type A, with the fracture surfaces of the lowest strength bars featuring broad, flat fracture planes. The range in fracture strengths can be attributed to the depth and width of the scratches, and the resulting underlying damage to the bar, as well as to the location of the initiating scratches.

An image of one of these types of machining scratches is shown in Figure 5.17. This figure is a composite SEM image of the side surface of a very low strength bend bar, Bar A ($\sigma_f$ = 155 MPa). In this case, the side of the bend bar was scratched at a perpendicular or high angle to the long axis of the bend bar, along the whole side of the bar. In this example, two evident scratches can be seen. A 30μm wide scratch runs down the side of the bend bar. It can be seen that the fracture path follows the scratch for the

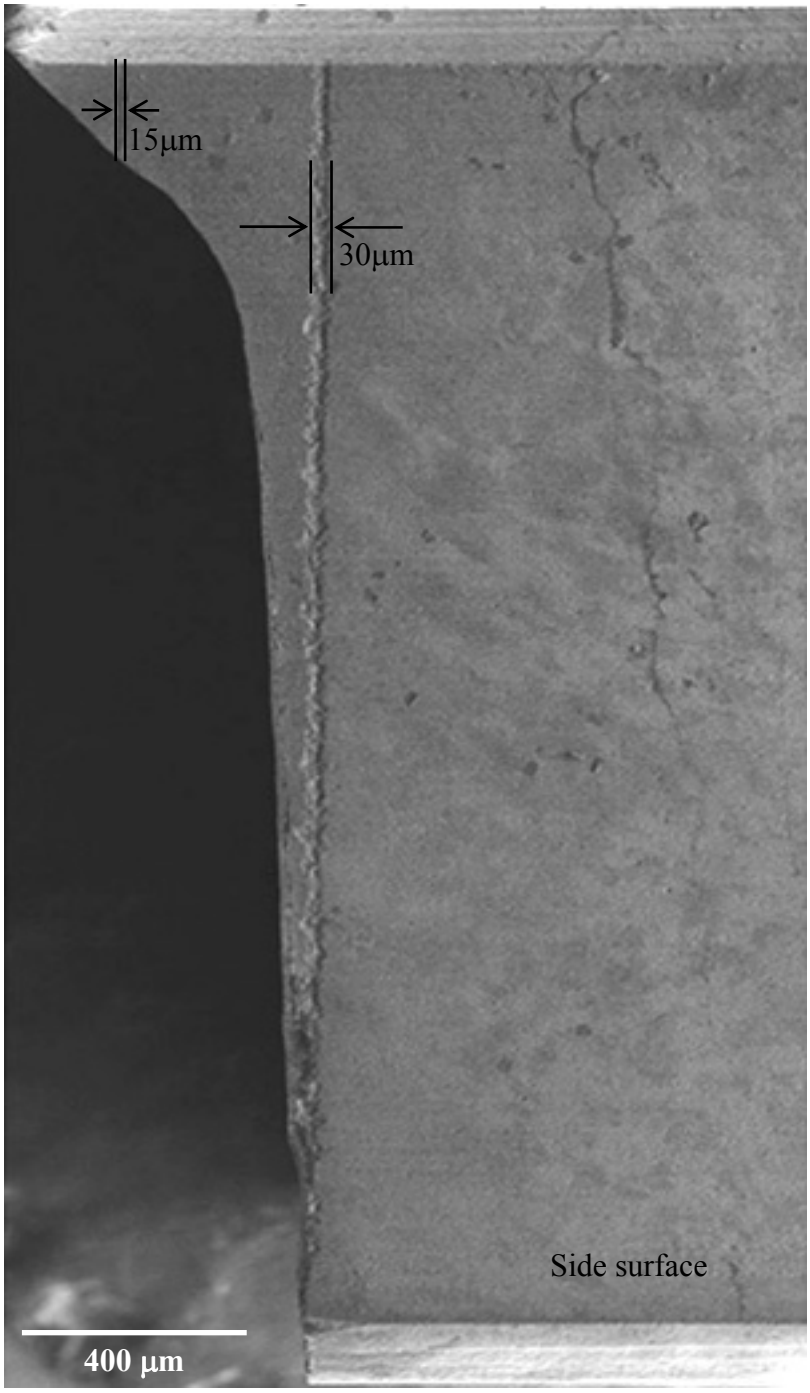


**Figure 5.17** Bar A. Side surface of a low strength bend bar ($\sigma_f$ = 155 MPa). Fracture is believed to have initiated at damage from deep machining scratches. Composite image. 200x magnification

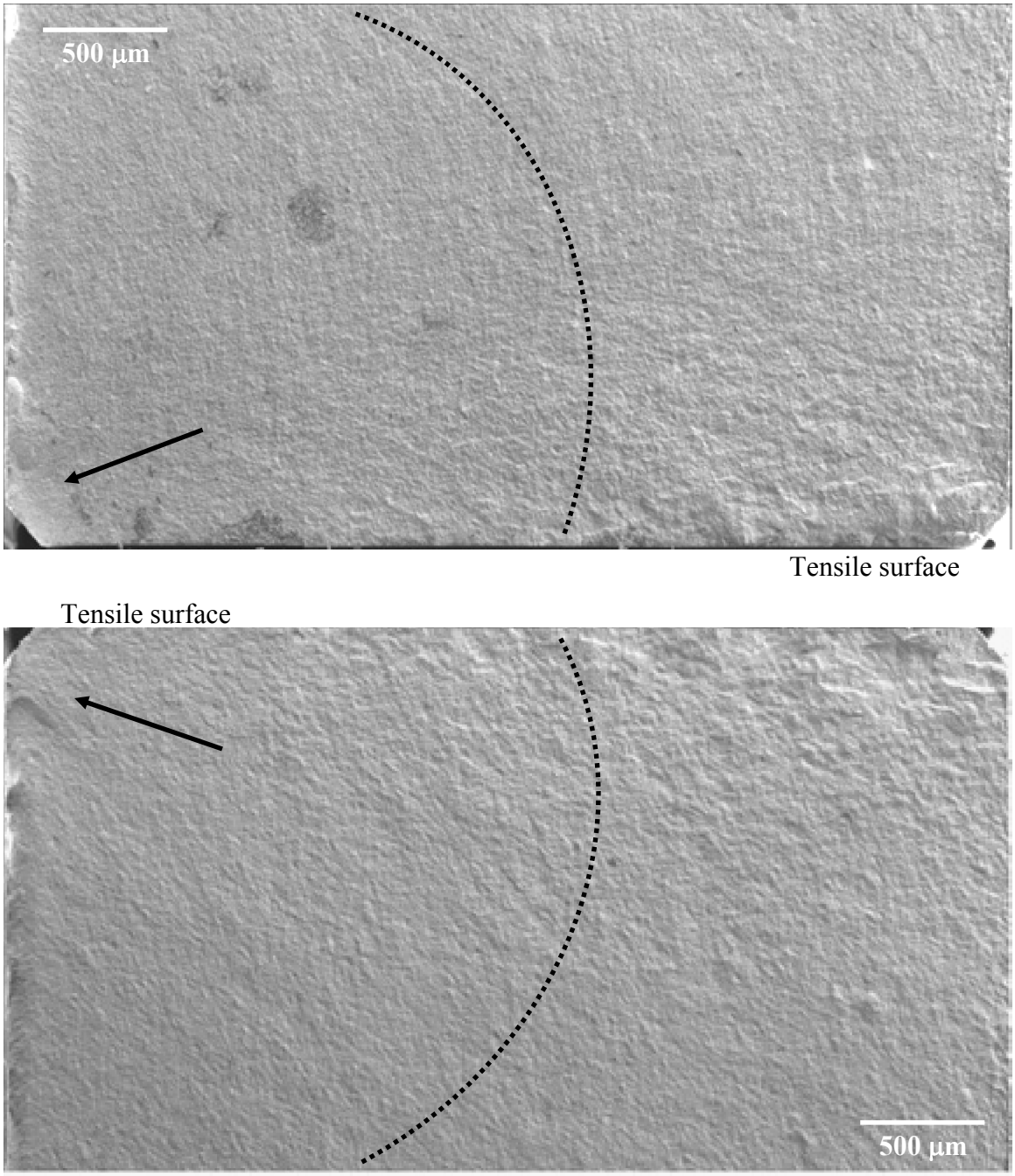


**Figure 5.18** Bar A. Primary fracture surface, left and right faces of a low strength flexure bar ($\sigma_f$ = 155 MPa). Fracture appears to have initiated from the lower edge of the bar, just above the tensile surface. Composite images. 200x magnification

first 0.5mm of travel, and then branches off. Even if this scratch was not present, there is also a 15μm wide scratch that would have most likely caused fracture. This damage had to be induced before the chamfering operation during the machining process in order for the scratch to reach the tensile surface. Of the 630 Hexoloy® flexure bars tested, this bar broke at the lowest applied stress.

FESEM images of the left and right faces of the fracture surface of Bar B are shown in Figure 5.18. When the fracture surfaces for this bar were first examined, the fracture behavior was initially puzzling as the bar appeared to have fractured from the side. It is now known that this bar did in fact break from the lower corner, as shown in the previous image. As this was a low-strength bar, the horizontal fracture plane is again characterized by a broad, flat surface, as indicated by the dashed line.

A composite SEM image of the tensile surface of another low-strength bend bar ($\sigma_f$ = 238 MPa), denoted as Bar B, is shown in Figure 5.19. This image contains a very evident example of a second type of damage. There are a number of scratches that can be discerned in the image, two of which have been indicated by long black arrows. Although these scratches can be challenging to discern in the FESEM, they become much more evident when viewed with an optical microscope. The scratch, which is believed to have been the initiation point of fracture, makes an angle of approximately 75° with the long axis of the bend bar, intensifying the degree of stress concentration. It can be seen that in the area the crack initiated, the fracture path followed the machining scratch for a period of time. This is denoted by the two, short horizontal arrows in the image. As the applied stress field changed during fracture, the fracture initiating crack changed direction and grew perpendicularly to the edges of the long axis of the bend bar.

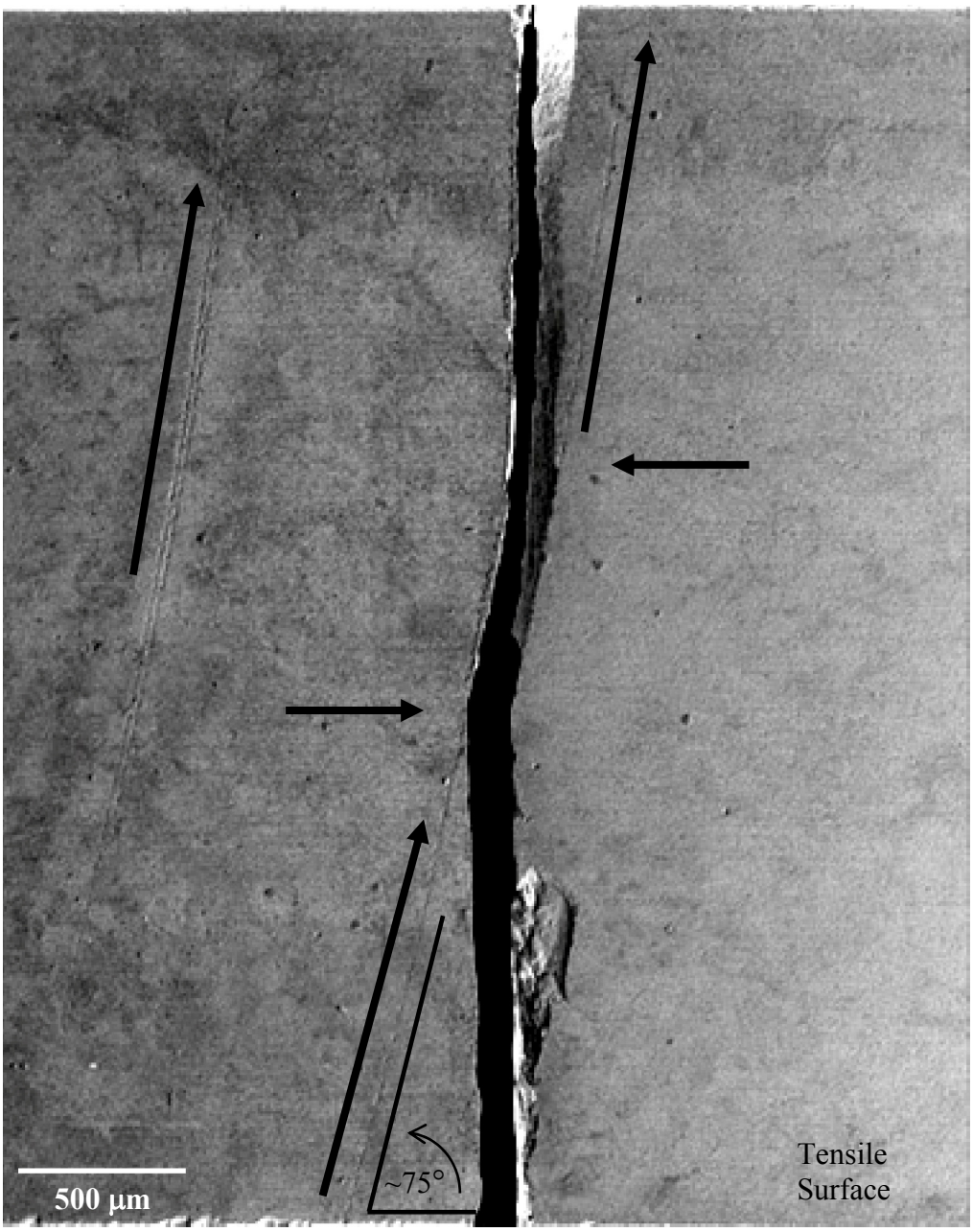


**Figure 5.19** Bar B. Tensile surface of a low strength flexure bar ($\sigma_f$ = 238 MPa). Machining scratches make an angle of 75° with the long axis of the bend bar, acting as a failure initiation point. Composite image. 185x magnification

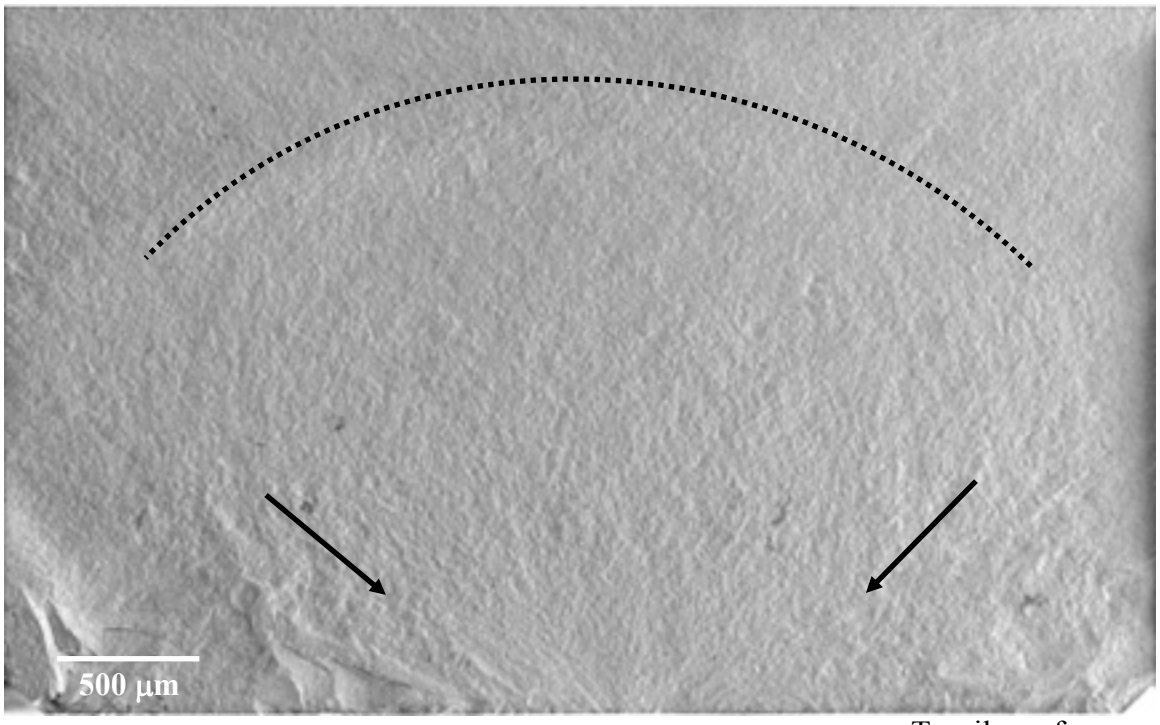


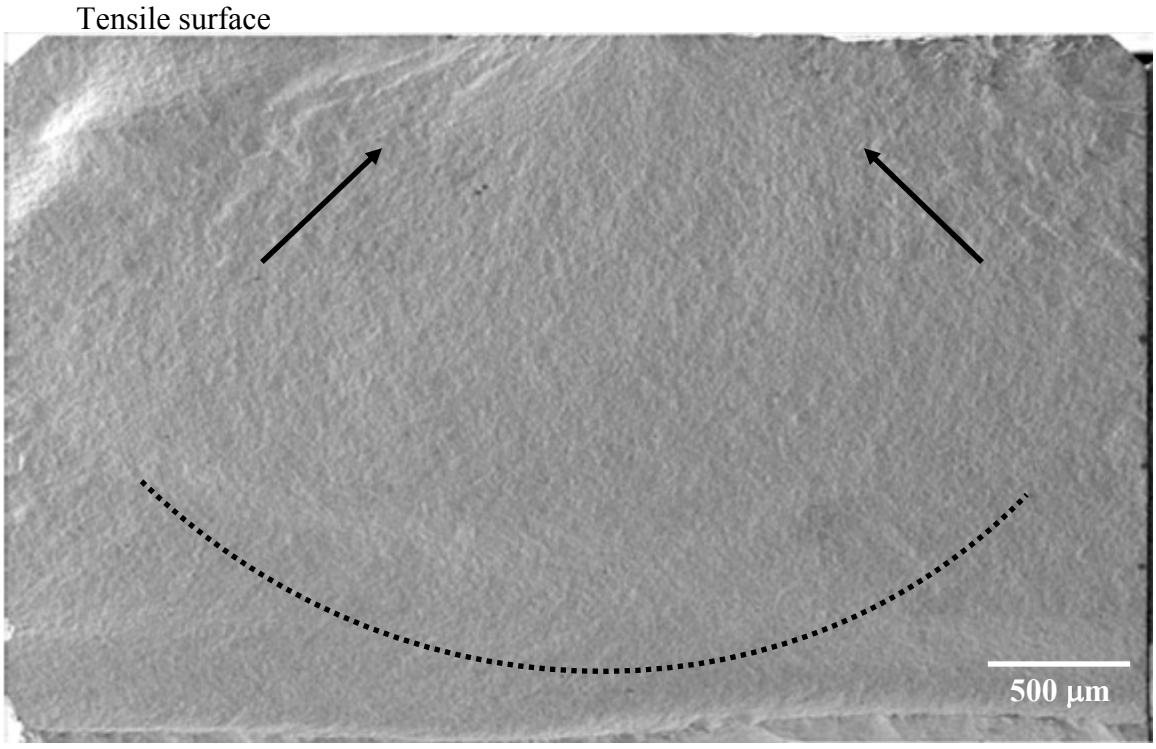


**Figure 5.20** Bar B. Primary fracture surface, left and right faces, of a low strength flexure bar ($\sigma_f$ = 238 MPa). Fracture appears to have initiated near the center of the bend bar. Composite images. 200x magnification

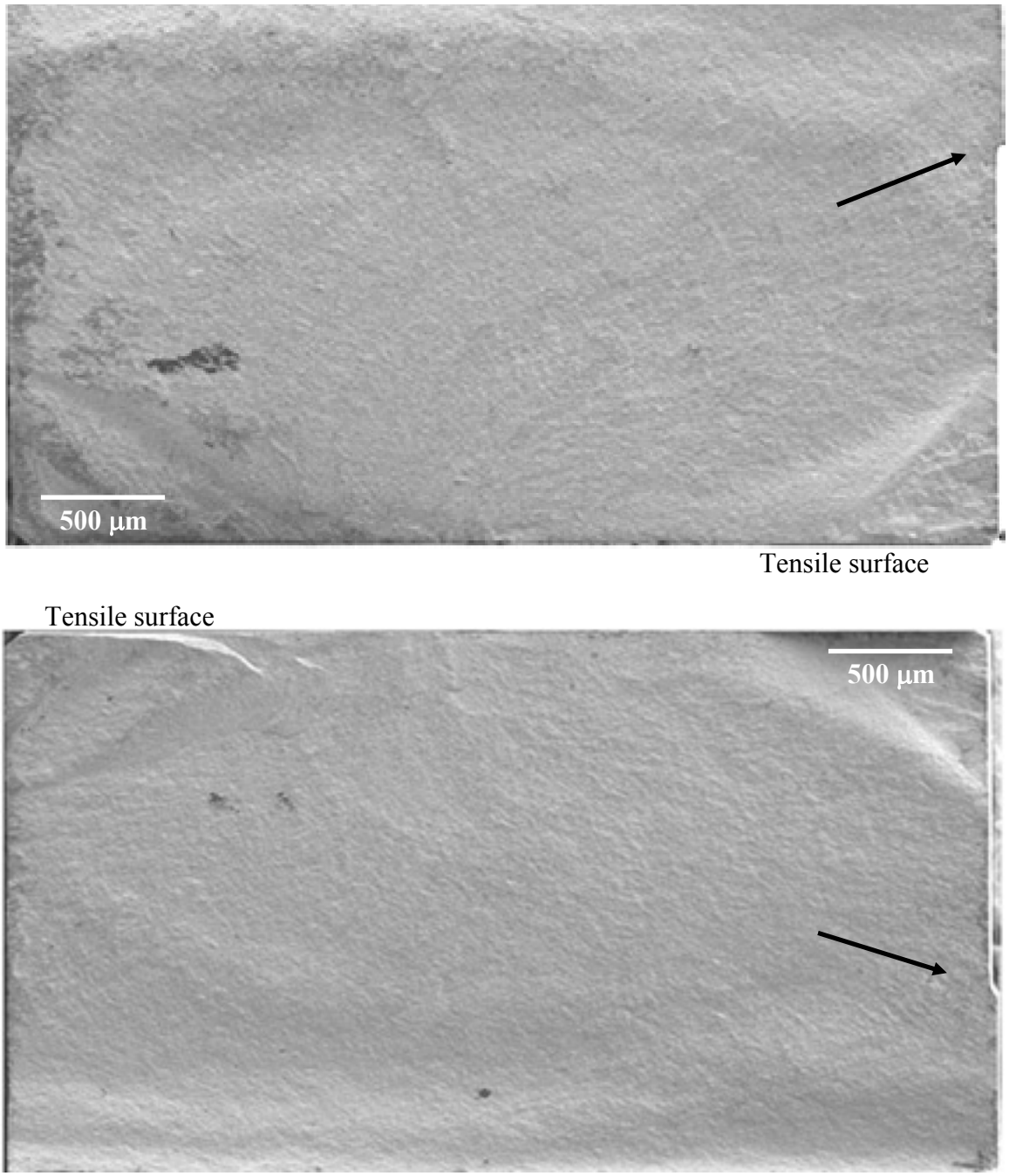


**Figure 5.21** Bar C. Primary fracture surface, left and right faces, of a low strength flexure bar ($\sigma_f$ = 282 MPa). A "step" was machined into the side surface of the bar, resulting in a non-uniform stress distribution during the flexure test. Composite images. 200x magnification

Confirmation that this was the fracture initiation location is shown in Figure 5.20. This figure contains composite FESEM images of the two sides of the primary fracture

location of Bar A. A broad fracture plane, shown by the dashed line, can be found on both end faces, which is indicative of low fracture strength.[182] As shown by the arrows, texture on the fracture surface indicates that fracture began at the tensile surface near the center of the bar. This is an agreement with the approximate location determined from the previous image.

A related type of machining damage is detailed in the next set of images. The fracture surfaces of a third low-strength bend bar ($\sigma_f$ = 282 MPa), labeled Bar C, is shown in Figure 5.21. This resulted in a non-uniform stress distribution within the loading zone of the bar during the flexure test. It should be noted that the tensile surface of this bar also contained the same type of transverse machining scratches attributed to Bar B.

#### 5.1.3.8 Longitudinal Machining Scratches

The flexure bars examined in the previous section where found to have fractured due to damage from scratches which were perpendicular to either the tensile or side surfaces of a bar. For the bars examined in this section, fracture is believed to have initiated at the locations corresponding to machining scratches located on the tensile surface which are parallel to the long axis of the bar.

Bars which were believed to have fractured due to these types of scratches exhibited a range of fracture strengths between 275 and 365 MPa. The predominant fracture behavior was Type A, while higher strength bars did exhibit Type C fractures, which are characterized by the presence of a double-cantilever curl. Of the two examples discussed in this section, both bars experienced horizontal fracture path branching. As

with the previous examples, the range of fracture strengths is again attributed to the severity of the damage, which in these cases is the width and depth of the machining scratch.

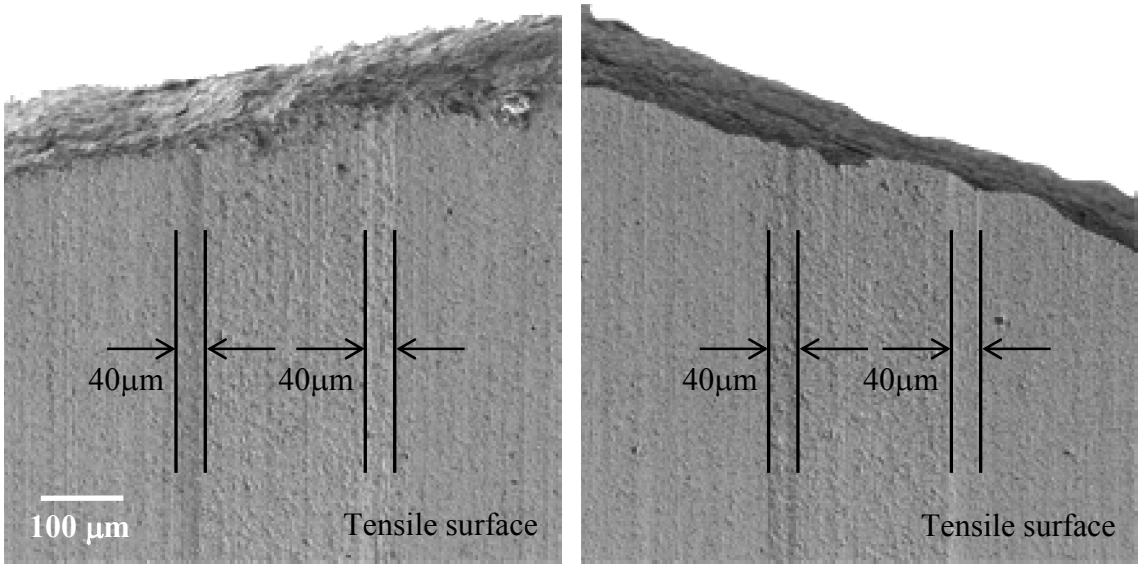


**Figure 5.22** Bar D. Longitudinal machining scratches on tensile surface of low strength flexure bar ($\sigma_f$ = 278 MPa). Scratches measure approximately 40mm in width. 200x magnification

Images of longitudinal machining scratches on the tensile surface of a low-strength bend bar ($\sigma_f$ = 278 MPa), denoted as Bar D, are shown in Figure 5.22. The two images seen in the figure are of the left and right edges of the primary fracture location of this bar. The locations of two 40μm wide machining scratches are indicated in both of the images. Evidence of horizontal crack branching, as shown by the diagonal fracture edge, can be seen in the images. Fractures of this type result in the bar breaking into at least three pieces. As shown in Figure 5.16, this includes two larger sections of the bar, and also a V-shaped portion removed from between them.


**Figure 5.23** Bar D. Semi-circular fracture features corresponding to locations of longitudinal machining scratches on tensile surface of low strength flexure bar ($\sigma_f$ = 278 MPa). 1750x magnification

An image of a section of the primary fracture surface of this bar is shown in Figure 5.23. This side of the fracture surfaces corresponds to the image on the right in Figure 5.22. Arrows placed in the image correspond to the approximate locations of the longitudinal scratches referenced in the previous set of images. A semi-circular fracture plane surrounding the location of the right arrow can be seen in the image. A second semi-circular shaped fracture plane can also be seen in the area of the left arrow. A vertical crack also originates from this location. While it is difficult to determine exactly where in this region fracture originated, this is believed to be the area containing the fracture initiation feature.

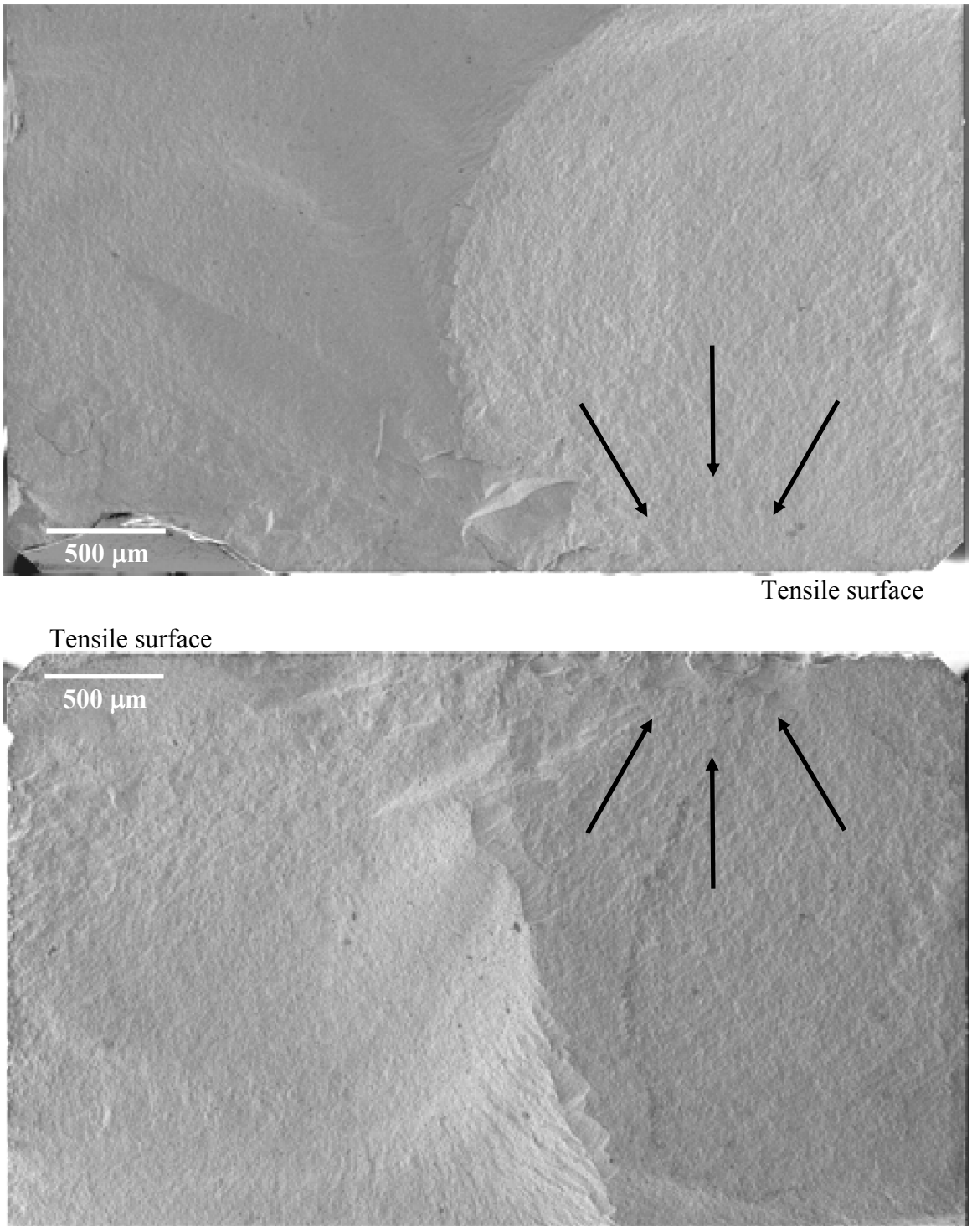


**Figure 5.24** Bar D. Primary fracture surface, left and right end faces, of a low strength flexure bar ($\sigma_f$ = 278 MPa). Bar experienced horizontal crack branching during fracture. Composite images. 200x magnification

Composite FESEM images of the primary fracture surface of Bar D are shown in Figure 5.24. The fracture surface is characterized by a broad fracture plane, indicative of low fracture strength, on the right of both images. Beyond the broad, mostly flat fracture plane, the cracking behavior becomes more complex. The boundary between these regions, which may be discerned by the change in brightness in the images, results from the horizontal crack branching, and may be thought of as the vertical component of this branching. This was considered to be Type A fracture behavior, with a minimal degree of curl in the vertical fracture plane.

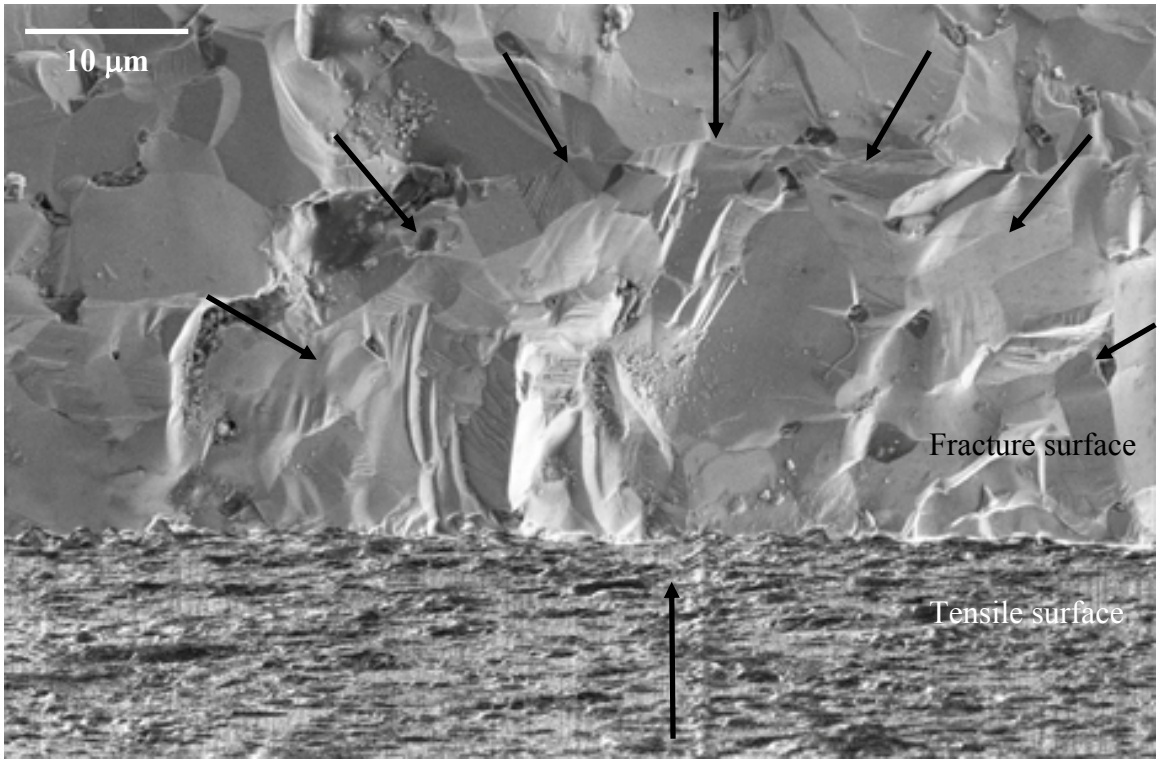


**Figure 5.25** Bar E. Semi-circular fracture feature and longitudinal machining scratch in tensile surface of a low to medium strength flexure bar ($\sigma_f$ = 360 MPa). Composite image. 5000x magnification

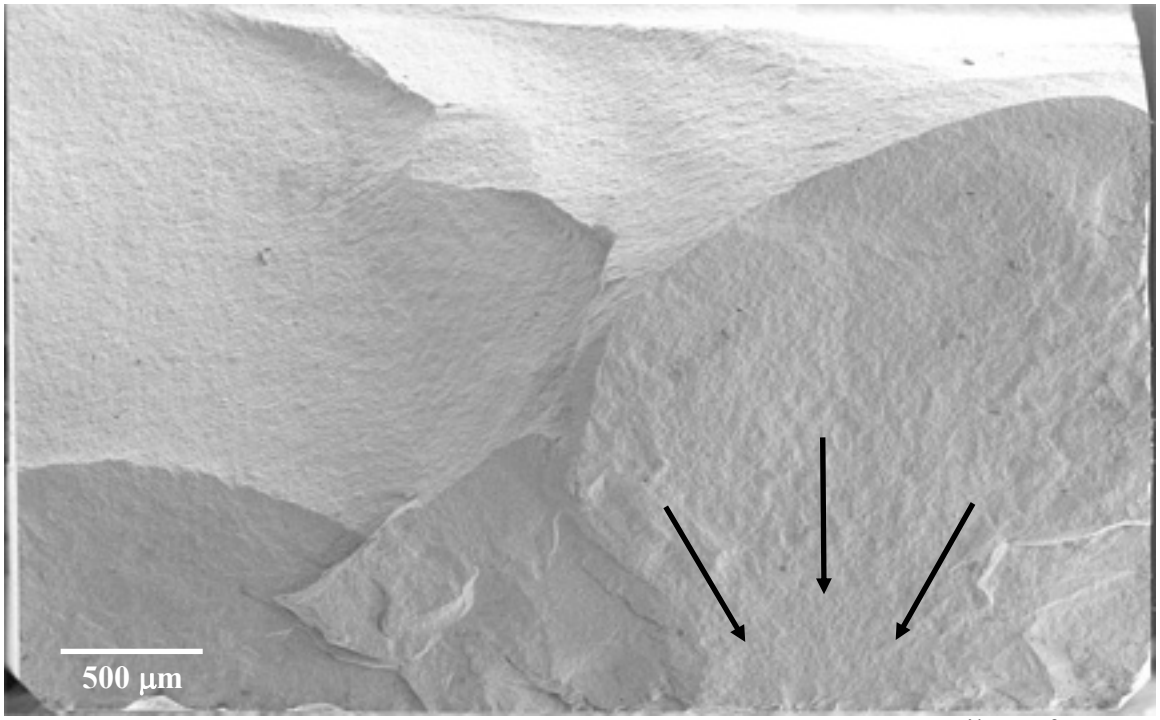


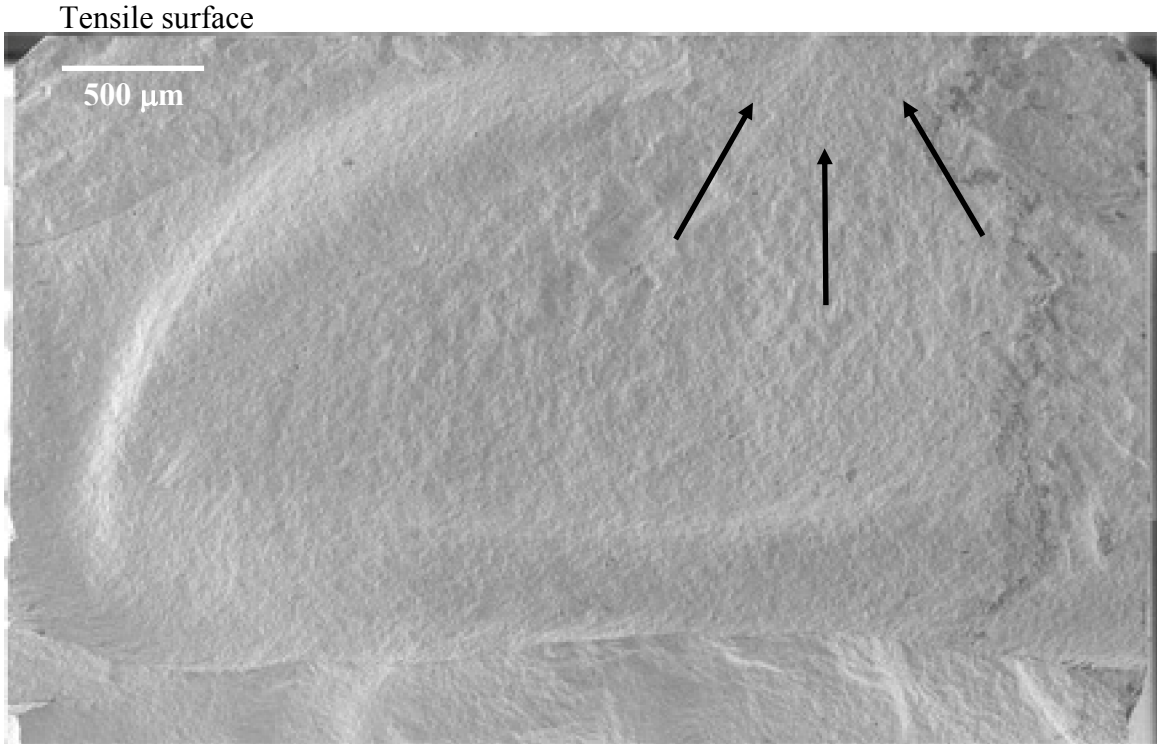


**Figure 5.26** Bar E. Primary fracture surface, left and right end faces, of a low to medium strength flexure bar ($\sigma_f$ = 360 MPa). Bar experienced significant horizontal crack branching during fracture. Composite images. 200x magnification

The next example is of a bar which is also believed to have fractured due to damage resulting from longitudinal grinding during the machining process. This bar, labeled Bar E, fractured at a relatively higher fracture strength ($\sigma_f$ = 360 MPa). An image of a section of the primary fracture surface of this bar is shown in Figure 5.25. This image is a composite FESEM image. Due to the tilting of the sample stage in the microscope required to capture this image, it was not possible to resolve the both the fracture and tensile surfaces in the same image. Images of the two surfaces were resolved separately, and then combined with image processing software during the analysis afterward.

An arrow has been placed in the image just to the left of a longitudinal machining scratch. This is a small scratch, measuring approximately 2μm in width. The edge between the fracture and tensile surfaces contain many small, semi-circle shaped cracks. These are indicative of machining damage from longitudinal grinding.[182] It is also possible to discern smaller scratches parallel to the indicated one on the tensile surface. As with the scratches discussed in Section 5.1.3.7, these scratches are more easily discerned in an optical microscope.

Composite images of the primary fracture position of this bar are shown in Figure 5.26. This fracture behavior is more indicative of Type C, with the presence of double cantilever curl in the vertical plane, and horizontal crack branching. As this was a higher strength bar in comparison to Bar D, the flat portion of the fracture plane is narrower, with the crack branching appearing to be more severe.

Upon initial examination of the strength distribution results it was found that a bi-modal distribution was more representative of the strength data for the flexure bars

machined from the six commercial Hexoloy® tiles. This was indicative of the high degree of spread within the data, despite the fact that the original six tiles were fully-dense production samples of the same material. For this reason, it was expected that flexure bars would have broken at fairly consistent fracture strengths, and a tight distribution of strength data would have existed.

Fractographic analysis of not only the fracture surfaces but also the side and tensile surfaces of these low strength bars revealed the presence of the machining scratches. The effect of a scratch on the strength of a bar was dependent on the scratch location, width, and orientation. The easiest and perhaps the most obvious case to consider is the effect of location of a scratch. Scratches which are located on the bottom of bar under tensile loading will have a much more negative effect on strength than a scratch which is located on the top or compressive surface of the bar.

As was to be expected, bars containing narrow longitudinal scratches, similar to Bar E, broke at much higher fracture strengths than those bars where fracture was attributed to wider longitudinal scratches, such as those found on the tensile surface of Bar D. The effect on strength of the width of a scratch can be explained by an examination of traditional fracture mechanics. Given a particular stress condition, the fracture strength can be calculated as: [39]

$$\sigma_f = \frac{K_C}{Y\sqrt{c}} \qquad \text{Eq. 83}$$

Where Y is a unit-less dimensionality constant based upon the crack shape, $K_C$ is the critical stress intensity factor, $c$ is the initial crack length, and $\sigma_f$ is the fracture stress. Based upon this equation, it can be seen that the fracture strength of a bar and the size of the fracture initiating crack have an inverse relationship.

Taking this into account, it can be seen how the orientation of a machining scratch in relation to the applied stress affects fracture strength. The uniaxial applied stress in a flexure test is parallel to the long axis of the bar. Fracture strength of a sample is dependent on the width of a crack which is perpendicular to the applied stress. For a longitudinal machining scratch, the starting crack length is the width of the scratch. This was shown in the fractures test results where, for a similar scratch width, bars which broke due to longitudinal machining scratches broke at higher strengths compared to scratches which where oriented differently to the applied stress. Transverse machining scratches have a much more deleterious effect on strength as the effective length of the scratch, the width which is perpendicular to the applied stress, is much longer. In the example of Bar B, the scratch indicated in Figure 5.19 makes an angle of ~75 ° with the long axis of the bar. This scratch was measured at approximately 12μm in width. Taking into account the angle of the scratch in relation to the applied stress, the effective width of the scratch is almost four times as long.

Of the five examples given, only the narrow machining scratches located on the tensile surface of Bar E are representative of machining damage that one would expect to find in a longitudinally ground ASTM bend bar.[182] Surface finishing of flexure bars is to be carried out parallel to the long axis of the bar. This was in response to studies which showed that for the same material, fracture strengths of longitudinally ground bars were higher than transverse ground bars.[183]

As set forth in Standard C1161, machining of flexure bars is to be conducted in a series of steps, with grinding wheels containing a coarse to a medium to a fine media size. As with the polishing operations discussed in previous sections, the intent of each

step is to remove the damage, or scratches, from the previous steps while inducing a minimum of new damage. To this end, there are specifications which determine the maximum material removal rate per pass in order to limit the degree of induced damage.

The SAE grit sizes and average media diameters corresponding to each ASTM grinding step are shown in Table 5.15. By examining the measured scratch widths in Figures 5.17, 5.19, and 5.20, it is possible to relate the sizes of the remaining machining scratches to the grinding step. It can be seen that the scratches attributed to Bars A and D could have been introduced in the intermediate steps in the machining process. Another possibility, as in the case of Bars A and B, is that these scratches where the result of the process of cutting each bar from the original tile. In all three cases, the remaining damage could have resulted from either contamination of the next finer wheel, improper washing of the samples between steps, or an even deeper/wider scratch which was not removed in subsequent steps.

**Table 5.15** Grinding steps for longitudinally ground flexure bars. Included is the Society of American Engineers (SAE) grit size, along with the approximate diameter of the diamond media contained in the diamond wheels corresponding to each step of the process

| Step | Grit Size | Media Diameter (μm) |
|---|---|---|
| | | |
| Coarse | 150 | 93.0 |
| Medium | 240 - 320 | 53.6 - 36.0 |
| Fine | 400 - 600 | 23.6 - 16.0 |

As can be expected, the damage shown in examples A, B, C, and D had a deleterious effect on the strength values for the different sets of bars, especially

considering that the damage occurred on the tensile or lower-side surface of the bars. Eighty-five bars where found to have fractured from either transverse tensile, "large" longitudinal tensile or side surface scratches. A breakdown of each type of damage for the six groups of bend bars is shown in Table 5.16. For some tile groups, the number was close to twenty percent of the bars. A further three bars were found to have had steps machined into the sides of the bars.

**Table 5.16** Number of flexure bars machined from each group of commercial SiC tiles that fractured due to transverse or "large" longitudinal tensile or side surface scratches

| Type of Damage | Tile 8 | Tile 11 | Tile 4 | Tile 31 | Tile 2 | Tile 19 |
|---|---|---|---|---|---|---|
| | (# of bars) | | | | | |
| | | | | | | |
| Side | 5 | 9 | 19 | 6 | 1 | 10 |
| Tensile | 10 | 8 | 1 | 10 | 4 | 2 |

### 5.1.3.9 Intrinsic Strength-Limiting Features

Inhomogeneities in the microstructure of a ceramic material can become locations of stress concentration under uniaxial loading, reducing the fracture strength of the part. In sintered ceramic materials, these can include large or anisotropic grains, pores or voids, as well as agglomerates of additives such as sintering activators.[60] These are considered to be intrinsic, strength-limiting features, as they were present within the original tile before bend bar machining. For the examples examined in this section, it can be seen that the effectiveness of the initial processing stages can have a great effect on the final properties of the sintered piece.

### 5.1.3.10 Compaction Relics

A composite FESEM image of the primary fracture surface of a low to medium strength bend bar ($\sigma_f$ = 365 MPa), referred to here as Bar F, is shown in Figure 5.27. Fracture appears to have initiated in the lower right region of the image, along the tensile surface. This was a Type C fracture, with horizontal crack branching occurring approximately a third of the way across the width of the bar. Compared to the lower strength bars examined in previous sections, the flat portion of the fracture plane is considerably reduced in area.

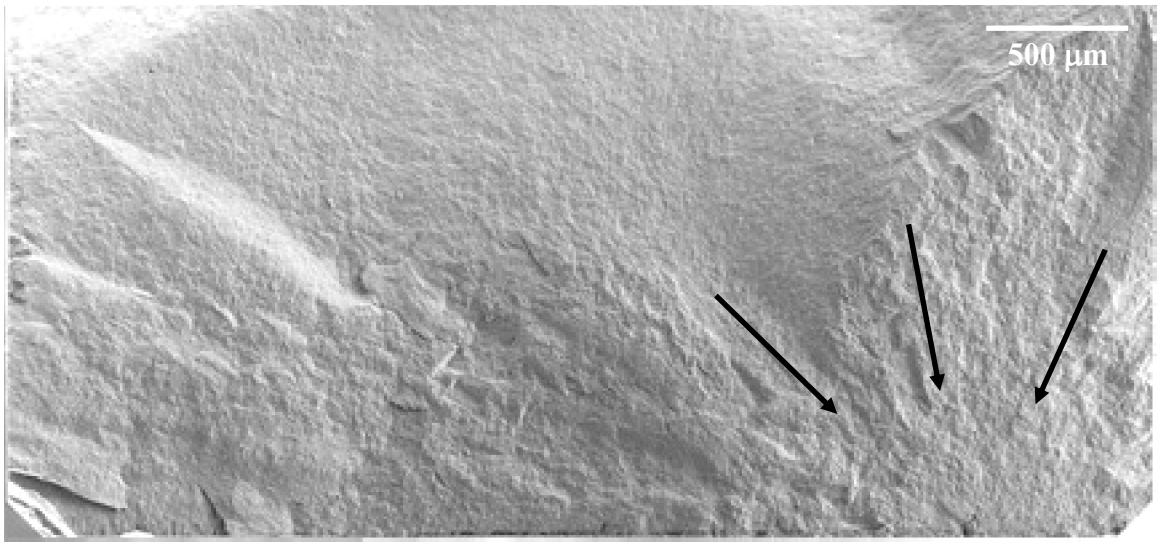


**Figure 5.27** Bar F. Primary fracture surface, right end face, of a low to medium strength flexure bar ($\sigma_f$ = 365 MPa). Fractures appear to have initiated in the lower right region of the bar. Composite image. 200x magnification

An image of the area surrounding what is believed to be the fracture-initiating feature for this bar is shown in Figure 5.28. Arrows in the image indicate the likely fracture path. A dotted rectangle has been placed around the region which is thought to have contained the strength-limiting feature.

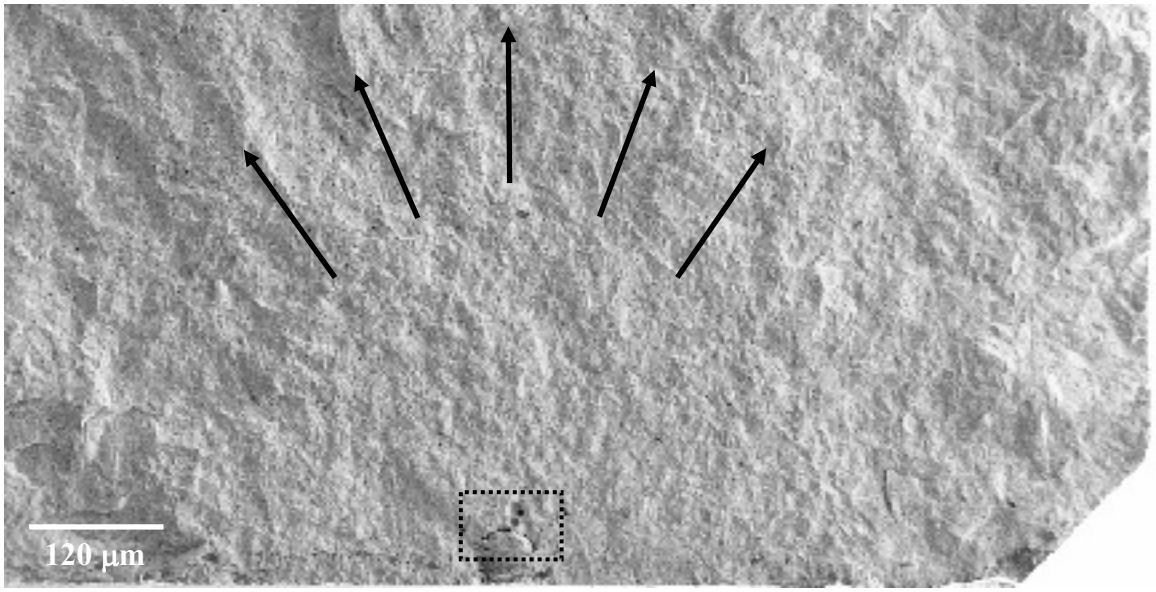


**Figure 5.28** Bar F. Low to medium strength flexure bar ($\sigma_f$ = 365 MPa). Arrows in the image indicate the likely fracture path. 200x magnification

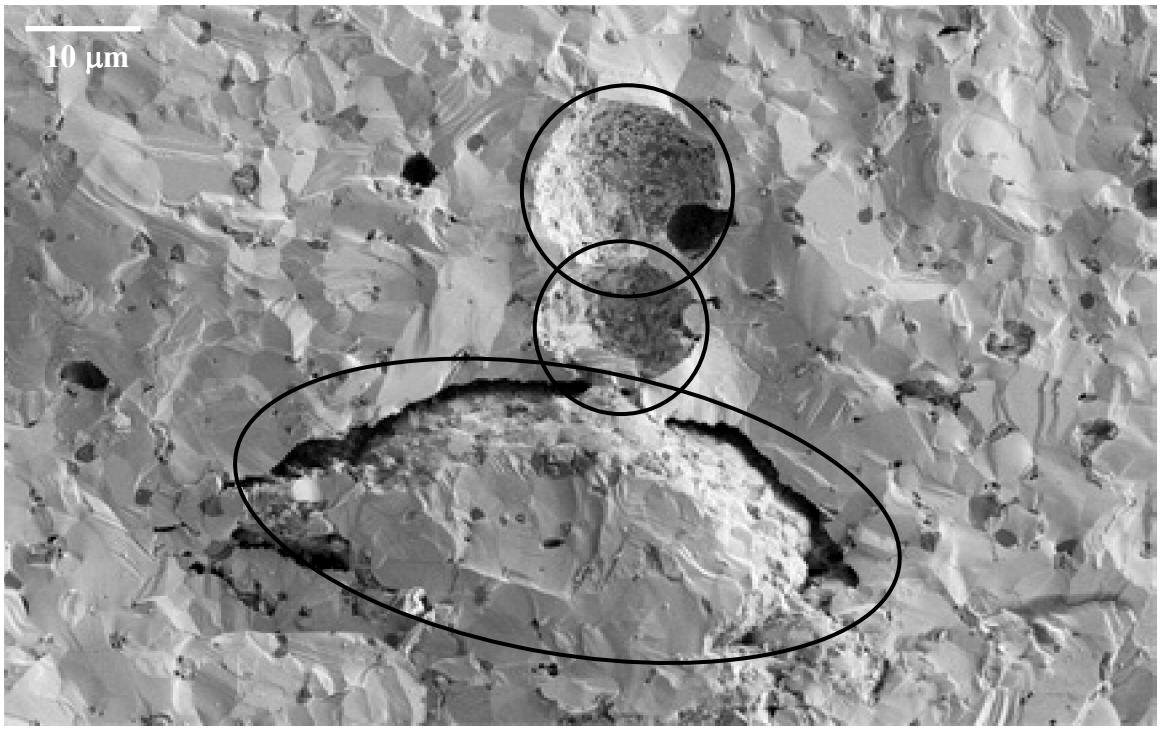


**Figure 5.29** Bar F. Low to medium strength flexure bar ($\sigma_f$ = 365 MPa). Fracture appears to have initiated at a granulated compaction relic. 2750x magnification

A higher magnification image approximately corresponding to the rectangular region in the above image is shown in Figure 5.29. Three distinct circular features have been outlined in the image. All three of these features are believed to be the relics of spray-dried granules. The largest of these is believed to be the fracture initiating feature for this flexure sample.

The forming of ceramic tiles involves the compaction of granulated powders into a cohesive form referred to as a green body. The intent of the compaction process is to produce the greatest degree of particle packing with a minimum of porosity in the green body.[184] Excessive void spaces, or porosity, can extend sintering times or even prevent densification from occurring. For bodies with simple geometries, such as a tile, the most common forming method is dry pressing, which involves the compaction, or consolidation, of a powder within a die cavity between two punches.[184] This is a rapid process which can be automated, with throughput capabilities of anywhere from 1 to 15 parts per minute.[185]

Granulation refers to the process of intentionally agglomerating fine particles into larger clusters. Individual particles are held together within the agglomerate through the use of a binder, which acts as a bridge between particles. There are beneficial properties attributed to larger clusters as it relates to dry pressing. Larger clusters flow better to fill the die, and also have a uniform bulk density.[186] These lead to more consistent pressing and a more homogeneous green body, with a minimum of density gradients. One of the intents is to enable isotropic sintering, with a minimum of shrinkage, which can result in cracking of the fired part.[185]

The most widely employed method for granulating ceramic powders is the process of spray drying. Spray drying is used to rapidly produce spherical, homogenous ceramic granules.[186] This is based upon the phenomenon of atomization, which involves forcing a fluid through a small orifice under pressure. The ceramic powder is mixed with an organic binder and suspended in a fluid, usually water, to form a slurry. The slurry is pumped through a nozzle, forming droplets. Due to surface tension, these droplets form spherical shapes which are then dried by heated airflow.[186] The result of this operation is the formation of agglomerates of individual precursor powder particles which are held together by binder.

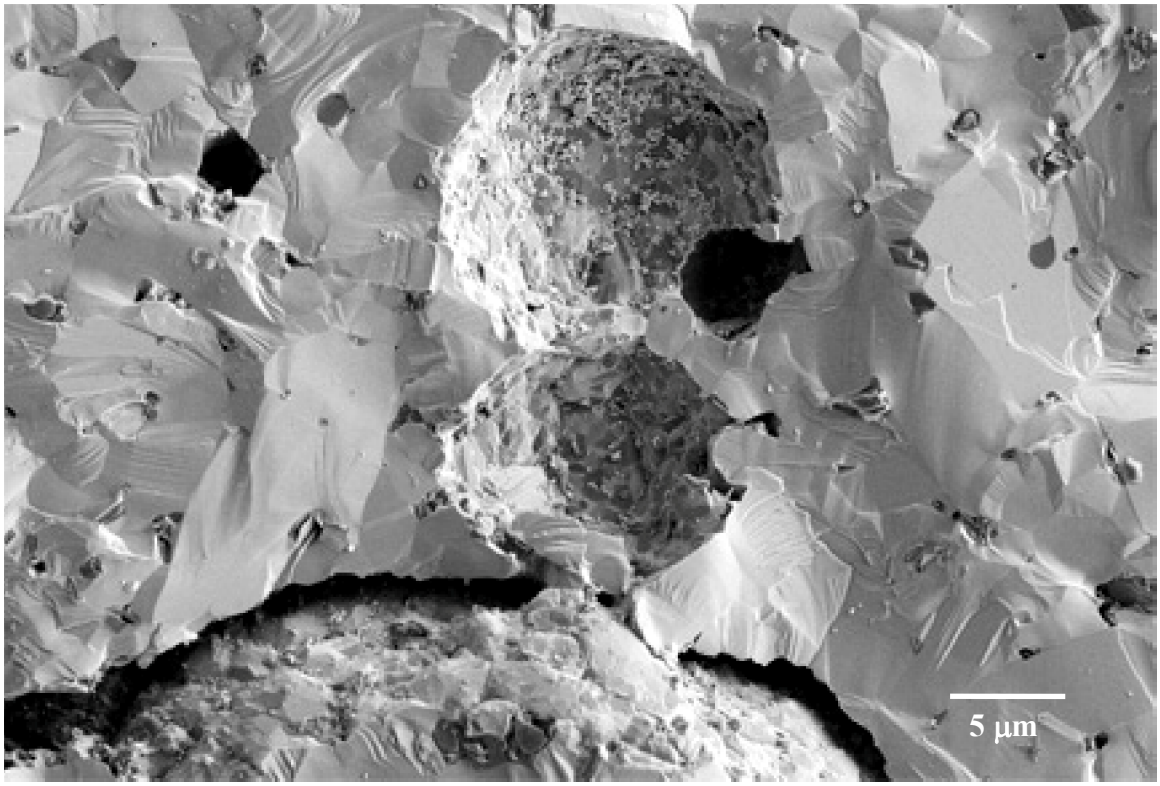


**Figure 5.30** Bar F. Low to medium strength flexure bar ($\sigma_f$ = 365 MPa). Circular features are believed to be remnants of spray dried granules. 5000x magnification

Evidence that these features are spray-dried granules is shown in Figure 5.30. This is a higher magnification image of the three circular features. Based upon the visible portion of the large bottom feature, it is apparent that it is spherical in nature. It appears to be comprised of many smaller, faceted particles. The surface texture of the feature matches the relief pattern in the circular features near the center of the image. Further analysis of features similar to these will be provided in Section 5.2.2.6.

#### 5.1.3.11 Porous Sintering Aid Inclusions

Composite FESEM images of the primary fracture surface of a low strength bar are shown in Figure 5.31. This bar, designated Bar G, fractured at an applied stress of 378 MPa. Classified as a Type C fracture, the fracture surface is characterized by significant horizontal and vertical crack branching. Fracture appears to have originated in the lower right region of the top image.

The appearance of the left and right sides of the primary fracture surface are very different. The fracture pattern of this bar revealed the formation of a double cantilever curl. A high degree of secondary fractures occurred on the side opposite the critical feature. The flat fracture plane in the area of the critical fracture is not reflected in the lower image. The fragment corresponding to this area has broken away from the residual bar on this side of the primary fracture location.

An image of the fracture plane immediately surrounding what is believed to be the strength-limiting feature is shown in Figure 5.32. The arrows in the image indicate the likely fracture path which radiated from the likely initiation location.

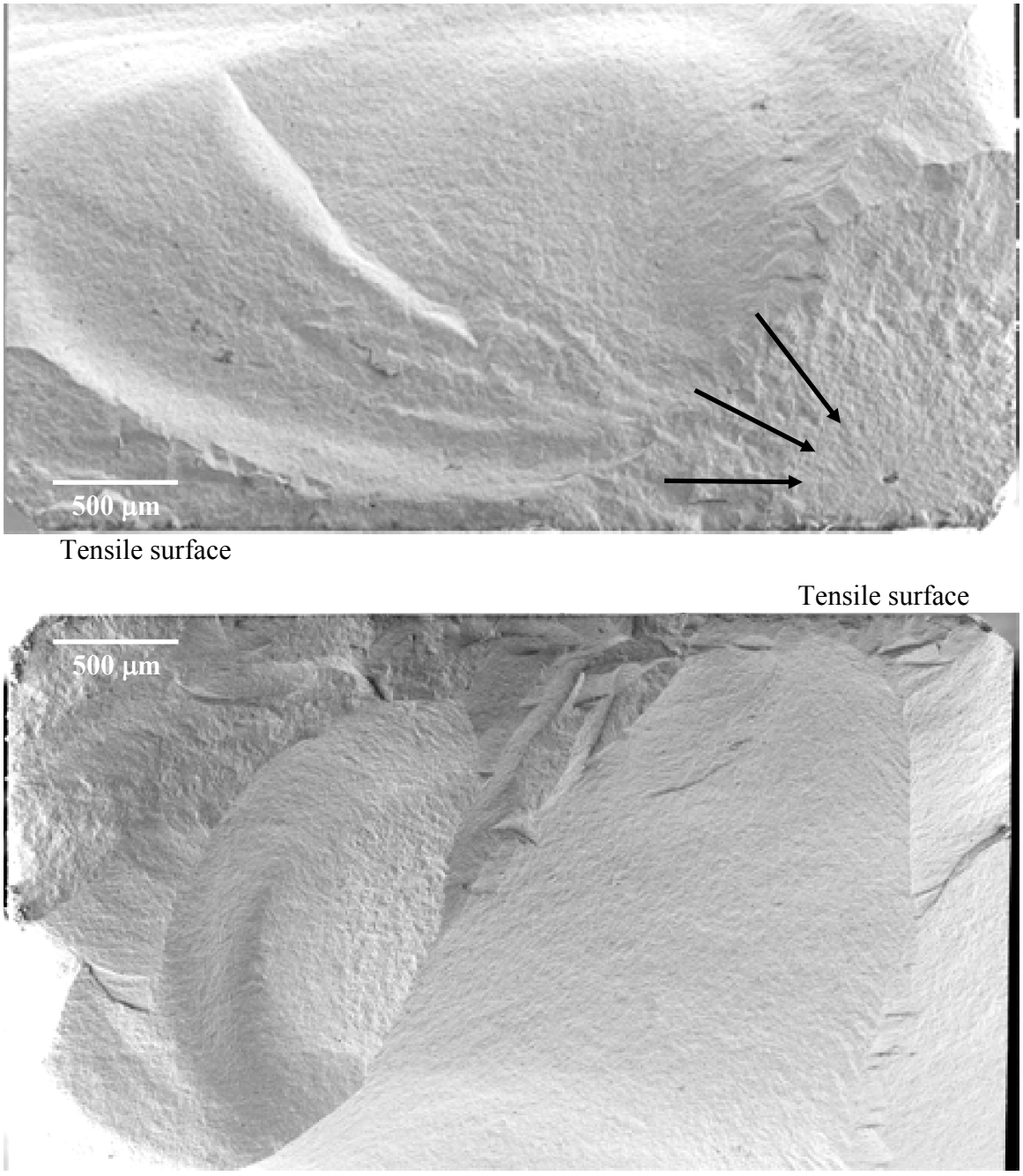


**Figure 5.31** Bar G. Primary fracture surface, left and right faces, of a low to medium strength bend bar ($\sigma_f$ = 378 MPa). Fracture appears to have initiated in the lower right region of the top image. Composite images. 200x magnification

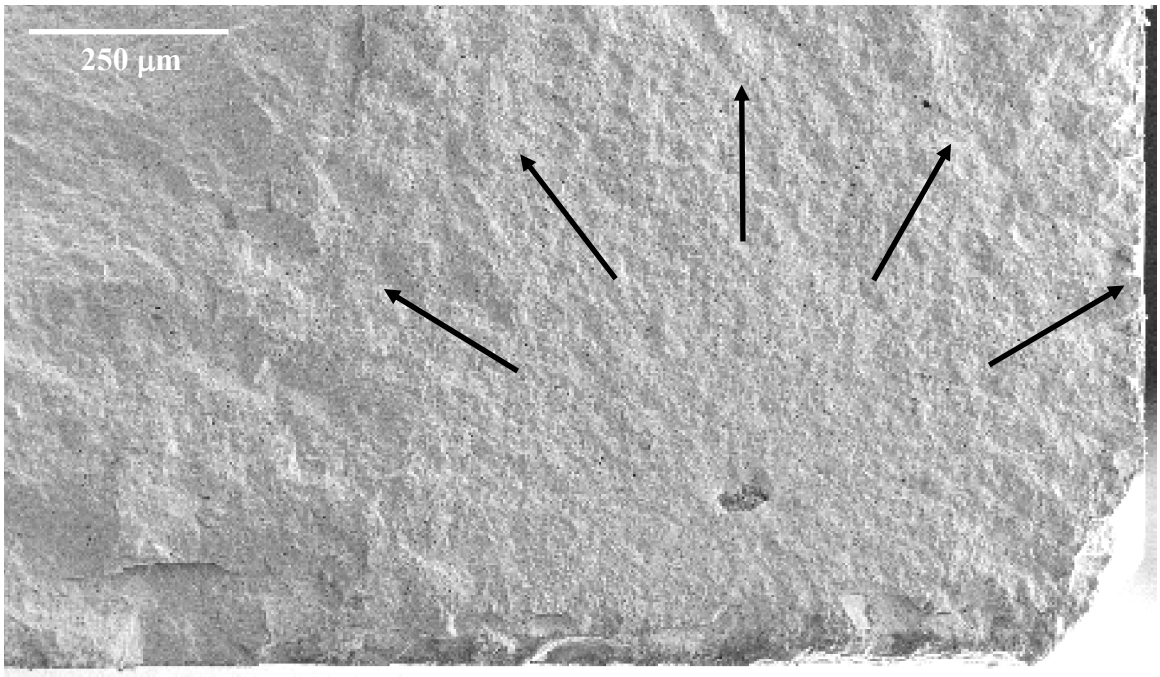


**Figure 5.32** Bar G. Low to medium strength flexure bar ($\sigma_f$ = 378 MPa). Arrows in the image indicate the likely fracture path. 200x magnification

A higher magnification, composite image of this feature is shown in Figure 5.33. This feature appears to be a porous, polycrystalline inclusion. EDS analysis of this inclusion, shown in Figure 5.34, indicated that this feature is comprised of boron carbide. The X-ray $K_{\alpha 1}$ emission energies for B and C are 0.185 eV and 0.282 eV, respectively. This explains the overlap in the shape of the peaks. Separation of these peaks required an increased processing time to be applied to the analysis of the detected X-ray energies. This feature is most likely an agglomerate of sintering aid.

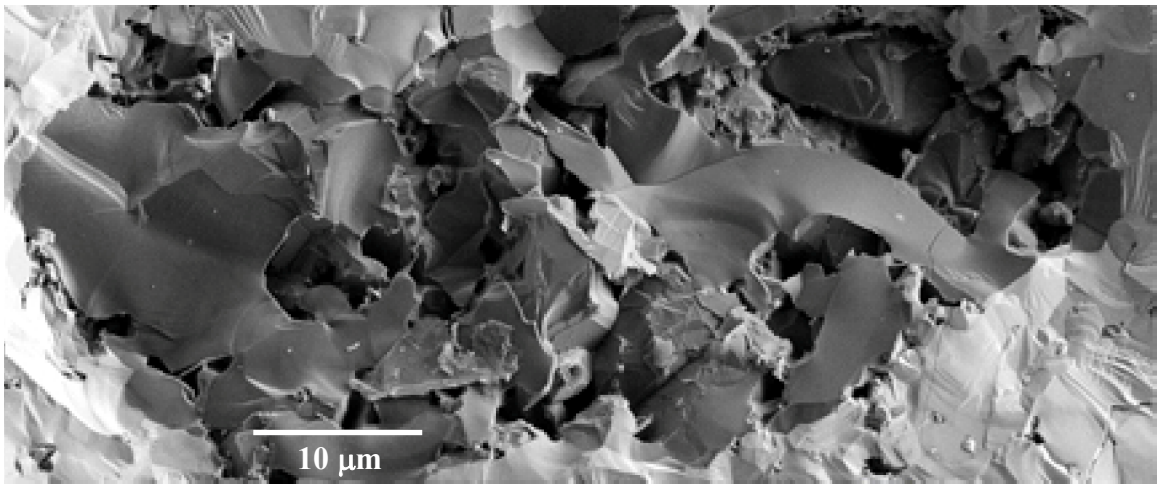


**Figure 5.33** Bar G. Low to medium strength flexure bar ($\sigma_f$ = 378 MPa). Porous boron carbide inclusion. Composite image. 7150x magnification

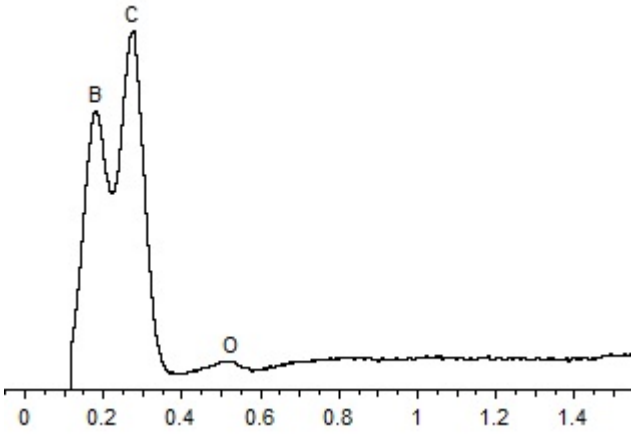


**Figure 5.34** EDS spectrum which shows peaks corresponding to the presence of boron, carbon, and oxygen. The X-axis scale is in units of electron-volts (eV)

As has been stated previously, densification of silicon carbide requires the addition of sintering additives. The method in which these are added has an effect on the final properties of the sintered piece. The presence of sufficient quantity of sintering aids is required for densification to occur.

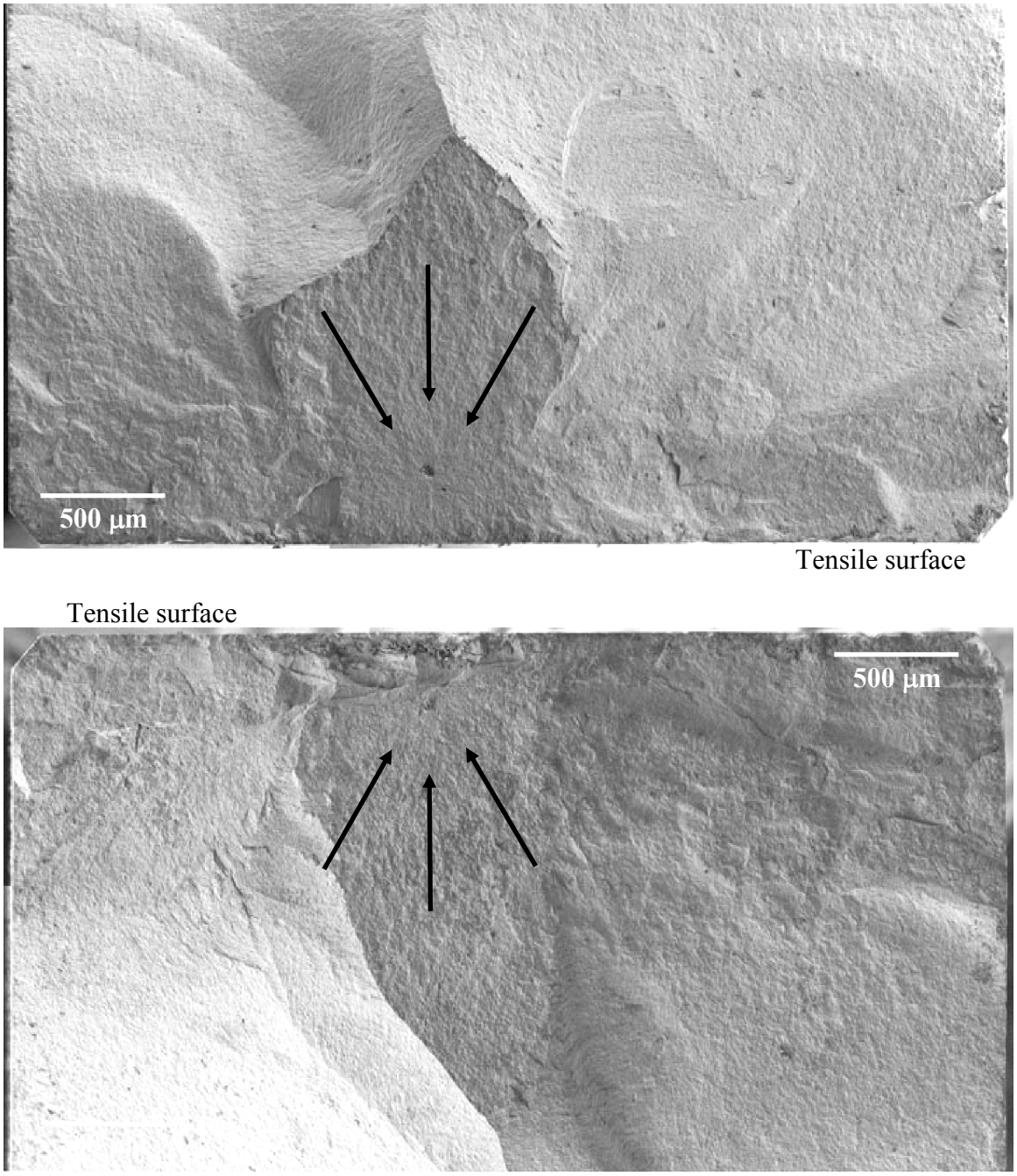


**Figure 5.35** Bar H. Primary fracture surface, left and right faces, of a low to medium strength flexure bar ($\sigma_f$ = 383 MPa). Fracture appears to have initiated near the center of the bar. Composite images. 200x magnification

Agglomerates are masses of particles which are bonded together by attractive surface forces.[187] They are formed by collisions between particles during mixing.

Particles become bonded due to van der Waals forces when in close proximity to each other.[187] During drying, bridges are formed by capillary bridging of residual liquid. Interparticle necks then form during the initial stages of sintering.

The attractive force of submicron particles is very high, as the surface force per unit weight is inversely proportional to the particle size.[187] The loose bonding within the agglomerate leads to the formation of large void spaces. Agglomerates which are not broken up during mixing become part of the compacted green body. During sintering, shrinkage of individual particles leads to an increase in interparticle void space. This leads to the formation of the large, porous agglomerates examined in this section.

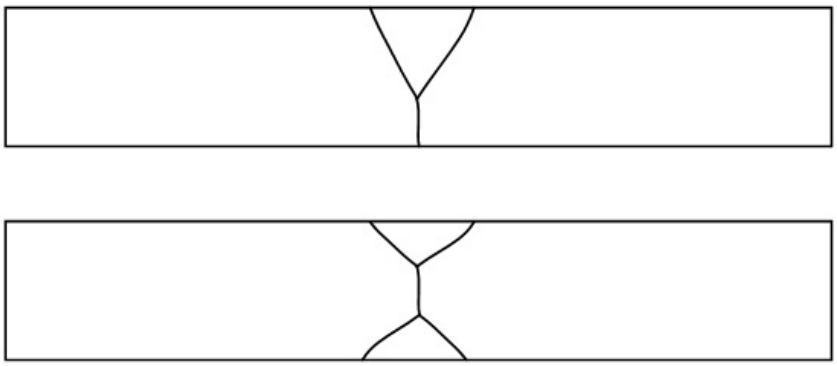

**Figure 5.36** Two examples of crack branching across the tensile surface of a medium strength flexure bar. In the lower example, fracture initiated near the center of the bar, with crack branches to either side of this location

Composite images of the primary fracture surface of another low strength bar ($\sigma_f$ = 383 MPa) are shown in Figure 5.35. In contrast to Bars F and G, evidence of the likely fracture initiating feature was found on either side of the primary fracture position. The fracture pattern of the bar differed in comparison to the previous example. While this was still considered to be a Type C fracture, as with Bars F and G, it can be seen that fracture initiated near the center of the width of the bar. Horizontal crack branching then

occurred on either side of the fracture initiation location. This is in contrast to the two previous examples, where the fracture location was biased to one side of the bar, and only one horizontal crack branch was present. Examples of the two fracture patterns are shown in Figure 5.36. This was found to be a function of the initiation location, and not the fracture strength.

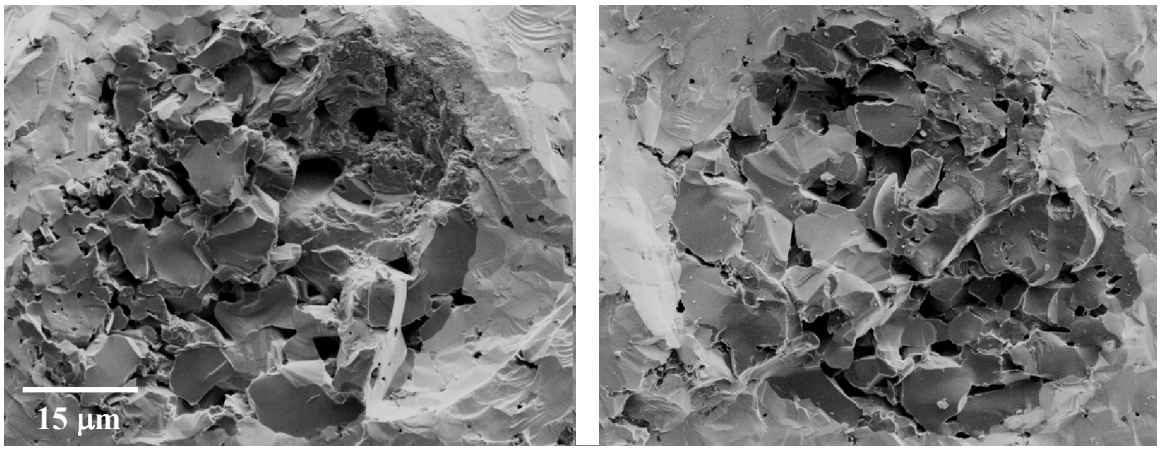


**Figure 5.37** Bar H. Low to medium strength flexure bar ($\sigma_f$ = 383 MPa). Porous boron carbide inclusion. Critical feature appears on both sides of the primary fracture surface. 3500x magnification

Images of what is believed to be the critical feature of this flexure bar are shown in Figure 5.37. The image on the left corresponds to the upper image in Figure 5.32. This feature is also believed to be a porous boron carbide inclusion. It appears that this feature was split during fracture, with secondary fractures occurring, as the features of the inclusion within the two images do not match up.

Besides the composition, the inclusions examined in Figures 5.33 and 5.37 share other similar properties. It can be seen in these images that these inclusions are comprised of multiple grains, and are porous in nature. These inclusions were most likely agglomerates of sintering aid which were present within the original green body.

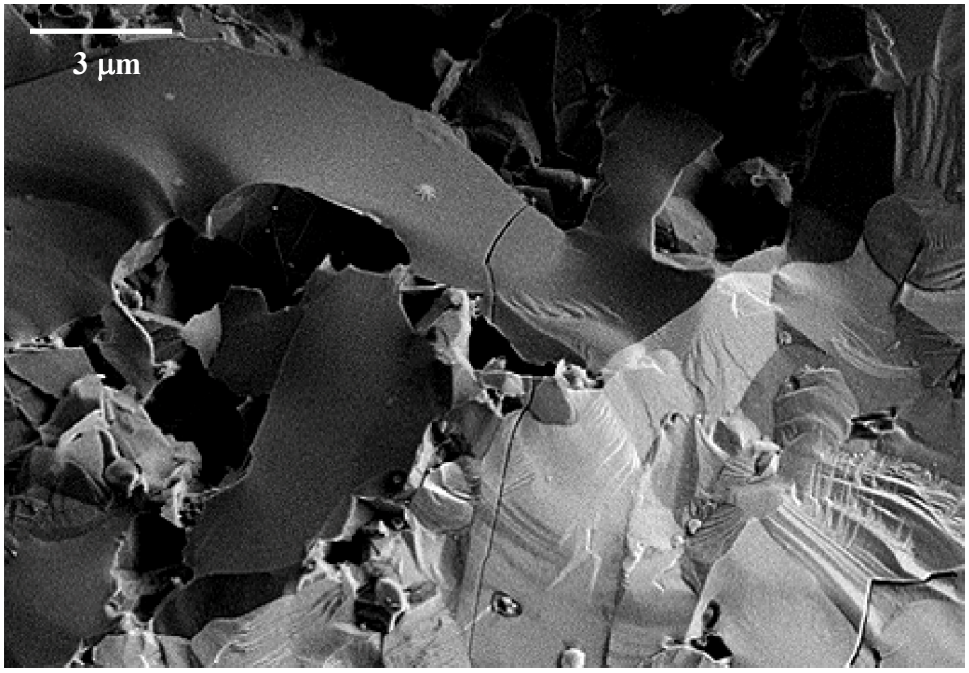


**Figure 5.38** Multi-grained, porous boron carbide inclusion. Grains on the periphery of the inclusion appear to be very well bonded to the silicon carbide matrix. 7150x magnification

An image of a section of one of these inclusions is shown in Figure 5.38. This is the inclusion from Bar G. The multi-grained, porous nature of these types of inclusions is evident in the image. Pores were present within the original agglomerate that were so large that they were not eliminated during densification. Those grains which are located around the periphery of the inclusion appear to be very well bonded to the SiC structure. This is shown in the image by the cracking which occurred within the SiC matrix, or through grains in the inclusion, but not at the boundary between the two. These inclusions become stress intensifiers in a quasi-static strength test due to their porous nature. While the Young's modulus of sintered boron carbide is equal to or greater than that of sintered silicon carbide, the effective modulus of these boron carbide inclusions is much lower due to the amount of voids present.[22] Further discussion of these types of inclusions will be found in Section 5.2.3.6.

### 5.1.3.12 Strength Testing Statistics/Weibull Analysis

As has been stated previously, initial analysis of the strength data resulted in Weibull plots which exhibited bi-modal distribution behavior. This refers to the presence of more than one distinct slope within the data in the plot. An example of strength data which exhibits a bi-modal Weibull distribution is shown in Figure 5.39.

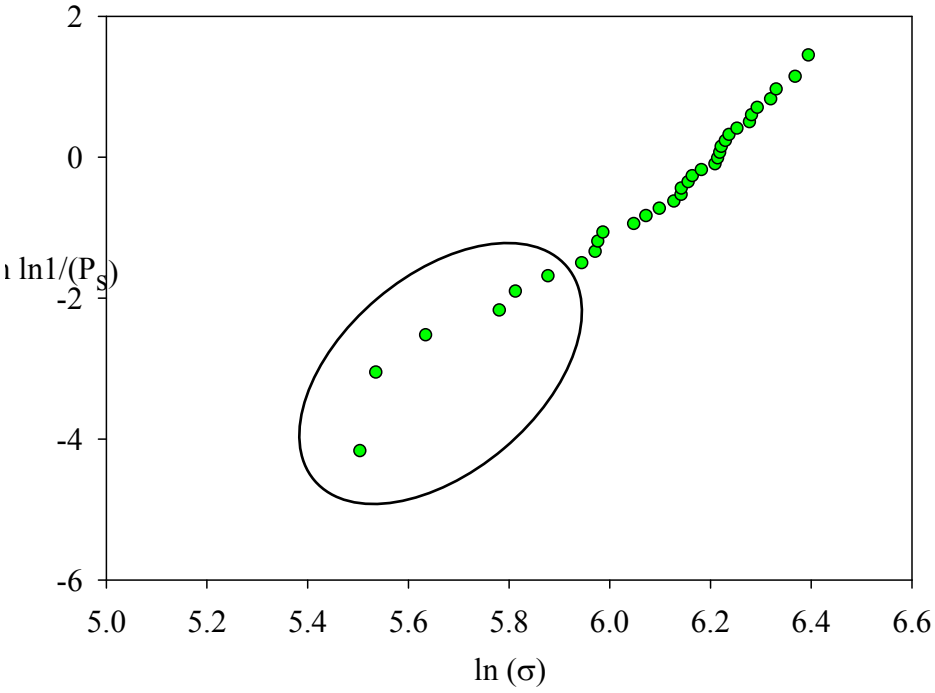


**Figure 5.39** Weibull distribution of strength values from commercial SiC tile which shows bi-modal behavior

The presence of low strength bars within the results, termed outliers, contributes to the bi-modal distribution. Strength-limiting features within sintered silicon carbide may be grouped into two categories: extrinsic and intrinsic features. As stated previously, intrinsic strength limiting features are those which are present in the starting tile. Extrinsic features which have an effect on strength are the result of damage which is induced during handling and/or machining. With the exception of a study which seeks to

examine the effect of surface finish on mechanical strength, strength values which result from extrinsic features such as machining damage should be removed from strength statistics as they do not represent the design of the actual material. This is what is referred to as segregated strength results.[72]

Segregated Weibull plots for the six groups of flexure bars from the original Hexoloy® tiles are shown in Figures 5.40 through 5.45. Data points which correspond to flexure bars from the top layer are shown in black, fracture strengths corresponding to the middle layer are shown in red, and strength values of bars from the bottom layer are shown in green. Linear fit regression lines have been added to the plots. The slope of these regression lines is considered to be the Weibull modulus (*m*), which describes the spread within the data. The average strengths for each layer of bars, along with the associated Weibull moduli, are shown in Tables 5.17 through 5.19.

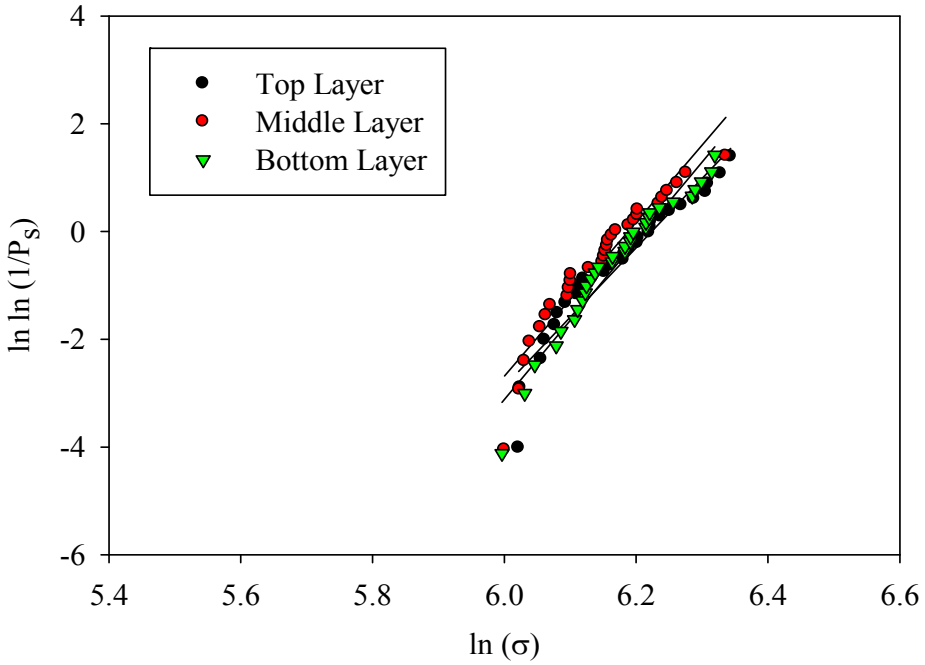


**Figure 5.40** Weibull plot. Tile 8. Group 1. Top layer: black, Middle layer: red, Bottom layer: green

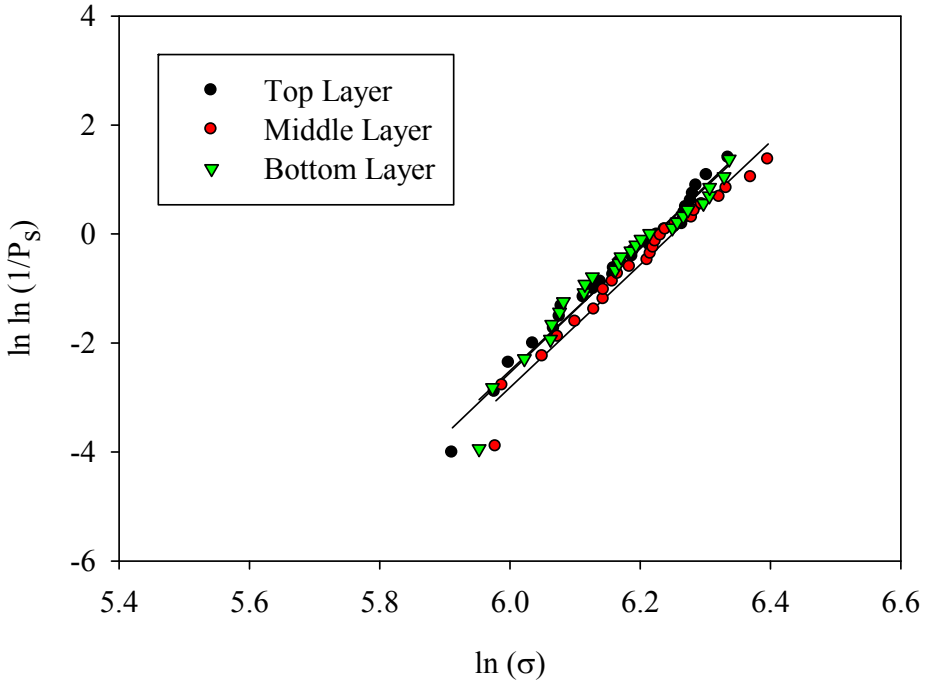


**Figure 5.41** Weibull plot. Tile 11. Group 2. Top layer: black, Middle layer: red, Bottom layer: green

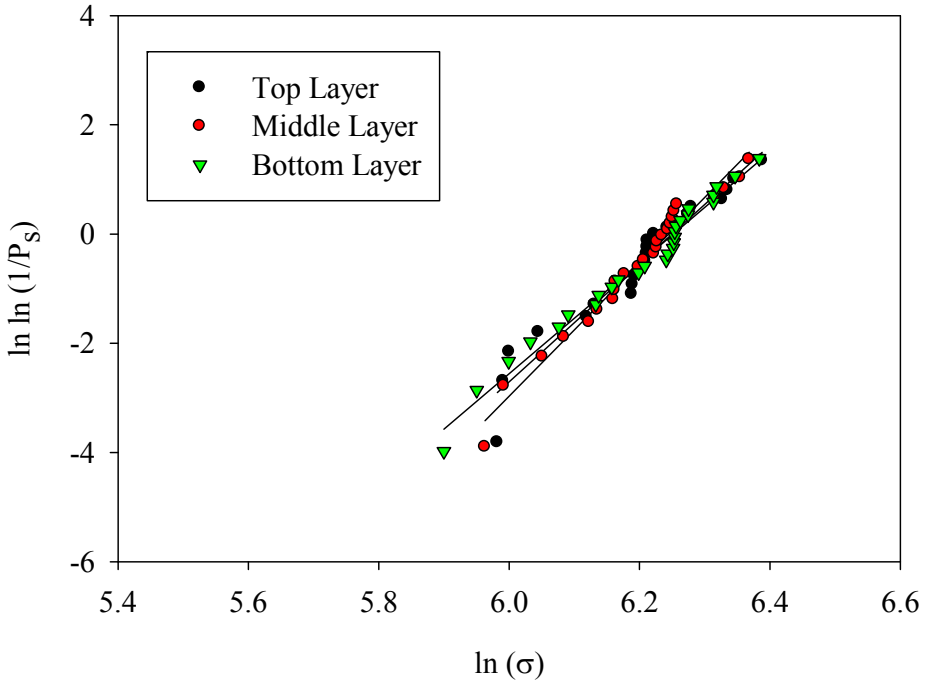


**Figure 5.42** Weibull plot. Tile 4. Group 3. Top layer: black, Middle layer: red, Bottom layer: green

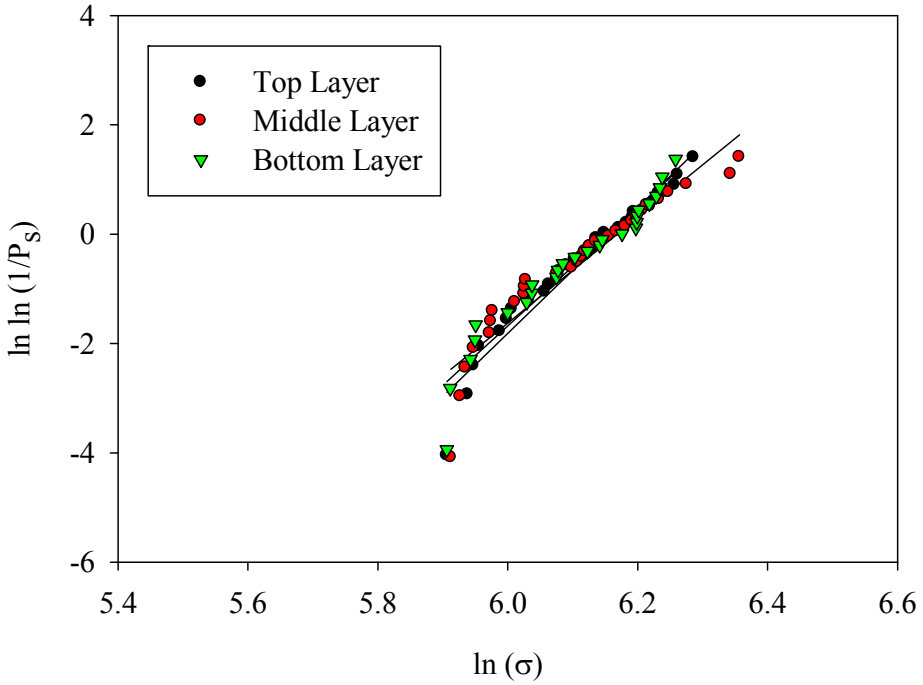


**Figure 5.43** Weibull plot. Tile 31. Group 4. Top layer: black, Middle layer: red, Bottom layer: green

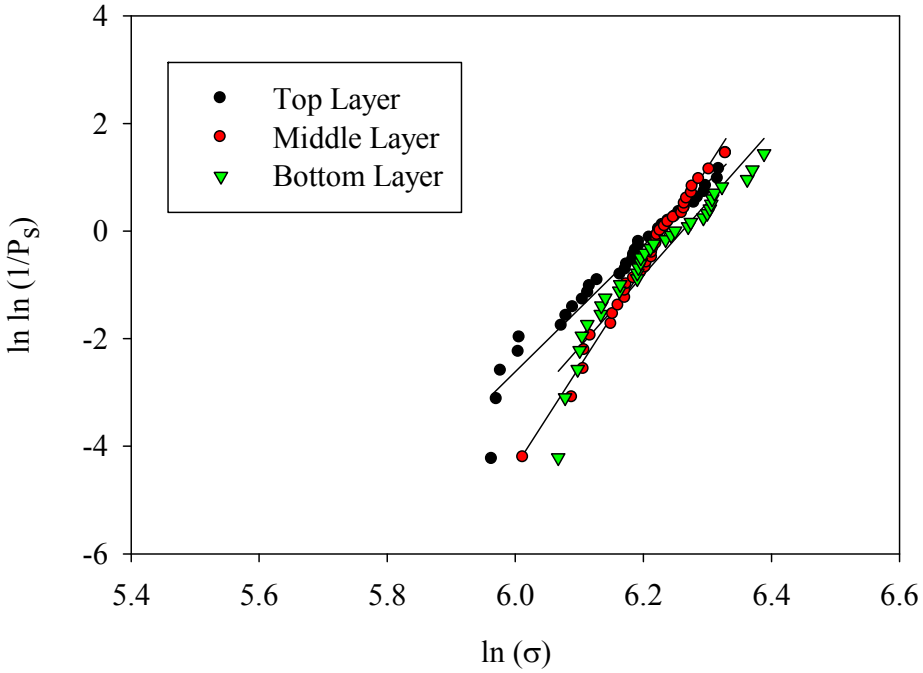


**Figure 5.44** Weibull plot. Tile 2. Group 5. Top layer: black, Middle layer: red, Bottom layer: green

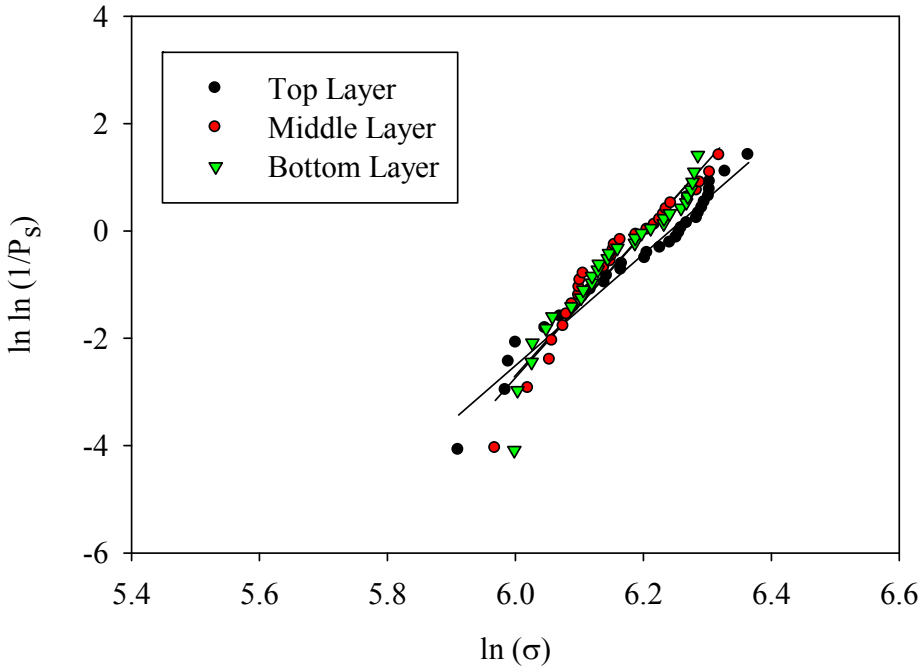


**Figure 5.45** Weibull plot. Tile 19. Group 6. Top layer: black, Middle layer: red, Bottom layer: green

Initial fractography work focused on the lowest strength bars, which were found to have resulted from the presence of transverse scratches, or scratches which were perpendicular to the applied stress, on the tensile and side surfaces of the bars. Strength values attributed to these types of scratches ranged from 150 to 350 MPa. The range of strengths within this category where based upon varying scratch widths and depths. These scratches were categorized as anomalous, as the directions and width of the scratches were not consistent with the type of machining that would be present in a longitudinally ground flexure bar.

A second type of extrinsic feature which contributed to the bi-modal distributions where longitudinal machining scratches, where the induced damage was parallel to the

long axis of the bar, and the direction of the applied stress. Fractures which initiated from these types of features occurred over a range from 275 to 365 MPa.

This category of scratches was divided into two groups based upon the width of the scratches. The lowest strength bars were found to have broken at “large” longitudinal machining scratches. This covered a range from 275 to 320 MPa. As with the previous category, these scratches were believed to have been anomalous as, based upon the measured size, these scratches should have been removed in subsequent machining steps.

In total, almost fourteen percent of the bars in this study fractured due to one of these three types of damage. In addition, three bars were found to have had a “step” machined into the side of the bar, which resulted in a non-uniform stress distribution within the bar during the test.

The final sub-category of machining scratches ranged in strength from 320 to 365 MPa. These scratches where much narrower than those in the previous category, and where considered to be more representative of what would be expected for a longitudinally ground flexure bar, as the direction of the scratches was parallel to the long axis of the bar, and the sizes corresponded to the grit size of the final stage of machining.

Features which were intrinsic to the original SiC tiles which were found to cause below average fracture strengths include green pressing relics and porous boron carbide inclusions. Strength values attributed to these features ranged from 365 to 390 MPa. In the bars attributed to pressing relics, evidence of spray-dried SiC balls which did not fully sinter, or densify, were found. The porous boron carbide inclusions are believed to be agglomerates of sintering aids, which were of a large enough size and reduced effective modulus to act as stress concentrators during quasi-static loading.

**Table 5.17** Average strength and Weibull moduli for each layer of flexure bars from commercial SiC tiles. Tile 8 and Tile 11

| Layer | avg (MPa) | *m* |
|---|---|---|
| | | |
| Top | 485 | 12.9 |
| Middle | 469 | 14.3 |
| Bottom | 481 | 14.6 |

| Layer | avg (MPa) | *m* |
|---|---|---|
| | | |
| Top | 482 | 11.4 |
| Middle | 495 | 11.3 |
| Bottom | 482 | 11.2 |

**Table 5.18** Average strength and Weibull moduli for each layer of flexure bars from commercial SiC tiles. Tile 4 and Tile 31

| Layer | avg (MPa) | *m* |
|---|---|---|
| | | |
| Top | 495 | 10.8 |
| Middle | 494 | 12.2 |
| Bottom | 494 | 10.2 |

| Layer | avg (MPa) | *m* |
|---|---|---|
| | | |
| Top | 452 | 11.5 |
| Middle | 454 | 9.7 |
| Bottom | 450 | 10.9 |

**Table 5.19** Average strength and Weibull moduli for each layer of flexure bars from commercial SiC tiles. Tile 2 and Tile 19

| Layer | avg (MPa) | *m* |
|---|---|---|
| | | |
| Top | 483 | 11.7 |
| Middle | 497 | 18.5 |
| Bottom | 504 | 13.5 |

| Layer | avg (MPa) | *m* |
|---|---|---|
| | | |
| Top | 490 | 10.4 |
| Middle | 476 | 13.4 |
| Bottom | 475 | 13.3 |

The presentation of segregated Weibull statistics necessitated the removal of strength values from the analysis which were attributed to extrinsic features. For the concentration of this dissertation, these amounted to transverse tensile and side surface

scratches, as well as "large" and "small" longitudinal tensile machining scratches. In total, fractures of 108 of the 624 tested flexure bars were attributed to one of these four types of features. As is to be expected, removal of these strength values had a profound effect on the strength statistics. The average strength increased for all groups of bars, and the tighter distribution of values resulted in an increase in the resultant Weibull moduli.

Examination of the Weibull plots showed that there were still strength results which would be considered to be outliers. In terms of this analysis, a "low strength bar" was considered to be a bar which fractured at less than 390 MPA, which corresponded to the upper bound of strength attributed to the identified intrinsic features. The lower bound for strength values which appear in the Weibull plots was 365 MPa. The classification of a strength value as an outlier was dependent upon the average strength for the bars from each tile. Examination of the data from Tiles 31 and 2 provided clarification of this point. The Weibull plot for Tile 2 appeared to have many more low strength outliers when compared to the Tile 31 plot. This was due to the higher average strength attributed to the bars from Tile 2. The lowest strength value from the Tile 2 data, 408 MPa, was in fact higher than the 20 lowest strength bars from Tile 31.

It can also be seen that many of the Weibull plots contain clusters of data points. Assigning regression lines to these clusters would show that the slopes are different. The different slopes and spread within these clusters are most likely attributed to different flaw types of various sizes. Possible flaw types attributed to higher strength fractures could include clusters of pores or exaggerated anisotropic grains.[182] As it related to this dissertation, the decision was made to focus on features which contributed to the low strength bars, as these would correspond to the largest, most visible flaws, along with the

belief that large anomalous features would affect the ultrasound results to the greatest degree.

The average strengths for all of the bars from each tile, as well as the resultant Weibull moduli, are shown in Table 5.20. It can be seen that a linear correlation between average strength and Weibull modulus does not exist. A group of bars which have a high average strength may contain a number of low strength bars, increasing the spread within the data and decreasing the Weibull modulus.

**Table 5.20** Average strength and Weibull moduli for six commercial SiC tiles

| Tile | avg (MPa) | *m* |
|---|---|---|
| | | |
| 4 | 496 | 11.5 |
| 2 | 494 | 14.0 |
| 11 | 487 | 11.5 |
| 19 | 482 | 12.6 |
| 8 | 479 | 14.0 |
| 31 | 465 | 10.9 |

In comparison to the total number of flexure bars tested, very few strength values were attributed to the intrinsic features examined in previous sections. These results adhere to the weakest link theory which underlies the failure of ceramic bodies. What has occurred with the flexure testing was to divide each tile up into cells, or small areas of volume. As these intrinsic features would have been represented in a small number of cells, the majority of the bars would have had a high strength. However, consideration of the individual elements together under the premise that failure of one element would have

resulted in failure of the entire piece, each group of elements would have had a greatly reduced virtual strength.

#### 5.1.3.13 Correlation of Strength Values and Ultrasound Results

One of the goals of this research was to determine if a detectable correlation exists between ultrasonically measured acoustic properties and quasi-static strength results. This was determined two ways: qualitatively and quantitatively.

#### 5.1.3.14 Qualitative Analysis/Fracture Position Diagrams

The primary fracture located for each tested bend bar was used in the analysis of the correlation between the presence of an acoustic anomaly in the ultrasound maps and fracture location. In this analysis, a scale diagram of the bend bar machining diagram was overlaid on top of the ultrasound map of the starting tile for each group of flexure bars. The locations of the primary fracture position for each valid test sample were indicated on the diagrams as hash marks. Fracture positions corresponding to the top layer are indicated in black, positions from the middle layer are shown in white, while positions from the bottom layer are shown in red. The primary loading region of the 4-pt bend test is also indicated in the diagram by a black rectangle. The assembled fracture overlay diagrams for the groups of bend bars from the six commercial tiles are shown in Figures 5.46 through 5.51. In these maps, red regions are “high” value regions, while blue regions are scaled as “low” value regions. It should be noted that some of the bend bar positions contain less than three hash marks. The hash marks were removed for those

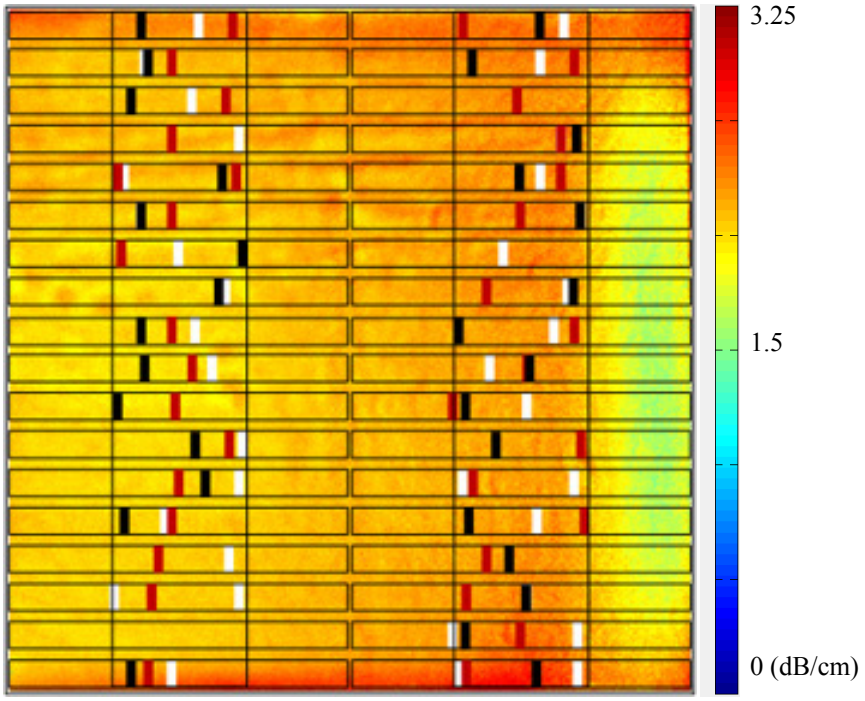


**Figure 5.46** Fracture Position Overlay Diagram. Tile 8. Group 1. 20MHz Attenuation Coefficient map. Fracture positions of bend bars depicted on ultrasound map. Top layer: black; Middle layer: white; Bottom layer: red

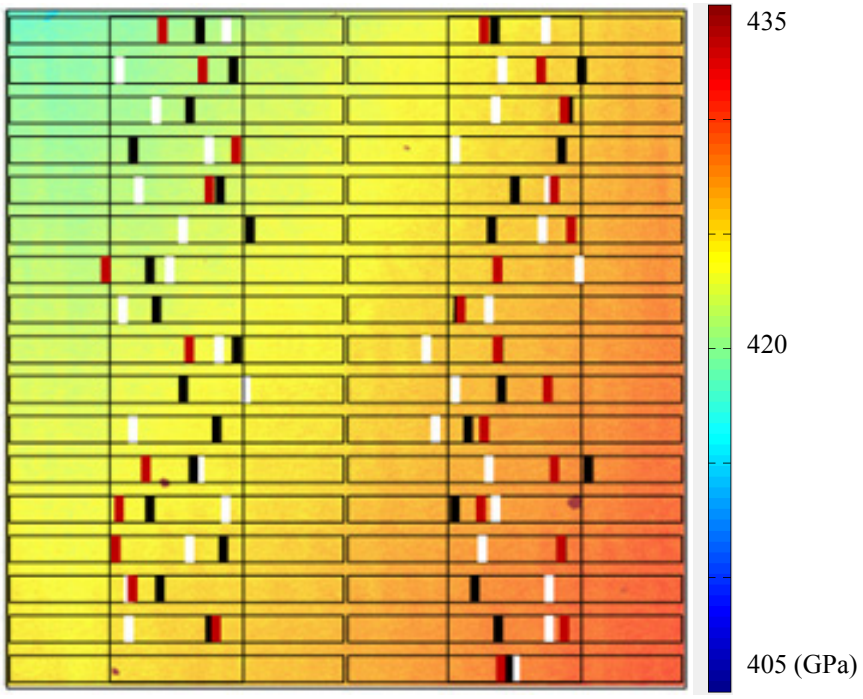


**Figure 5.47** Fracture Position Overlay Diagram. Tile 11. Group 2. Young's Modulus map. Fracture positions of bend bars depicted on ultrasound map. Top layer: black; Middle layer: white; Bottom layer: red

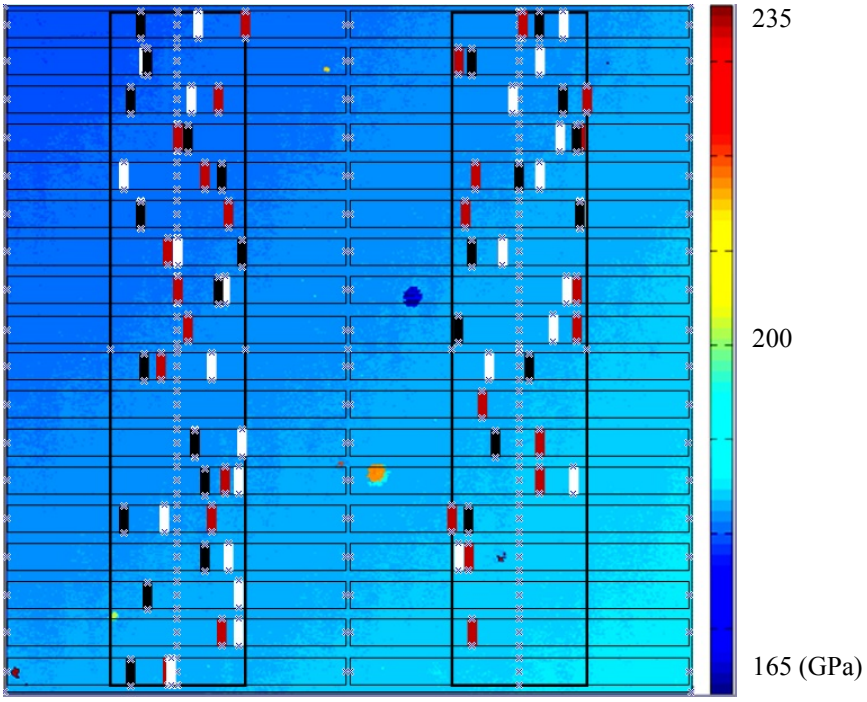


**Figure 5.48** Fracture Position Overlay Diagram. Tile 4. Group 3. Shear Modulus map. Fracture positions of bend bars depicted on ultrasound map. Top layer: black; Middle layer: white; Bottom layer: red

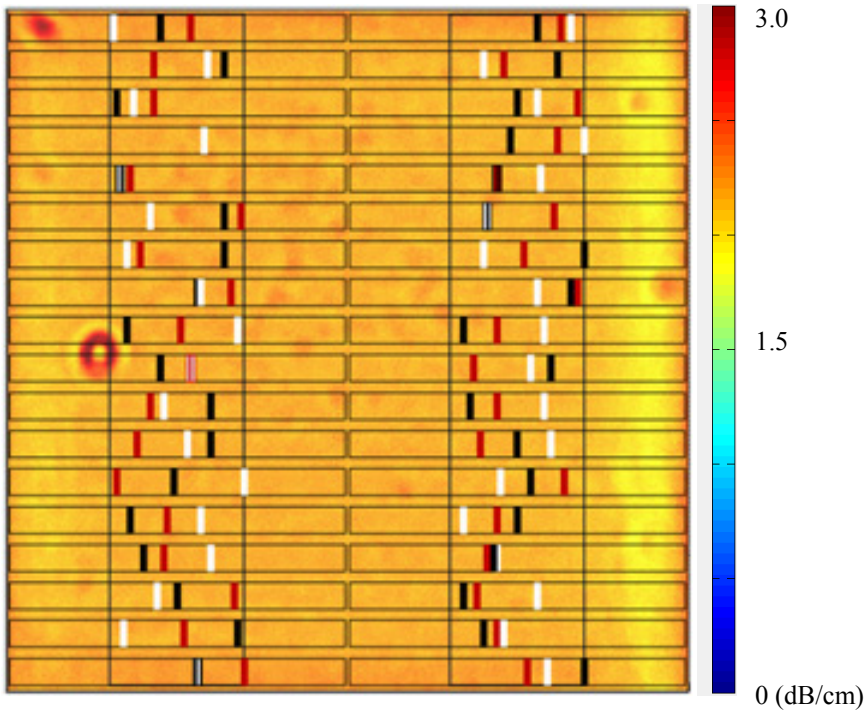


**Figure 5.49** Fracture Position Overlay Diagram. Tile 31. Group 4. 20 MHz Attenuation Coefficient map. Fracture positions of bend bars depicted on ultrasound map. Top layer: black; Middle layer: white; Bottom layer: red

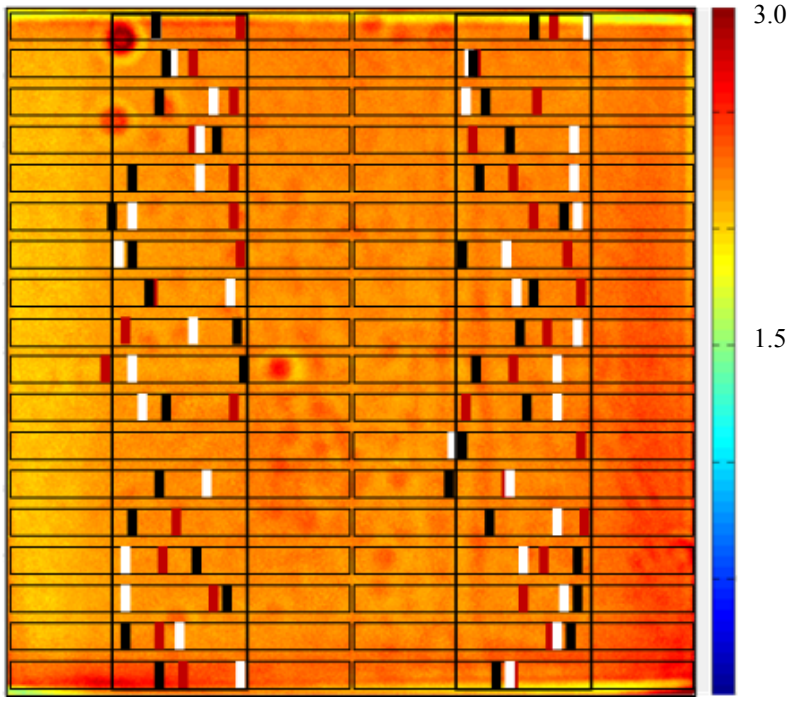


**Figure 5.50** Fracture Position Overlay Diagram. Tile 2. Group 5. 20 MHz Attenuation Coefficient map. Fracture positions of bend bars depicted on ultrasound map. Top layer: black; Middle layer: white; Bottom layer: red

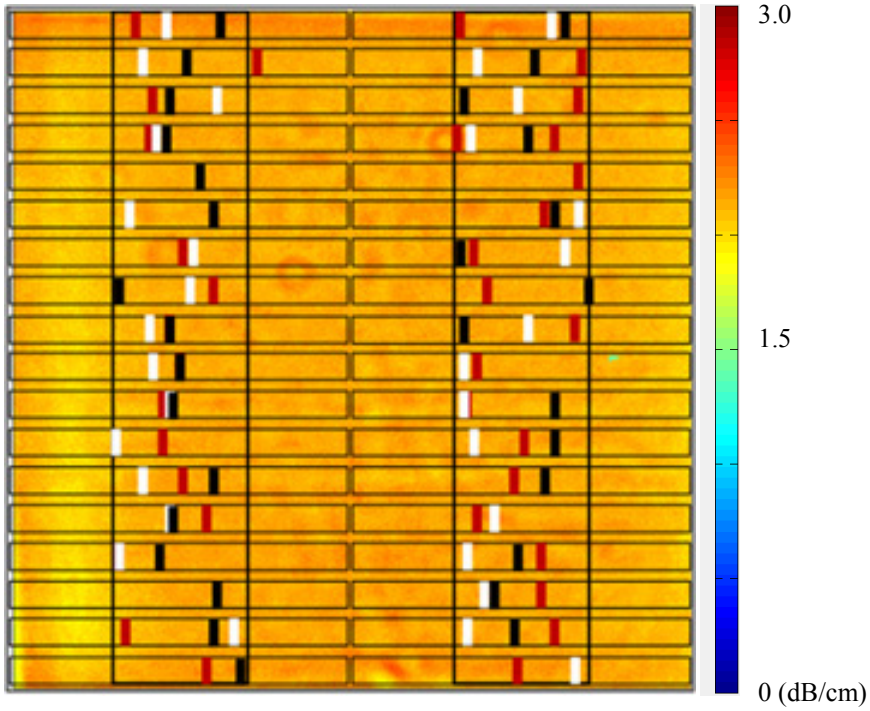


**Figure 5.51** Fracture Position Overlay Diagram. Tile 19. Group 6. 20 MHz Attenuation Coefficient map. Fracture positions of bend bars depicted on ultrasound map. Top layer: black; Middle layer: white; Bottom layer: red

fracture locations which corresponded to flexure bars where fracture is believed to have originated due to extrinsic features.

Upon examination of the fracture positions for each group of bars, there does not appear to be a pattern within the primary fracture locations. In Figure 5.46, there is a region of reduced attenuation coefficient along the right side of the tile. This region did not appear to have an effect on fracture location, as it was located outside of the primary loading zone of the flexure test. In Figure 5.47, the values of Young's modulus increase when moving from the upper-left region to the lower-right region of the map. The gradient in values did not appear to have an influence on fracture position. In Figure 5.48, it can be seen that although the ultrasound tests have resulted in a consistent shear modulus map, there appears to be no discernible pattern to the location of primary fracture for this group of bend bars. Figures 5.49, 5.50, and 5.51 all contain fracture location diagrams overlaid over 20 MHz attenuation coefficient maps. Overall, it is challenging to make a definitive statement about the correlation between the position of the primary fracture location and features found within the NDE maps. Figure 5.49 does contain a prominent acoustic anomaly, but it appears to be located just outside the primary loading zone of the flexure test. Figure 5.50 contains acoustic anomalies which are located within the loading region of the test, but fracture positions do not correspond to these locations.

One of the possible explanations for this outcome is the phenomenon of acoustic resonance. As discussed, acoustic resonance is the harmonic coupling of oscillations in the presence of a driving force. The propagation of acoustic energy within a material may cause the resonance of a small feature of correct size and sonic velocity. The

acoustic waves given off by the resonating feature may then be detected by the transducer during the receiving portion of each cycle. It is now believed that this is the cause of the acoustic anomalies seen in the ultrasound maps.[116]

A second explanation takes into account the statistical likelihood of encountering a strength-limiting feature within the high stress zone of a sample during a flexure test. As was discussed in Section 2.3.4.1, during a tensile test, stress is applied to the entire volume of a circular or rectangular sample. The strength-limiting feature which results in the failure of the sample may be found anywhere in this volume.

As shown in Figure 2.11, the application of stress to a 4-pt flexure sample undergoing quasi-static loading is not constant. The degree of stress is dependent upon the spatial location within the length and height of the bar. The maximum tensile stress occurs along the bottom surface of the bar between the locations of the upper loading pins. It then reduces to zero at the location of the bottom support pins. This represents a small proportion of the volume of the bar. Therefore, the probability of encountering an inclusion within the volume of the bar under the maximum stress is low.

During ultrasound scanning, the measured signal at any scanning position represents the sum of the contributions from interaction with features throughout the entire depth of the sample, within the area encompassed by the beam diameter. The beam diameter is dependent upon the frequency of the ultrasound energy as well as the propagation material. For the sintered silicon carbide samples examined, the beam diameter was approximately 4mm.[122] Three layers of bars were machined from the commercial tiles. In order to predict the strength of these flexure bars, the contribution of

a strength-limiting feature inclusion located near the surface of a bar would have needed to be discerned in the scans.

#### 5.1.3.15 Quantitative Analysis/Acoustic Attenuation Plots

As a means to examine the relationship between the ultrasound and strength testing results, scatter plots of 20 MHz attenuation coefficient and 4-pt flexure strength were assembled. The strength data for each layer of bars machined from a tile was handled separately. The linear best fit line and the correlation coefficient for this line was calculated for each group of flexure bars.

The attenuation coefficient values corresponding to the area around each primary fracture position were tabulated using the Rutgers Hermes software. The software package allows the average value of an acoustically generated acoustic property over a specified X,Y space to be calculated. For each bend bar position, the average value of the attenuation coefficient was calculated over an area ranging from one millimeter to the right and left of each primary fracture location. This corresponded to an area of approximately 8 $mm^2$.

In this analysis, both the strength values and ultrasound results were segregated. MOR values and fracture positions which corresponded to extrinsic, strength-limiting features were not included. When examining the attenuation coefficient data, it was found that the two upper and lower bend bar positions may have exhibited a substantial increase in attenuation coefficient compared to the bulk of the tile. This is believed to have resulted from the diffraction at the edges of the sample. The increased attenuation at these positions resulted from a greater proportion of the ultrasound beam being

directed away from the transducer, and therefore not being detected. This condition can be exacerbated when the top and bottom surfaces of the tile are not exactly parallel to one another, which helps explain why this effect was more noticeable in the results for some of the tiles and not for others. Attenuation coefficient values which corresponded to these locations where also removed from the analysis.[188] Where the increase was found to be greater than 5% of the average bulk value, these data points were excluded.

Scatter plots comparing the 20 MHz attenuation coefficient and flexure strength results for the bars from the six commercial tiles are shown in Figure 5.52 through 5.57. In these plots, black data points indicate fracture positions in the top layer, red data points correspond to the middle layer, and green data points indicate the bottom layer. Linear best fit lines for each group of bars have been determined, along with the coefficients of determination. For this analysis, it was decided to compare all six tiles based upon the respective attenuation coefficient data associated with each tile. This was done even though two of the group headings were originally based upon elastic property values.

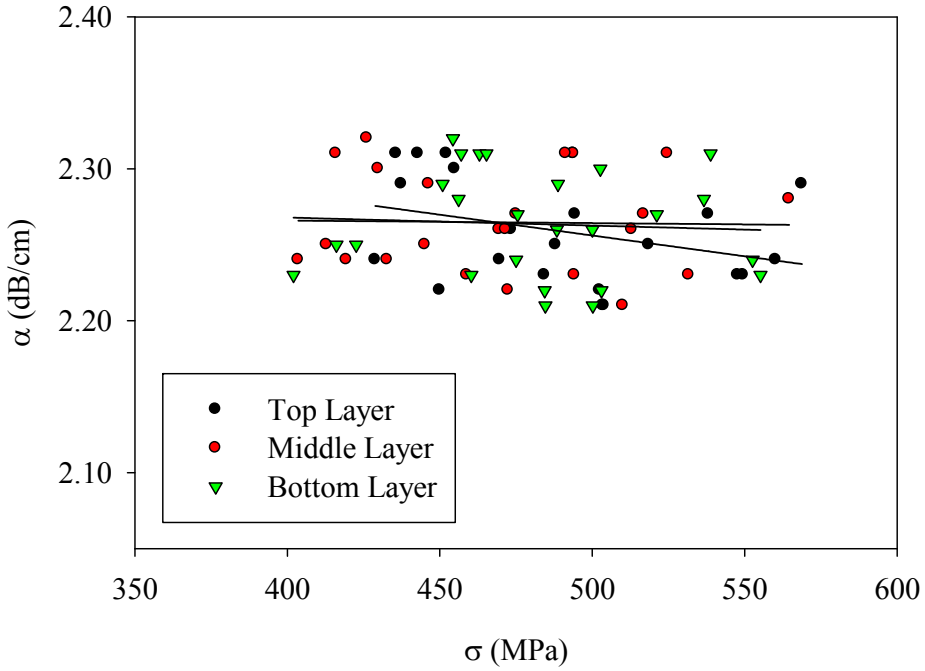


**Figure 5.52** Comparison of 20 MHz Attenuation Coefficient and 4-pt flexure strength results. Tile 8. Group 1

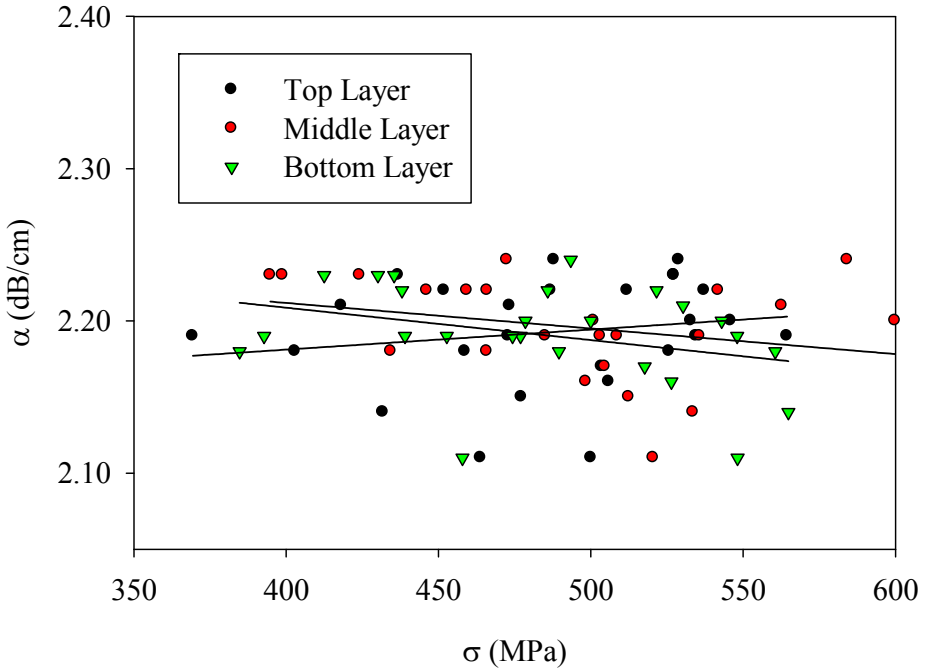


**Figure 5.53** Comparison of 20 MHz Attenuation Coefficient and 4-pt flexure strength results. Tile 11. Group 2

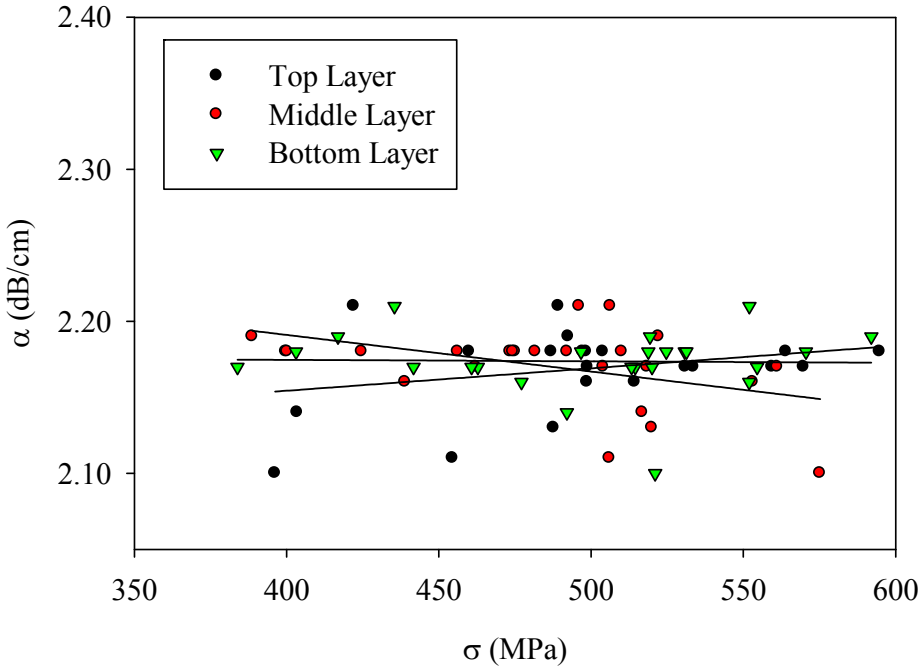


**Figure 5.54** Comparison of 20 MHz Attenuation Coefficient and 4-pt flexure strength results. Tile 4. Group 3

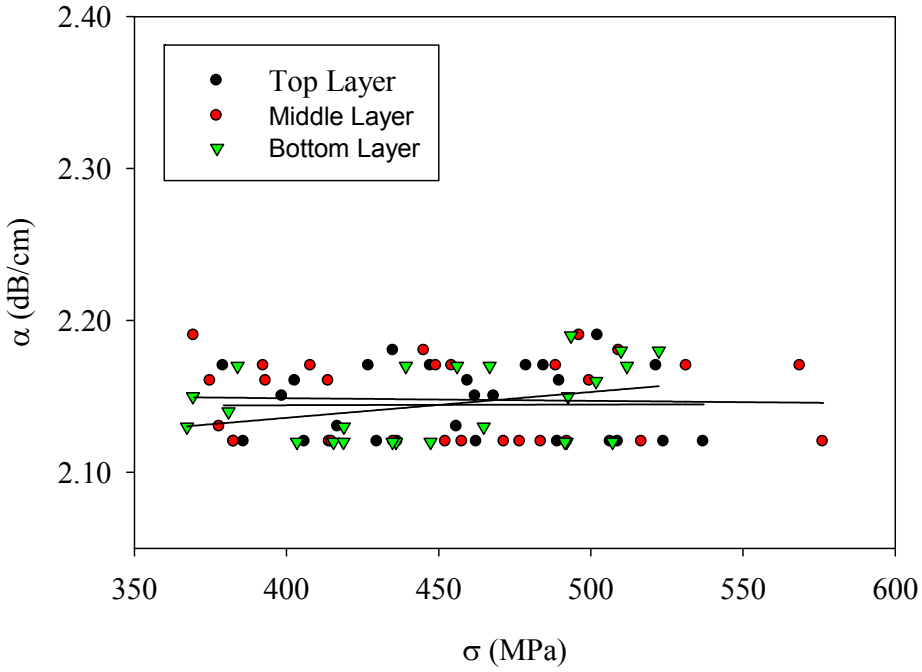


**Figure 5.55** Comparison of 20 MHz Attenuation Coefficient and 4-pt flexure strength results. Tile 31. Group 4

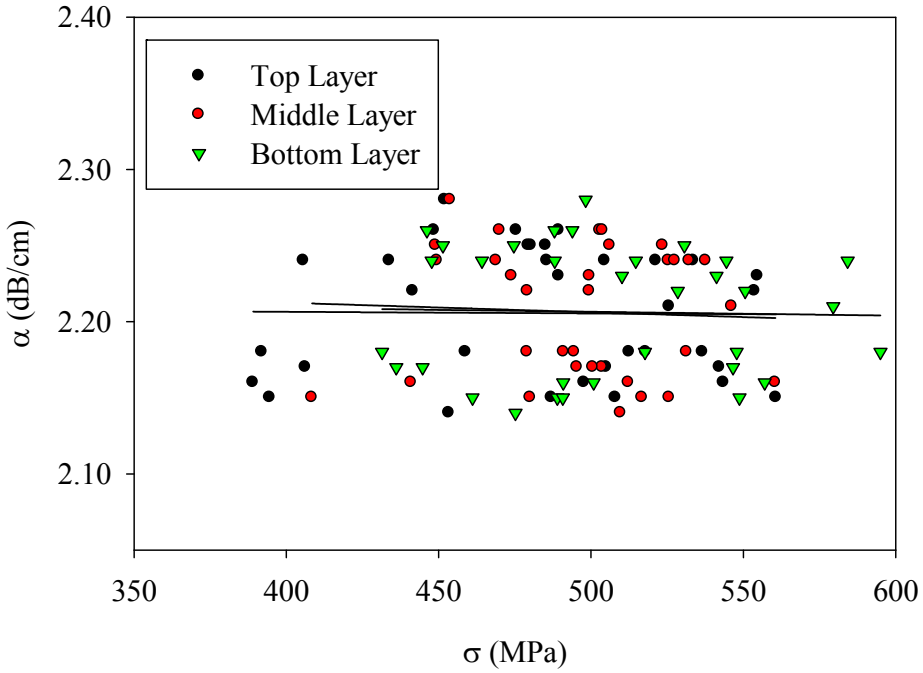


**Figure 5.56** Comparison of 20 MHz Attenuation Coefficient and 4-pt flexure strength results. Tile 2. Group 5

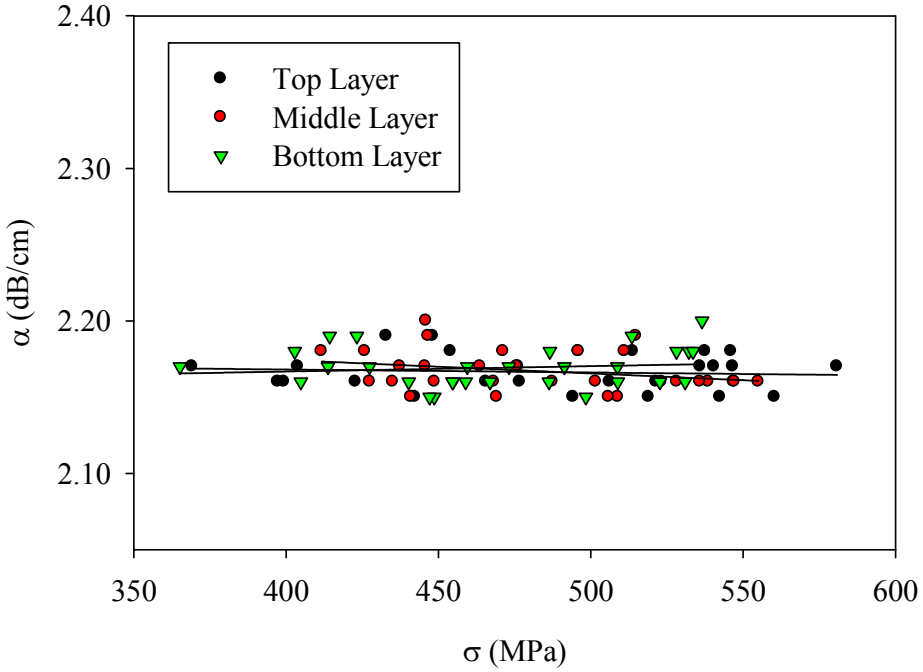


**Figure 5.57** Comparison of 20MHz Attenuation Coefficient and 4-pt flexure strength results. Tile 19. Group 6

**Table 5.21** Coefficients of determination and linear fit line slopes of 20 MHz attenuation coefficient/strength testing scatter plots

| | | Tile 8 | Tile 11 | Tile 4 | Tile 31 | Tile 2 | Tile 19 |
|---|---|---|---|---|---|---|---|
| | | | | | | | |
| Top Layer | $b_1$ | -3.00E-04 | 1.00E-04 | 1.00E-04 | 4.00E-06 | -1.00E-05 | -2.00E-05 |
| | $R^2$ | 1.11E-01 | 3.10E-02 | 8.89E-02 | 7.00E-05 | 1.00E-04 | 8.80E-03 |
| Middle Layer | $b_1$ | -2.00E-05 | -2.00E-04 | -2.00E-04 | -2.00E-05 | -6.00E-05 | -9.00E-05 |
| | $R^2$ | 5.00E-04 | 7.19E-02 | 1.76E-01 | 1.40E-03 | 2.40E-03 | 7.32E-02 |
| Bottom Layer | $b_1$ | -5.00E-05 | -2.00E-04 | -1.00E-05 | 2.00E-04 | -3.00E-05 | 4.00E-05 |
| | $R^2$ | 3.60E-03 | 1.07E-01 | 6.00E-04 | 1.11E-01 | 7.00E-04 | 1.61E-02 |

From the scatter plots, it is challenging to make the determination that a linear relationship is present between the attenuation coefficient and strength data. The linear fit lines appear to have either very moderate slopes, or no slope at all. This is confirmed by the values shown in Table 5.21. This table contains the fit line slopes and coefficients of determination for the different groups of bars in the analysis.

The slopes of the lines range from a minimum $-3.00 \times 10^{-4}$ to a maximum of $2.00 \times 10^{-4}$. The smaller the slope, either positive or negative, the closer each fit line is to a flat line, with a lack of a linear relationship. The $R^2$ values range from a maximum of $7.00 \times 10^{-5}$ to a minimum of $1.76 \times 10^{-1}$. A value closer to one is indicative of the "*goodness*" of the linear fit.

It can be seen from these results that a linear relationship does not exist between the 20 MHz attenuation coefficient data and the 4-pt flexure test results. One of the conclusions that can be drawn from this is that the microstructural features which have an effect on the strength results are not the same features that affect the attenuation

coefficient. Or that these features have a much greater effect on the strength results than on the ultrasound results.

**Table 5.22** Average, standard deviation, standard deviation as a percentage of the average value of strength results for original six Hexoloy® tiles

| Tile | avg (MPa) | std dev (MPa) | % of average |
|---|---|---|---|
| | | | |
| 2 | 494 | 43 | 8.7 |
| 4 | 494 | 53 | 10.7 |
| 11 | 487 | 52 | 10.7 |
| 19 | 480 | 48 | 10.0 |
| 8 | 479 | 42 | 8.8 |
| 31 | 453 | 50 | 11.0 |

A further analysis of the strength and attenuation coefficient results reveals that there is much greater variation within the strength testing results than in the ultrasonically generated acoustic property values. The average strength value and standard deviation of the original six tiles are shown in Table 5.22. The percentage of the standard deviation to the average value was calculated for the bars from each tile. Values ranged between 8.7% and 10.7%.

The same analysis was performed for the commercial tile ultrasound results. The results of this are shown in Table 5.23. For both elastic property maps, the standard deviation was less than two percent of the average value. Variation within the attenuation coefficient maps was also low. The standard deviations of this measurement ranged between 0.05 dB/cm and 0.09 dB/cm. In the time since these measurements were performed a full characterization of the ultrasound test set was carried out. It was found

that the minimum detectable variation within the attenuation coefficient measurement was 0.05 dB/cm. For three of the original six tiles, the standard deviation within the attenuation coefficient maps matched this value. For the remainder of the three tiles, the deviation within the measurement exceeded the minimal value by 0.01, 0.02, and 0.04 dB/cm.

**Table 5.23** Ultrasound data. Standard deviation of measurement as a percentage of average value

| Tile # | Type of map | unit | Average value | Std dev | Std dev as a % of average |
|---|---|---|---|---|---|
| | | | | | |
| 8 | att coeff | dB/cm | 2.31 | 0.09 | 3.9 |
| 11 | speed of sound | m/s | 12044 | 113 | 0.9 |
| 11 | att coeff | dB/cm | 2.20 | 0.06 | 2.8 |
| 4 | shear modulus | GPa | 182 | 3 | 1.6 |
| 4 | att coeff | dB/cm | 2.18 | 0.05 | 2.3 |
| 31 | att coeff | dB/cm | 2.15 | 0.05 | 2.3 |
| 2 | att coeff | dB/cm | 2.21 | 0.07 | 3.2 |
| 19 | att coeff | dB/cm | 2.17 | 0.05 | 2.3 |

## 5.2 Production and Characterization of Targeted Samples

The characterization and analysis of the commercial SiC tiles showed that the expected local scale variability in acoustic properties was not present for the tiles in the sample set. This resulted in different degrees of variation in fracture strengths and ultrasonically determined acoustic properties.

In a further exploration of this correlation, specialty silicon carbide samples, referred to as targeted samples, were produced. The intent of these samples was to emphasize specific aspects of the microstructure such that a corresponding variation in acoustic and mechanical properties would be detected.

Two avenues of production were identified. One was to produce tiles with a sintered density less than that of the commercial tiles. The second approach involved manufacturing tiles with increased boron additives content. These tiles will be referred to as the Reduced Density (RD) tiles and the Enhanced Boron Content (EBC) tiles. In choosing these approaches, the intent was to focus on intrinsic features which contributed to below average strength fractures in the commercial SiC flexure bars.

Production and the motivation for each type of tiles will be examined. Production of both sample sets will be done by using a variation of the process used to manufacture the commercial SiC tiles. The characterization scheme will be similar to what was utilized in the evaluation of the commercial tiles.

### 5.2.1 Reduced Density Tiles

#### 5.2.1.1 Production and Motivation

The first approach involved producing silicon carbide tiles with increased levels of residual porosity, and therefore reduced density. This was accomplished by compaction of the green body to a lower green density.

As was discussed in Section 5.1.3.10, the forming of ceramic bodies involves the compaction of a powder mixture into a semi-cohesive form referred to as a green body. In addition to a low liquid content and an organic binder, the green body is composed of

compacted granules.[184] Granules are considered to be loosely-bonded formations of particles that have been purposely agglomerated. When produced by the process of spray drying, the granules take the form of free-flowing spherical shaped powder.[186] As has been stated, one of the most common methods of compaction is the process of dry pressing. Spherical particles are preferred as they flow better to fill the pressing dye, and have a higher packing factor, resulting in fewer void spaces.

The most important aspect of compaction is to produce a homogeneous green body with a uniform green density.[185] For this to be accomplished, the pressure applied to the powder mixture must be high enough to break-down and deform the spray dried granules.[185] This is what is referred to as knitting, and is necessary to reduce the void spaces between the particles. Small pores, which are located at the junctions between grains, tend to shrink and disappear during sintering. Larger pores, or voids, which are located at the intersection of macro-scale features such as granules, do not shrink during sintering and will remain in the fired part as intergranular porosity.[185] This underscores the need to properly compact and deform spray dried granules during dry pressing. Evidence of improper compaction was shown in Figure 5.29 in Section 5.1.3.10. The three features which are indicated in the image all show a spherical shape, indicating that sufficient deformation did not occur.

The production procedures of both sets of targeted samples were based upon a variation of that used to manufacture the commercial samples. Both sets of tiles were sintered without pressure assistance. In the instance of the Reduced Density tiles, B and C sintering aids were added in amounts of approximately 0.5% and 3.0%, respectively.[42, 50] The firing temperature of 2100° C was the same as the commercial

samples, as was the firing time. Typical pressing pressures for fine-grained technical ceramic are in the range of 200 – 300 MPa.[185, 189] The pressure applied in the instance of these samples can be considered to be lower than this range.

Three tiles were produced. Each tile was 60mm W x 60mm L x 6mm H. This represented a volume that was approximately 15% the volume of the commercial SiC tiles.

#### 5.2.1.2 Archimedes Density

Archimedes density measurements were carried out on the three Reduced Density tiles. The results of these measurements are shown in Table 5.24. The mean value was found to be 3.08 g/cm$^3$. This represents a reduction of 0.08 g/cm3, or approximately 2.5%, when compared to the commercial SiC tiles.

**Table 5.24** Archimedes density values of Reduced Density SiC tiles. Mean value: 3.08 g/cm$^3$

| Tile | 1 | 2 | 3 |
|---|---|---|---|
| | | | |
| Bulk Density (g/cm$^3$) | 3.08 | 3.09 | 3.08 |

#### 5.2.1.3 Ultrasound Evaluation

Non destructive evaluation of the Reduced Density SiC tiles was carried out by immersion-based ultrasound C-Scans utilizing an Olympus planar unfocused transducer with a central frequency of 20 MHz in pulser/receiver configuration. The average value of the attenuation coefficient for each tile is shown in Table 5.25. The mean value for the

three tiles was 3.25 dB/cm. This represented a 48% increase over the average attenuation coefficient value of the commercial SiC tiles.

**Table 5.25** Ultrasound C-Scan average values. 20 MHz attenuation coefficient. Reduced Density SiC tiles. Mean value: 3.25 dB/cm

| Tile | 1 | 2 | 3 |
|---|---|---|---|
| | | | |
| $\alpha_{(20\ MHz)}$ | 3.25 | 3.24 | 3.26 |

Assembled 20 MHz attenuation coefficient C-Scan maps are shown in Figures 5.58, 5.59, and 5.60. These maps were scaled from 0 to 6 dB/cm. All three maps have a mottled appearance, which corresponds to the standard deviation within each map, which measured approximately 0.3 dB/cm, or just under 10% of the average value.

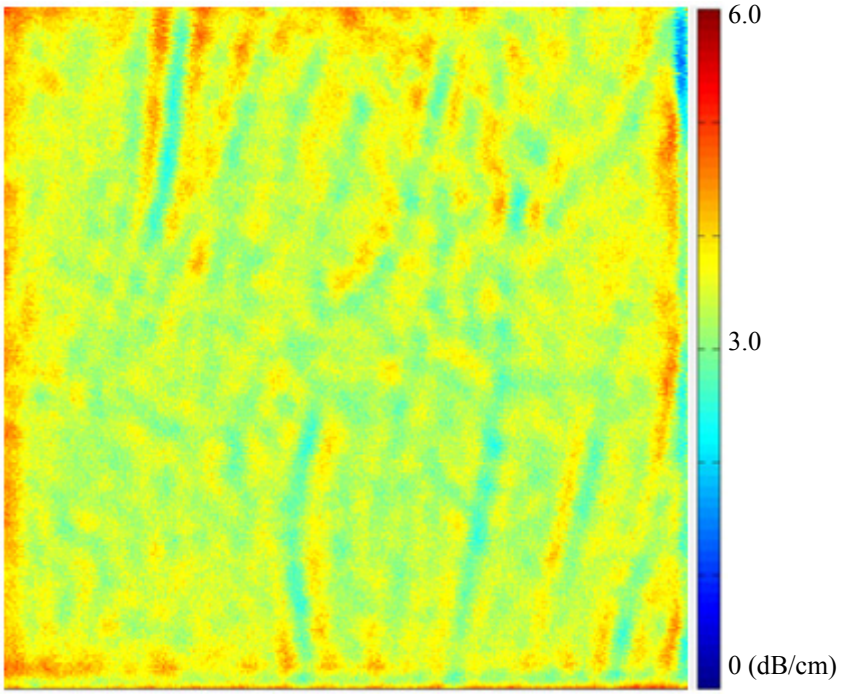


**Figure 5.58** Ultrasound C-Scan map of Reduced Density SiC tile. 20 MHz Attenuation Coefficient. Tile 1

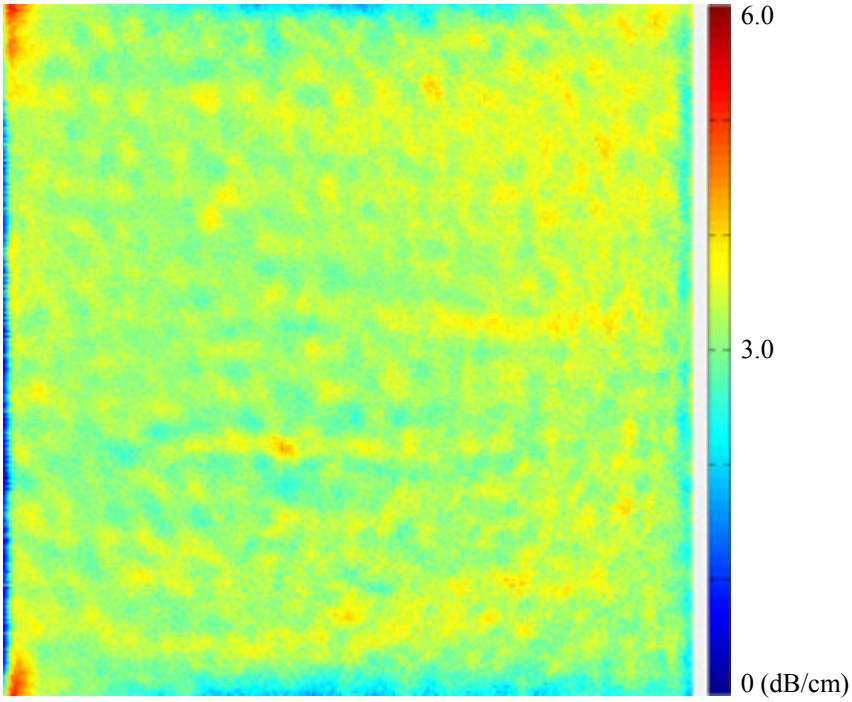


**Figure 5.59** Ultrasound C-Scan map of Reduced Density SiC tile. 20 MHz Attenuation Coefficient. Tile 2

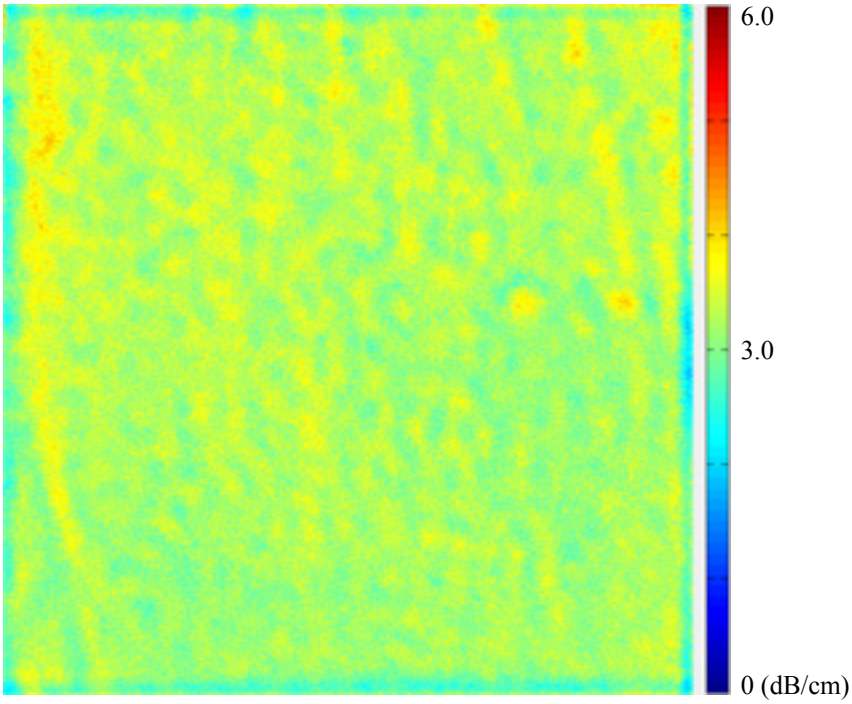


**Figure 5.60** Ultrasound C-Scan map of Reduced Density SiC tile. 20 MHz Attenuation Coefficient. Tile 3

### 5.2.1.4 Flexure Bar Machining

All three bars were chosen for machining into flexure bars. As with the commercial tiles, the ASTM B-type bar was chosen, to allow for comparisons with the previous samples. The machining configuration for these tiles is shown in Figure 5.61. The diagram depicts the actual size of the tile and flexure bars. The 4mm dimension of the bars was machined to be parallel to the 6mm dimension of the tile in contrast to the commercial tiles, where the 4mm dimension was parallel to the 101.5 mm x 101.5 mm plane of the tile. Do to the small size of the Reduced Density tiles, this was done to allow for the minimum separation of 1mm between the bars. Bars were labeled 1 to 10, starting at the top of the tile.

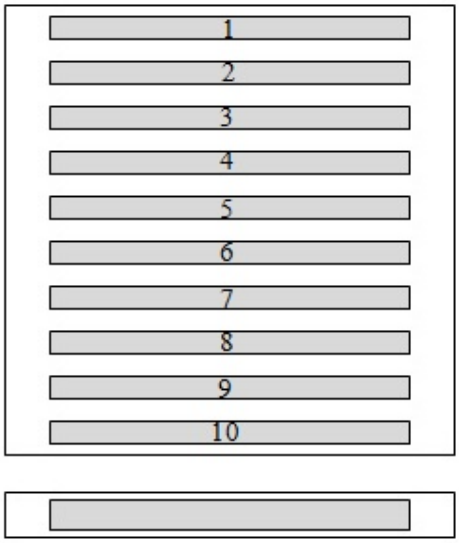


**Figure 5.61** Flexure bar machining diagram of Reduced Density SiC tile. One layer of bars, 10 bars per tile, 3 tiles underwent machining. 3mm dimension of bar parallel to 60mm x 60mm plane of tile

### 5.2.1.5 Flexure Testing/Weibull Analysis/Fracture Type

All thirty bars survived the machining operation. Testing was carried out in accordance of the procedures in ASTM Standard C1161. The results of the flexure testing are shown in Table 5.26. The average value and standard deviation have been calculated for the ten bars from each tile.

The average strength value of all of the tested samples was found to be 317 MPa, with a standard deviation of 19 MPa. This represented a deviation of only 6%. The range of values was between 280 and 360 MPa. In addition, the Weibull modulus was determined to be 20.4. Weibull parameters were not calculated for the individual tiles as the calculation of a Weibull modulus requires a minimum of thirty values.[72]

**Table 5.26** Flexure testing results for Reduced Density SiC tiles. Mean value: 317 MPa

| | avg (MPa) | std dev (MPa) | *m* |
|---|---|---|---|
| | | | |
| Tile 1 | 306 | 17 | - |
| Tile 2 | 324 | 18 | - |
| Tile 3 | 322 | 18 | - |
| Three Tiles | 317 | 19 | 20.4 |

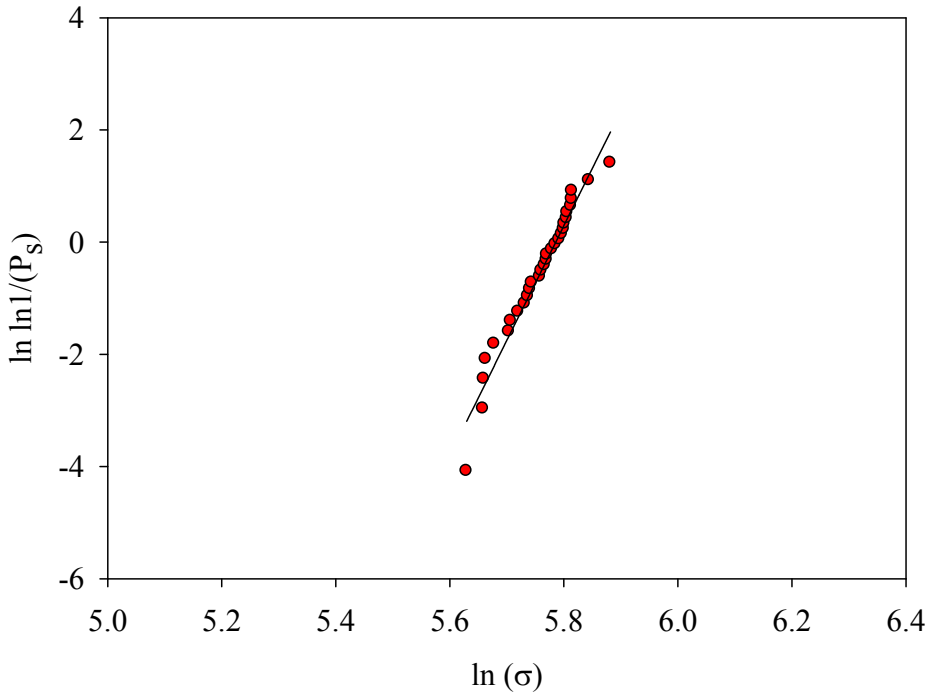


**Figure 5.62** Weibull plot. Reduced Density SiC tiles. 30 bars

The Weibull plot for the Reduced Density SiC flexure bars is shown in Figure 5.62. The distribution of strength values is quite tight, as the Weibull modulus is almost twice that which was attributed to the commercial SiC tiles. Although there appear to be outliers at the top and bottom ends of the Weibull plot, as will be shown in Section 5.2.2.6, all fractures were attributed to the same type of critical feature.

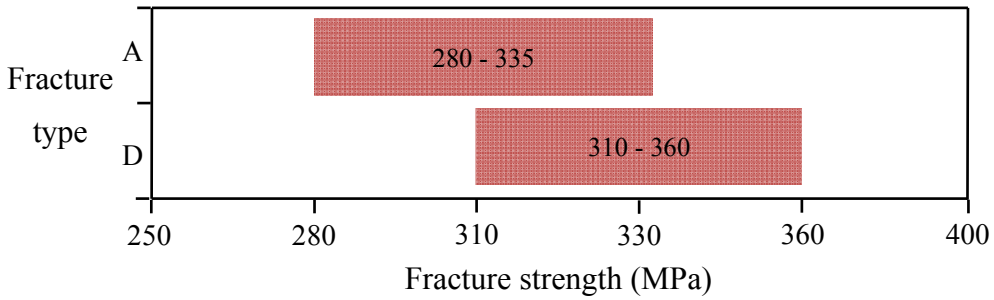


**Figure 5.63** Bend strengths of Reduced Density SiC flexure bars attributed to each type of fracture behavior. Type A: 280-335 MPa, Type D: 310-360 MPa

Fracture types were attributed to both Type A and Type D fractures, with a significant degree of overlap in fracture strength between the two types. This is shown in Figure 5.63. Type A fractures were attributed to strength values between 280 and 335 MPa, while the range in fracture strengths which corresponded to Type D fractures was 310 to 360 MPa.

#### 5.2.1.6 Strength-Limiting Features

The fracture of all thirty bend bars was attributed to the presence of spray dried relics that were not completely compacted and deformed during dry pressing, which resulted in porous regions within the microstructure of the material. Three examples will be discussed in order of increasing fracture strength. Fracture strengths have been divided into three regions, as shown in Table 5.27. Region A is comprised of the five lowest strength bars, while Region C contains the two highest strength bars. The balance of the bars has been grouped into Region B. In comparison to the flexure bars from the commercial SiC tiles, these would be considered to be low and low to medium strength bars.

**Table 5.27** Strength regions of flexure bars from Reduced Density SiC tiles

| | |
|---|---|
| $\sigma_f < 300$ | Region A |
| $300 \leq \sigma_f < 345$ | Region B |
| $345 \leq \sigma_f < 360$ | Region C |

Composite FESEM images of the primary fracture surface of Bar I are shown in Figure 5.64. Bar I broke at a strength of 287 MPa, which placed it within Region A.

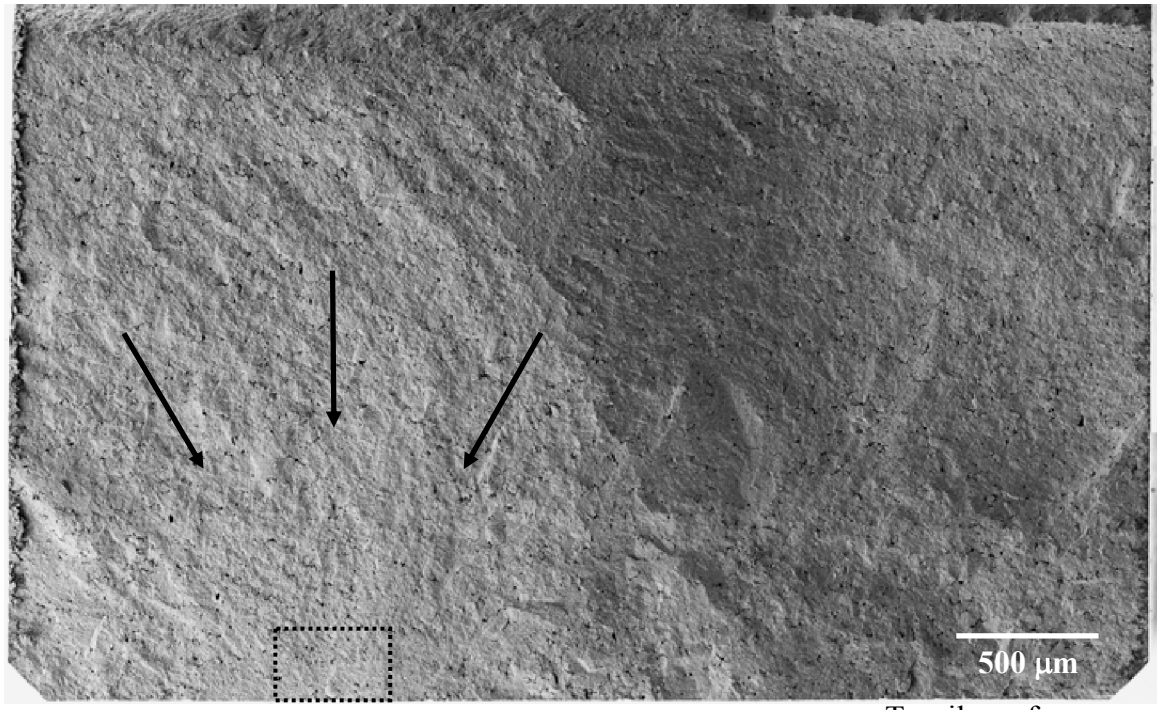


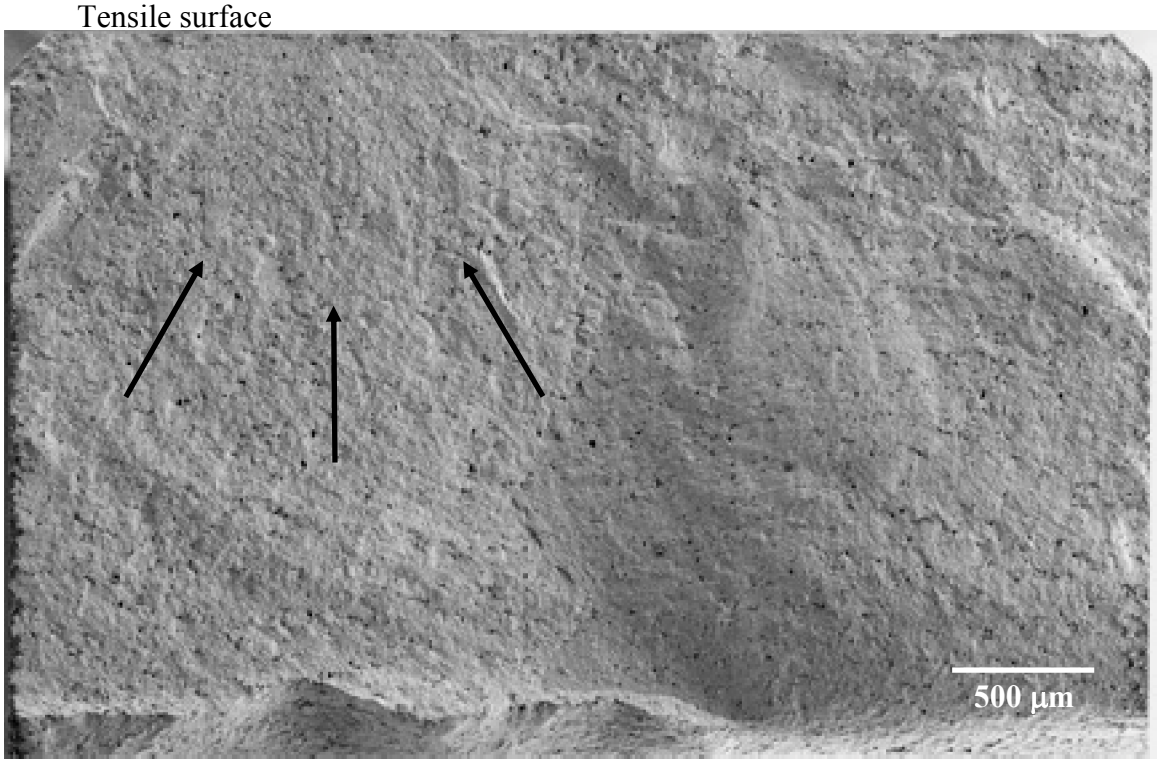


**Figure 5.64** Bar I. Primary fracture surface, left and right end faces, Reduced Density flexure bar ($\sigma_f$ = 287 MPa), Region A. Fracture appears to have initiated towards the left side of the bar. Composite images. 200x magnification

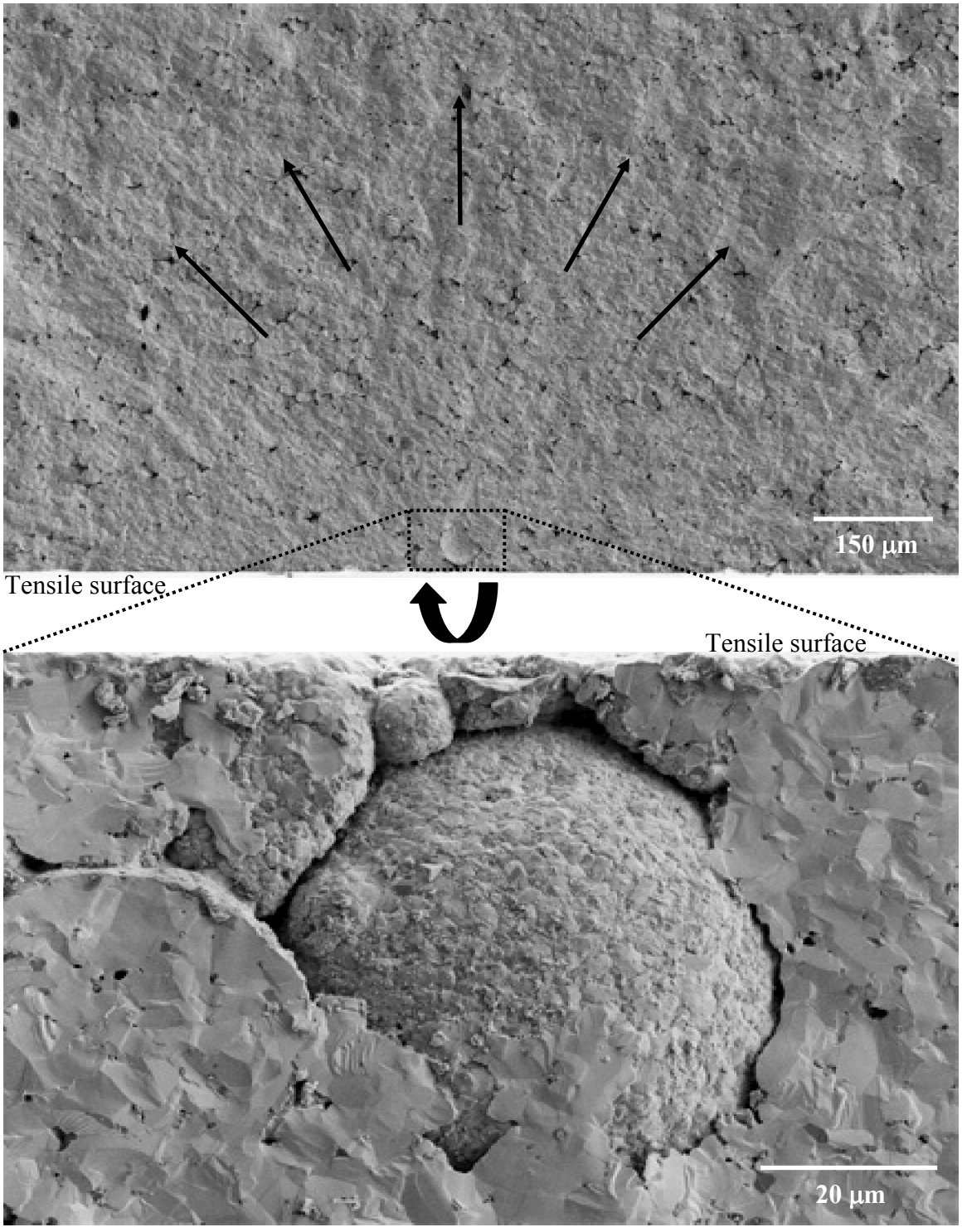


**Figure 5.65** Bar I. Fracture surface, Reduced Density Flexure bar ($\sigma_f$ = 287 MPa). 200x magnification (top), 2850X magnification (bottom). Fracture appears to have originated from the location of an unbonded spray dried granule

This was considered to be a Type A fracture, with a cantilever curl, noticeable in the bottom image, and horizontal crack branching. Arrows in the images point to where fracture is believed to have initiated, while a rectangular box has been placed around the region which is thought to contain the critical feature.

Two images from this region are shown in Figure 5.65. The upper image, resolved at 200x, approximately corresponds to the area within the rectangle in Figure 5.64. Arrows have been added to the image to indicate the fracture path.

The lower image in Figure 5.65 contains a higher magnification (2850x) FESEM micrograph of what is believed to be the fracture initiating feature of this flexure bar. This orientation of this image has been rotated 180° in relation to the image above it. The dominating feature in the image is believed to be a spray-dried granule.

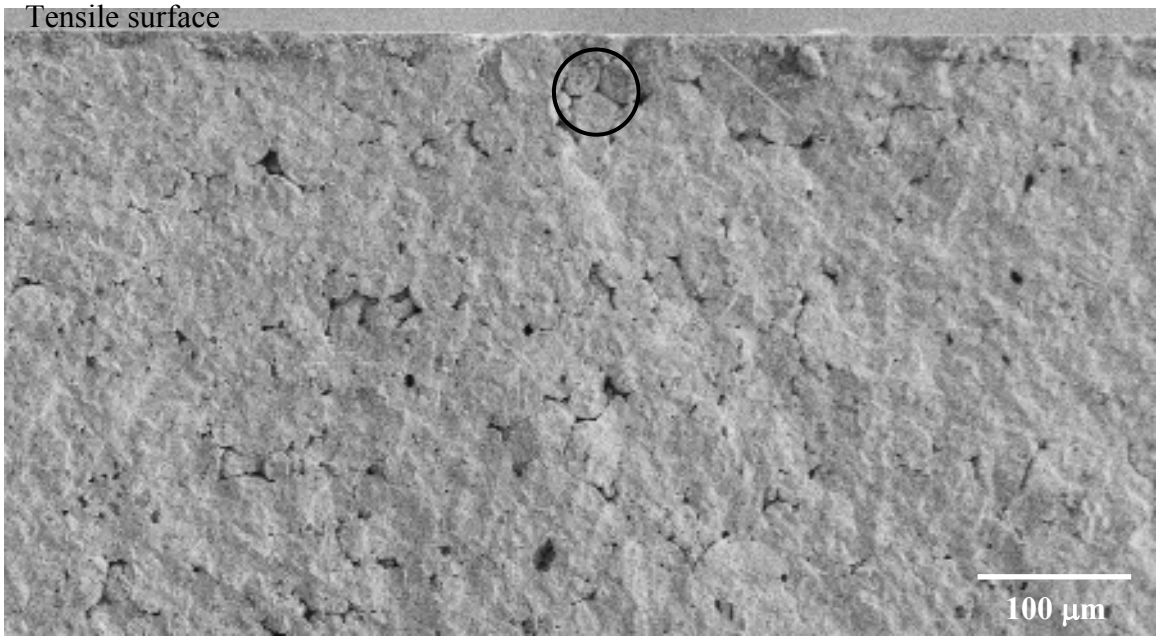


**Figure 5.66** Bar I. Fracture surface, Reduced Density Flexure bar ($\sigma_f$ = 287 MPa). Image of the opposite side of the primary fracture surface. Circle marks the location of the spray dried granule seen in Figure 5.65. 200x magnification

As has been mentioned previously, granulation refers to the process of intentionally agglomerating fine powders into larger clusters. This granule was quite large, as the portion of it that can be seen measured over 55μm in width and height, and is located very near to the tensile surface. The remnants of two smaller granules can also be seen in the image. One of these, located near the top left of the large granule, appears to still be relatively spherical. The other, located at the left of the middle of the large granule, appears to be almost compacted and deformed.

An image of the fracture surface on the portion of the bend bar opposite to that in Figure 5.65 is shown in Figure 5.66. A black circle has been placed in the image which corresponds to the location of the visible portion of the large spray dried granule. Intergranular pores which occur at the interfaces of granules can be seen in this area.

A higher magnification image of the large spray dried granule is shown in Figure 5.67. The surface of the granule is very similar in appearance to the features in Figure 5.30, which were found to be one of the intrinsic strength limiting features in the commercial SiC tiles. Where in that image, the majority of the surface of the granule was concealed, in this image, the consolidated and agglomerated nature of the granule can be discerned. Present in the image are what appear to be two tetrahedra on the surface of the large granule, located near the partially deformed small granule, as indicated by the circles in the image. These corresponded to symmetrical stacking of individual $SiC_4$ tetrahedra, as described in Section 2.1.1.

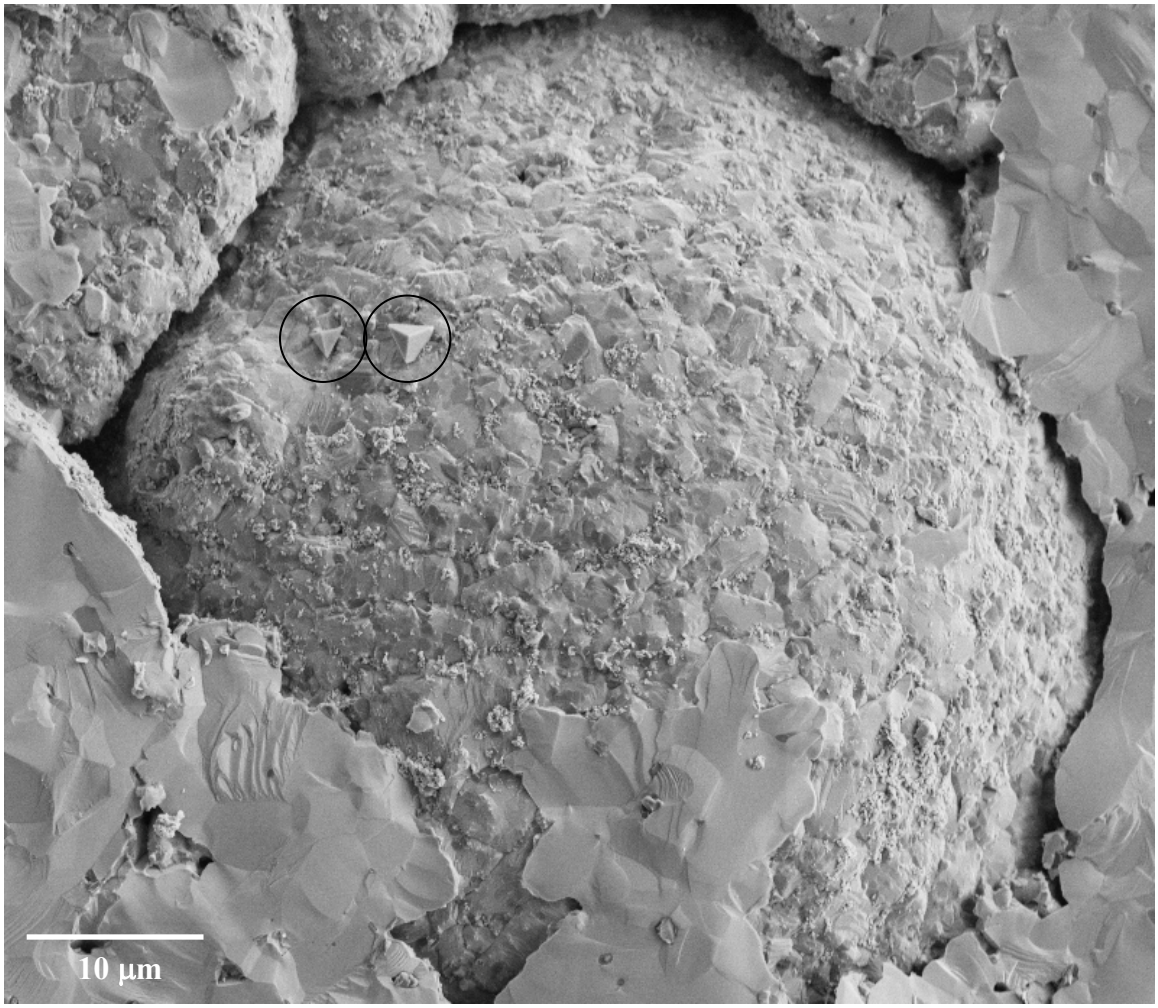


**Figure 5.67** Bar I. Reduced Density Flexure bar ($\sigma_f$ = 287 MPa). Large spray dried granule. 3680x magnification

Composite images of the primary fracture surface of Bar J are shown in Figure 5.68. This bar fractured at an applied stress of 326 MPa, which placed it within Region B. The likely fracture initiation point was offset from the center of the bar. Therefore, horizontal crack branching occurred on only one side of the fracture location. The fracture behavior of this bar was classified as Type A.

An image of the likely fracture initiation location is shown in Figure 5.69. The region in the image is located just above the tensile surface of the flexure bar, and corresponds to the area enclosed by the rectangle in Figure 5.68. Arrows in the image

indicate the likely point of fracture. As can be seen in Figure 5.70, fracture is believed to have initiated at the location of a cluster of semi-deformed compaction granules. Between the granules are intergranular pores which did not sinter out.

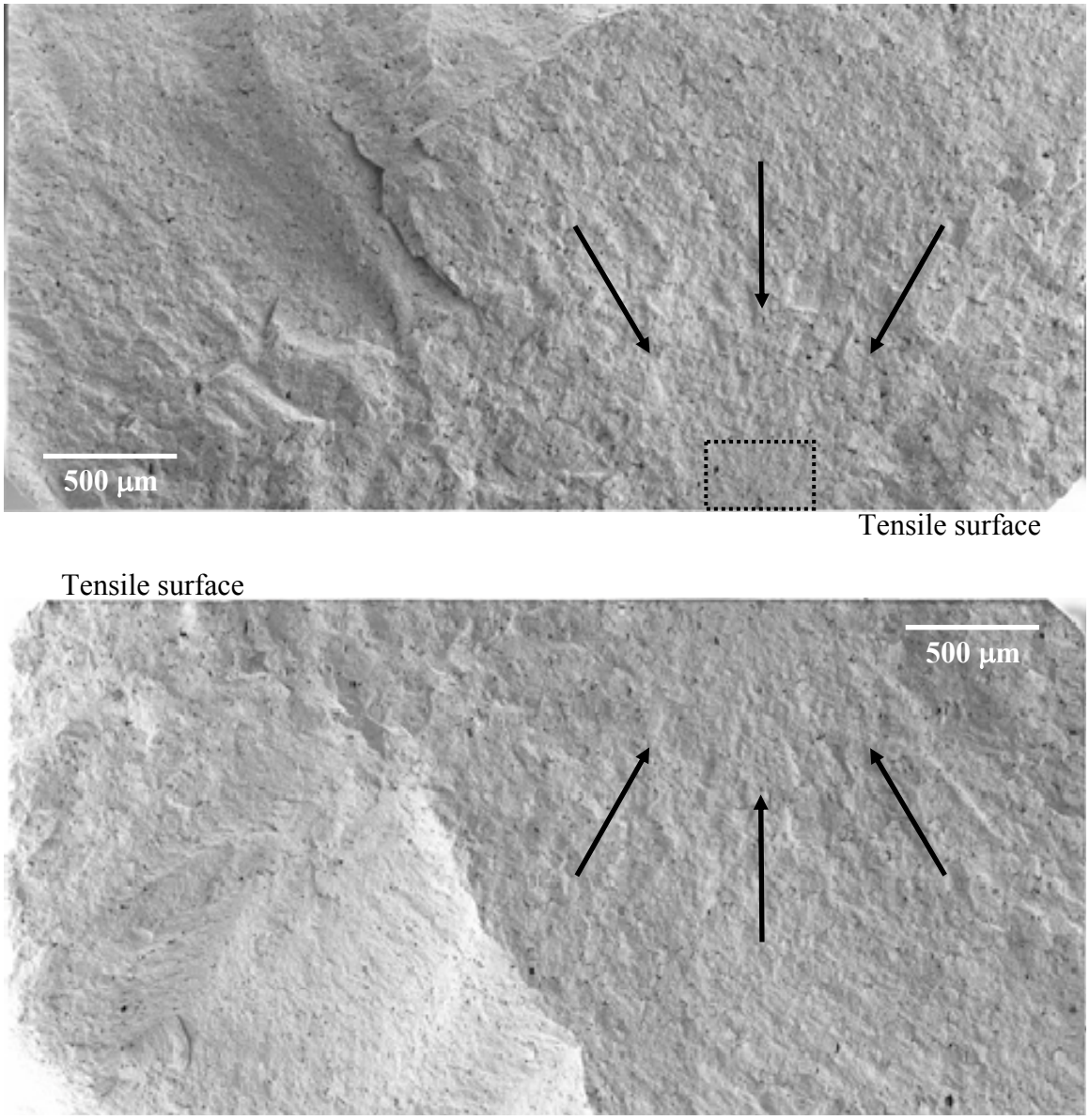


**Figure 5.68** Bar J. Primary fracture surface, left and right end faces, Reduced Density flexure bar ($\sigma_f$ = 326 MPa), Region B. Fracture appears to have initiated near the tensile surface towards the right side of the bar. Composite images. 200x magnification

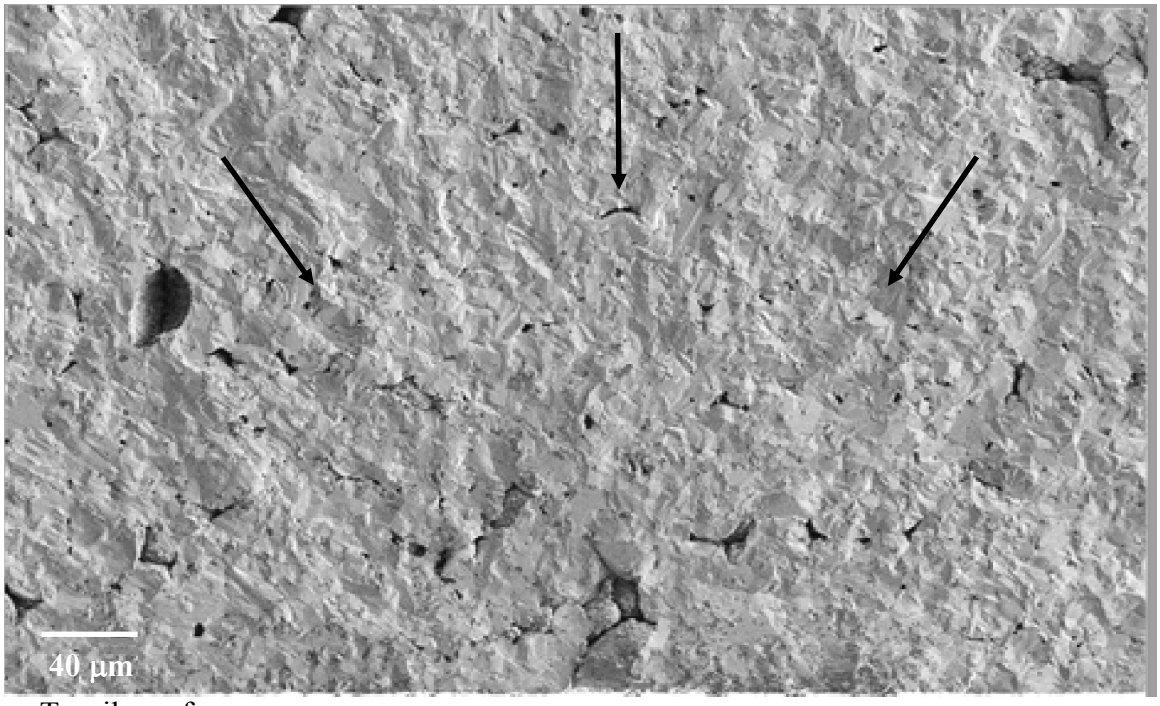


Tensile surface

**Figure 5.69** Bar J. Fracture surface, Reduced Density Flexure bar ($\sigma_f$ = 326 MPa). Fracture appears to have originated at a cluster of semi-compacted spray dried granules. 500x magnification

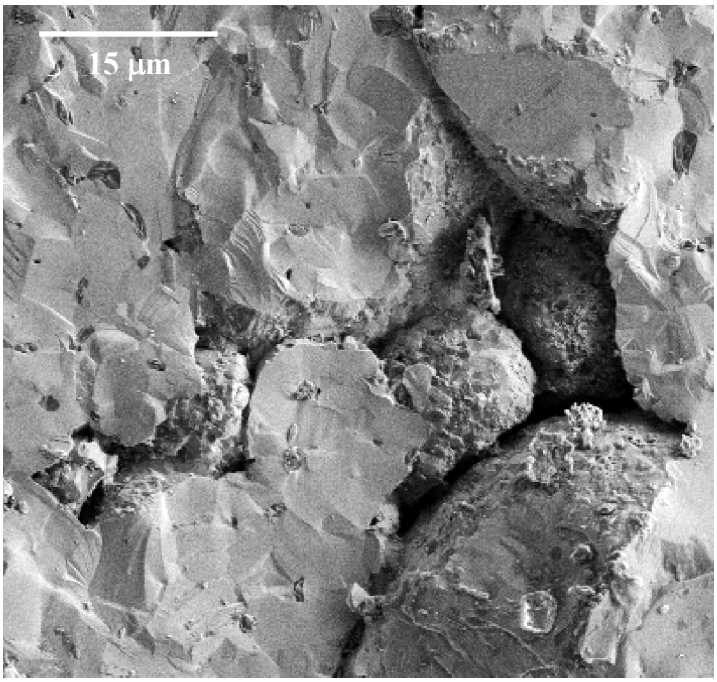


**Figure 5.70** Bar J. Fracture surface, Reduced Density Flexure bar ($\sigma_f$ = 326 MPa). Cluster of semi-compacted compaction granules. 2000x magnification

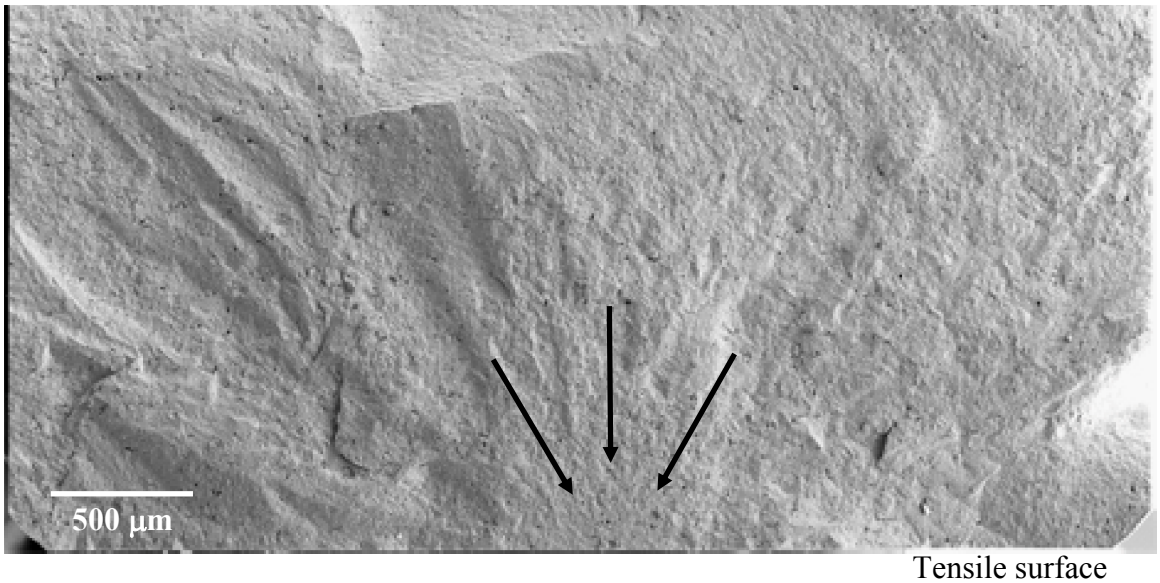


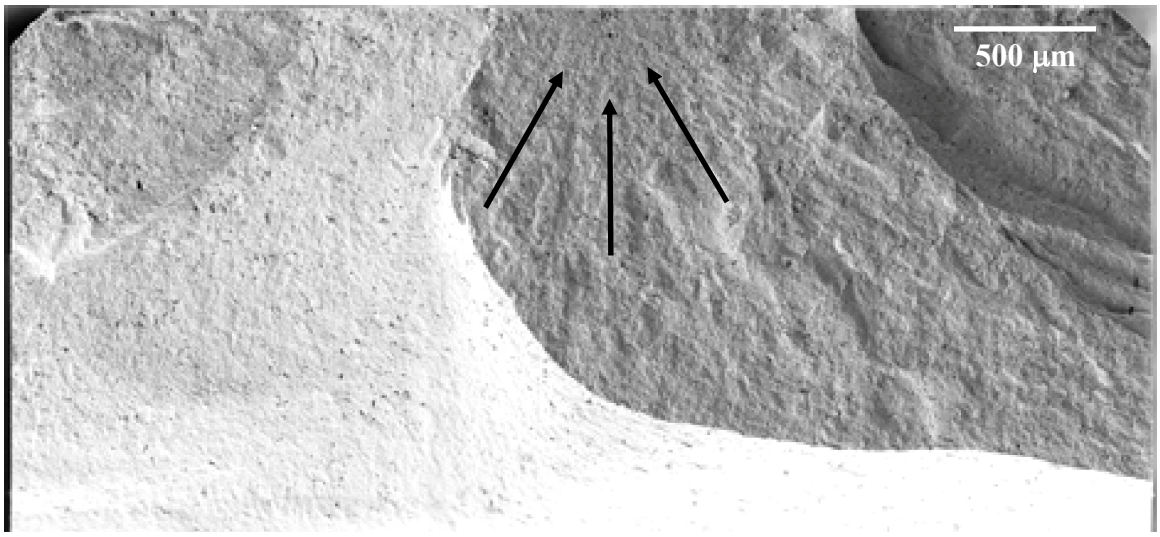


**Figure 5.71** Bar K. Primary fracture surface, left and right end faces, Reduced Density flexure bar ($\sigma_f$ = 345 MPa), Region C. Fracture appears to have initiated near the tensile surface near the center of the bar. Composite images. 200x magnification

Composite images of the primary fractures surfaces of Bar K ($\sigma_f$ = 345 MPa) are shown in Figure 5.71. Of the flexure bars tested that were machined from the Reduced Density SiC tiles, this bar broke at the second highest applied stress, placing it within Region C. The fracture surfaces of this bar differ somewhat from the two previous

examples. It can be seen that fracture likely initiated near the center of the bar, close to the tensile edge. Therefore, in this example, horizontal crack branching took place on either side of the fracture location.

Images of the area surrounding the fracture location on either side of the fracture surface for this bar are shown in Figure 5.72. As with the previous examples, fracture is thought to have started within a cluster of semi-bonded spray dried granules.

This set of images provided a relevant example of the process of compaction and consolidation during the fabrication of a fine-grained ceramic tile. Granules of various sizes can be found in close proximity to one another. It is possible to determine where features in the different images fit into one another. Alignment of the images is accomplished by determining features which appear in both images, as indicated by arrows in the two images. The largest granule in the top image sticks out from the surface, and is believed to fit into the relief in the bottom image. The three smaller granules towards the right of the bottom image appear to fit in the relief in the same area of the top image.

In these examples, it can be seen that fracture tended to initiate near the location of a large granule, or clusters of small granules. While the presence of these clusters brought about fracture, it is believed that fracture initiated at intergranular voids which are present between these features. As will be discussed in Section 5.4.1.4, both the Young's modulus and strength of a material are dependent upon the degree of porosity within a region.

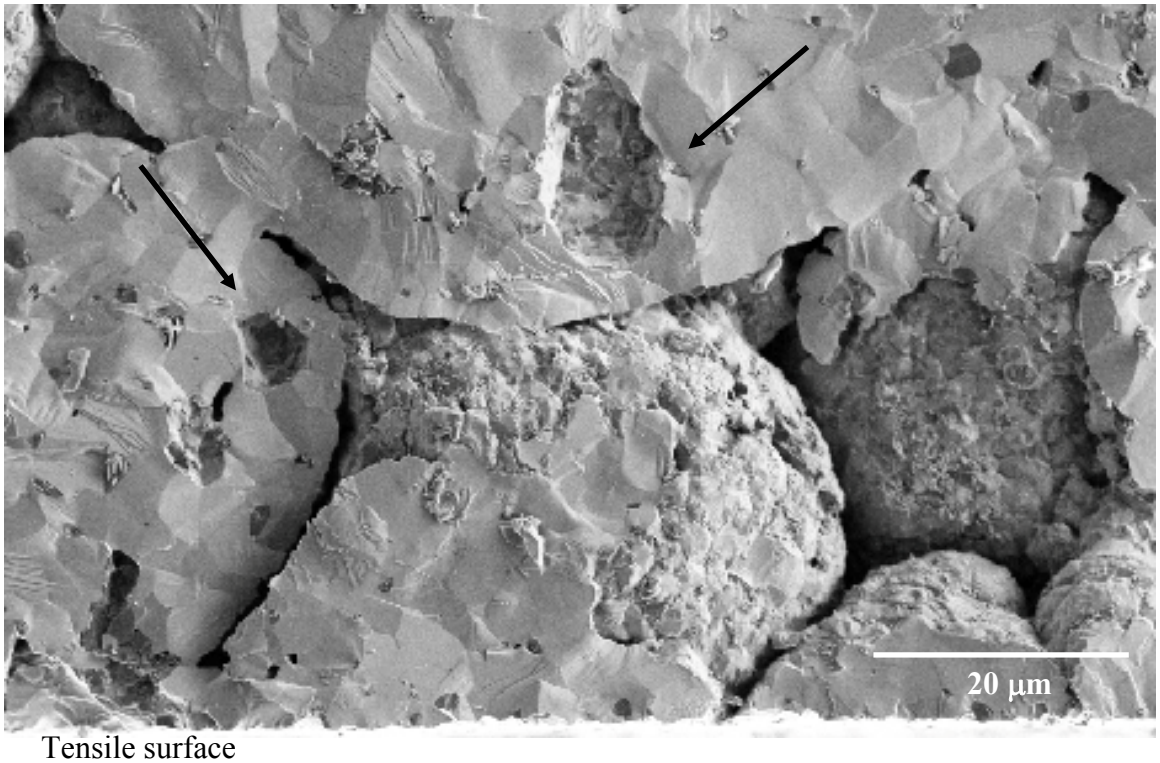


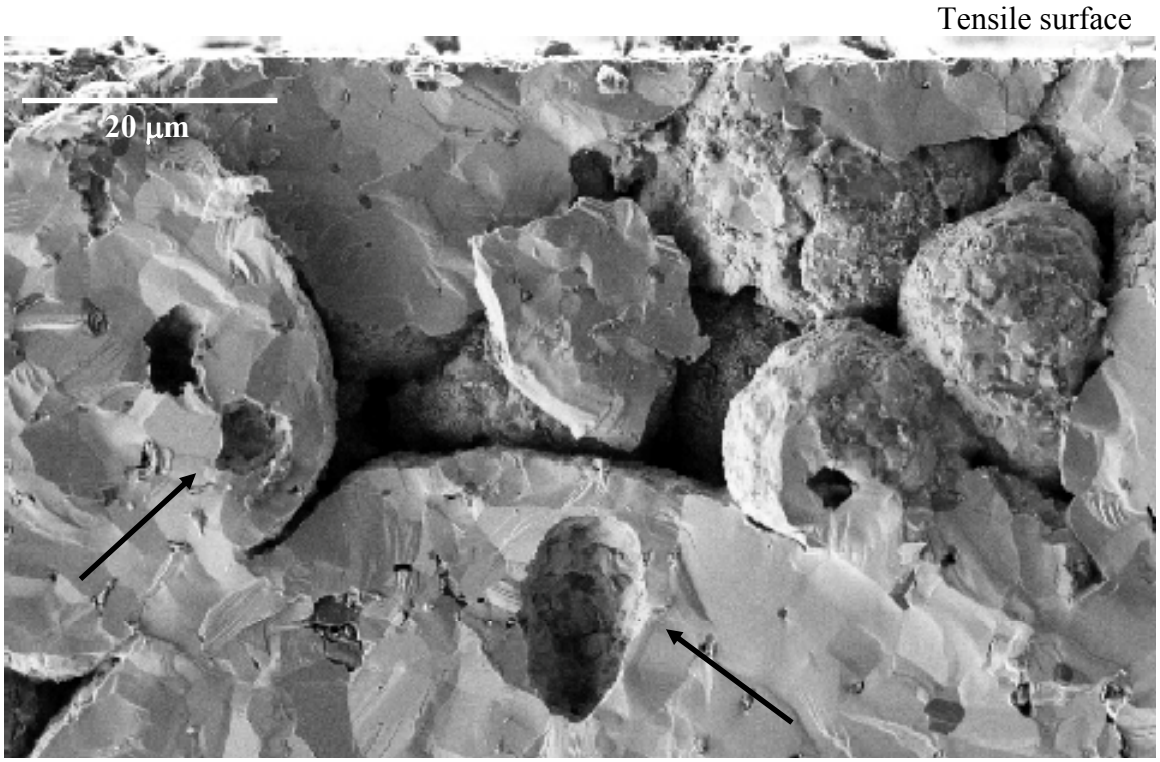


**Figure 5.72** Bar K. Fracture surface, left and right end faces, Reduced Density Flexure bar ($\sigma_f$ = 345 MPa). Cluster of semi-deformed compaction granules. 2000x magnification

### 5.2.2 Enhanced Boron Content Tiles

#### 5.2.2.1 Production and Motivation

The second approach relied upon producing silicon carbide tiles that contained an excess of boron sintering additives. As has been stated previously, the pressureless sintering of silicon carbide ceramic materials requires the presence of sintering activators, typically boron and carbon, the roles of which have been discussed in Sections 2.2.4.1 and 2.2.4.2. The challenge for silicon carbide manufacturers is to ensure the presence and consistent mixing of these activators on a local level in order to produce a homogenous densified part. Sufficient concentrations of sintering aids must be present to properly react the silicon and carbon contained in the green body. Localized regions of additive excess can result in the formation of inclusions, which may become a source of stress concentration during loading if there is a sufficient elastic property mismatch between the inclusion and the host matrix.

Inclusions of sintering aid are typically the result of agglomerates which form during the powder mixing process. These are considered to be a loosely bonded mass of individual particles.[187] Sufficient energy mixing is required to break-up agglomerates and ensure that they are not present in the green body. If this is the case, they are manifested as inclusions in the fired part. Agglomerates which are particularly large remain in the microstructure as large, porous inclusions.

Commercially available silicon carbide material typically contain between 0.3 and 0.6% boron carbide additives.[190] In the instance of these tiles, boron sintering activators were added at a concentration of 3%. This took the form of the collected “fines” (particle size < 10 μm) from a boron carbide spray dry run. These fines were blended into the

powder mix before dry pressing. The pressing pressure was comparable to that of the commercial tiles, and can be considered to be in the range of 200 – 300 MPa.[185, 189] Firing temperature and time were also commensurate to that for the commercial samples. It was intended with this procedure to produce silicon carbide samples which contained greatly increased numbers of porous boron carbide inclusions.

Two tiles were produced. Each tile was 101.5 mm W x 101.5 mm L x 6mm H. While the cross section of each tile was comparable to the commercial SiC tiles, the difference in height between the two sets of tiles was approximately half.

#### 5.2.2.2 Archimedes Density

Archimedes density measurements were carried out on the three Enhanced Boron Content SiC tiles. As shown in Table 5.28, the mean value for the two tiles was 3.14 g/cm$^3$. This represented a decrease in density of less than 1% when compared to the commercial SiC tiles.

**Table 5.28** Archimedes density values of Enhanced Boron Content SiC tiles. Mean value: 3.14 g/cm$^3$

| Tile | 1 | 2 |
|---|---|---|
| | | |
| Bulk Density (g/cm$^3$) | 3.14 | 3.14 |

#### 5.2.2.3 Ultrasound Evaluation

Non destructive evaluation of the Enhanced Boron Content SiC tiles was carried out by immersion-based ultrasound C-Scans utilizing an Olympus planar unfocused

transducer with a central frequency of 20 MHz in pulser/receiver configuration. As shown in Table 5.29, the average attenuation coefficient value for the two tiles was 8.64 dB/cm. This amounted to an increase of almost 4x when compared to the commercial SiC tiles.

**Table 5.29** Ultrasound C-Scan average values. 20 MHz attenuation coefficient. Enhanced Boron Content SiC tiles. Mean value: 8.64 dB/cm

| Tile | 1 | 2 |
|---|---|---|
| | | |
| $\alpha_{20\ MHz}$ | 8.83 | 8.45 |

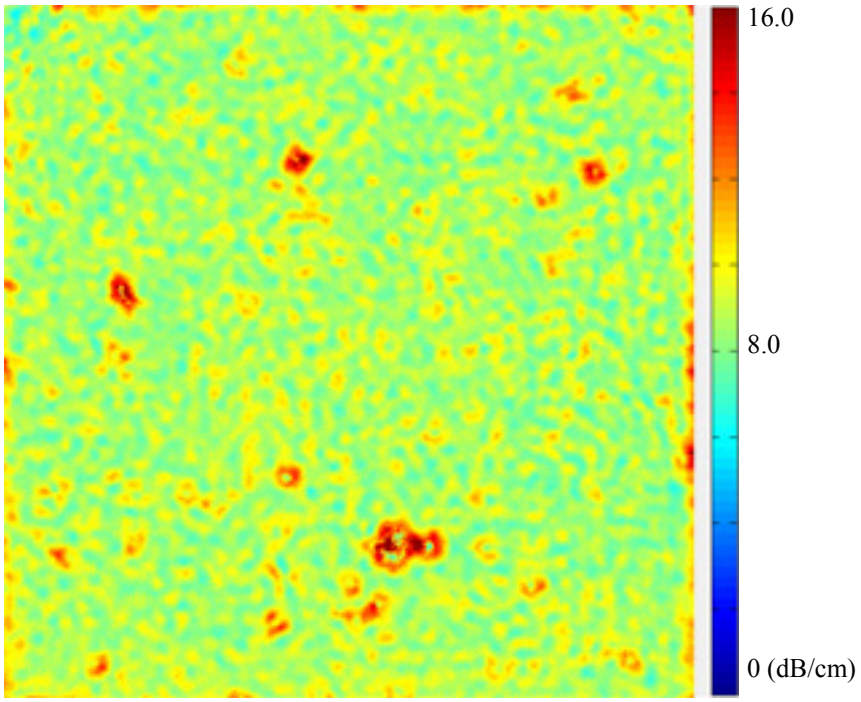


**Figure 5.73** Ultrasound C-Scan map of Enhanced Boron Content SiC tile. 20 MHz Attenuation Coefficient. Tile 1

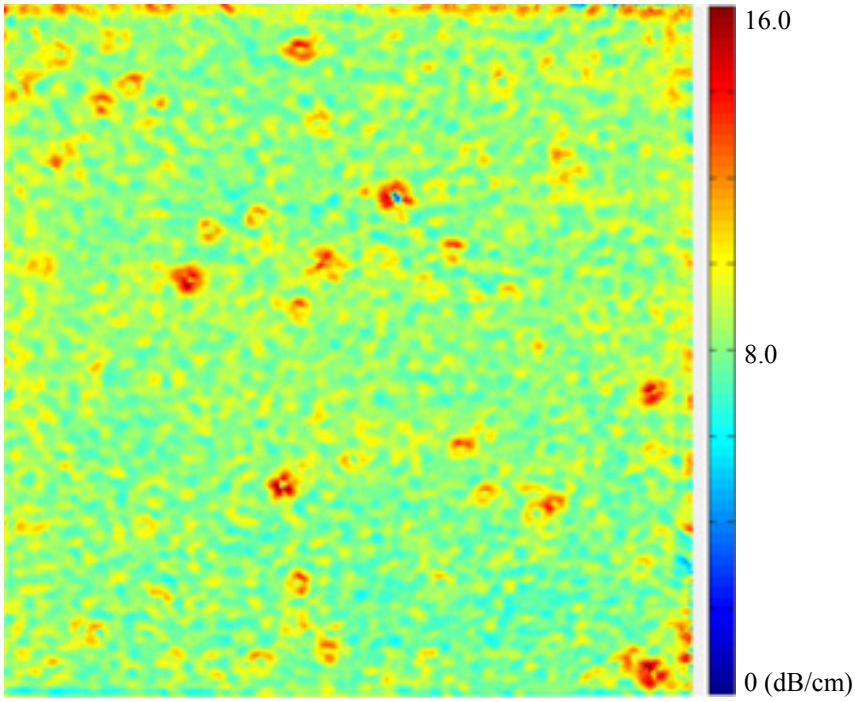


**Figure 5.74** Ultrasound C-Scan map of Enhanced Boron Content SiC tile. 20 MHz Attenuation Coefficient. Tile 2

The ultrasound C-Scan maps of the 20 MHz attenuation coefficient are shown in Figure 5.73 and 5.74. As with the RD tiles, the maps have a mottled appearance. The standard deviation of the attenuation coefficient within the two maps was 0.92 and 0.95 dB/cm, respectively. This deviation is over 10% of the average value. Both of the maps contained confined regions of highly increased attenuation coefficient. These were different in appearance from the circular, resonant acoustic anomalies seen in the ultrasound maps of the commercial tiles.

#### 5.2.2.4 Flexure Bar Machining

Both tiles were chosen for machining into ASTM B-type flexure bars. The flexure bar machining diagram for these tiles is shown in Figure 5.75. The diagram depicts the actual size of the tiles and flexure bars. Fifteen bars were machined from

each of two tiles, for a total of 30 bars. In contrast to the commercial and Reduced Density tiles, the long axis of the bars were oriented up and down as opposed to left and right in relation to the starting tile. This was done in order for the bar positions to coincide with the regions of the tile where the acoustic anomalies were located. Bars were numbered from 1 to 15, starting at the left side of the tile.

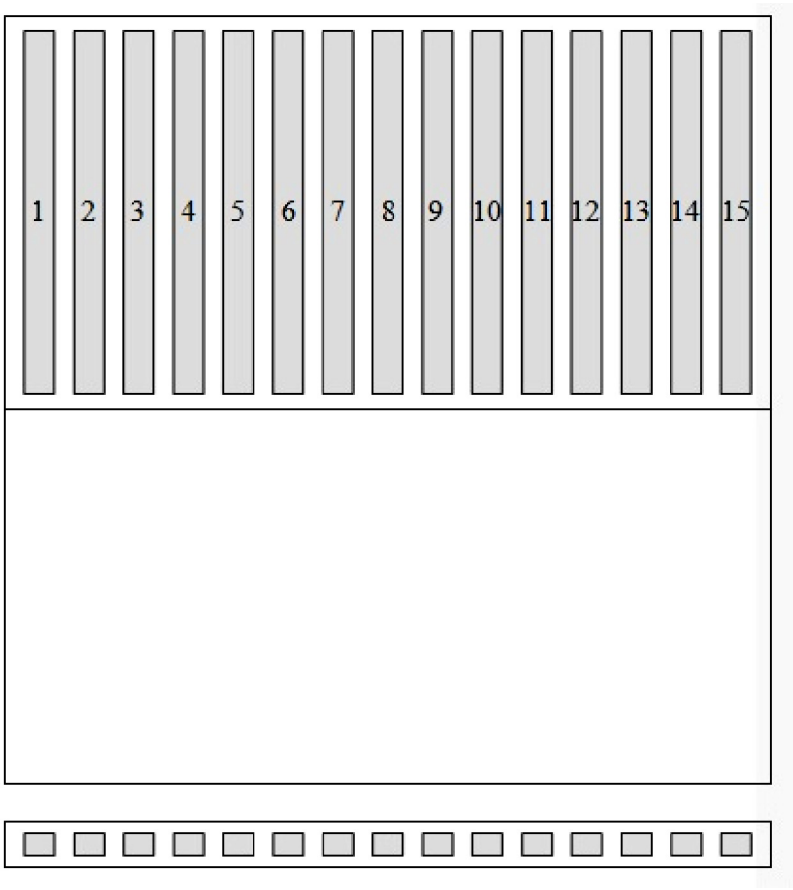


**Figure 5.75** Flexure bar machining diagram of Enhanced Boron Content SiC tile. One layer of bars, 15 bars per tile, 2 tiles underwent machining. 4mm dimension of bar parallel to 100mm x 100mm plane of tile. Lower portion of each tile returned from machinist for further evaluation (if needed)

### 5.2.2.5 Flexure Testing/Weibull Analysis/Fracture Type

All 30 bars were returned from the machinist. Testing was performed in accordance with the procedures set forth in ASTM Standard C1161. One bar was broken without result during the flexure testing.

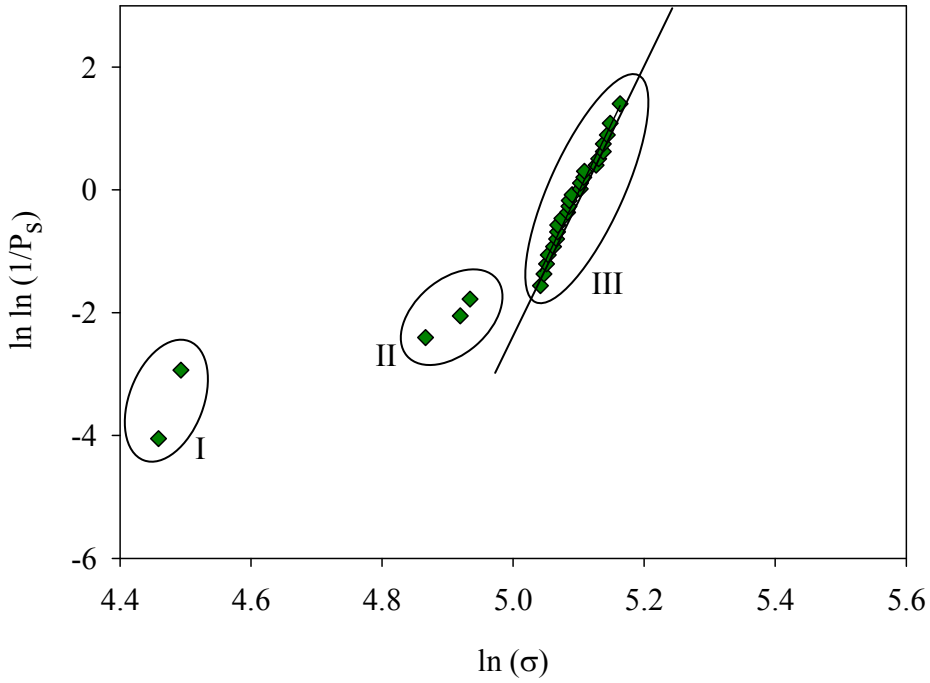


**Figure 5.76** Weibull plot. Enhanced Boron Content tiles. 29 bars

The Weibull plot which corresponds to the strength testing results of the EBC flexure bars is shown in Figure 5.76. As can be seen in the figure, there appears to be three regions of strength values within the results. These have been designated I, II, and III. The range of strength values corresponding to each region is shown in Table 5.30. Examples of strength limiting flaws attributed to each region will be examined in Section 5.2.3.6. Overall, fracture strength varied between 86 MPa and 175 MPa. The fracture

behavior of all bars was considered to be Type A fractures. The strength statistics and Weibull modulus will be presented after the examination of strength limiting features.

**Table 5.30** Strength regions of flexure bars from Enhanced Boron Content SiC tiles

| | |
|---|---|
| $\sigma_f < 100$ | Region I |
| $100 \leq \sigma_f < 140$ | Region II |
| $140 \leq \sigma_f \leq 175$ | Region III |

**5.2.2.6 Strength-Limiting Features**

Composite images of the primary fracture surface of the lowest strength Enhanced Boron Content flexure bar are shown in Figure 5.77. One of the two bars from Region I, this bar, designated as Bar L, broke at a strength of 86 MPa. As a very low fracture strength bar, the fracture plane was almost completely vertical, without horizontal crack branching. The bar appears to have broken at a millimeter-sized, large mass of boron carbide. This mass appears to be a continuous vein that stretched from the tensile edge to the vertical extent of the image. Also present on the surface are many sub-200μm inclusions, which were shown by EDS analysis to be comprised of boron carbide.

This bar and the other bar from Region I both fractured due to large masses of porous boron carbide. Each tile originally contained one of these bars, the mean strength of which was just over half that of the average for the remainder of the sample set. The other bars within the sample set all fractured at boron carbide inclusions which were more isolated. For this reason, the strength values for the flexure bars from Region I will not be included in the strength statistics, as they are not reflective of the strength limiting feature for the sample set as a whole.

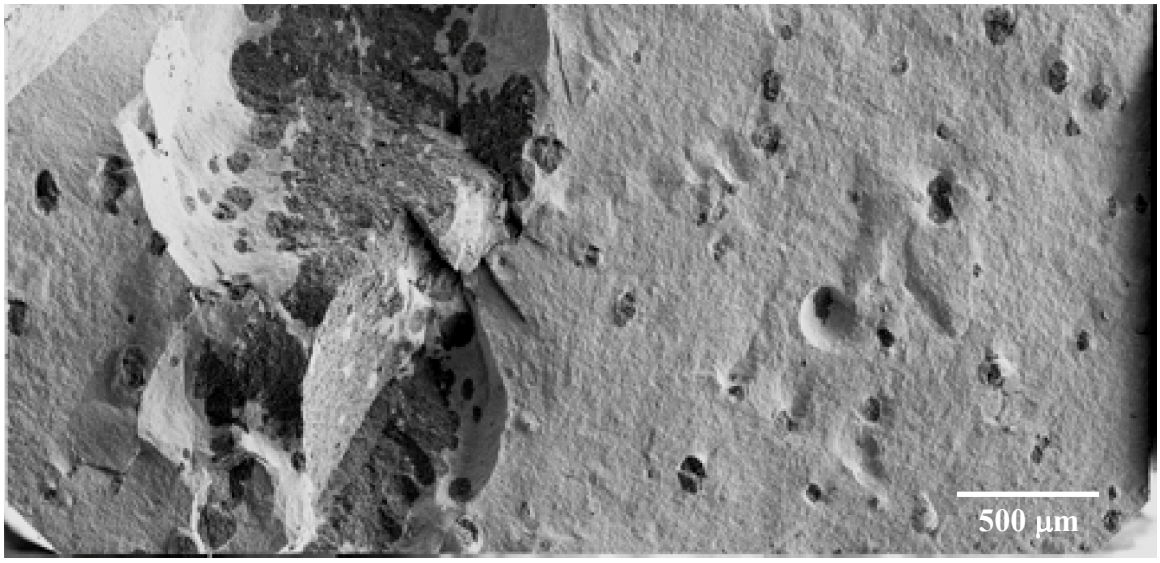


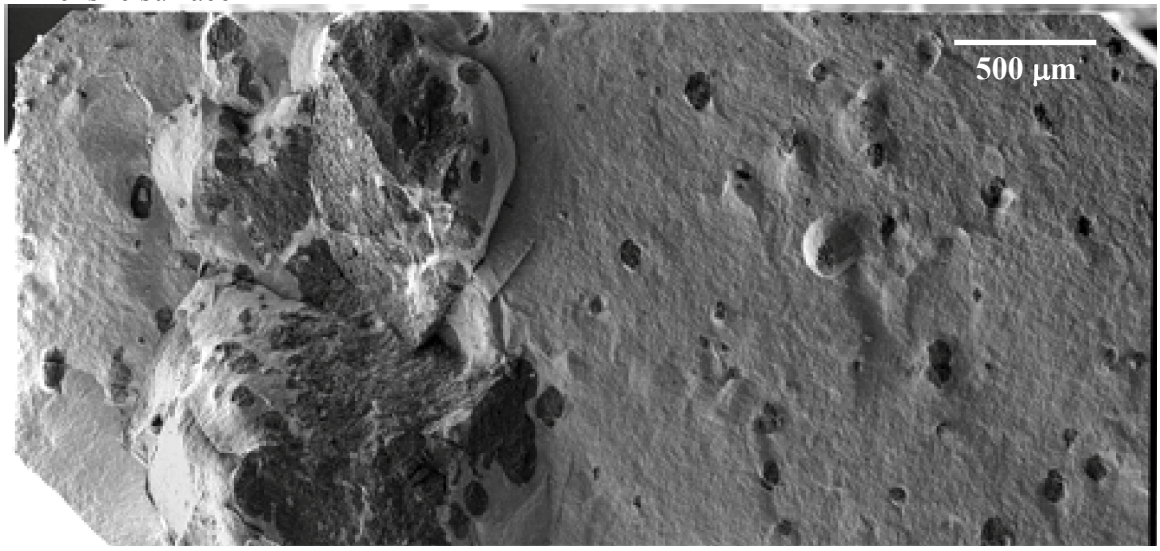


**Figure 5.77** Bar L. Primary fracture surface, left and right end faces, Enhanced Boron Content flexure bar ($\sigma_f$ = 86 MPa), Region I. Well below average strength. Composite images. 200x magnification

The composite images of the primary fracture position of Bar M are shown in Figure 5.78. This was a below average strength Enhanced Boron Content flexure bar ($\sigma_f$ = 130 MPa), which was categorized within Region II. As with the previous example,

the fracture plane appears to be almost completely vertical, without horizontal crack branching.

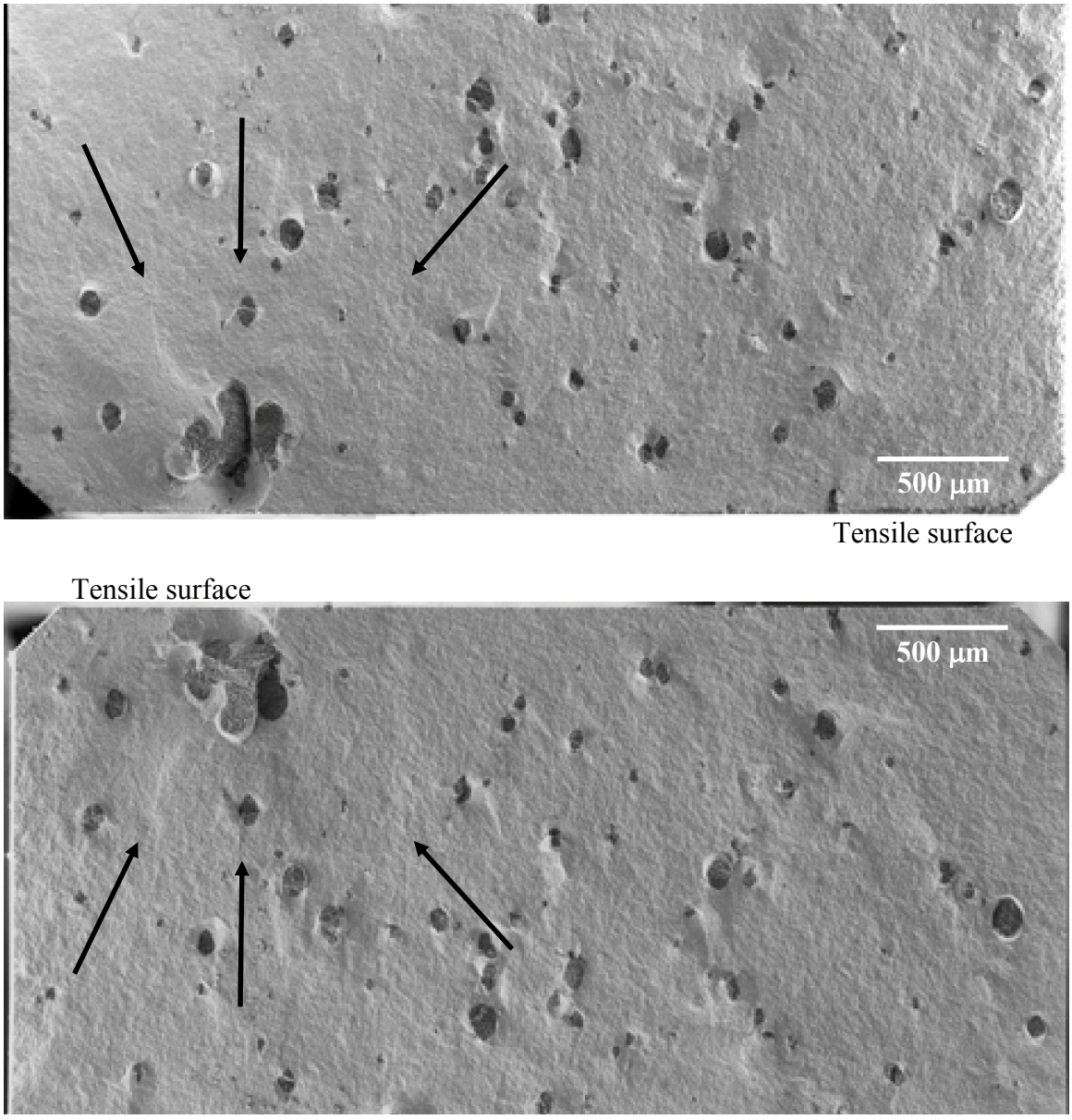


**Figure 5.78** Bar M. Primary fracture surface, left and right end faces, Enhanced Boron Content flexure bar ($\sigma_f$ = 130 MPa), Region II. Below average strength bar. Composite images. 200x magnification

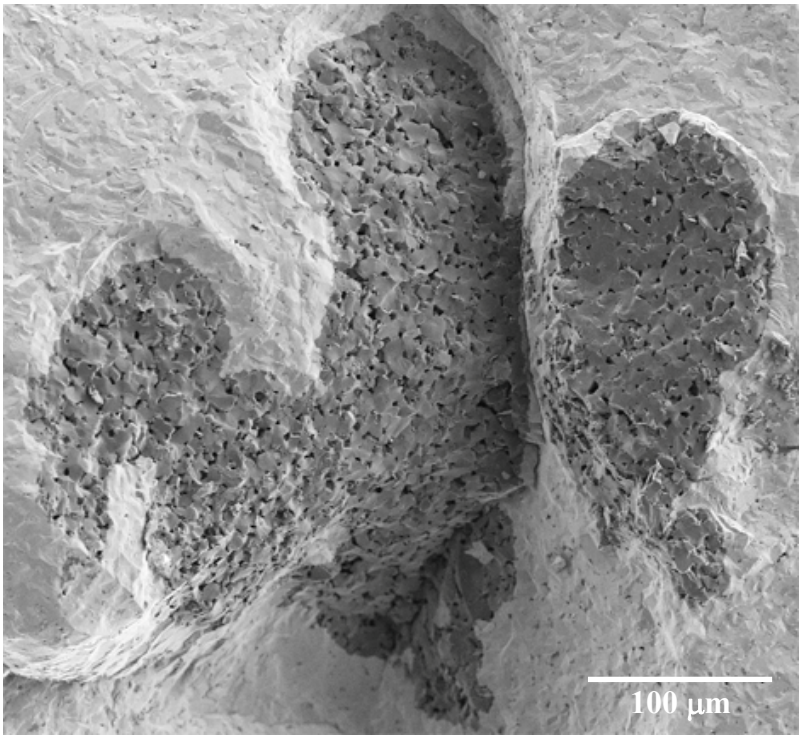


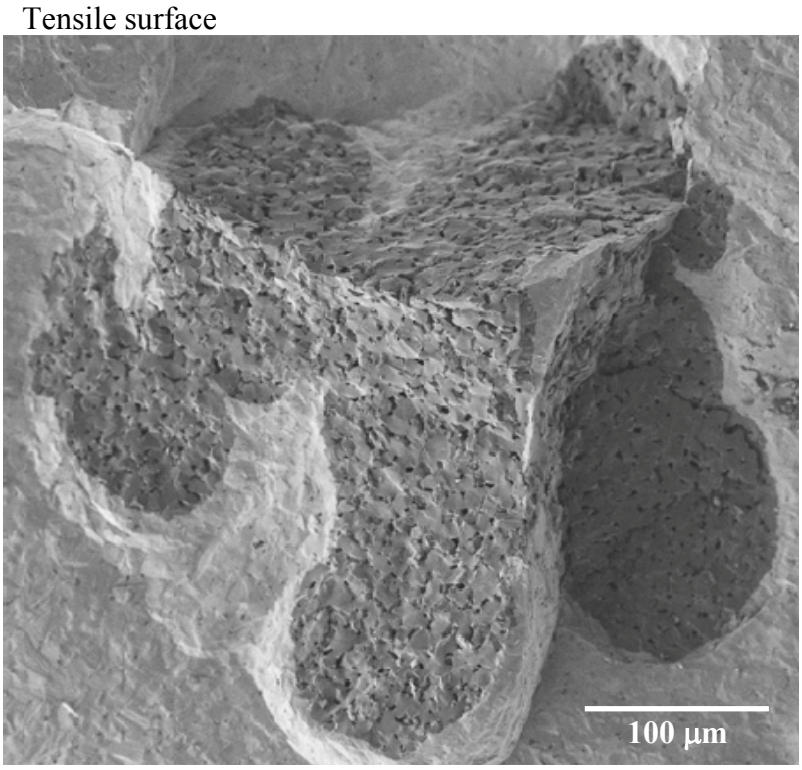


**Figure 5.79** Bar M. Fracture surface, Enhanced Boron Content flexure bar ($\sigma_f$ = 130 MPa), Region II. Cluster of connected boron carbide inclusions. 500X magnification

Increased magnification images of the likely fracture initiating feature are shown in Figure 5.79. These appear to be a cluster of interconnected boron carbide inclusions. Whereas fracture of the flexure bars from Region I were attributed to large masses of porous boron carbide, these types of features where considered to be separate inclusions which were located in close proximity to one another. The largest of these inclusions measures approximately 400 μm in length.

In the images corresponding to this example, it is possible to discern the oval-like shape of the individual boron carbide inclusions, which are similar in appearance to the examples provided in Section 5.1.3.11. However, the cross sections of the porous boron carbide inclusions which were found in the commercial samples were between $^1/_2$ to $^1/_4$ the size of the inclusions found here. It appears that a dome-shaped section of the fracture surface broke away from the bottom of the largest inclusion. This section contained portions of the multiple inclusions in the cluster.

The following two examples were considered to be average strength Enhanced Boron Content flexure bars. As with the other examples of EBC flexure bars, these were both considered to be Type A fractures with almost completely vertical fracture planes. Composite images of the primary fracture surface of Bar N ($\sigma_f$ = 162 MPa) are shown in Figure 5.80. The initial fracture location appears to be biased towards the left side of the bar.

Images of the region containing the likely fracture initiating features are shown in Figure 5.81. In this example, fracture appears to have initiated near a cluster of smaller, separate porous boron carbide inclusions. There is one large inclusion, one medium inclusion, and one smaller inclusion. The fracture path cuts through both the large and

medium inclusions, and then arcs upward. A second fracture line emanates near the top of the large inclusion, and then changes direction after travelling a short distance.

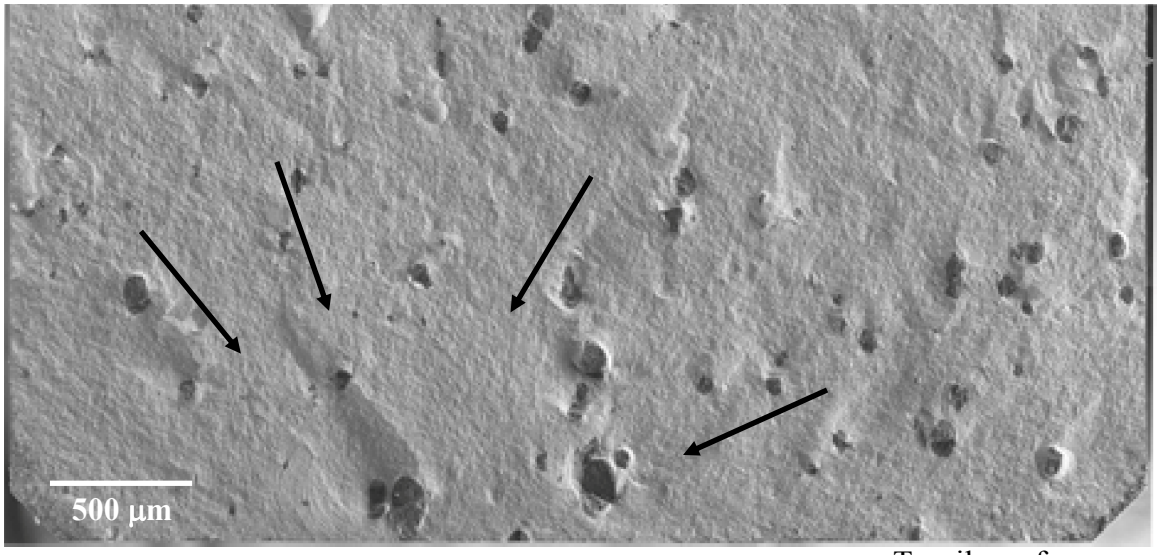


Tensile surface

Tensile surface

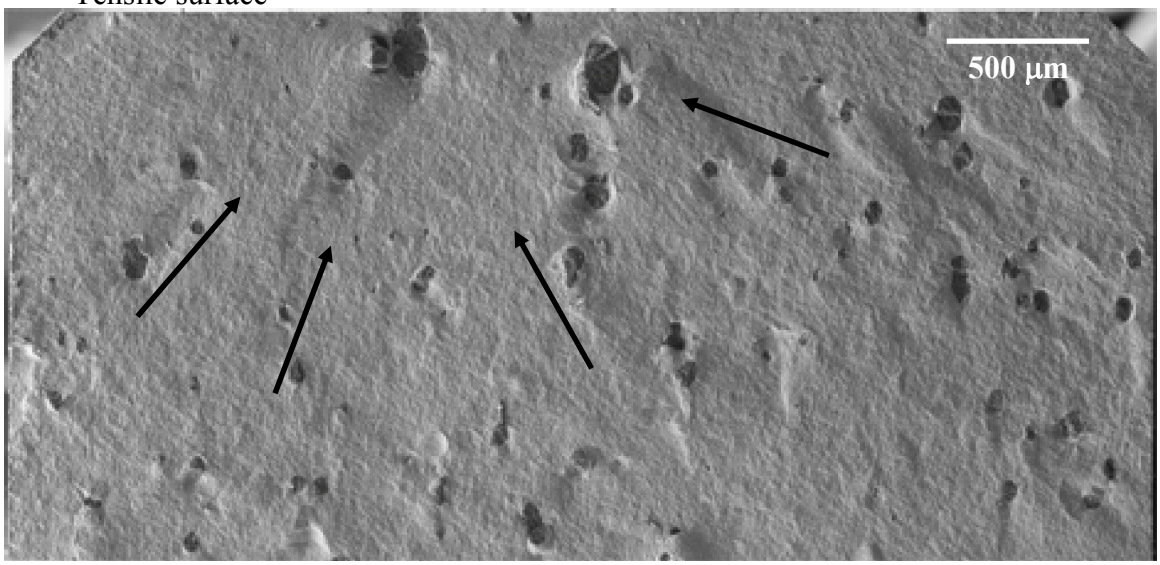


**Figure 5.80** Bar N. Primary fracture surface, left and right end faces, Enhanced Boron Content flexure bar ($\sigma_f$ = 162 MPa), Region III. Average strength bar. Composite images. 200x magnification

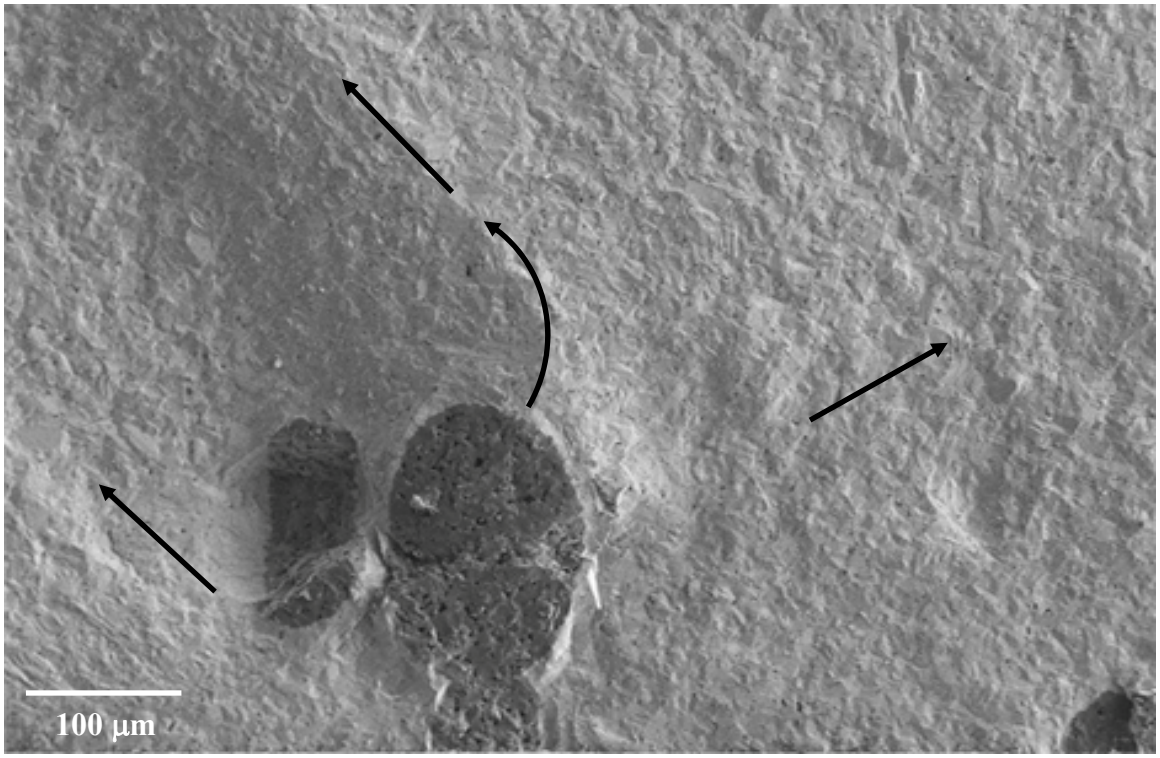


Tensile surface

Tensile surface

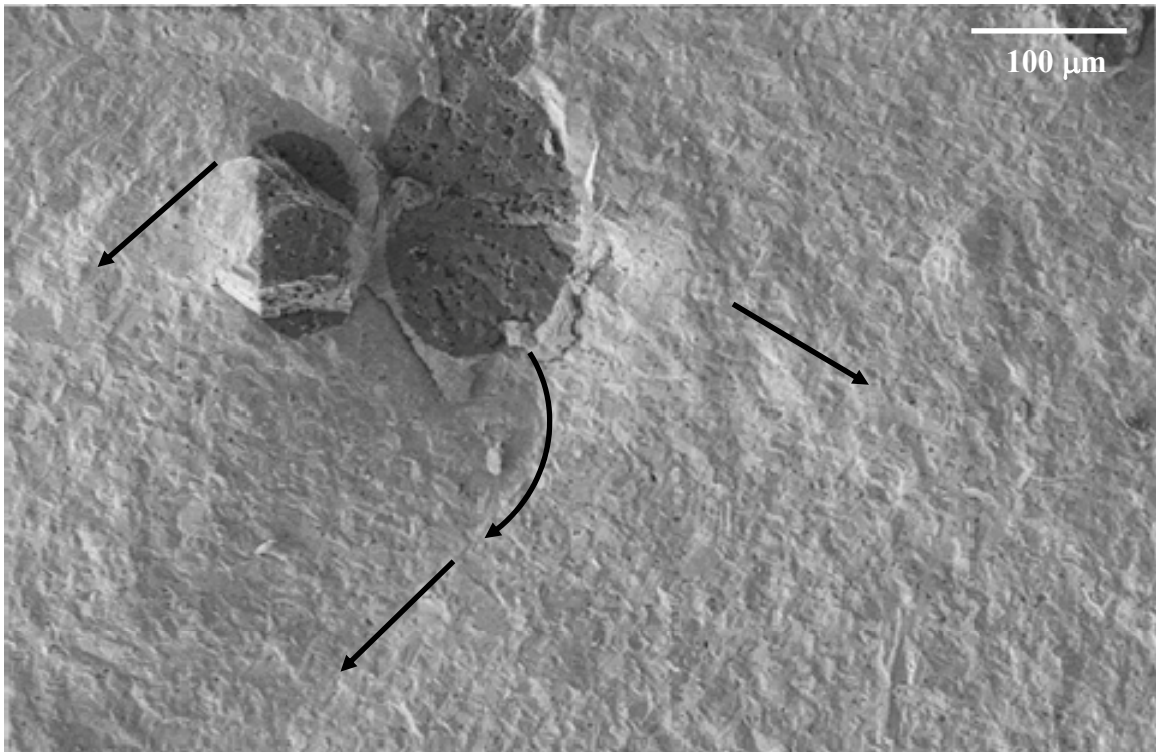


**Figure 5.81** Bar N. Fracture surface, Enhanced Boron Content flexure bar ($\sigma_f$ = 162 MPa), Region III. Porous boron carbide inclusions. 300x magnification

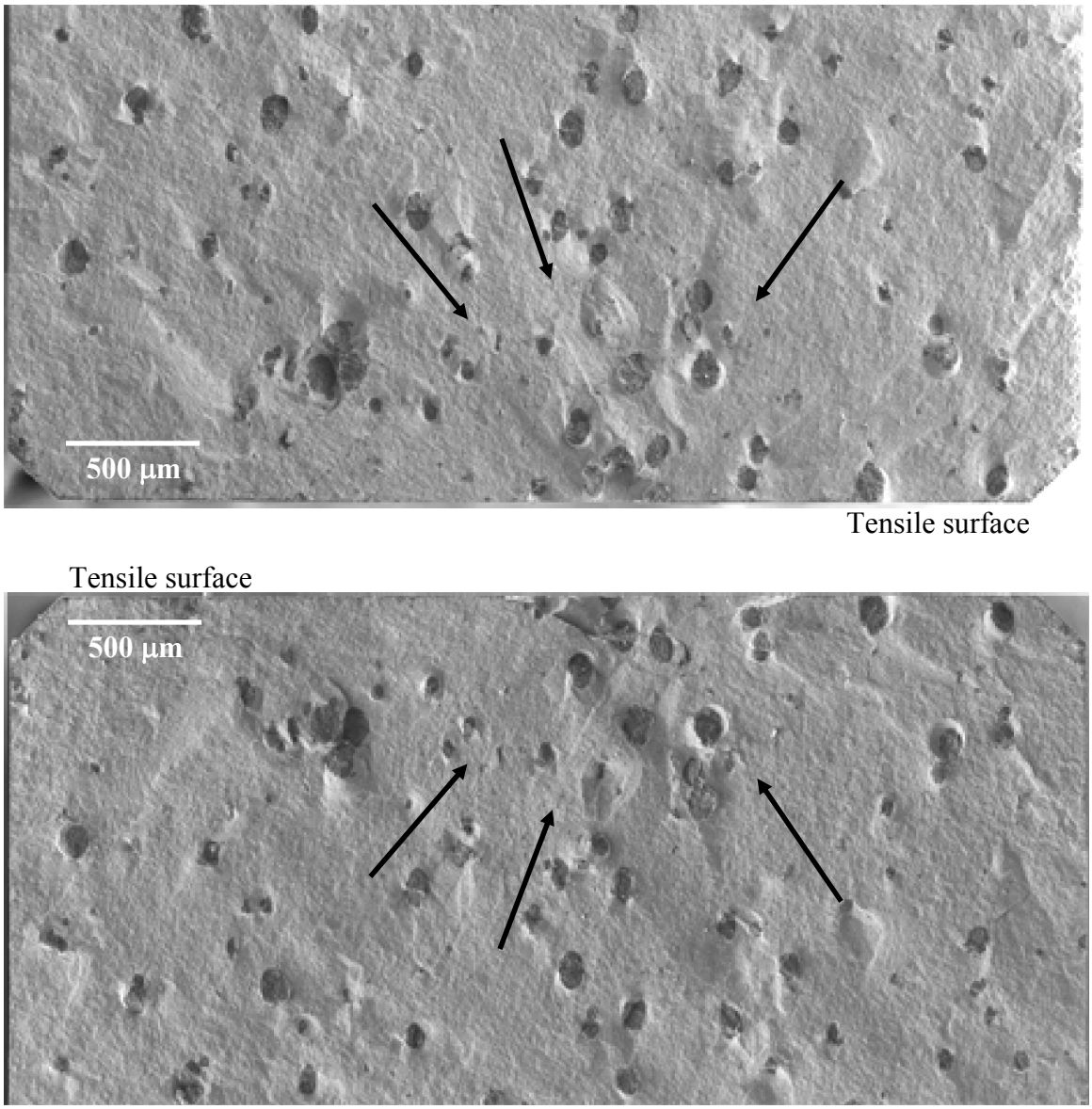


**Figure 5.82** Bar O. Primary fracture surface, left and right end faces, Enhanced Boron Content flexure bar ($\sigma_f$ = 164 MPa), Region III. Average strength bar. Composite images. 200x magnification

The composite images of the final example, Bar O, are shown in Figure 5.82. This was considered to be an average strength ($\sigma_f$ = 164 MPa) EBC SiC flexure bar. Fracture appears to have initiated towards the center of the bar, but the fracture strength was so low that horizontal crack branching did not occur.

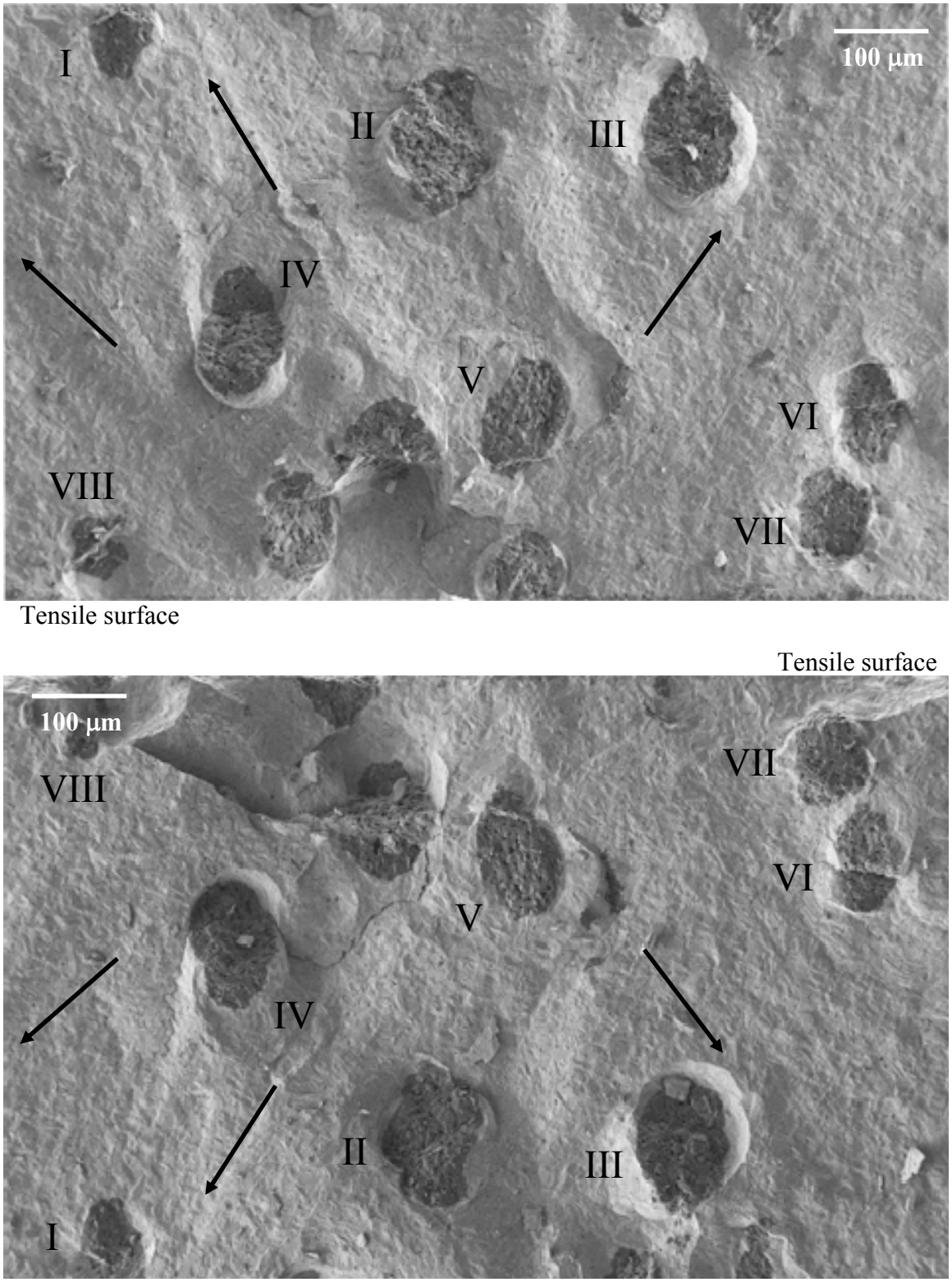


**Figure 5.83** Bar O. Fracture surface, Enhanced Boron Content flexure bar ($\sigma_f$ = 164 MPa), Region III. Porous boron carbide inclusions. 300x magnification

Images of the regions where fracture is believed to have initiated are shown in Figure 5.83. The region contains many separate sub-150 μm porous boron carbide inclusions. Arrows in the image indicate the likely facture path. Examination of the images shows that not all of the locations in the images are mirrored on both sides of the fracture surface. Inclusions with a cross-section that is greater than 45 μm in size have been numbered. Those inclusions which have not been labeled are thought to have directly contributed to the initiation on fracture. There is a triangular shaped relief formed between the three unlabeled inclusions near the bottom of the center of the image. This corresponds to a protuberance in the same region of the bottom image. The fracture plane appears to have split the inclusion located at the top vertex of the triangle

The average strength and number of bars from each region are shown in Table 5.31. One bar from Region I was found in each tile, while the three bars from Region II were originally located in Tile 1. The remainder of the bars from Region III was split between Tiles 1 and 2. The average strength and standard deviation for the bars from each tile are shown in Table 5.32. The average strength of the bars from Tile 1 is lower than that from Tile 2 due to the presence of the three Region II bars. The calculated Weibull modulus takes into account only the strength values from Region III.

**Table 5.31** Average strength and number of bars from each region of Enhanced Boron Content SiC tiles

| | | |
|---|---|---|
| Region I | 88 MPa | 2 bars |
| Region II | 135 MPa | 3 bars |
| Region III | 163 MPa | 24 bars |

**Table 5.32** Average strength and standard deviation for flexure bars from each Enhanced Boron Content SiC tile. Weibull modulus was calculated only for the bars from Region III

| | avg (MPa) | std dev (MPa) | *m* |
|---|---|---|---|
| | | | |
| Tile 1 | 152 | 22 | - |
| Tile 2 | 159 | 21 | - |
| Both Tiles | 155 | 21 | 22.2 |

## 5.3 Ultrasound and Strength Correlation of Targeted Samples

Fracture position overlay maps and attenuation coefficient scatter plots were constructed for selected targeted samples. These were two of the methods employed to determine if a correlation existed between the 20 MHz attenuation coefficient and the quasi-static strength results for the commercial SiC tiles.

The fracture position overlay diagram which corresponds to the flexure bars from Tile 2 of the Enhanced Boron Content samples is shown in Figure 5.84. The black hash marks in the diagram designate the primary fracture position of each bar, which are numbered from 1 to 15 from left to right. Bar 1 was broken without result during the testing and does not appear in the diagram. The black rectangle in the diagram indicates the primary loading zone of the flexure rest.

A number of confined regions of increased attenuation can be seen which overlap the areas from which flexure bars were machined. The fracture positions of these bars do not appear to correlate to the locations of increased attenuation.

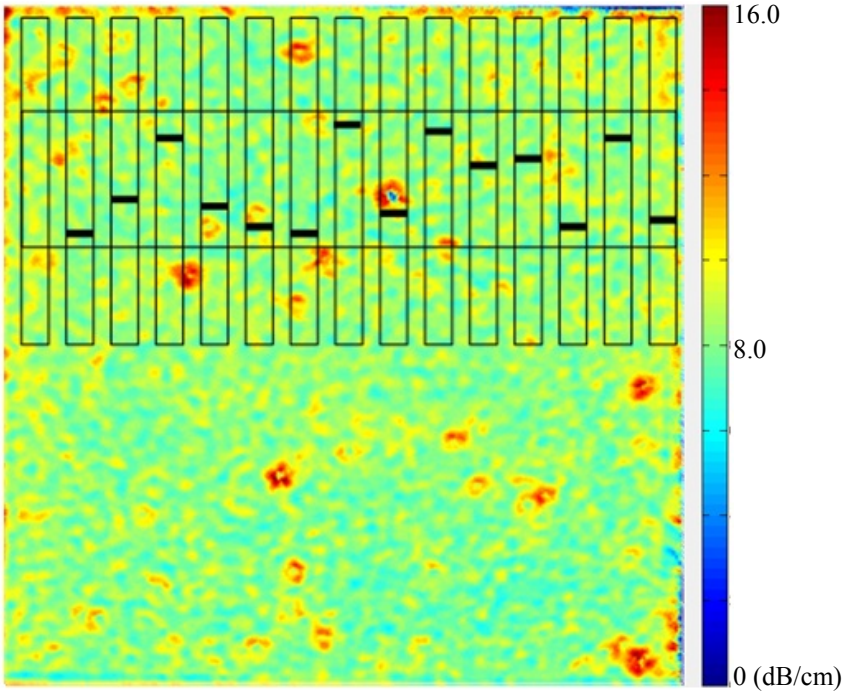


**Figure 5.84** Fracture Position Overlay Diagram. Enhanced Boron Content Tile 2. 20 MHz Attenuation Coefficient map. Fracture positions of bend bars depicted on ultrasound map with black hash marks

A section of the attenuation coefficient map of EBC Tile 1 is shown in Figure 5.85. A prominent region of increased attenuation was located within the defined region corresponding to Bar 7. However, the fracture location of this bar was located 12 mm from the point of this feature.

What can be concluded is that the microstructural features within the tiles which caused these anomalies do not appear to correspond to the specific clusters of boron carbide inclusions which were identified as causing fracture of these bend bars. Fracture position overlay diagrams were not constructed for the Reduced Density tiles as they did not contain acoustic anomalies or localized regions of increased attenuation.

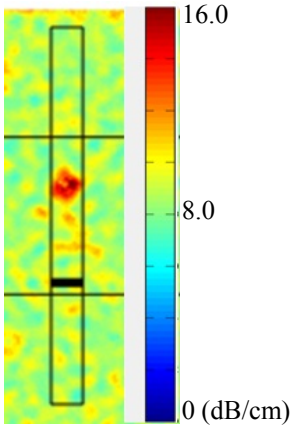


**Figure 5.85** Fracture Position Overlay Diagram. Enhanced Boron Content Tile 1. Portion of 20 MHz Attenuation Coefficient map. Fracture positions of bend bars depicted on ultrasound map with black hash marks. Fracture location does not appear to correspond to position of increased attenuation coefficient

Scatter plots which compare the 20 MHz attenuation coefficient and the quasi-static strength results for selected targeted samples are shown in Figures 5.86 and 5.87. These correspond to the Enhanced Boron Content Tile 2 and Reduced Density Tile 1, respectively. Least squares linear regression fits were performed for both groups of data. In the case of both plots, there does not appear to be a linear relationship between the 20 MHz attenuation coefficient and the 4-pt flexure strength values. The correlation coefficients and slope of the fit lines are shown in Table 5.33.

**Table 5.33** Coefficients of determination and linear fit line slopes of 20 MHz attenuation coefficient/strength testing scatter plots. Targeted samples

| | | $b_1$ | $R^2$ |
|---|---|---|---|
| | | | |
| Reduced Density | Tile 1 | -2.60E-03 | 3.24E-02 |
| Enhanced Boron Content | Tile 2 | -1.00E-05 | 2.00E-06 |

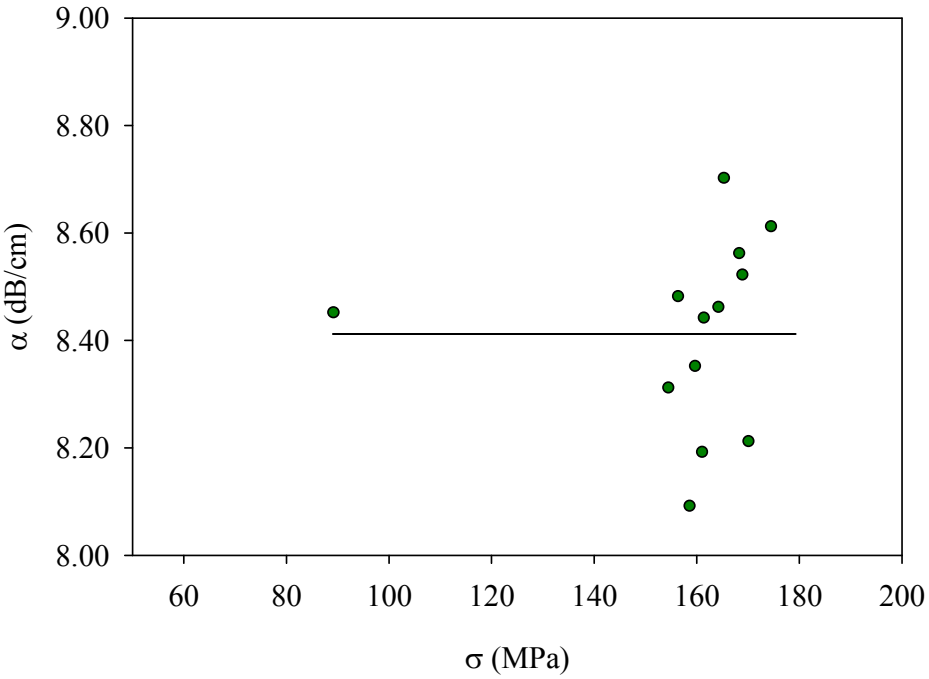


**Figure 5.86** Comparison of 20 MHz Attenuation Coefficient and 4-pt flexure strength results. Enhanced Boron Content Tile 2

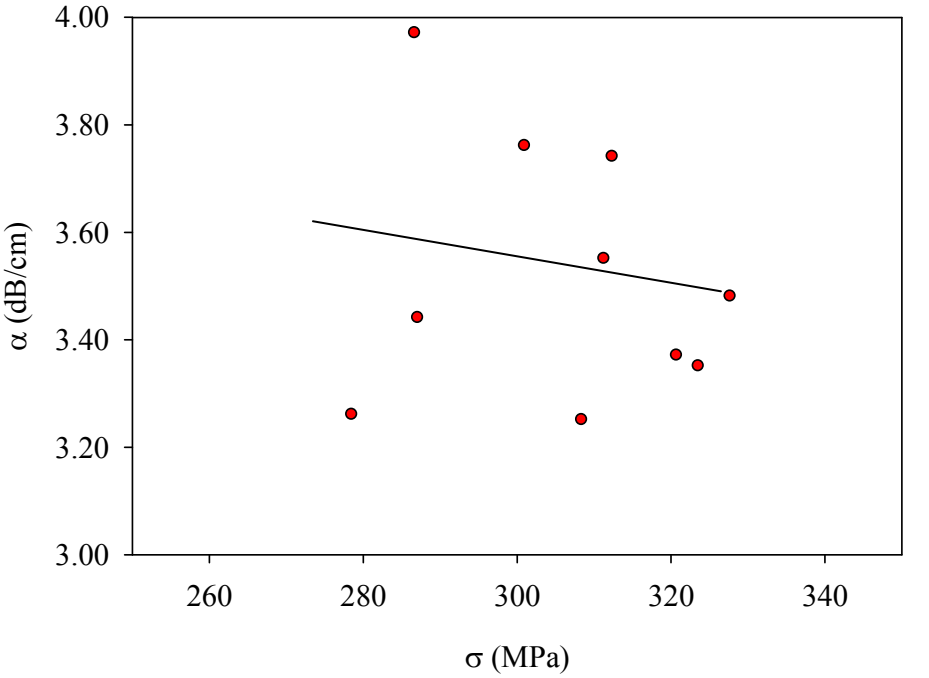


**Figure 5.87** Comparison of 20 MHz Attenuation Coefficient and 4-pt flexure strength results. Reduced Density Tile 1

### 5.4 Relationship between Strength, Density, and Attenuation Coefficient

A scatter plot which compares the 4-pt flexure testing results and the average bulk density of the tiles from the three sample sets is shown in Figure 5.88. The fit of the trend line which was applied to the data points indicates a lack of a linear relationship between the measured density of the starting tiles and the flexure strength of mechanical testing samples machined from these tiles.

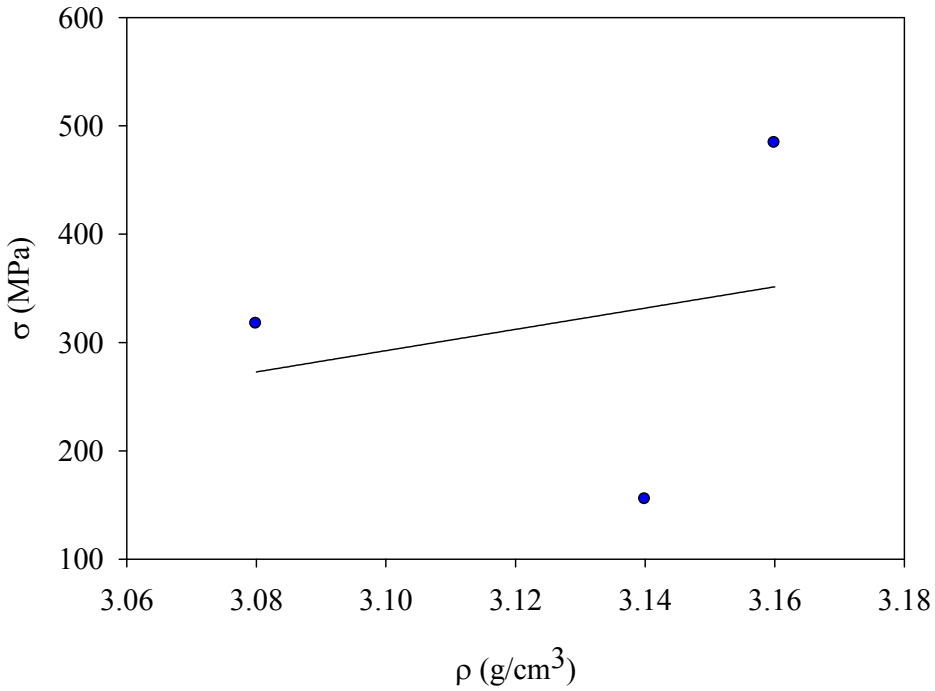


**Figure 5.88** Comparison of 4-pt flexure testing and bulk density. Commercial, Reduced Density, and Enhanced Boron Content tiles

This result was not entirely unexpected as fracture of a flexure sample required the presence of at least one strength-limiting feature within the high stress zone of the sample. The presence of a single strength-limiting feature within the volume which corresponded to each flexure bar was unlikely to alter the measured density of the starting tile.

A scatter plot which compares the 4-pt flexure testing results and the average 20 MHz attenuation coefficient of the tiles from the three sample sets is shown in Figure 5.89. The fit of the trend line to the data gives a strong indication of the presence of a linear relationship between the quasi-static flexure strength and the 20 MHz attenuation coefficient. This result indicated that while the contributions of individual strength limiting features were not able to be resolved in the acoustic testing, the acoustic testing was sensitive to bulk changes within the microstructures of the starting tiles.

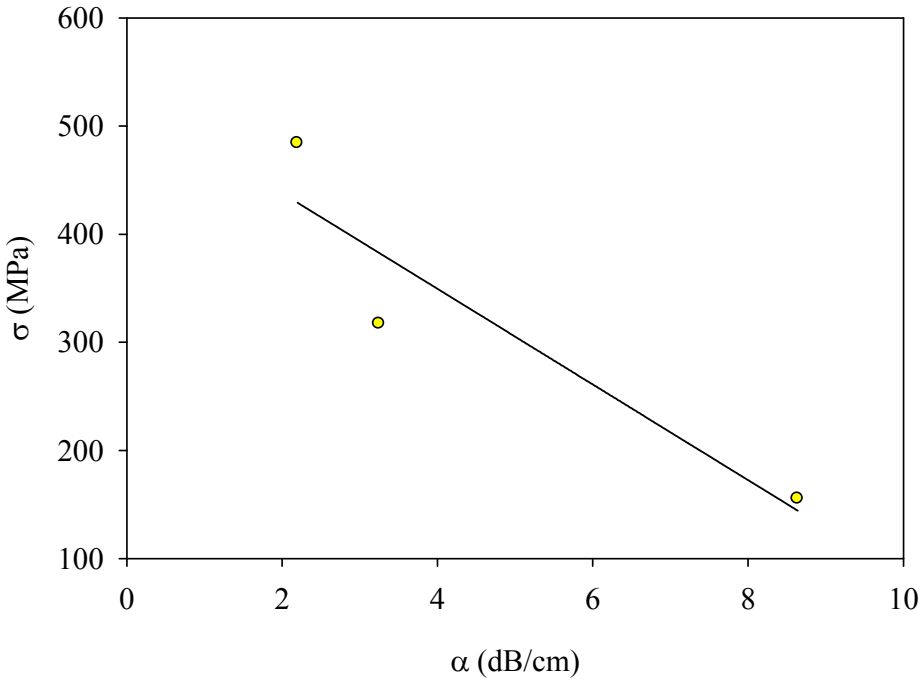


**Figure 5.89** Comparison of 4-pt flexure testing and 20 MHz attenuation coefficient. Commercial, Reduced Density, and Enhanced Boron Content tiles

## 5.5 Representative Microstructures of Sample Sets

### 5.5.1 Polished Sections

As a means of examining differences in the microstructure between the sample sets, images of polished sections were resolved in the FESEM. An empirical analysis as well as a determination of the average feature size within each of the images was performed. This section will include examples from each of the three groups of flexure bars.

As was discussed in Section 4.10, the quantitative image analysis conducted for this dissertation involved determining the number of pixels, and therefore the area, which comprised each identified feature within the images. A number of criteria were applied to the counting operation to exclude features in the images which were not inclusions.

#### 5.5.1.1 Shape Factor Determination

The shape factor, or circularity, of an object is a relation of the area of an object to its perimeter. It is given as:[179]

$$Circularity = 4\pi\left(\frac{Area}{Perimeter^2}\right) \quad \text{Eq. 84}$$

It is used as a method to distinguish a pullout or inclusion from a pore during image processing of a polished section. A pullout is a microstructural feature which weakens during the polishing operation and "*pulls out,*" or becomes detached from the microstructure.

Objects with a shape factor higher than the set value will be excluded from the counting operation. A perfect circle will have a value of 1.0.[191] A value of 0.7 – 0.8 has been applied in previous work in this area.[61]

As a means to establish the form factor which would be utilized during image processing, the inclusion shown in Figure 5.90 was analyzed using a number of different form factor values. This feature was identified by EDS to be a 1.7 μm by 1.6 μm boron carbide inclusion.

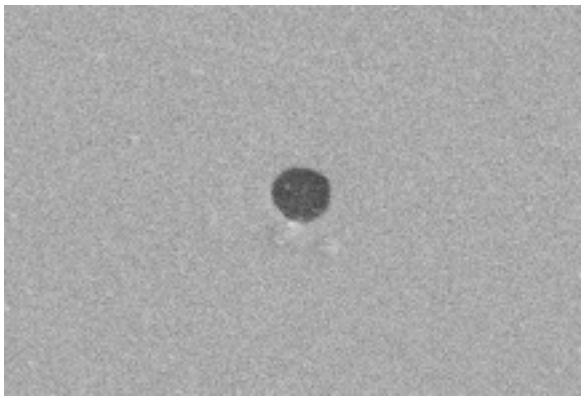

**Figure 5.90** Image of boron carbide inclusions used for shape factor determination. 12500x magnification

It was found that using the recommended value of 0.7 resulted in this feature being excluded from the counting operation. Values of 0.75, 0.8, and 0.85 were also tried with the same result. This feature was not identified during the counting operation until a shape factor value of 0.98 was utilized. Taking this result into account, a shape factor value was not used during the analysis of microstructural features.

#### 5.5.1.2 Size Factor Determination

During image processing, a criterion may also be applied to exclude objects outside of a size range from the counting operation. This may be used as a lower bound to eliminate "noise" or scattered pixels within the image from the counting statistics. The user may also choose to concentrate on features within a particular size range.

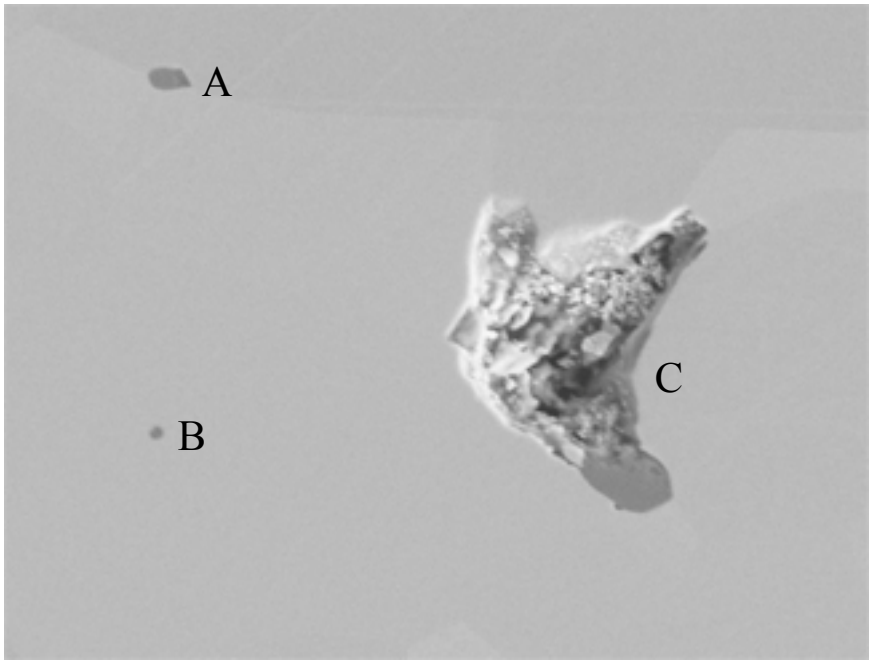


**Figure 5.91** Micrograph of polished SIC surface. Image includes two carbon inclusions and a pullout. 15000x magnification

Initial image processing iterations found that there were significant amounts of sub-micron features being counted during the operation. The following is an example of the tests done to determine if these small features represented inclusions, or where merely the result of noise within the image.

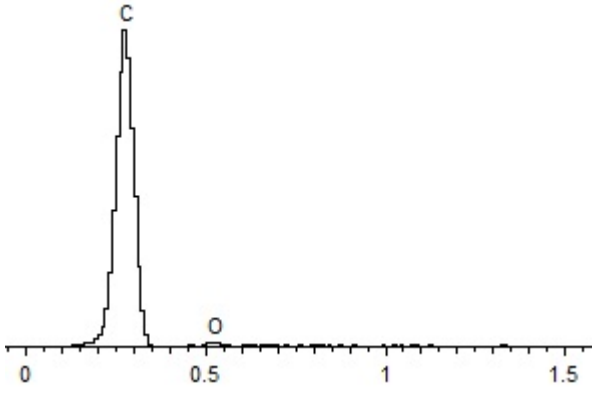


**Figure 5.92** EDS spectrum of carbonaceous inclusion. X-axis is in units of eV

In order to determine this, a series of images were analyzed. Two submicron microstructural features were located within a 15000x FESEM image of a polished SiC surface, as shown in Figure 5.91. Features A and B were found by EDS analysis to be carbon inclusions, with a peak corresponding to an X-ray $K_{\alpha 1}$ emission energy of 0.282 eV, as shown in Figure 5.92. The area of these inclusions was found to be 0.12 and 0.021 $\mu m^2$, respectively. Feature C appeared to be a pullout of an inclusion.

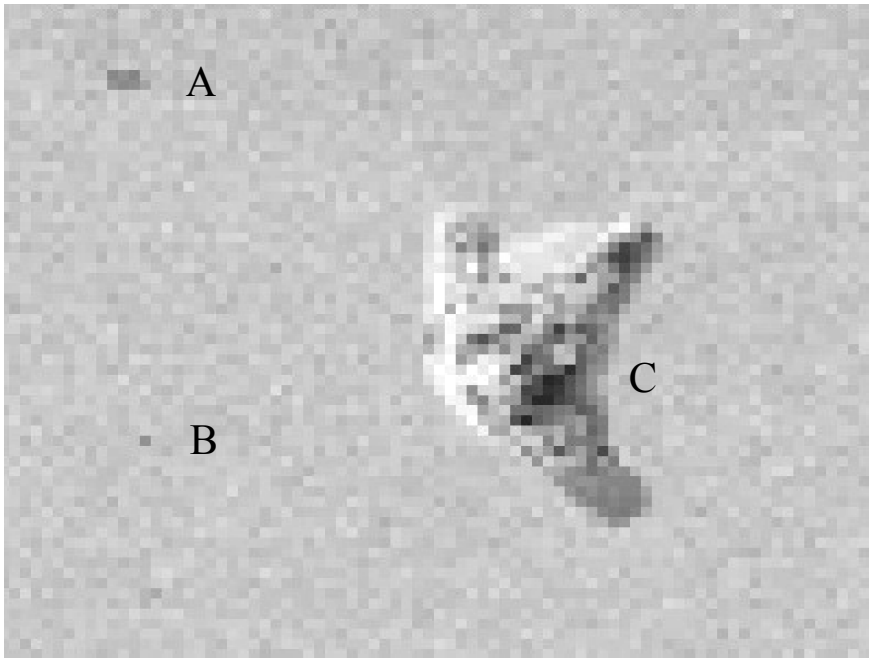


**Figure 5.93** Micrograph of polished SiC surface which corresponded to the same area as the image in Figure 5.85. Image included two carbon inclusions and a pullout. 1000x magnification

A portion of a 1000x magnification image is shown in Figure 5.93. This image corresponded to the same region of the sample surface shown in Figure 5.91. Based upon this image, the measured area of Feature A was 0.13 $\mu m^2$, an increase of 0.01 $\mu m^2$, while the area measurement of Feature B was constant at 0.021 $\mu m^2$. It was found that for a 1000x magnification FESEM image recorded at a resolution of 2048 x 1536 pixels, the

smallest feature area that was resolved was 0.021 $\mu m^2$. Taking this into account, for this dissertation, the image analysis of polished sections was undertaken without a lower bound for the size factor.

#### 5.5.1.3 Analysis of Second Phases

FESEM images of polished sections of SiC flexure bars are shown in Figures 5.94 through 5.99. Two examples from each group of bars were examined. Polished surfaces of the commercial samples are shown in Figure 5.94 and 5.95, images of the Enhanced Boron Content tiles are shown in Figure 5.96 and 5.97, while images of the Reduced Density tiles are shown in Figures 5.98 and 5.99. The number and the area of the features within the images were analyzed according to the procedures established in Section 4.10, using the criteria determined in Sections 5.4.1.1 and 5.4.1.2.

All images were resolved at 1000x. The microstructures of the flexure bars appeared to be comprised of grains of the SiC matrix, small inclusions (area < 25 $\mu m^2$), as well as polishing pullouts. Figure 5.96 is an image of an Enhanced Boron Content flexure bar. Within the image are three large porous boron carbide inclusions, with measured areas of 1339 $\mu m^2$, 924 $\mu m^2$, and 453 $\mu m^2$. Figure 5.97 is of a region of the surface of this same flexure bar which contains a portion of two large porous boron carbide inclusions. Images of the polished surface of a Reduced Density flexure bar are shown in Figure 5.98 and 5.99. The features shown in these images are indicative of the microstructure of these samples as they contain dispersed clusters of partially compacted and deformed spray dried granules and associated intergranular pores.

**Table 5.34** Polished section image analysis. Average feature size and area fraction. Commercial samples, Reduced Density samples, and Enhanced Boron Content samples

| | Hexoloy A | Hexoloy B | Enhanced Boron Content A | Enhanced Boron Content B | Reduced Density A | Reduced Density B |
|---|---|---|---|---|---|---|
| | | | | | | |
| Average Size ($\mu m^2$) | 0.87 | 0.83 | 0.82 | 0.85 | 0.87 | 0.84 |
| Area Fraction (%) | 3.2 | 3.6 | 3.4 | 3.6 | 3.5 | 3.4 |
| % sub-micron features | 72.1 | 73.2 | 72.3 | 70.5 | 70.9 | 71.8 |
| Area % sub-micron features | 19.1 | 23.2 | 22.8 | 20.4 | 21.2 | 22.5 |

The results of the feature counting operations are shown in Table 5.34. For the Enhanced Boron Content flexure bars, the area corresponding to the large porous boron carbide inclusions were removed from the statistics. Likewise, the values which corresponded to the clusters of compacted granules were removed from the statistics for the Reduced Density tiles. For all of the sample groups, area values which correlated to large, visible pullouts (area > 4 $\mu m^2$) were also removed from the counting statistics. The average size of features within the six images ranged between 0.82 and 0.87 $\mu m^2$. This amounted to an average area fraction of 3.5%. It was found for the six samples that while the number of sub-micron features accounted for approximately 72% of the measured features, the area occupied by these features was only 21.5%.

For Figure 5.96, the counting statistics correlated to the area enclosed by the dashed rectangle. The intent with this operation was to determine the difference in feature size both near and away from large porous boron carbide inclusions. The results indicated a difference of approximately 2% in feature size between the two images. This equaled the measured difference in average feature size amongst the six images.

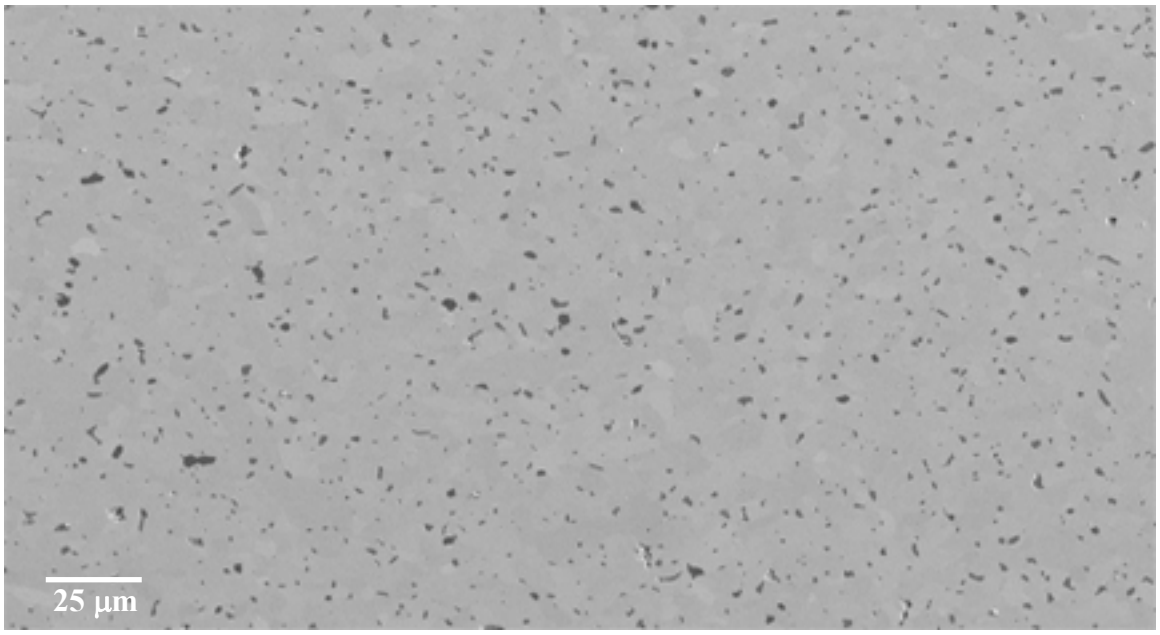


**Figure 5.94** Polished section of Hexoloy® flexure bar. Imaged area included numerous (<12 $\mu m^2$) inclusions, and polishing pullouts. Image analysis performed over entire region. Largest feature is a 23 $\mu m^2$ boron carbide inclusion. 1000x magnification

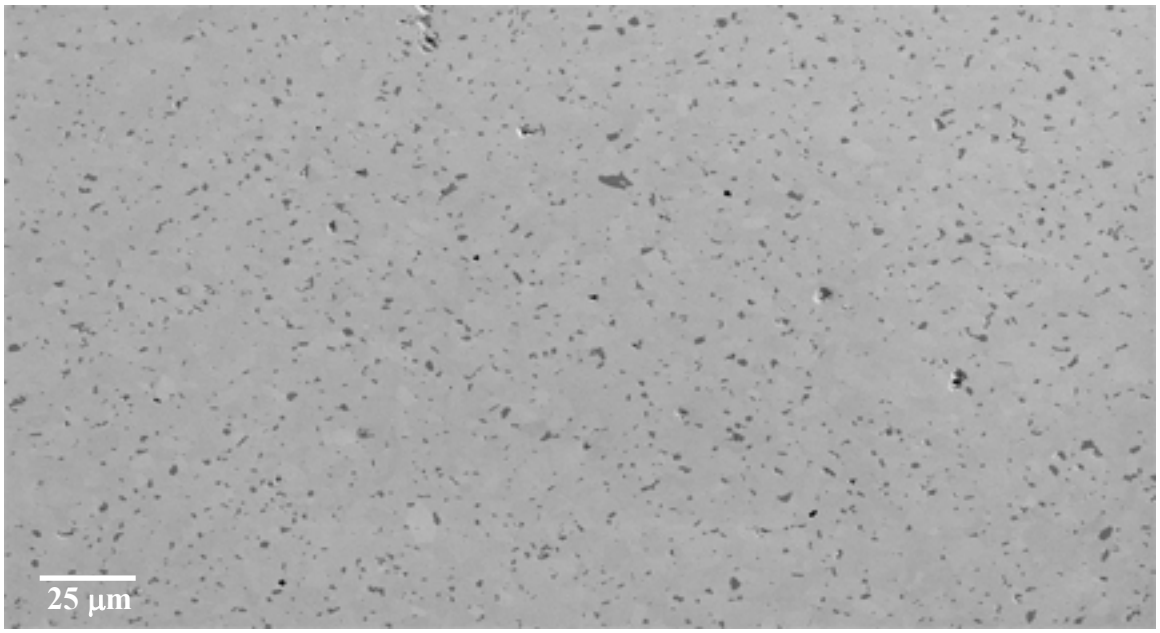


**Figure 5.95** Polished section of Hexoloy® flexure bar. Imaged area numerous (<12 $\mu m^2$) inclusions, and polishing pullouts. Image analysis performed over entire region. Largest feature is a 18 $\mu m^2$ boron carbide inclusion. 1000x magnification

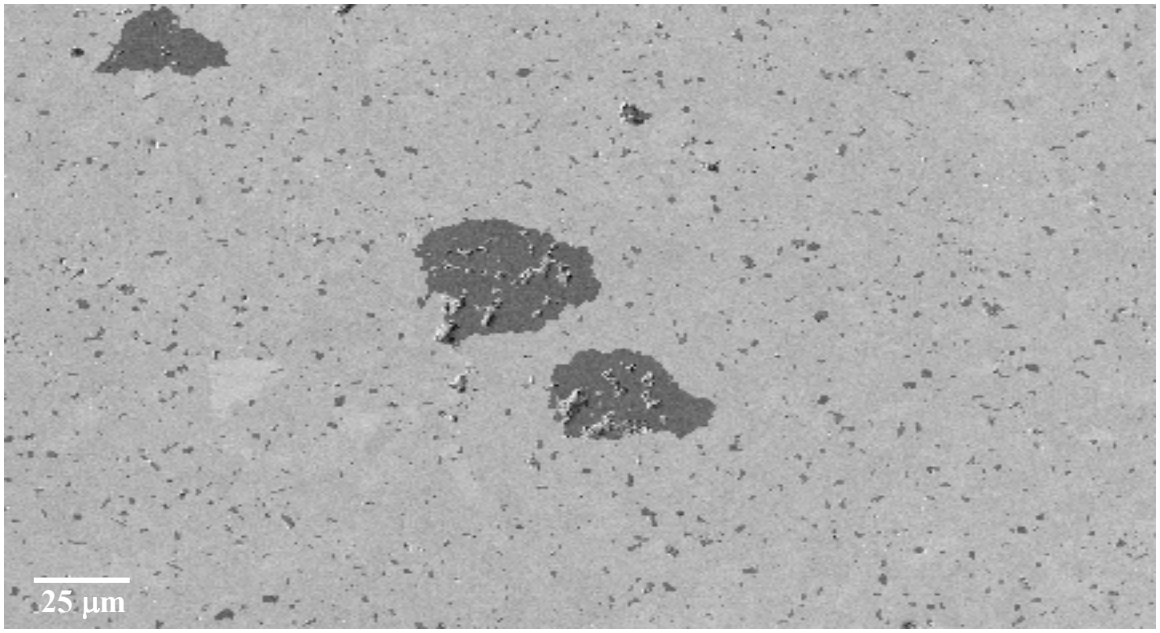


**Figure 5.96** Polished section of Enhanced Boron Content flexure bar. Imaged area contained three *"large"* porous boron carbide inclusions, as well as numerous (<12 $\mu m^2$) inclusions, and polishing pullouts. Image analysis performed over entire region. 1000x magnification

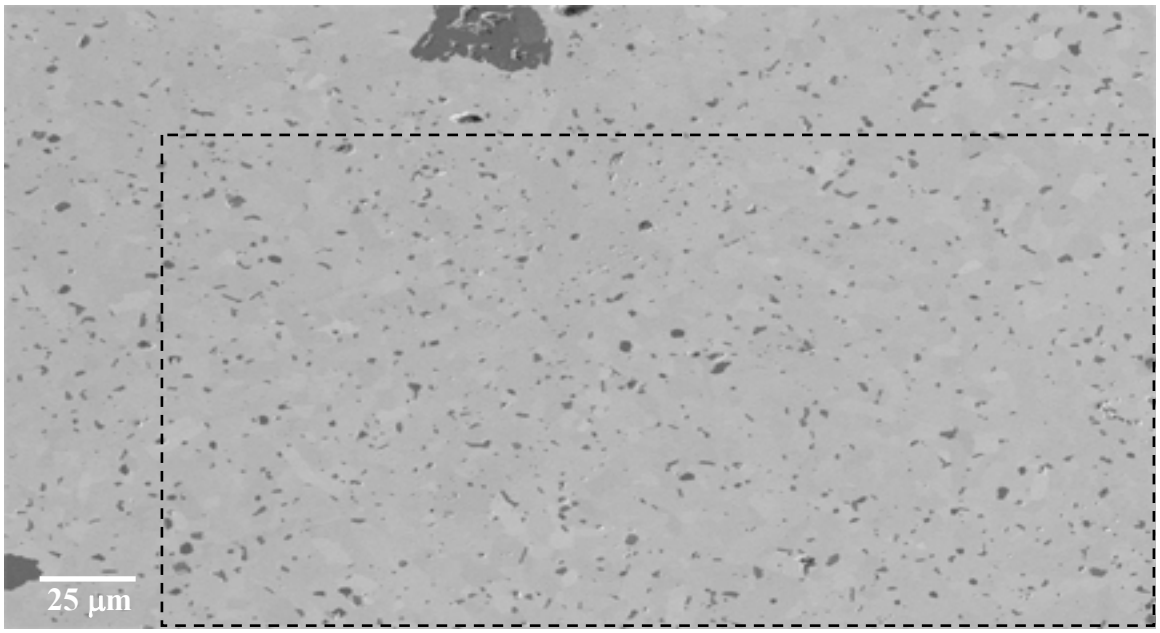


**Figure 5.97** Polished section of Enhanced Boron Content flexure bar. Imaged area contained portions of "*large"* porous boron carbide inclusions, as well as numerous (<12 $\mu m^2$) inclusions, and polishing pullouts. Image analysis from portion enclosed by rectangle. 1000x magnification

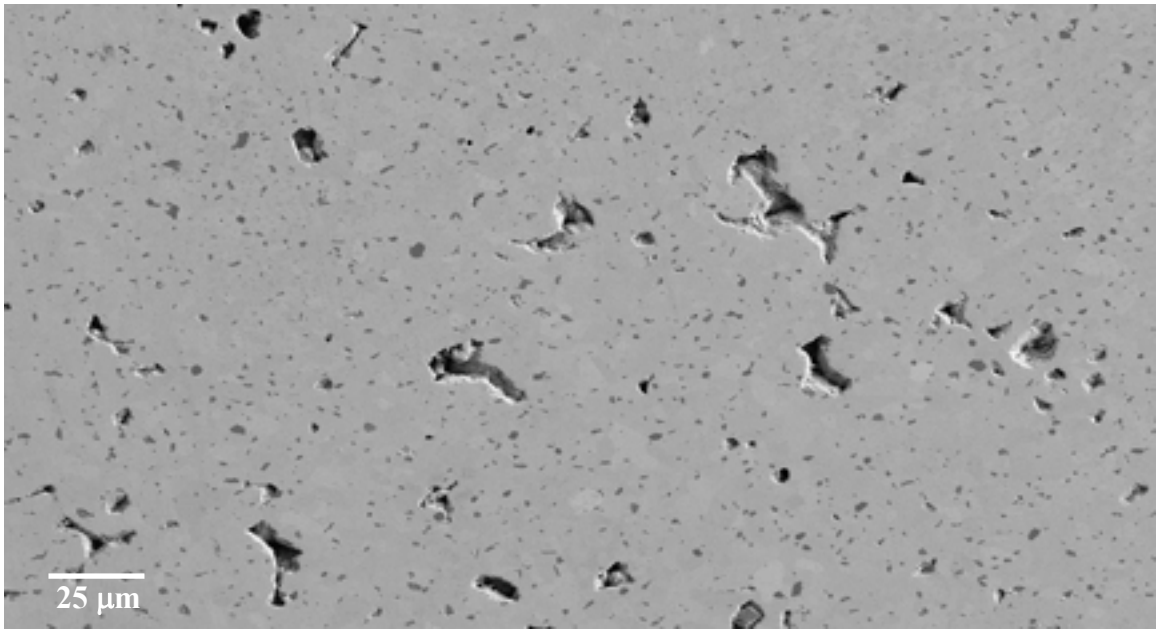


**Figure 5.98** Polished section of Reduced Density flexure bar. Imaged area contained many clusters of partially compacted spray dried granules, as well as numerous (<12 $\mu m^2$) inclusions, and polishing pullouts. 1000x magnification

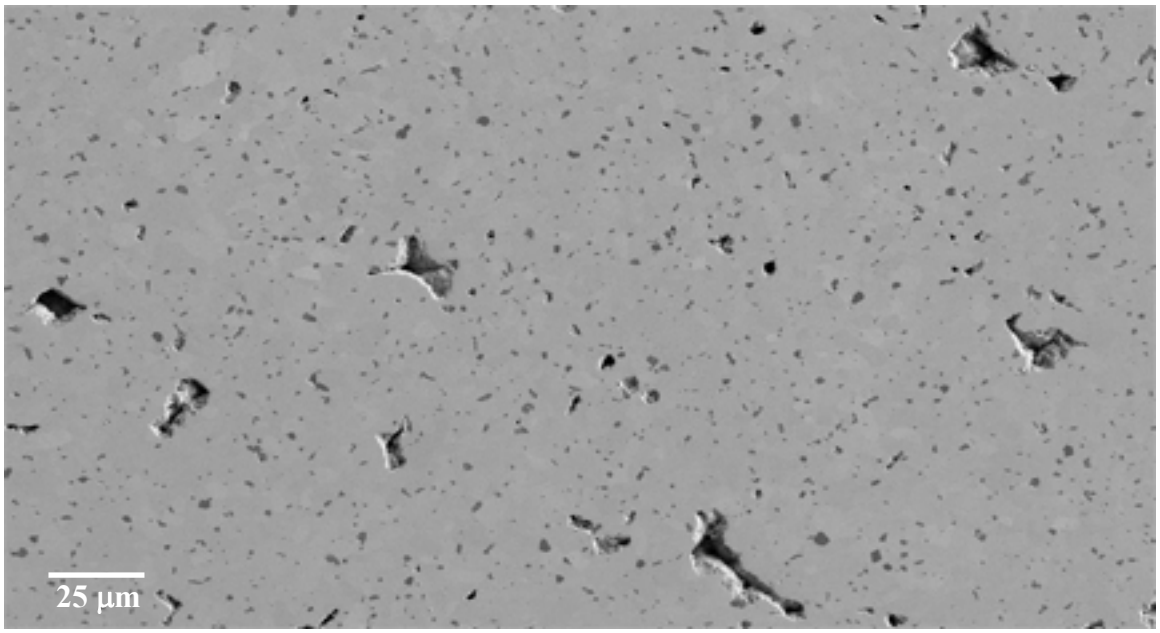


**Figure 5.99** Polished section of Reduced Density flexure bar. Imaged area contained many clusters of partially compacted spray dried granules, as well as numerous (<12 $\mu m^2$) inclusions, and polishing pullouts. 1000x magnification

#### 5.5.1.4 Analysis of Porous Boron Carbide Inclusions

An image of a polished cross section from an Enhanced Boron Content flexure bar is shown in Figure 5.100. The feature of interest is a porous boron carbide inclusion, which measured 141 μm by 95 μm. Fracture surfaces which contained features such as these were examined in Sections 5.1.3.11 and 5.2.2.6. Those flexure bars machined from the EBC tiles were found to have fractured at clusters of inclusions such as these. In comparison to the commercial samples and the Reduced Density tiles, the bars from these tiles were found to have fractured at drastically reduced strengths. In comparison to the largest such inclusion found in the Hexoloy® tiles, the cross section of this inclusion was over three times the area.

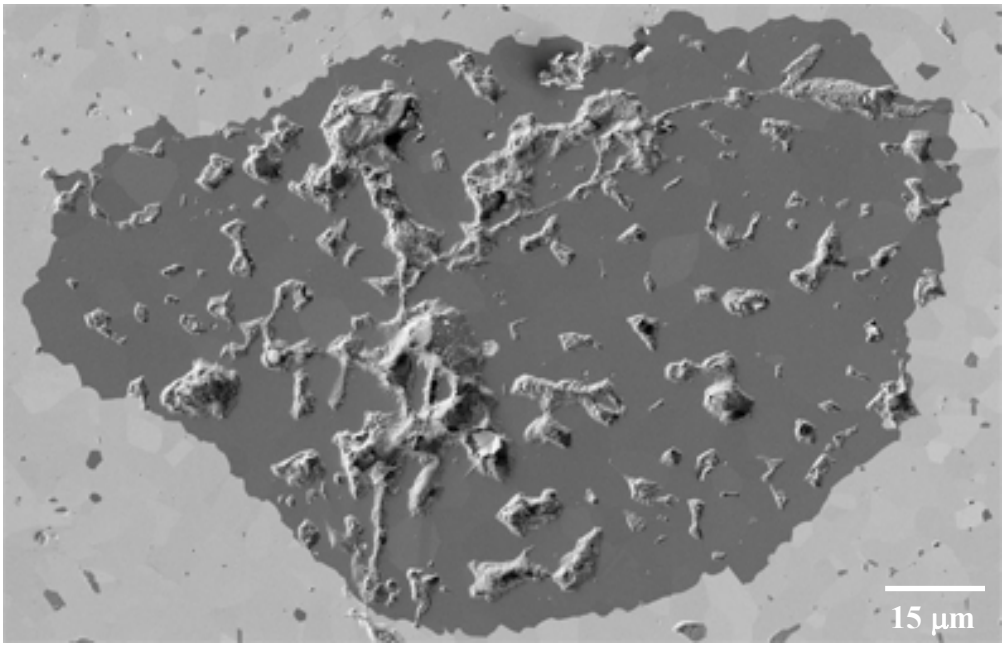


**Figure 5.100** Porous boron carbide inclusion in polished section of an Enhanced Boron Content flexure bar. 2000x magnification

Image processing was applied to the polished cross section of this inclusion to determine the amount of void space as a percentage of the overall area of the inclusion. The procedures set forth in Section 4.10 were used to determine the overall area of the inclusion, and the total area of the void space within it.

A cropped image of this inclusion is shown in Figure 5.101. Pixels in the image which were not contained with the cross section of the inclusion were removed. The image was then converted to binary, with the black pixels corresponding to the area of the cross section of the inclusion, as shown in Figure 5.102. The image analysis counting operation determined the area of this inclusion to be 9236 $\mu m^2$.

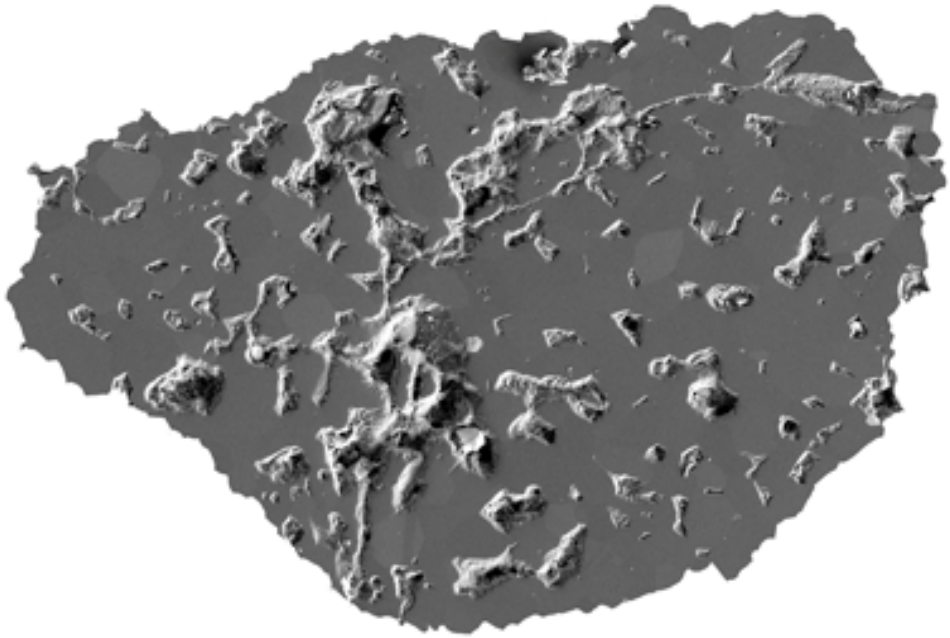

**Figure 5.101** Porous boron carbide inclusion on polished section of SiC flexure bar. Image has been cropped such that it contains only the inclusion

**Figure 5.102** Porous boron carbide inclusion on polished section of SiC flexure bar. Image has been converted to binary. Filled area corresponds to visible cross section of inclusion

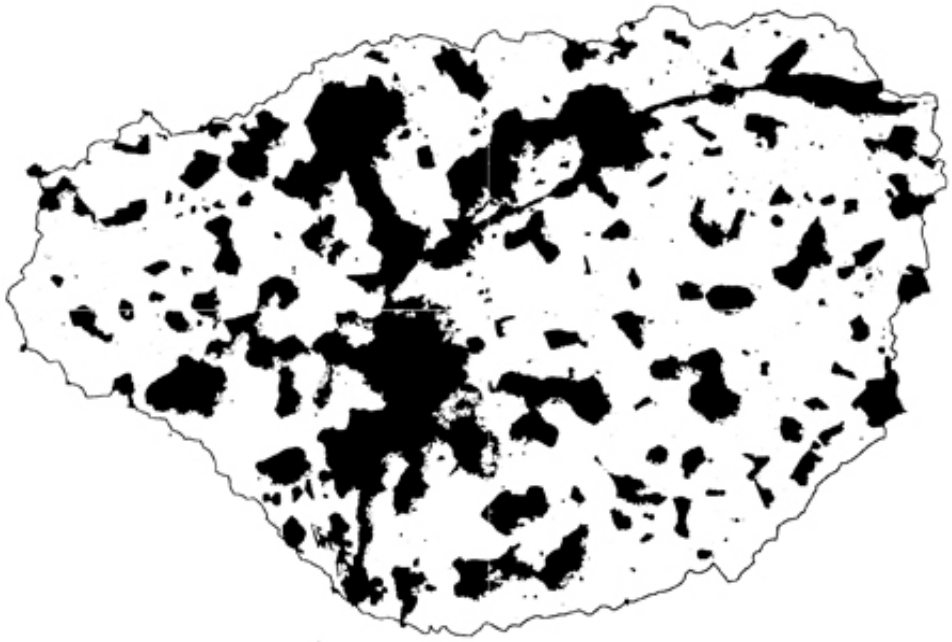

**Figure 5.103** Porous boron carbide inclusion on polished section of SiC flexure bar. Image has been converted to binary. Filled area corresponds to void space within the cross section of the inclusion

The image of the inclusion in Figure 5.101 was divided into four quarters. The number of pixels corresponding to the void space within each quarter was determined. Following the counting operation, it was shown that the void space within the four quarters totaled 2752 $\mu m^2$. This corresponded to an area fraction of 29.8%. The void space analysis of the four quarters was combined, as shown by the combined binary image in Figure 5.103. The cross sections of two additional inclusions were analyzed in the same manner. For these examples, the void space amounted to 25.3% and 28.2% of the area of the inclusion.

The strength of the flexure bars which contained these large boron carbide inclusions can be attributed to the porous nature of these features. Both the Young's modulus and strength of material have been empirically shown to be related to porosity according to the equations:[192]

$$E = E_o e^{-bP} \quad \text{Eq. 85}$$

$$\sigma = \sigma_o e^{-bP} \quad \text{Eq. 86}$$

Where $E_o$ is the Young's modulus at zero-porosity, $\sigma_o$ is the strength at zero-porosity, $P$ is the ratio of the volume of porosity to the total volume, and $b$ is a material constant. These are known as the Ryshkewitch-Duckworth equation and the Spriggs' equation, respectively.[193, 194] Values for $b$ have been determined through experimentation, with a value of 4 being extrapolated from an analysis of alumina bending strength samples.[195]

When applied to the results of the image analysis and strength testing of the commercial and enhanced boron content samples, the strength values as calculated by Eq. 86 were in agreement with the tested results. In this analysis, the zero-porosity strength value was taken to be the average strength of the commercial sample flexure bars, while the area fraction of porosity calculated above was assumed to be analogous to the volume fraction of porosity. The results of this analysis are shown in Table 5.35. The predicted value was found to vary from the measured value by less than 4 %.

**Table 5.35** Spriggs analysis of Hexoloy® and Enhanced Boron Content flexure bars

| $\sigma_o$ (MPa) | $b$ | $P$ | $\sigma$ (MPa) |
|---|---|---|---|
| | | | |
| 485 | 4 | 0.275 | 161 |

### 5.5.1.5 Analysis of Granule Compaction

A FESEM image of a polished section of a Reduced Density flexure bar is shown in Figure 5.104. The dominant feature in the image is an intergranular pore which is located between clusters of partially compacted spray dried granules. For the Reduced Density flexure bars, fracture was thought to have initiated at the locations of intergranular pores within these clusters. Circles which approximate the outline of four interconnected granules have been added to the image.

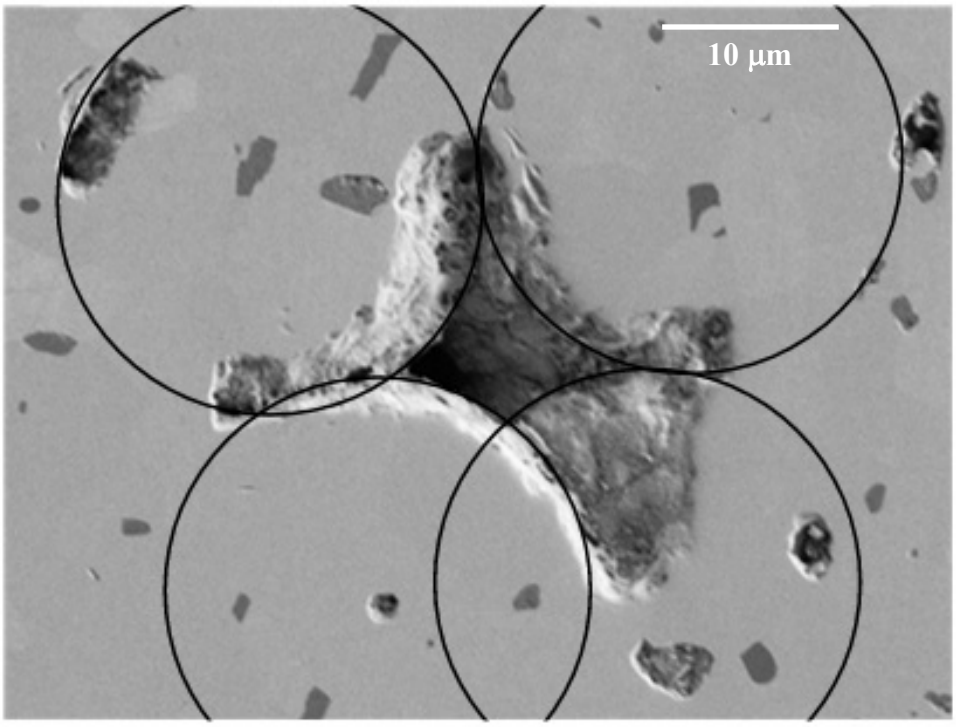


**Figure 5.104** Partially compacted granules in a polished section of a Reduced Density flexure bar. The circles approximate the shape and separation of the granules. 3000x magnification

As previously stated, one of the important aspects of dry pressing is to compact and deform the spray dried granules such that they knit together, as well as a reduction in the void space between granules occurs. As shown in Figure 5.105, the stability of a pore

during sintering is dependent on the dihedral angle between grains and the number of grains surrounding the pore. At the conditions above the line in the image, a pore will tend to shrink during sintering. Below the line, pores will grow during sintering and remain in the fired part. When granules are well compacted, the dihedral angle between grains on the periphery of these granules are large. As can be seen, for large dihedral angles, the shrinkage behavior of the pore is independent of the number of grains surrounding it. For un-knitted granules, where dihedral angles are small, the stability of a pore is dependent on the number of grains which surround the pore.

The total number of pores should be considered in three dimensions. In Figure 5.104, within the cross-section of the intergranular pore, it can be seen that the pore makes contact with four granules, which prevented shrinkage of the pore during sintering.

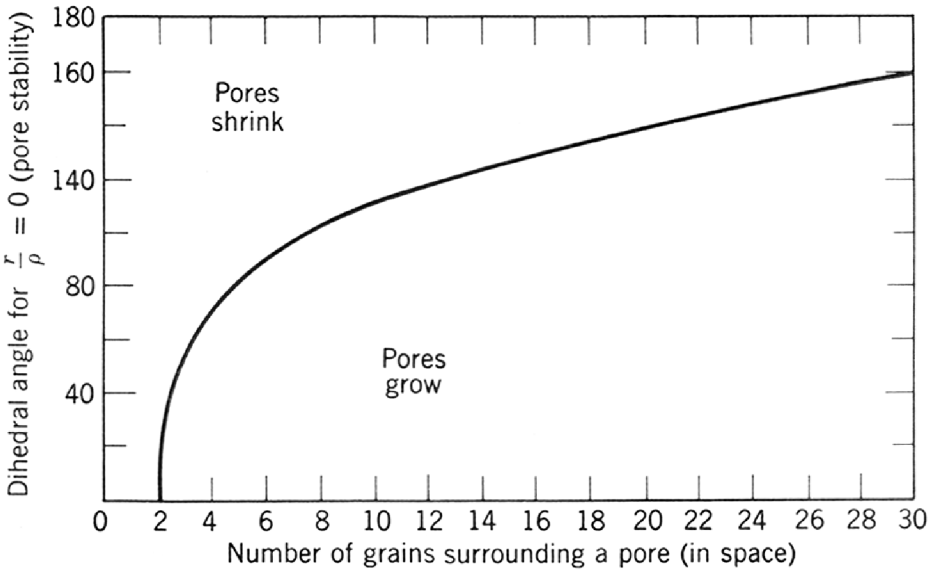


**Figure 5.105** Relationship of dihedral angle and number of surrounding pores in determining pore behavior during sintering[39]

### 5.5.2 Fracture Surfaces

SEM images of fracture surfaces of each type of bar are shown in Figures 5.106 – 5.108. This group of images was recorded at 1000x, which corresponded to an area of approximately 300 μm x 200 μm. The three bars examined in this section were all broken under quasi-static loading conditions.

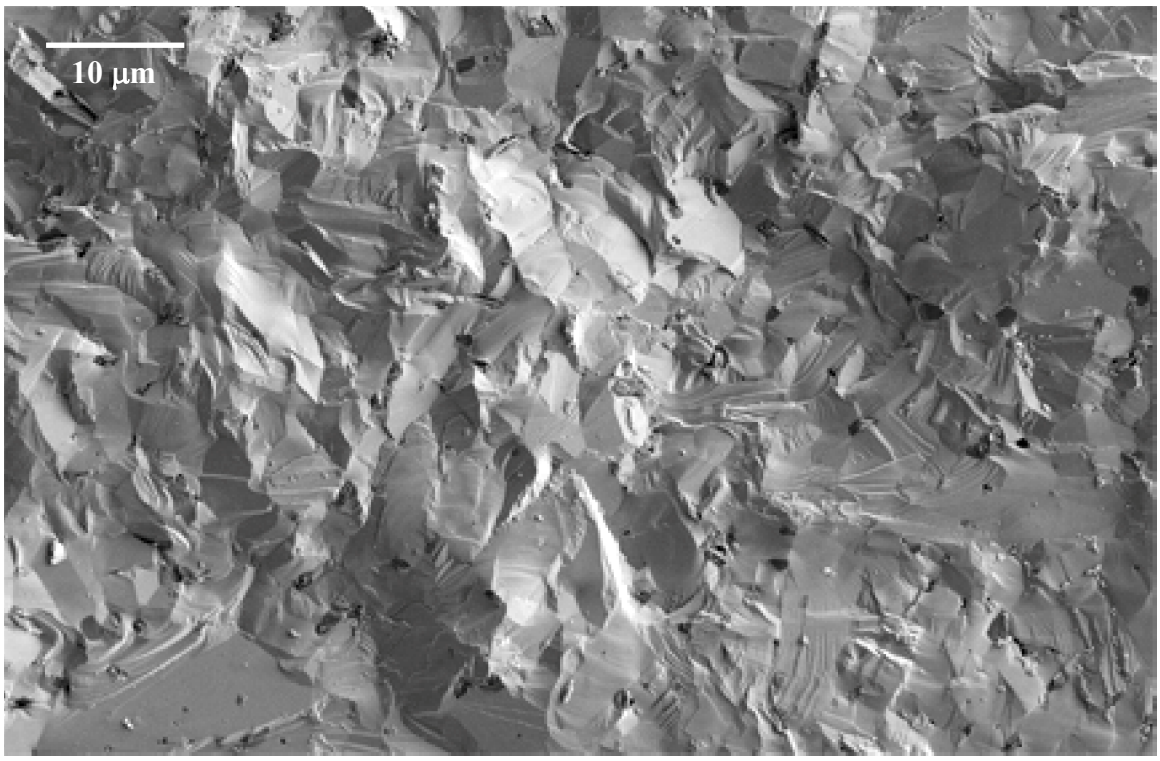


**Figure 5.106** Fracture surface. Hexoloy® bar. 2500x magnification

The fracture surface of a commercial Hexoloy flexure bar is shown in Figure 5.106. The fracture behavior appears to be pre-dominantly transgranular. This is where the fracture path tends to travel through a grain rather than through the grain boundary. Examples of intergranular verses transgranular fracture were examined in Section 2.4.2. The presence of hackle lines can be discerned in the image. These are lines in the fracture surface that are parallel to the localized stress field. Also included within the

microstructure are numerous micron-sized boron and carbon inclusions, which correspond to the sintering additives for this type of material.

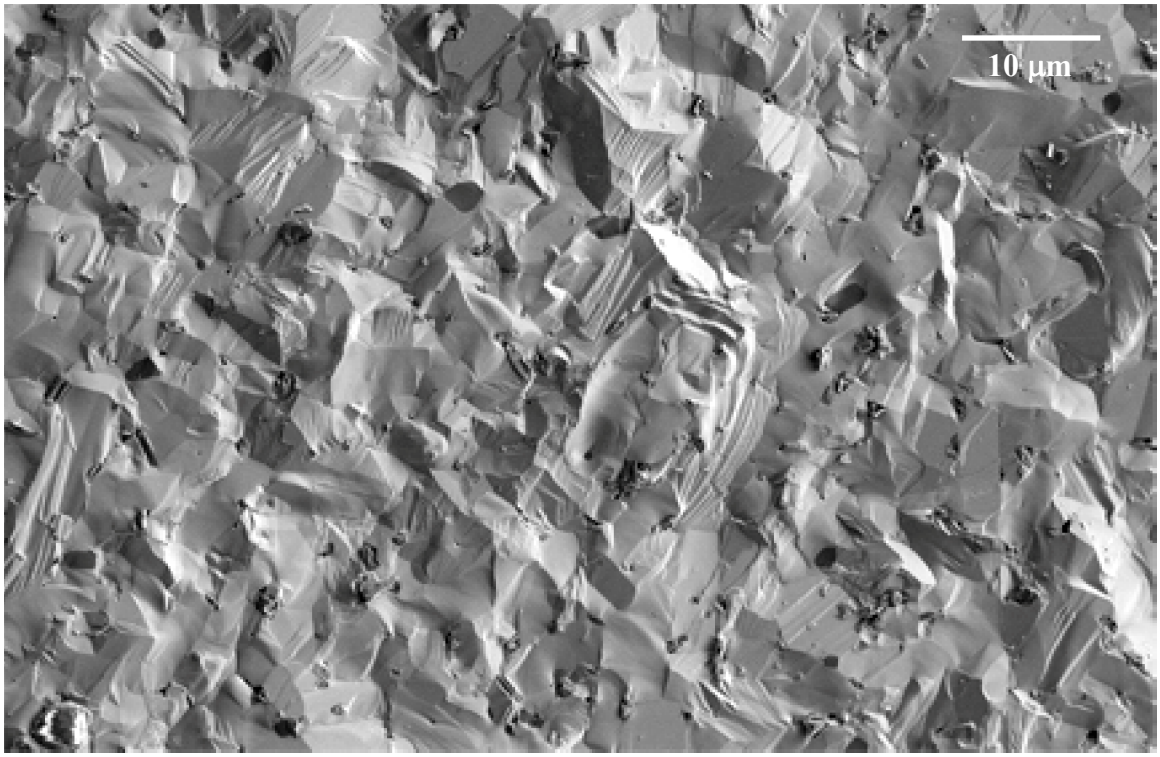


**Figure 5.107** Fracture surface. Enhanced Boron Content bar. 2500x magnification

An image of the fracture surface of an Enhanced Boron Content flexure bar is shown in Figure 5.107. The region shown here was located away from the large, porous boron carbide inclusions examined in Section 5.2.3.6. It can be seen that the fracture behavior is very similar to that which corresponded to the commercial SiC sample. It is believed that the excess boron content which was added to the powder batch for these tiles formed large agglomerates which were consolidated into the green body, while the remainder of the microstructure developed in a way that was similar to the commercial samples.

The third fracture surface example is shown in Figure 5.108. This image is of a Reduced Density flexure bar. As with the polished section of this bar, the dominant features on the fracture surface are the clusters of partially compacted granules and the voids located around them. As with the EBC flexure bar, the fracture surface gives clues to microstructural development during firing in that the fracture surface around these clusters again looks similar to the commercial sample. This was to be expected as the same amount of boron and carbon sintering activators were added to these tiles as was used to sinter the commercial samples.

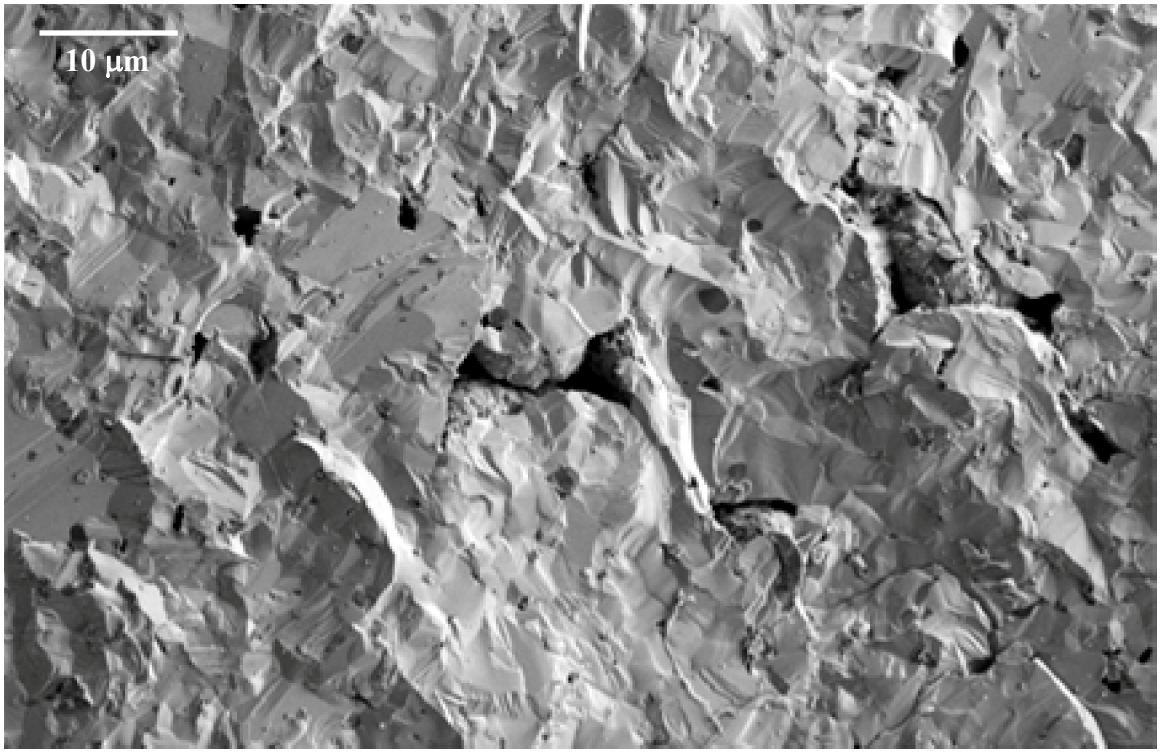


**Figure 5.108** Fracture surface. Reduced Density bar. 2500x magnification

## 6. Conclusions

Multiple sample sets of sintered silicon carbide tiles were examined to determine the extent of microstructural and acoustic and mechanical property variability. These included both commercially available silicon carbide tiles as well as specially prepared sample sets. Several analysis tools were employed to examine the variability of these properties within each sample set and between sample sets.

Three sample sets were examined. One was comprised of Hexoloy® sintered silicon carbide tiles. Two additional sample sets were produced specifically for the purposes of this study. Designated "targeted samples," both groups of tiles were pressurelessly sintered and contained sintering additives which are utilized in the densification of commercial silicon carbide materials. One group of tiles was compacted to a reduced green density and was found to contain clusters of partially compacted spray dried granules. The other group of tiles contained an excess of boron sintering additive, which was added in the form of boron carbide, and was found to contain clusters of 100 – 200 μm sized porous inclusions of this material.

Non destructive evaluation was performed on the Hexoloy® commercial sample set to separate the tiles and select samples for mechanical testing. For those tiles selected for mechanical testing, the average bulk density and 20 MHz acoustic attenuation coefficient were found to be 3.16 g/cm$^3$ and 2.20 dB/cm, respectively. The average 4-pt flexure strength was measured at 484 MPa. This was the average strength of those bars which were found to have fractured due to intrinsic features. These included spray dried granule compaction relics and porous agglomerates of boron carbide sintering aid.

The correlation between the quasi-static strength results and ultrasonically determined acoustic properties was examined both qualitatively and quantitatively. It was found that fracture location did not correlate with the presence of acoustic anomalies within the ultrasound C-Scan property maps. It was determined that a correlation did not exist between average strength and acoustic property values in the vicinity of the fracture location. This was thought to have resulted from insufficient measured variation in the acoustic properties, specifically the 20 MHz attenuation coefficient.

The first group of targeted samples was comprised of the SiC tiles which were pressed to a reduced green density and then pressurelessly sintered. These tiles were designated the Reduced Density (RD) tiles. Average bulk density and 20 MHz attenuation coefficient values were 3.08 g/cm$^3$ and 3.25 dB/cm, respectively. In comparison to the commercial samples, these values represented a decrease and an increase of approximately 2.5% and 150%, respectively. Four-point flexure testing of machined samples resulted in an average strength of 317 MPa. This amounted to a decrease of 33% when compared to the commercial samples. Examination of the fracture surfaces and polished sections of these flexure samples revealed the presence of partially compacted and deformed spray dried granules. Fracture was found to have resulted at the location of clusters of these granules, and the intergranular porosity between them.

The second group of targeted samples was comprised of pressurelessly sintered SiC tiles which contained an excess of boron sintering additives. Designated the Enhanced Boron Content (EBC) tiles, they contained additive amounts which were six times that utilized for densification of the commercial samples. Bulk density was measured to be 3.14 g/cm$^3$, which amounted to only a 1% reduction from the Hexoloy®

samples. The mean 20 MHz acoustic attenuation coefficient was found to be 8.64 dB/cm, which represented an increase of 400% in comparison to the commercial tiles. Flexure samples machined from these tiles were also tested, which resulted in an average strength value of only 155 MPa, for a reduction in average strength of 66%.

Large porous inclusions are believed to have resulted from agglomerates of sintering aid which were not broken up during the mixing process and were therefore present in the green body. During firing of these green bodies, those portions on the periphery of these agglomerates densify and become well-bonded to the surrounding silicon carbide material, while the void spaces within these agglomerates are too large to close during sintering and then remain in the fired part. Image analysis of polished sections of these features showed that they contained between 25 to 30% void space.

In a similar way, the intergranular porosity present between partially compacted spray granules decreased the fracture strength of a flexure bar during a strength test. Proper compaction and deformation of spherical shaped, spray dried granules during dry pressing was required to ensure sufficient densification during the firing of the green body. Image analysis of the dihedral angles and number of grains surrounding the pores between granules showed that sufficient compaction and knitting of granules did not occur during dry pressing of the Reduced Density samples.

Determination of the critical features of low strength flexure bars machined from the commercial samples showed that isolated cases of these two types of features were found in these tiles. The flexure strength of bars where fracture was attributed to these features was similar. It can be seen that the affect of these types of features on density and average strength was exacerbated by clustering and/or the size of the feature

The reduction in density of the Reduced Density SiC tiles appeared to be a function of the intergranular pores located between spray dried granules. As these tiles were pressed to a reduced green density, sufficient compaction and deformation of the granules did not occur, leading to porosity which did not close during sintering. The very low average strength of the Enhanced Boron Content tiles in comparison to the commercial samples has been attributed to the presence of clusters of porous boron carbide inclusions, which resulted from agglomerates of boron sintering additives in the green body. While the bulk density of these tiles was only reduced by 1% when compared to commercial tiles, there was a reduction in strength of over 66%. As was shown by the results of the evaluation of the commercial tiles, neither of these microstructural features is likely to be found in a commercially produced SiC tile to this degree. Both results show the role that proper processing has on the final properties of a sintered ceramic tile.

The porous regions in the Reduced Density tiles had a greater effect on the bulk density measurements than the porous inclusions in the Enhanced Boron Content tiles, while these inclusions are much more deleterious to strength values than their contribution to the overall density. This is thought to be attributed to the size and the porous nature of these inclusions, which results in a localized reduction in elastic modulus and strength.

Within the context of these three sample sets, there does not appear to be a correlation between the measured bulk density of a tile and the average strength of a flexure bar machined from this tile. The fit of the trend line applied to the data indicated a lack of linear relationship between the bulk density of the starting tiles and the fracture

strength of flexure bars machined from these tiles. This was not unexpected, as fracture of a bend bar depends upon the presence of a single strength limiting feature, such as an inclusion or compaction relic, in the high stress region of the flexure test. A single strength-limiting feature within the volume attributed to each flexure bar is unlikely to alter the measured density of the tile.

The correlation between mechanical and acoustic properties was examined for all three sample sets. In the analysis of the commercial samples, it was found that ultrasound C-Scans performed at 20 MHz were unable to detect local scale differences, on the scale of a fracture inducing defect, in acoustic properties in sintered silicon carbide materials. There was much greater variability in the strength results than what was detected in the acoustic testing within each tile.

Ultrasonic testing showed that there were differences in the measured value of the acoustic attenuation coefficient across the different sample sets. The fit of the trend line applied to the data indicated that a strong relationship existed between the average acoustic attenuation coefficient of the starting tiles and the strength of the flexure bars machined from these tiles. It can be concluded that while localized differences in strength or microstructure are not manifested in the ultrasound measurements, bulk changes in the microstructure are resolved in the average value of the 20 MHz attenuation coefficient between the three sample sets.

## 7. Future Work

This dissertation sought to determine the effect which the variability present in the microstructure of sintered silicon carbide samples had on the mechanical and acoustic properties of these materials. It is believed that the results of this study lead to many possibilities for further experimentation within this area.

The initial stage of this dissertation involved the comparison of the results of quasi-static flexure testing and ultrasound acoustic testing for a group of commercially available sintered silicon carbide tiles. The strength of samples undergoing this type of testing relies upon the weakest link theory, in that the weakest flaw results in the failure of the entire test body.

One option for further experimentation would be to conduct a similar study that employed tensile testing. During flexure testing, only a small proportion of the volume of the sample is under maximum stress. As discussed in Section 2.3.4.2, the maximum tensile stress of a rectangular flexure sample occurs along the bottom surface of the bar, within the zone between the upper loading pins. The stress along the bottom surface is not constant, and decreases from the maximum value to zero between the locations of the upper and lower pins. The degree of applied stress also varies depending on the position within the height of the sample. Between the lower support pins, the applied stress decreases linearly from a maximum at the bottom surface to zero at the neutral axis, which his located halfway between the top and bottom surfaces.

Within the gage length of a tensile testing sample, the application of stress is constant over the entire cross-section.[71] Therefore, a much larger volume of the sample is put under maximum stress. This greatly increases the likelihood of exposing the presence

of a large strength-limiting feature within the sample. Additionally, the fracture strength of flexure testing samples is very susceptible to the presence of scratches on the tensile surface. During this study, a significant proportion of the commercial tile flexure bars were found to have fractured at the locations of machining scratches. While the machining of tensile testing samples does have an effect on the measured strength, this type of sample is much less susceptible to surface machining scratches.

A second option for future work would be to carry out a similar study involving ballistic testing. One of the intents of this dissertation was to be a step in the process of developing a quick non destructive evaluation of ceramic tiles, specifically those used for armor applications. As was stated previously, strength testing of samples in the quasi-static strain rate region is dependent upon the weakest link theory, which requires the presence of one strength-limiting flaw in the high stress region of the sample. During high strain rate ballistic events, it is believed that since the application of the load occurs over such a short timescale that every *'flaw'* within the sample activates.[196] It is envisioned that a similar study could be carried out where ultrasound evaluation is performed on a group of commercial tiles, which are then separated into groups. A number of tiles from each group would then undergo ballistic evaluation testing. The intention would be to determine if there are differences in the ballistic testing results and microstructure between the tiles within each acoustically similar group.

One of the results of this study showed that the fracture location of flexure bars did not correspond to the location of acoustic anomalies within the NDE property maps. It is believed that these anomalies where the result of acoustic resonance of features within the microstructure. With respect to the commercial tiles, three layers of flexure

bars were machined from each tile. The values of the acoustic attenuation coefficient at each scanning position was the sum total of all of the interactions between the ultrasound energy and microstructural features through the entire depth of the tile. This made it difficult to determine where in the depth of the tile the resonant feature may have been located.

A study could be conducted to determine the identity of the resonant microstructural features. It would involve the selection of three acoustically similar tiles, chosen from a large group of 4" x 4" commercial samples which have undergone ultrasound evaluation. Following this, sections of each tile which correspond to layers of flexure bars would be machined away. For the first tile, the volume corresponding to the top and bottom layers would be removed. For the second tile, the volume corresponding to the bottom and middle layers would be removed, while for the third tile, the material which corresponds to the top and middle layer of bars would be machined away. The resultant machined sections would then be re-scanned, where the values of the acoustic property at each scanning position would then more closely correspond to the volume encompassed by each layer of bars. Flexure bars would then be machined from the layered sections from which the correlation of strength result, fracture position, and acoustic properties would be compared.

The production of targeted samples performed in this dissertation amounted to what would be a worst-case scenario for silicon carbide producers in terms of the changes in the microstructure which were encountered. Tiles were produced after increasing the sintering additive content by five times and also by altering the density of the green body through a drastic reduction in the dry pressing pressure. This produced corresponding

changes in the value of the attenuation coefficient and flexure strength for these sample sets. When compared to the results of the commercial samples, this showed that the ultrasound testing was sensitive to bulk changes within the microstructure between the three samples sets.

It is believed that future work in this area should involve producing additional targeted sample sets to determine the sensitivity of the ultrasound testing to minor changes in the microstructure. This would involve systematic changes to the processing history of these tiles to determine the effect on the measured attenuation coefficient from subtle changes in the microstructure which would likely be encountered during production of commercial silicon carbide tiles. This would involve altering the additive content by 0.1% or 0.5% and determining the effect on attenuation coefficient and strength. Likewise, the effect of subtle changes in green body density or homogeneity on strength, attenuation coefficient, and fired density could be explored by varying the dry pressing pressure and mixing process.

## References


1. Karandikar, P.G., et al., *A Review of Ceramics for Armor Applications*, in *Advances in Ceramic Armor IV: Ceramic Engineering and Science Proceedings, Volume 29, Issue 6*. 2009, John Wiley & Sons, Inc. p. 163-175.
2. Prochazka, S. and R.M. Scanlan, *Effect of Boron and Carbon on Sintering of SIC.* Journal of the American Ceramic Society, 1975. **58**(1-2): p. 72-72.
3. van Rijswijk, W. and D.J. Shanefield, *Effects of Carbon as a Sintering Aid in Silicon Carbide.* Journal of the American Ceramic Society, 1990. **73**(1): p. 148-149.
4. Shaffer, P.T.B., *A Review of the Structure of Silicon Carbide.* Acta Cryst., 1968. **25**: p. 23.
5. Lundquist, D., *On the Crystal Structure of Silicon Carbide and its Content of Impurities.* Acta Crystallographica Section B, 1948. **2**: p. 177-191.
6. Jepps, N.W. and T.F. Page, *Polytypic transformations in silicon carbide.* Progress in Crystal Growth and Characterization, 1983. **7**(1–4): p. 259-307.
7. Cheung, R., ed. *Silicon Carbide Microelectromechanical Systems for Harsh Environments*. 2006, Imperial College Press: London, UK.
8. Ramsdell, L.S., *Studies on silicon carbide*. 1947: Mineralogical Society of America.
9. Shih, C.J., *DYNAMIC DEFORMATION OF SILICON CARBIDE*, in *Materials Science*. 1998, University of California San Diego: San Diego. p. 355.
10. Schwetz, K.A., *Silicon Carbide Based Hard Materials*, in *Handbook of Ceramic Hard Materials*. 2008, Wiley-VCH Verlag GmbH. p. 683-748.
11. Leatherman, G.L. and R.N. Katz, *Superalloys, Supercomposites and Superceramics*. 1989, New York: Academic Press.
12. Madar, R., *Materials science: Silicon carbide in contention.* Nature, 2004. **430**(7003): p. 974-975.
13. Liethschmidt, K. and J. Garbes, *Silicon Carbide*, in *Ullmann's Encyclopedia of Industrial Chemistry*. 2000, Wiley-VCH Verlag GmbH & Co. KGaA.
14. Biswas, K., *LIQUID PHASE SINTERING OF SIC CERAMICS WITH RARE EARTH SESQUIOXIDES*. 2002, Max Planck Institute for Metallurgy: Stuttgart, Germany. p. 138.
15. Morrell, R., *Ceramics, Structural*, in *Kirk-Othmer Encyclopedia of Chemical Technology*. 2000, John Wiley & Sons, Inc.
16. Wright, N.G., *Silicon Carbide*, in *Kirk-Othmer Encyclopedia of Chemical Technology*. 2000, John Wiley & Sons, Inc.
17. *Ceramic Armor*. Available from: http://www.hexoloy.com/product-applications/armor/armor.
18. *Hexoloy SA Silicon Carbide*. Available from: http://www.hexoloy.com/data-sheets/silicon-carbide-products/pdf/b-1045.pdf.
19. Schneider, S.J., *Engineered Materials Handbook: Ceramics and Glasses*, ASM International.
20. Holmquist, T.J., et al., *A Ceramic Armor Material Database*, U.S.A. TARDEC, Editor. 1999, TARDEC: Warren, MI. p. 240.

21. Telle, R., *Boride and Carbide Ceramics*, in *Materials Science and Technology*. 2006, Wiley-VCH Verlag GmbH & Co. KGaA.
22. Medvedovski, E., *Alumina Ceramics for Ballistic Protection Part 1.* American Ceramic Society Bulletin, 2002. **81**(3): p. 27-32.
23. Sandstrom, D.J., *Armor anti-Armor materials by design.* Los Alamos Science 1989. **Summer 1989**: p. 15.
24. Martin, S.R., *EXPERIMENTAL CHARACTERIZATION OF THE EFFECT OF MICROSTRUCTURE ON DYNAMIC BEHAVIOR OF SiC*, in *Mechanical Engineering*. 2004, Georgia Institute of Technology: Atlanta. p. 99.
25. LaSalvia, J.C., *Recent Progress on the Influence of Microstructure and Mechanical Properties on Ballistic Performance.* Ceramic Transactions, 2002. **134**: p. 557-570.
26. Normandia, J., *Ceramics Research Leads to Improved Armor Performance.* AMPTIAC, 2004. **8**(4): p. 9.
27. Fink, B.K., *Performance Metrics for Composite Integral Armor.* Journal of Thermoplastic Composite Materials, 2000. **13**: p. 417-431.
28. Ray, D.A. and e. al. *Effect of Microstructure and Mechanical Properties on Ballistic Performance of SiC-Based Ceramics*. in *30th International Conference on Advanced Ceramics and Composites*. 2005.
29. *Mineral Data Processing*. 2005 [cited 2012 1-16]; Available from: http://www.handbookofmineralogy.org/pdfs/moissanite.pdf.
30. Brezeanu, G., *Silicon Carbide (SiC): A Short History and an Analytical Approach for SiC Power Device Design.* Proceedings of the 2005 International Semiconductor Conference, 2005. **2**: p. 345-348.
31. Acheson, E.G., *Production of Artificial Crystalline Carbonaceous Materials*, U.S.P. Office, Editor. 1893: United States.
32. Gupta, G., et al., *Heat-transfer model for the acheson process.* Metallurgical and Materials Transactions A, 2001. **32**(6): p. 1301-1308.
33. Sone, H., T. Kaneko, and N. Miyakawa, *In situ measurements and growth kinetics of silicon carbide chemical vapor deposition from methyltrichlorosilane.* Journal of Crystal Growth, 2000. **219**(3): p. 245-252.
34. Hoerner, A., J. Vierhaus, and E.P. Burte, *Chemically vapor-deposited silicon carbide films for surface protection.* Surface and Coatings Technology, 1998. **100–101**(0): p. 149-152.
35. Coble, R.L. and J.E. Burke, *Sintering in Ceramics*. Progress in Ceramic Science, ed. J.E. Burke. Vol. 3. 1963, New York: Pergamon Press.
36. Braginsky, M., V. Tikare, and E. Olevsky, *Numerical simulation of solid state sintering.* International Journal of Solids and Structures, 2005. **42**(2): p. 621-636.
37. Barsoum, M.W., *Fundamentals of Ceramics*. Vol. 1. 1997, New York: The McGraw-Hill Companies, Inc.
38. Reed, J.S., *Principle of Ceramics Processing 2nd edition*. 1995, John Wiley & Sons Inc.: Alfred,NY.
39. Kingery, W.D., H.K. Bown, and D.R. Uhlmann, *Introduction to Ceramics*. 2nd ed. 1976, New York, NY: John Wiley & Sons.
40. Prochazka, S. and W.S. Coblenz, *Silicon carbide-boron carbide sintered body*, U.S.P. Office, Editor. 1978: United States.

41. Rączka, M., et al., *Effect of carbon content on the microstructure and properties of silicon carbide-based sinters.* Materials Characterization, 2001. **46**(2-3): p. 245-249.
42. Lange, F.F. and T.K. Gupta, *Sintering of SiC with Boron Compounds.* Journal of the American Ceramic Society, 1976. **59**(11-12): p. 537-538.
43. Alliegro, R.A., L.B. Coffin, and J.R. Tinklepaugh, *Pressure-Sintered Silicon Carbide.* Journal of the American Ceramic Society, 1956. **39**(11): p. 386-389.
44. Aalund, R. *Spark Plasma Sintering*. 2008 [cited 2011 3-28]; Available from: www.thermaltechnology.com/pdf/SPS%20Reprint%20may08.pdf.
45. Guillard, F., et al., *Densification of SiC by SPS-effects of time, temperature and pressure.* Journal of the European Ceramic Society, 2007. **27**(7): p. 2725-2728.
46. Tokita, M., *Mechanism of Spark Plasma Sintering*. 1999, Sumitomo Coal Mining Company, Ltd.: Tokyo, Japan. p. 13.
47. Maddrell, E.R., *Pressureless sintering of silicon carbide.* Journal of Materials Science Letters, 1987. **6**(4): p. 486-488.
48. Omori, M. and H. Takei, *Pressureless Sintering of SiC.* Journal of the American Ceramic Society, 1982. **65**(6): p. c92-c92.
49. Cannon, W.R., et al., *Ceramics, Advanced Structural Products*, in *Ullmann's Encyclopedia of Industrial Chemistry*. 2000, Wiley-VCH Verlag GmbH & Co. KGaA.
50. Stobierski, L. and A. Gubernat, *Sintering of Silicon Carbide I. Effect of Carbon.* Ceramics International, 2003. **29**(3): p. 287-292.
51. Ermer, E., P. Wiesław, and S. Ludosław, *Influence of sintering activators on structure of silicon carbide.* Solid State Ionics, 2001. **141-142**(0): p. 523-528.
52. Stobierski, L. and A. Gubernat, *Sintering of Silicon Carbide II. Effect of Boron.* Ceramics International, 2003. **29**(4): p. 355-361.
53. Hamminger, R., G. Grathwohl, and F. Thuimmler, *Microanalytical Investigation of Sintered SiC.* Journal of Material Science, 1983. **18**(2).
54. Clegg, W.J., *Role of Carbon in the Sintering of Boron-Doped Silicon Carbide.* Journal of the American Ceramic Society, 2000. **83**(5): p. 1039-1043.
55. Miller, P.D., J.G. Lee, and I.B. Cutler, *The Reduction of Silica with Carbon and Silicon Carbide.* Journal of the American Ceramic Society, 1979. **62**(3-4): p. 147-149.
56. Prochazka, S., C.A. Johnson, and R.A. Giddings. *Atmosphere Effects in Sintering of Silicon Carbide*. in *International Symposium on Densification of Oxide and Non-Oxide Ceramics*. 1979. Hakone, Japan.
57. Pultz, W.W. and W. Hertl, *SiO2+SiC reaction at elevated temperatures. Part 1.-Kinetics and mechanism.* Transactions of the Faraday Society, 1966. **62**: p. 2499-2504.
58. Gu, H., Y. Shinoda, and F. Wakai, *Detection of Boron Segregation to Grain Boundaries in Silicon Carbide by Spatially Resolved Electron Energy-Loss Spectroscopy.* Journal of the American Ceramic Society, 1999. **82**(2): p. 469-472.
59. Greskovich, C. and J.H. Rosolowski, *Sintering of Covalent Solids.* Journal of the American Ceramic Society, 1976. **59**(7-8): p. 336-343.
60. Ziccardi, C., et al., *Means of Using Advance Processing to Eliminate Anomalous Defects on SiC Armor*, in *Advances in Ceramic Armor: A Collection of Papers*

*Presented at the 29th International Conference on Advanced Ceramics and Composites, January 23-28, 2005, Cocoa Beach, Florida, Ceramic Engineering and Science Proceedings*. 2008, John Wiley & Sons, Inc. p. 271-277.

61. Demirbas, M.V., *MICROSTRUCTURE-PROPERTY RELATIONSHIP IN SILICON CARBIDE ARMOR CERAMICS*, in *Materials Science and Engineering*. 2008, Rutgers the State Univ. of New Jersey: Piscataway, NJ. p. 240.
62. Hamminger, R., *Carbon Inclusions in Sintered Silicon Carbide.* Journal of the American Ceramic Society, 1989. **72**(9): p. 1741-1744.
63. Zhang, Y., et al., *Characterization of processing pores and their relevance to the strength in alumina ceramics.* J. Mater. Res., 1999. **14**: p. 3370-3374.
64. Hamminger, R., G. Grathwohl, and F. Thümmler, *Microanalytical investigation of sintered SiC Part 1. Bulk Material and Inclusions.* Journal of Materials Science, 1983. **18**(2): p. 353-364.
65. Zhang, X.F., M.E. Sixta, and L.C. De Jonghe, *Secondary Phases in Hot-Pressed Aluminum-Boron-Carbon–Silicon Carbide.* Journal of the American Ceramic Society, 2001. **84**(4): p. 813-820.
66. Bakas, M.P., V.A. Greenhut, and D.E. Niesz, *Anomalous Defects and Dynamic Failure of Armor Ceramics.* International Journal of Applied Ceramic Technology, 2004. **1**(3): p. 8.
67. Obata, S., et al., *Fabrication of dense silicon carbide through aqueous slurries containing well-dispersed carbon as a sintering aid.* Journal of Materials Science, 2005. **40**(3): p. 757-760.
68. Rosa, L.G., et al., *A method to distinguish extrinsic and intrinsic fracture-origin populations in monolithic ceramics.* Journal of the European Ceramic Society, 2006. **26**(16): p. 3887-3895.
69. Bourdillon, A.J., et al., *An application of EELS in the examination of inclusions and grain boundaries of a SiC ceramic.* Journal of Microscopy, 1981. **124**(1): p. 49-56.
70. Quinn, J.B. and G.D. Quinn, *A practical and systematic review of Weibull statistics for reporting strengths of dental materials.* Dental Materials, 2010. **26**(2): p. 135-147.
71. Wachtman, J.B., W.R. Cannon, and M.J. Matthewson, *Mechanical Properties of Ceramics*. 2nd ed. 2009, New York, NY: John Wiley & Sons, Inc.
72. Quinn, G.D. and R. Morrell, *Design Data for Engineering Ceramics: A Review of the Flexure Test.* Journal of the American Ceramic Society, 1991. **74**(9): p. 2037-2066.
73. Griffith, A.A., *The Phenomena of Rupture and Flow in Solids.* Philosophical Transactions of the Royal Society of London, 1921. **221**(A): p. 163-198.
74. Gaskell, D.R., *Introduction to the Thermodynamics of Materials*. 3rd ed. 1995, Washington, DC: Edwards Brothers, Inc.
75. Inglis, C.E. *Stresses in a Plate Due to the Presence of Cracks and Sharp Corners*. in *54th Session of Institution of Naval Architects*. 1913.
76. Irwin, G.R., *Onset of fast crack propagation in high strength steel and aluminum alloys*. 1956, Naval Research Lab, Defense Technical Information Center: Washington D.C.

77. Young, W.C., R.J. Roark, and R.G. Budynas, *Roark's Formulas for Stress and Strain*. 2002: McGraw-Hill.
78. *Creep and Stress Rupture Properties*. Available from: http://www.ndt-ed.org/EducationResources/CommunityCollege/Materials/Mechanical/Creep.htm.
79. Wachtman, J.B., *Mechanical Properties of Ceramics*. 1996, New York: Wiley - Interscience.
80. Materials, A.S.f.T.a., *Standard Test Method for Flexural Strength of Advanced Ceramics at Ambient Temperature*. 2008.
81. *Extreme Value Distributions*. Available from: http://www.mathwave.com/articles/extreme-value-distributions.html.
82. Weibull, W., *A Statistical Distribution Function of Wide Applicability*. ASME Journal of Appliced Mechanics, Transactions of the American Society of Mechanical Engineers, 1951: p. 293-297.
83. Kitchens, L.J., *Exploring Statistics: A Modern Introduction to Data Analysis and Inference*. 2nd ed. 1998, Pacific Grove, CA: Duxbury Press.
84. Stewart, J., *Calculus: Early Transcendentals*. 3rd ed. 1995, Pacific Grove, CA: Brooks/Cole Publishing Company.
85. *What is Linear Regression?* ; Available from: http://stattrek.com/regression/linear-regression.aspx.
86. Varner, J.R., *Descriptive Fractography*, in *Engineered Materials Handbook: Ceramics and Glasses*, A.I.H. Committee, Editor. 1991, ASM International. p. 1217.
87. Cutnell, J.D. and K.W. Johnson, *Physics*. 4 ed. 1998, New York: Wiley.
88. *Wave Propagation*. [cited 2011 4-27]; Available from: http://www.ndt-ed.org/EducationResources/CommunityCollege/Ultrasonics/Physics/wavepropagation.htm.
89. Bhardwaj, M.C., *Evolution, Practical Concepts and Examples of Ultrasonic NDC*. Ceramic Monographs, 1992: p. 7.
90. *Modes of Sound Wave Propagation*. Available from: http://www.ndt-ed.org/EducationResources/CommunityCollege/Ultrasonics/Physics/modepropagation.htm.
91. Serway, R.A. and R.J. Beichner, *Physics for Scientists and Engineers, Fifth Edition*. 2000: USA.
92. Rossing, T., *The Science of Sound*. 1990, Reading, MA: Addison-Wesley.
93. Finch, R.D., *Introduction to Acoustics* 2005, Upper Saddle River, NJ: Pearson Education 653.
94. Kuttruff, H., *Ultrasonics Fundamentals and Applications*. 1991, Elsevier Applied Science: New York.
95. Ghatak, A. and K. Thyagarajan, *Introduction to Fiber Optics*. 1 ed. 1998, Cambridge, UK: Cambridge University Press.
96. Senior, J.M., *Optical Fiber Communications, Principles and Practice*. 2 ed. 1992, Hertfordshire, UK: Prentice Hall Europe. 921.
97. Krautkramer, J. and H. Krautkramer, *Ultrasonic Testing of Materials*. 4th Fully Revised ed. 1990, Berlin: Springer-Verlag.

98. Brennan, R.E., *ULTRASONIC NONDESTRUCTIVE EVALUATION OF ARMOR CERAMICS*, in *Materials Science and Engineering* 2007, Rutgers, the State University of New Jersey: Piscataway, NJ. p. 521.
99. Bhardwaj, M.C. and A.S. Bhalla, *Non Destructive Characterization of Superconductors*. 1991, Chapman and Hall. p. 210-213.
100. Brown, A.E., *RATIONALE AND SUMMARY OF METHODS FOR DETERMINING ULTRASONIC PROPERTIES OF MATERIALS AT LAWRENCE LIVERMORE NATIONAL LABORATORY*. 1997, Lawrence Livermore National Laboratory.
101. Zhang, C. and D. Gross, *On Wave Propagation in Elastic Solids with Cracks*. 1998, Computational Mechanics Publications: Boston, USA.
102. Achenbach, J.D., *Quantitative nondestructive evaluation.* International Journal of Solids and Structures, 2000. **37**: p. 13-27.
103. *National Institute of Standards and Technology Property Data Summaries for Advanced Materials*. Available from: http://www.ceramics.nist.gov/srd/summary/advmatdb.htm/.
104. Aslan, M., et al., *Relations Between Microstructure and Mechanical Properties of Pressureless Sintered SiC.* Ceramic Transactions, 1995. **51**: p. 757-761.
105. *A Summary of the Early Development of Ultrasonics Prior to the 1950s Leading to Medical Applications*. Available from: http://www.ob-ultrasound.net/ultrasonics_history.html/.
106. *Reflection and Transmission Coefficients*. Available from: http://www.ndt-ed.org/EducationResources/CommunityCollege/Ultrasonics/Physics/reflectiontransmission.htm.
107. Chiffoleau, G.J.A., T.A. Steinberg, and M. Veidt, *Reflection of structural waves at a solid/liquid interface.* Ultrasonics, 2003. **41**: p. 347-356.
108. *Refraction and Snell's Law*. Available from: http://www.ndt-ed.org/EducationResources/CommunityCollege/Ultrasonics/Physics/refractionsnells.htm.
109. Mix, P.E., *Introduction to Nondestructive Testing*. 1987, New York: John Wiley & Sons.
110. *American Society of Nondestructive Testing.* [cited 2011 3-30]; Available from: www.asnt.org/.
111. Lynnworth, L.C., *Industrial Applications of Ultrasound -A Review II. Measurements, Tests, and Process Control Using Low-Intensity Ultrasound.* IEEE Transactions on sonics and ultrasonics, 1975. **22**(2): p. 31.
112. Bray, D.E. and R.K. Stanley, *Nondestructive Evaluation A Tool in Design, Manufacturing, and Service*. 1997, New York: CRC Press.
113. Bottiglieri, S. and R.A. Haber, *Corrective Techniques for Ultrasonic Nondestructive Evaluation.* Proceedings of the 34th ICACC, 2010.
114. Flax, L. and H. Uberall, *Resonant scattering of elastic waves from spherical solid inclusions.* J. Acoust. Soc. Am., 1980. **67**: p. 1432-1442.
115. Uberall, H., et al., *Dynamics of acoustic resonance scattering from spherical targets: Application to gas bubbles in fluids.* J. Acoust. Soc. Am., 1979. **66**(4): p. 12.

116. Bottiglieri, S., et al. *Non-Destructive Ultrasound Characterization (NDC) of High-Density, High-Hardness Ceramics*. in *Ceramic, Composites, and Optical Materials Center Meetings*. 2010. Rutgers University.
117. Baaklini, G.Y., E.R. Generazio, and J.D. Kiser, *High-Frequency Ultrasonic Characterization of Sintered Silicon Carbide.* J. Am. Ceram. Soc., 1989. **72**: p. 383-387.
118. Vary, A., *Materials Analysis by Ultrasonics Metals, Ceramics, Composites*. 1987, Noyes Data Corporation: New Jersey.
119. Beyer, R.T. and S.V. Letcher, *Physical Ultrasonics*. 1969, Academic Press: New York.
120. Dukhin, A.S. and P.J. Goetz, *Ultrasound for Characterizing Colloids: Particle Sizing, Zeta Potential Rheology*. 2002, Amsterdam, Netherlands: Elsevier Science B.V.
121. Bhatia, A.B., *Ultrasonic Absorption*. 1967, Oxford: Clarendon Press.
122. Portune, A.R., *NONDESTRUCTIVE ULTRASONIC CHARACTERIZATION OF ARMOR GRADE SILICON CARBIDE*, in *Materials Science and Engineering* 2010, Rutgers, the State University of New Jersey Piscataway, NJ. p. 489.
123. Ishimaru, A., *Theory and Application of Wave Propagation and Scattering in Random Media.* Proceedings of the IEEE, 1977. **65**(7): p. 32.
124. Evans, A.G., et al., *Ultrasonic attentuation in ceramics.* J. Appl. Phys., 1978. **49**(5): p. 11.
125. Portune, A.R., S. Bottiglieri, and R.A. Haber, *Non-Destructive Evaluation (NDE) of Ceramics*. 2010, Rutgers University: Ceramics, Composites, and Optical Materials Center: Piscataway.
126. Urick, R.J., *The Absorption of Sound in Suspensions of Irregular Particles.* THE JOURNAL OF THE ACOUSTICAL SOCIETY OF AMERICA, 1948. **20**: p. 283-289.
127. Epstein, P.S. and R.R. Carhart, *The Absorption of Sound in Suspensions and Emulsions.*I. Water Fog in Air.* J. Acoust. Soc. Am., 1953. **25**(3): p. 13.
128. Allegra, J.R. and S.A. Hawley, *Attenuation of Sound in Suspensions and Emulsions: Theory and Experiments.* J. Acoust. Soc. Am., 1971. **51**(5): p. 20.
129. Luo, L., et al., *Ultrasound absorption and entropy production in biological tissue: a novel approach to anticancer therapy.* Diagnostic Central, 2006. **1**(35): p. 6.
130. Sehgal, C.M., *Ultrasonic Absorption and Dispersion in Biological Media: A postulated Model.* Journal of the Acoustical Society of America, 1982. **72**(6): p. 1711-1718.
131. Burlak, G.N. and V. Ostrovskii, *Acoustic hysteresis phenomena due to the dislocation nonlinearity in crystals.* Technical Physics Letters, 1997. **23**(9): p. 725-726.
132. Lucke, K., *Ultrasonic Attenuation Caused by Thermoelastic Heat Flow.* Journal of Applied Physics, 1956. **27**: p. 1433-1438.
133. Hartmann, B. and J. Jarzynski, *Ultrasonic Hysteresis Absoprtion in Polymers.* Journal of Applied Physics, 1972. **43**(11): p. 9.
134. Zener, C., *Internal Friction in Solids.* Physical Review, 1937. **52**: p. 6.
135. Zener, C., *Internal Friction in Solids I. General Theory of Thermoelastic Internal Friction.* Physical Review, 1940. **52**(152): p. 15.

136. Zener, C., *Internal Friction in Solids II. General Theory of Thermoelastic Internal Friction.* Physical Review, 1938. **53**: p. 10.
137. Lessen, M., *Thermoelastic Damping at the Boundary Between Dissimilar Solids*.* Journal of Applied Physics, 1956. **28**(3): p. 364-366.
138. Greene, G.A., Y.I. Cho, and A. Bar-Cohen, *Advances in Heat Transfer*. Vol. 41. 2009, San Diego: Academic Press.
139. Ying, C.F. and R. Truell, *Scattering of a Plane Longitudinal Wave by a Spherical Obstacle in an Isotropically Elastic Solid.* Journal of Applied Physics, 1956. **27**(6): p. 12.
140. Nicoletti, D.W., N. Bilgutay, and B. Onaral, *SCALING PROPERTIES OF ATTENUATION AND GRAIN SIZE.* ULTRASONICS SYMPOSIUM, 1990: p. 1119-1122.
141. Hirsekorn, S., *The scattering of ultrasonic waves by polycrystals.* J. Acoust. Soc. Am., 1982. **72**: p. 1021-1031.
142. Rayleigh, *Theory of Sound*. 1877, London, UK: Macmillan and Company.
143. Strutt, J.W., *The Theory of Sound*. Vol. II. 1945, New York: Dover Publications.
144. Mie, G., *Beitrage zur Optik truber Medien, speziell kolloidaler Metallosungen.* Ann. Phys., 1908(330): p. 377-445.
145. Cox, A.J., *An experiment to measure Mie and Rayleigh total scattering cross sections*, A.J. DeWeerd, Editor. 2002, American Association of Physics Teachers: American Journal of Physics. p. 620-625.
146. Papadakis, E.P., *Ultrasonic Instruments and Devices Reference for Modern Instrumentation, Techniques, and Technology*. 1999, USA: Academic Press.
147. Luo, L., et al., *Effects of Mn doping on dielectric and piezoelectric properties of $0.71Pb(Mg_{1/3}Nb_{1/3})O_3$-$0.29PbTiO_3$ single crystals.* Applied Physics Letters, 2007. **90**.
148. *Piezoelectric Ceramic Products*. [cited 2011 5-4]; Available from: http://www.piceramic.de/pdf/KATALOG_english.pdf.
149. *Characterisitics of Piezoelectric Transducers*. 2010 [cited 2011 5-4]; Available from: http://www.ndt-ed.org/EducationResources/CommunityCollege/Ultrasonics/EquipmentTrans/characteristicspt.htm.
150. *Olympus - Ultrasonic Transducers Technical Notes*. 2010 [cited 2011 5-5]; Available from: http://www.olympus-ims.com/en/knowledge/.
151. *Transducer Types*. [cited 2011 5-9]; Available from: http://www.ndt-ed.org/EducationResources/CommunityCollege/Ultrasonics/EquipmentTrans/transducertypes.htm.
152. *Inside a Phased Array Transducer*. [cited 2011 5-9]; Available from: http://www.olympus-ims.com/en/ndt-tutorials/transducers/inside/.
153. *JSR Ultrasonic Pulser-Receivers*. [cited 2011; Available from: http://www.jsrultrasonics.com/pulsereceivers.html.
154. *TRPP 5810 Remote Pulser/Preamplifier*. Available from: http://www.olympus-ims.com/en/trpp5810/.
155. *Pulser-Receivers*. [cited 2011 5-10]; Available from: http://www.ndt-ed.org/EducationResources/CommunityCollege/Ultrasonics/EquipmentTrans/pulserreceivers.htm.

156. *Gage - High Speed PCI Digitizers*. [cited 2011 5-11]; Available from: http://www.gage-applied.com/Products/pci_digitizers.htm.
157. *Techno Inc. CNC Routers. Linear Motion. Grippers*. Available from: http://www.techno-isel.com/.
158. *The Ultran Group. Ultrasound Redefined*. [cited 2011 5-11]; Available from: http://www.ultrangroup.com/.
159. Kennelly, A.E. and R.P. Siskind, *The Acoustic Impedance of Straight Cylindrical Air Columns in Brass Tubes.* Proceedings of the American Philosophical Society, 1927. **66**: p. 89.
160. Charlesworth, J.P. and J.A.G. Temple, *Engineering applications of ultrasonic time-of-flight diffraction*. 2001: Research Studies Press.
161. Kautz, H.E., *Acousto-Ultrasonics to Assess Material and Structural Properties*. 2002, Cleveland State University. p. 45.
162. Blitz, J. and G. Simpson, *Ultrasonic Methods of Non-destructive Testing*. 1996, London: Chapman and Hall.
163. Schmerr, L.W., *Fundamentals of Ultrasonic Nondestructive Evaluation A Modeling Approach*. 1998, Plenum Press: New York.
164. Bouda, A.B., S. Lebaili, and A. Benchaala, *Grain size influence on ultrasonic velocities and attenuation.* NDT&E International, 2003. **36**: p. 1-5.
165. Slusark, D. and R.A. Haber, *Defining Microstructural Tolerance Limits of Defects for SiC Armor*, in *Ceramic and Composite Materials Center*. 2008: Piscataway, NJ. p. 1-13.
166. *Introduction to Nondestructive Testing*. [cited 2011 4-26]; Available from: www.ndt.net/article/icem2004/papers/193/193.htm.
167. Roth, D.J., et al., *COMMERCIAL IMPLEMENTATION OF ULTRASONIC VELOCITY IMAGING METHODS VIA COOPERATIVE AGREEMENT BETWEEN NASA LEWIS RESEARCH CENTER AND SONIX, INC.*, NASA, Editor. 1996, Nasa: Cleveland, OH. p. 37.
168. Bottiglieri, S., *THE EFFECT OF MICROSTRUCTURE IN ALUMINUM OXIDE CERAMICS ON ACOUSTIC LOSS MECHANISMS*, in *Materials Science and Engineering* 2011, Rutgers, The State University of New Jersey: Piscataway, NJ. p. 375.
169. Ensminger, D., *Ultrasonics: Fundamentals, Technology, and Applications*. Vol. 2nd edition. 1988, New York, NY: Marcel Dekker, Inc.
170. Brennan, R., et al., *Elastic Property Mapping Using Ultrasonic Imaging*, in *Advances in Ceramic Armor III: Ceramic and Engineering Science Proceedings, Volume 28, Issue 5*. 2009, John Wiley & Sons, Inc. p. 213-221.
171. Callister, W., *Materials Science and Engineering: an Introduction.4th Edition*. 1997, John Wiley and Sons Inc.: USA.
172. Olympus, *OmniScan MXU Software: User's Manual*. 2007.
173. *Bureau International des Poids et Mesures*. Available from: http://www.bipm.org/utils/common/pdf/si_brochure_8_en.pdf.
174. *Basic Principles of Ultrasonic Testing*. [cited 2010 4-28]; Available from: http://www.ndt-ed.org.

175. Ness, E.A. and W. Rafaniello, *Origin of Density Gradients in Sintered β-Silicon Carbide Parts.* Journal of the American Ceramic Society, 1994. **77**(11): p. 2879-2884.
176. *ASTM C1161-02c: Standard Test Method for Flexural Strength of Advanced Ceramics at Ambient Temperature.* ASTM International, 2006.
177. Lide, D.R., *CRC Handbook of Chemistry and Physics: A Ready-reference Book of Chemical and Physical Data*. 2004: CRC Press.
178. Knudsen, F.P., *Dependence of Mechanical Strength of Brittle Polycrystalline Specimens on Porosity and Grain Size.* Journal of the American Ceramic Society, 1959. **42**(8): p. 376-387.
179. *Part II. Working with ImageJ*. Available from: http://rsbweb.nih.gov/ij/docs/guide/userguide-Part-II.html.
180. Russ, J.C., *Computer-Assisted Microscopy: The Measurement and Analysis of Images*. 1990, New York, NY: Springer.
181. Annese, J., Bomas Machine Specialities, *Tolerance Considerations for Bend Bar Machining*. 2011.
182. Quinn, G.D., *Fractography of Ceramics and Glasses*. 2006, Washington D.C.: US Government Printing Office.
183. Wereszczak, A.A., et al., *Effects of Machining on the Uniaxial and Equibiaxial Flexure Strength of CAP3 AD-995 Al2O3*, ARL, Editor. 2005, ARL: Aberdeen, MD. p. 66.
184. Richerson, D.W., *Forming and Predensification, and Nontraditional Densification Processes*, in *Engineered Materials Handbook: Ceramics and Glasses*, A.I.H. Committee, Editor. 1991, ASM International. p. 1217.
185. Matsumoto, R.L.K., *Mechanical Consolidation*, in *Engineered Materials Handbook: Ceramics and Glasses*, A.I.H. Committee, Editor. 1991, ASM International. p. 1217.
186. Lukasiewicz, S.J., *Granulation and Spray Drying*, in *Engineered Materials Handbook: Ceramics and Glasses*, A.I.H. Committee, Editor. 1991, ASM International. p. 1217.
187. Yan, M.F., *Solid-State Sintering*, in *Engineered Materials Handbook: Ceramics and Glasses*, A.I.H. Committee, Editor. 1991, A.I.M. International. p. 1217.
188. Xu, W. and J.J. Kaufman, *Diffraction Correction Methods for Insertion Ultrasound Attenuation Estimation.* IEEE transactions on Biomedical Engineering, 1993. **40**: p. 563-570.
189. Kingery, W.D., *Factors Affecting Thermal Stress Resistance of Ceramic Materials.* Journal of the American Ceramic Society, 1955. **38**(1): p. 3-15.
190. Datta, M.S., A.K. Bandyopadhyay, and B. Chaudhuri, *Sintering of nano crystalline α silicon carbide by doping with boron carbide.* Bulletin of Materials Science, 2002. **25**(3): p. 181-189.
191. *ImageJ User Guide*. Available from: http://rsbweb.nih.gov/ij/docs/guide/userguide-26.html#toc-Subsection-26.8.
192. Wang, J.C., *Young's modulus of porous materials.* Journal of Materials Science, 1984. **19**(3): p. 801-808.

193. Spriggs, R.M., *Expression for Effect of Porosity on Elastic Modulus of Polycrystalline Refractory Materials, Particularly Aluminum Oxide.* Journal of the American Ceramic Society, 1961. **44**(12): p. 628-629.
194. *Discussion of Ryshkewitch Paper by Winston Duckworth*.* Journal of the American Ceramic Society, 1953. **36**(2): p. 68-68.
195. Coble, R.L. and W.D. Kingery, *Effect of Porosity on Physical Properties of Sintered Alumina.* Journal of the American Ceramic Society, 1956. **39**(11): p. 377-385.
196. Paliwal, B. and K.T. Ramesh, *An interacting micro-crack damage model for failure of brittle materials under compression.* Journal of the Mechanics and Physics of Solids, 2008. **56**(3): p. 896-923.

# Curriculum Vita

Douglas M. Slusark

## Education:

| | |
|---|---|
| 2012 | PhD., Materials Science and Engineering, Rutgers University |
| 2011 | M.S., Materials Science and Engineering, Rutgers University |
| 2001 | B.S., Ceramic and Materials Engineering, Rutgers University |

## Work Experience:

| | |
|---|---|
| 2006 – 2012 | Graduate Research Assistant, Department of Materials Science and Engineering, Rutgers University, Piscataway, NJ |
| 2004 – 2006 | Optical Component Reliability Engineer, Government Communications Laboratory, Lucent Technologies, Murray Hill, NJ |
| 2001 – 2002 | Fiber Optics Measurements Engineer, Specialty Fiber Devices, Lucent Technologies, Somerset, NJ |
| 2000 – 2002 | Fiber Optics Splice Engineer, Specialty Fiber Devices, Lucent Technologies, Somerset, NJ |
| 1999 – 2000 | Engineering Intern, Ceramic Magnetics Inc., Fairfield, NJ |

## Publications:

D. Slusark, M.V. Demirbas, A. Portune, S. Miller, R.A. Haber, R. Brennan, W. Green, E. Chin, J. Campbell "Nondestructive Evaluation (NDE) of Sintered Silicon Carbide and Its Correlation to Microstructure and Mechanical Properties." *Proceedings of the Army Science Conference*, 2008

D. Slusark and R.A. Haber "Effect of Microstructural Variability on the Correlation Between non-Destructive Evaluation and Mechanical Properties in Silicon Carbide." 33rd *International Conference and Exposition on Advanced Ceramics and Composites*, 2009

D. Slusark and R.A. Haber "Microstructure-Property Relationship for Ceramic Armor Materials." *34th International Conference and Exposition on Advanced Ceramics and Composites*, 2010

Semi-annual program reports and presentations to representatives of the U.S. Army Research Laboratory and the Ceramic, Composite, and Optical Materials Center (an NSF/Rutgers University Co-operative Center) concerning research progress